# Measurement of Bubble Velocity Vectors in Bubbly Air Water Multiphase Flow

**Suman Raj Pradhan**

**August 2010**

A thesis submitted to the University of Huddersfield in partial fulfilment of the requirements for the degree of Doctor of Philosophy.

The University of Huddersfield

# Declaration

No portion of the work referred to in this thesis has been submitted in support of an application for another degree or qualification of this or any other university or other institute of learning.

**Acknowledgements**

I would like to express my gratitude to my supervisor, Prof. Gary Lucas, for giving me the opportunity to carry out this research. I would also like to thank him for his support and advice during the research, and for reading all the draft copies of this thesis. I would also like to thank my second supervisor Dr. R. Mishra for his support and guidance.

I would like to thank the technicians at the University of Huddersfield for their help in manufacturing, and repairing, the varied equipment that I have needed. I would particularly like to thank Jack Briggs, Dennis Town, Peter Norman, Richard Bailey and David Bray for tolerating me for almost three years and also for their valuable help and support when the technical work had to be carried out. Last not the least I would like to sincerely thank to colleague Dr. X. Zhao for his contribution and expertise that has been put into this research project.

Outside work I would like to acknowledge the endless help and support of my family who I know always meant well even if they didn't show it. Last, but by no means least, I would like to thank Sima Limbu for reading, editing my thesis and her almost endless support and patience throughout the research.

I would also like to thank Hannah Treasure, Christine Hunt and John Wilson for giving some of their valuable time to proof read the chapters from my thesis.

I would also like to acknowledge the financial assistance of the University Of Huddersfield (grant no. REU 010)

# Abstract

Measurement of the volumetric flow rate of each of the flowing components in multiphase flow is often required and this is particularly true in Production Logging applications. Thus, an increasing level of interest has been shown in making flow rate measurements in multiphase flow. A new generation of tomographic instrument, which enables measurement of the instantaneous local velocity vector and the instantaneous local volume fraction of the dispersed phase, is now being introduced. However validation and calibration of such instruments is necessary.

This thesis describes the development of a miniaturised local four-sensor conductivity probe capable of acquiring measurements of the local velocity vector, gas volume fraction and the local axial gas velocity in the bubbly gas-liquid flows. Experimental techniques in which the probe was used to obtain the local gas velocity vector and the local gas volume fraction in a bubbly gas-liquid flow are also described.

High speed cameras are introduced for the measurement of the reference velocity of the bubbles. The camera images are also used to plot the trajectory of any bubble that hits all four-sensor of the probe.

Extensive experimental results showing the distribution of the local gas volume fraction and the local axial, azimuthal and the radial bubble velocity components in vertical and swirling gas-liquid flows are presented.

# Table of Contents

# List of Figures

## List of Tables

# Nomenclature

| | |
|---|---|
| A | Pipe cross sectional area |
| $a_T$ | Major axis of the bubble |
| $b_T$ | Length of minor axis of top part of bubble |
| $D$ | Pipe diameter |
| $d$ | Diameter of bubble |
| $F$ | Frictional pressure loss |
| $f$ | Single phase friction factor |
| $fs$ | Sampling frequency |
| $h$ | Distance between pressure tapings |
| **i, j, k** | unit vectors in x, y and z direction (probe coordinate system(m)) |
| $\mathbf{i_p}, \mathbf{j_p}, \mathbf{k_p}$ | Unit vector in direction $x_p, y_{p,} z_p$ respectively |
| $K$ | Probe calibration factor |
| $M$ | Number of test run at a given set of experimental condition |
| $M_g$ | Gas mass flow rate |
| $m$ | $m^{th}$ test run at the given set of experimental condition |
| $m_1$ | Slope of the major axis of the bubble |
| $m_2$ | Slope of the minor axis of the bubble |

| | |
|---|---|
| $\hat{m}_i$ | Gradient between COG of bubble and $\omega_i$ |
| $N$ | Number of bubble striking sensor |
| $n$ | Refers to relevant value of $n^{th}$ bubble during $m^{th}$ test run |
| $\hat{n}_i$ | The unit vector in the direction of **r** |
| $\hat{n}_v$ | The unit vector in the direction of **V** |
| $P_{atm}$ | Atmospheric pressure |
| $P_{abs}$ | Absolute pressure |
| $Q_g$ | Gas volumetric flow rate ($m^3s^{-1}$) |
| $Q_w$ | Water volumetric flow rate ($m^3s^{-1}$) |
| $R$ | Internal radius of the working section |
| R | Radial position (pipe coordinate system (m)) |
| **r** | Position vector of point of first contact of bubble with sensor 0(m) |
| r | Magnitude of **r** (m) |
| $\mathbf{r_1}$ | Position vector of point of first contact of bubble with sensor 1(m) |
| $r_1$ | Magnitude of **r** (m) |
| S | Axial distance between the front and the rear sensor |
| $T$ | Sampling time (s) |
| $T_{abs}$ | Absolute Temperature |
| $t_{1f,i}$ , $t_{1r,i}$ | Time of first contact with the front and rear sensor for dual probe |

| | |
|---|---|
| $t_{2r,i}$ , $t_{2r,i}$ | Time of last contact with the front sensor for dual probe |
| $t_{dummy}$ | Dummy time threshold |
| $t_{res}$ | Residence time |
| $t_{thres}$ | Time threshold |
| $U_h$ | Homogeneous velocity, |
| $U_{gs}$ | Superficial velocities of gas |
| $U_{ws}$ | Superficial velocities of water |
| $u_{gl}$ | Local axial gas velocity |
| $\mathbf{V}$ | Velocity vector |
| $V_{amp}$ | Output voltage from op amp (V) |
| $V_{in}$ | Circuit input voltage (V) |
| $V_{l,thres}$ | Voltage level threshold |
| $V_{out}$ | Circuit output voltage (V) |
| $\mathbf{V_{bp}}$ | Velocity vector of the bubble relative to the probe coordinate system |
| $\mathbf{V_{btp}}$ | Bubble velocity vector relative to the tank coordinate system |
| $v$ | Velocity magnitude |
| $v_{meas}$ | Measured local velocity |

| | |
|---|---|
| $v_{meas,m,p}$ | Measured mean velocity magnitude of $m^{th}$ flow condition and the $p^{th}$ value of $\alpha_{ref}$ |
| $v_{meas,m,p,n}$ | Measured velocity magnitude of $n^{th}$ bubble $m^{th}$ flow condition and the $p^{th}$ value of $\alpha_{ref}$ |
| $v_r$ | Radial velocity or the velocity at the Y-axis |
| $v_{ref}$ | Reference velocity |
| $v_z$ | Axial velocity or the velocity at the z-axis |
| $v_\theta$ | Azimuthal velocity or the velocity at the X-axis |
| $X_c$, $Y_c$, $Z_c$ | Coordinate of Microscope |
| $x, y, z$ | Probe Coordinate |
| $x_{i,t}$ , $y_{i,t}$ and $z_{i,t}$ | Actual probe dimensions ( for sensitivity analysis) |
| $x_T , y_T , z_T$ | Tank coordinate system |
| $x_0, y_0, z_0$ | Origin of probe coordinate system (and position of sensor 0) (m) |
| $x_1, x_2, x_3$ | $x$ coordinates of sensor 1, 2 and 3 with respect to sensor 0 (m) |
| $\underline{\hat{x}}_p , \underline{\hat{y}}_p , \underline{\hat{z}}_p$ | Probe coordinate system described in Chapter 13 |
| $(x_c , z_c)$ | Centre of gravity (COG) of bubble |
| $(\tilde{x}, \tilde{z})$ | New coordinate system of bubble as described in Section 7.3 |
| $(\hat{x}, \hat{z})$ | Coordinate system of bubble as described in Section 7.3 |

| | |
|---|---|
| $y_1, y_2, y_3$ | $y$ coordinates of sensor 1, 2 and 3 with respect to sensor 0 (m) |
| $z_1, z_2, z_3$ | $z$ coordinates of sensor 1, 2 and 3 with respect to sensor 0 (m) |
| $\alpha$ | Polar angle |
| $\alpha^*$ | Inclination of hinged platform to create polar angle |
| $\alpha_c$ | Calculated polar angle |
| $\alpha_{meas}$ | Measured polar angle |
| $\alpha_{meas,m,p}$ | Measured mean polar angle of $m^{th}$ flow condition and the $p^{th}$ value of $\alpha_{ref}$ |
| $\alpha_{meas,m,p,n}$ | Measured polar angle of $n^{th}$ bubble $m^{th}$ flow condition and the $p^{th}$ value of $\alpha_{ref}$ |
| $\alpha_{ref}$ | Reference polar angle |
| $\alpha_t$ | Actual polar angle (reference for sensitivity analysis) |
| $\beta$ | Azimuthal angle |
| $\beta^*$ | Inclination of hinged platform to create azimuthal angle |
| $\beta_c$ | Calculated azimuthal angle |
| $\beta_{meas}$ | Measured azimuthal angle |

$\beta_{meas,m,p}$ Measured mean azimuthal angle of $m^{th}$ flow condition and the $p^{th}$ value of $\alpha_{ref}$

$\beta_{meas,m,p,n}$ Measured azimuthal angle of $n^{th}$ bubble $m^{th}$ flow condition and the $p^{th}$ value of $\alpha_{ref}$

$\beta_{ref}$ Reference azimuthal angle

$\beta_t$ Actual azimuthal angle (reference for sensitivity analysis)

$\Delta p$ Differential pressure

$\delta t_{0a}$ Time delays equal to zero (s)

$\delta t_{0a}$ Time taken for bubble to cross the sensor 0 (s)

$\delta t_{1,i}$ Time difference between $t_{2r,i}$ and $t_{1f,i}$

$\delta t_{1a}$ $\delta t_{1b}$ Time delay between first bubble contact with the sensor 0 and first and last bubble contacts respectively with sensor 1(s)

$\delta t_{2,i}$ Time difference between $t_{1r,i}$ and $t_{1f,i}$

$\delta t_{2a}$ $\delta t_{2b}$ Time delay between first bubble contact with the sensor 0 and first and last bubble contacts respectively with sensor 2(s)

$\delta t_{3a}$ $\delta t_{3b}$ Time delay between first bubble contact with the sensor 0 and first and last bubble contacts respectively with sensor 1(s)

$\delta t_{11}, \delta t_{22}, \delta t_{33}$ Time intervals defined in equations 2.29, 2.30 and 2.31 respectively

$\delta t_{ii,m,p,n}$ Time interval of $n^{th}$ bubble $m^{th}$ flow condition and the $p^{th}$ value of $\alpha_{ref}$ $(i = 1, 2 \text{ and } 3)$

$\delta t_{ii,m,p}$ Time interval of $m^{th}$ flow condition and the $p^{th}$ value of $\alpha_{ref}$

$\delta t_{ii,meas}$ Measured time intervals $(i = 1, 2 \text{ and } 3)$

$\delta t_{ii,t}$ Actual time intervals $(i = 1, 2 \text{ and } 3)$

$\delta V$ Threshold voltage value

$\varepsilon_{abs,\alpha}$ Absolute error in $\alpha$

$\varepsilon_{abs,\alpha,m,p}$ Absolute error in $\alpha$ for $m^{th}$ flow condition and the $p^{th}$ value of $\alpha_{ref}$

$\varepsilon_{abs,\beta}$ Absolute error in $\beta$

$\varepsilon_{abs,\beta,m,p}$ Absolute error in $\beta$ for $m^{th}$ flow condition and the $p^{th}$ value of $\alpha_{ref}$

$\varepsilon_{v}$ Percentage error in $v$

$\varepsilon_{abs,v,m,p}$ Absolute percentage error in $v$ for $m^{th}$ flow condition and the $p^{th}$ value of $\alpha_{ref}$

$\bar{\varepsilon}_{abs,\alpha,p}$ Mean value of absolute error in measured value of $\varepsilon_{abs,\alpha,m,p}$

$\bar{\varepsilon}_{abs,\beta,p}$ Mean value of absolute error in measured value of $\varepsilon_{abs,\beta,m,p}$

$\bar{\varepsilon}_{abs,v,p}$ Mean value of absolute error in measured value of $\varepsilon_{abs,v,m,p}$

$\boldsymbol{\eta}_{\mathbf{btp}}$ The unit vector in the direction of $\mathbf{V}_{\mathbf{btp}}$

$\lambda_i$ Point lies above the boundary of ellipse with the coordinate $(\hat{x}'_i, \hat{z}'_i)$ with same gradient $\hat{m}_i$.

$\lambda$ Gas volume fraction

$\lambda_l$ The local gas volume fraction

$\overline{\lambda}$ Mean gas volume fraction

$\overline{\lambda}_{ref}$ Reference mean gas volume fraction

$\rho_d$ Density of dispersed phase (air)

$\rho_w$ Density of water

$\rho_m$ Density of mercury

$\sigma_{abs,\alpha,p}$ Standard deviation of absolute error in measured value of $\varepsilon_{abs,\alpha,m,p}$

$\sigma_{abs,\beta,p}$ Standard deviation of absolute error in measured value of $\varepsilon_{abs,\beta,m,p}$

$\sigma_{abs,v,p}$ Standard deviation of absolute error in measured value of $\varepsilon_{abs,v,m,p}$

$\psi$ Inclination of pipe

$\omega_i$ Boundary of the upper part of the image of the bubble with coordinate $(\hat{x}_i, \hat{z}_i)$

# CHAPTER 1

# Introduction

## 1.1. Generalities

The main aim of the research was to design and build a probe that can be used to measure the local velocity vector of the dispersed phase in bubbly multiphase flow. The velocity vector can be defined in terms of a spherical coordinate system which requires velocity magnitude, a polar angle and an azimuthal angle [1-2]. Such a probe could be used to validate the images of the velocity vector obtained using tomographic devices [3]. However, a further objective was to explore other possible applications of this technology and to develop it as an industrial and laboratory tool.

In recent years, there has been an increase in the level of interest shown in flow rate measurements in multiphase flow. This, in part, has been brought about by the metering requirements of the oil and natural gas industries. Measurement of the volumetric flow rate of each of the flowing components is often required. This is particularly true in production logging applications, where it may be necessary to measure the flow rates of oil and water down-hole in vertical and inclined oil wells. Within the University of Huddersfield [1-14], work has previously been undertaken on the study of vertical and inclined multiphase flow. These studies were based on the use of local, dual-sensor conductance probes to obtain the local axial velocity and local volume fraction distribution of the dispersed phase in bubbly multiphase flows [3].

As all the experiments described in this thesis were carried out in a multiphase flow environment, it is wise to describe briefly the basic physics underlying multiphase flows. In general, there is a fundamental division between single phase and multiphase flows. A single phase flow is where the flow consists of only one component; whereas, if more than one component is flowing, it is a multiphase flow. The physics of the flow becomes more extreme and complicated when there is more than one component flowing in the system.

In a multiphase flow, the components that flow together are not mixed into a single fluid. Therefore, a multiphase flow can be gas-liquid, liquid-liquid (e.g. oil–water), liquid-solids, gas-solids, and gas-liquid-solids flows. The current investigation deals with gas-liquid flows, specifically air-water flows. Due to the fact that the behaviour of these types of flow changes with the inclination of the pipe [1], the current project only focuses on air-in-water multiphase flow in vertical pipes.

## 1.2 Types of multiphase flow

Due to the complex nature of the flow, it is difficult to accurately differentiate and define the number of flow regimes that exist in a vertical gas-liquid multiphase flow. However, they can be categorized into four basic types according to the flow structure (see Figure 1.1): (i) Bubbly flow; (ii) Slug flow; (iii) Churn flow and (iv) Annular flow. These flow regimes occur with increasing gas flow rate at a constant liquid flow rate.

The flow structure normally depends on the superficial velocities of the continuous and dispersed phases; in this case, water and air. It also depends on the diameter of the pipe. The *Superficial velocity* (ratio between volume flow rate to cross-sectional area)

of a phase in multiphase flow in a pipe is the velocity that it would have if it was flowing alone.

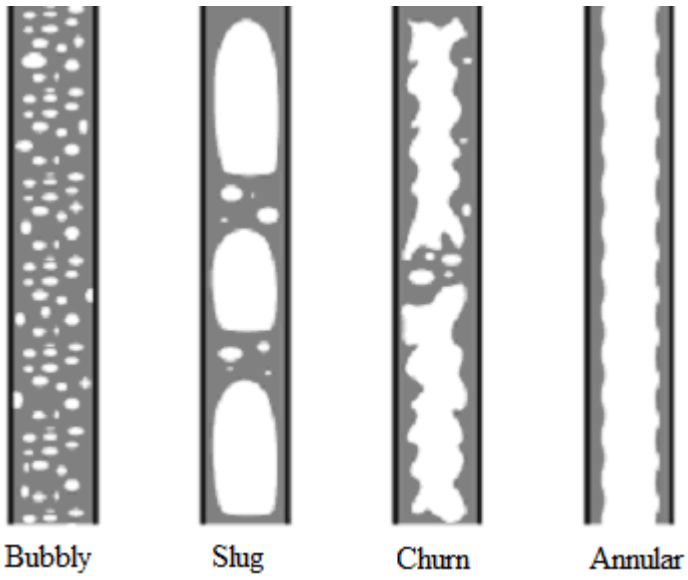


**Figure 1.1 Four different types of vertical gas-liquid multiphase flow, with an increasing proportion of gas from left to right**

***Bubbly flow***: - bubbly flows are frequently encountered in nature. In a bubbly flow, the flow rate of water (continuous phase) is much greater than the flow rate of air (dispersed phase). Bubbly flow is characterized by a distribution of bubbles of various sizes throughout the liquid. In a gas-liquid flow, if the dispersed phase flow rate increases then bubble coalescence occurs.

***Slug flow***: - with an increasing gas flow rate, the coalescence of small gas bubbles creates bigger bubbles and a transition occurs from the bubbly flow regime to the slug flow regime. Slug flow is characterized by large "bullet shaped" gas bubbles which occupy almost the whole cross-section of the pipe, but which do not touch the wall. These "bullet shaped" bubbles are axially separated from each other and between them there is a region where smaller bubbles may exist, immersed in the continuous phase (see Figure 1.1).

***Churn flow***: - if the gas flow rate is further increased, another transition occurs and the churn regime appears. The churn flow regime is characterized by the chaotic behaviour of the gas phase. The cross-section of the pipe is occupied by irregular shaped portions of gas and analysis of this kind of flow regime is extremely difficult.

***Annular flow***: - if the gas flow rate is increased even more, the flow regime becomes annular. This flow regime is characterized by a thin layer of liquid at the pipe wall and the rest of the tube is occupied by fast flowing gas with very small entrained liquid droplets.

In this thesis, the flow regime that is studied is the *bubbly flow regime,* for air-in-water flows.

Some key global parameters that are used to quantify the behaviour of multiphase flows are the *volume fraction* and *actual velocity* of a phase. *Volume fraction* is the fraction of the volume which is occupied by a phase, averaged over the time of interest. It is a dimensionless number between 0 and 1. Average *actual velocity* is the mean phase velocity, again averaged over the time of interest, and is equal to the phase superficial velocity divided by the phase volume fraction.

The properties that are considered in the current research are the local *volume fraction* and the local *velocity vector* of the dispersed phase. In a steady state multiphase flow, both the volume fraction and the velocity vector of the dispersed phase can vary within a given flow cross-section. Values of these properties at a given point in the flow cross-section are referred to as local properties. In many bubbly gas-liquid flows, the local gas bubble velocity is a vector quantity which is not necessarily parallel to the pipe axis. Local flow properties must be distinguished from global flow properties

which refer to the average values of a property over the flow cross-section. A detailed description of the local properties of multiphase flows will be described later in this thesis.

The reason for studying these local properties of multiphase flow is that, in many industries (e.g. oil, chemical and nuclear), knowledge of the local volume fraction and the local velocity profile of the dispersed phase is important for the optimal control of processes, the maximum exploitation of resources, and more importantly, the safety of the personnel. Some reasons why gas velocity and volume fraction profiles are important [6, 15-16] include:

(a) Knowledge of the local gas volume fraction distribution is essential when calculating the pressure gradient in gas-liquid pipelines.
(b) Optimization of chemical processes is essential in chemical engineering applications when bubbling gases into liquid solutions. Thus, knowledge of gas-liquid interface conditions is necessary for determining optimum reaction kinetics.
(c) Advanced nuclear reactor concepts rely on extremely high heat removal rates, which are only possible through liquid boiling. In this case, minor changes in local parameters can drastically change the flow conditions in steam-water systems. As a result, knowledge of the phase volume fraction and velocity distributions is important for producing reliable, accident-safe calculations.[6,15]
(d) Techniques for measuring the local properties of multiphase flows enable the characterisation of such multiphase flows for comparison with and validation of numerical models of multiphase flow.

## 1.3 Application of multiphase flows and the need to measure their properties.

### 1.3.1 Multiphase flow in the oil and gas industry

Multiphase flow in the oil and gas industries can be observed during both the drilling and extraction processes. In an oil well drilling operation, there is a possibility that the drill bit may encounter a pocket of natural gas which rises rapidly through the drilling mud to the surface causing a 'blowout', which can be highly dangerous to operating personnel and extremely damaging to the environment. The initial entry of gas into the well may be detected by the driller as a so called "gas kick" and, if the operator is to take measures to prevent a blowout, it is essential that he knows how quickly the gas will reach the surface. Software which enables drillers to take the necessary measures to prevent blowouts relies heavily on experimental data for the rise velocity of gas in vertical and inclined gas-liquid multiphase flows. An understanding of multiphase fluid mechanics therefore allows the implementation of appropriate control strategies to prevent a well-head explosion or environmental damage due to massive fluid leakage from the well-head.

During the process of extracting the oil from a well, a pump is often placed at the well head. In some cases the oils are too heavy to be pumped, so a process called *enhanced oil recovery* is used that involves drilling a second hole adjacent to the original well, and pumping steam into the second hole. The pressure created by the steam in the oil bearing formation helps to move oil into the original well and up to the surface. In some cases, water and gases are also injected into the adjacent well to aid extraction. During such extraction processes, oil, gas and water may flow

simultaneously up the well. This emphasizes the importance of the study of multiphase flow to quantify the multiphase flow in such pipes.

### 1.3.2 Multiphase flow in the mining industry

Today, hydraulic transportation is commonly used in the mining industry. After their extraction, minerals usually need to be transported to other sites either for use or for ongoing shipment, and may be transported in pipelines - sometimes over long distances - using water as the medium of transportation. Traditionally this transportation process was carried out either by road or rail, but now hydraulic transportation is often a more attractive option. Seshadri et al. [17] argue that the transportation of solids using pipelines is a better method than the traditional techniques because (i) it is technically and economically attractive; (ii) it offers a high degree of efficiency, reliability and round the year availability and (iii) it has a lower environmental impact, making it desirable as a mode of transportation [17-19]. For example, Constantini et al. [18] estimate that the capital cost of a proposed 900 mile potash pipeline in Western Canada capable of transporting six million tons of potash per year would be one third of the equivalent rail transport network.

To be able to specify the required pumps and to transport material successfully using the hydraulic transport method, the pressure drop per unit length must be known. It is also important to make sure the solids remain adequately suspended in the flow. Hence, accurate knowledge of the pressure drop and suspension velocity during the design of a hydraulic transportation pipeline can ultimately save considerable sums of money in the building and operating costs of the system. Constantini et al. [18] estimate the capital cost of a proposed 1000 mile coal pipeline in the USA capable of transporting 37 million tons of coal per year to be as much as $650 million, with an

estimated operating cost of $137 million per annum. These costs increase as the size of the hydraulic transportation pipeline increases.

One of the key parameters that must be known in order to predict pressure drop per unit length is the solids volume fraction; this is an essential parameter that must be identified in order to minimise building and operating costs [7, 20-21]. This is especially true when capital and operating costs become competitive. For example, with regards to the coal pipeline discussed by Constantini, if improved knowledge of the pumping loads resulted in even a 1% operating cost reduction this would result in a saving of $1.37 million per annum.

Suhashini et al. in [22] point out that quantitative information and accurate estimates of hydrodynamic properties are also essential for a safe and reliable design.

Because of these considerations of potential savings and improved safety and reliability, a wide range of investigations of the relevant multiphase flows is continually reported. However, a survey of the literature shows that examples of local measurements acquired in such flows are limited [7, 20-22].

### 1.3.3 Multiphase flow in nuclear plants

Multiphase-flow is also present in nuclear reactor plants where two phase flow occurs in cooling equipment. The nuclear reactor uses radioactive materials to heat the water and the resultant steam drives a steam turbine which, in turn, spins the generator to produce power. Then the steam is cooled before it re-enters the steam generator. The steam-water flow is two phase. It is essential to know bubble sizes and volume fractions, since these parameters are important for calculating heat transfer, which is an important parameter for both efficient and safe operation of the reactor [24].

Models of flow patterns of the two phase flows are important for design, optimization and safety analysis in nuclear plants, as stated by Lucas et al. [24].

The void fraction distribution in forced-convection, sub-cooled flow boiling in vertical channels is important for properly evaluating the flow stability and neutron moderation characteristics. Since the condensation rate in sub-cooled flow boiling is significantly affected by the lateral bubble distribution within the channel cross-section, adequate knowledge of the lateral bubble migration from the heating surface towards the sub-cooled liquid region is essential to accurately predict the net vaporization rate and also the axial development of void fraction [25].

### 1.3.4 Multiphase flow in the chemical industry

A vast number of multiphase flows occur in chemical processes. In gas-liquid reactions, sufficient contact of the two phases is important in order to attain optimal performance. In these kinds of cases, the interfacial area per unit volume and the mass transfer rate of the two phases are important parameters that must be measured and controlled for a better overall performance of the process [26].

Manufacturing techniques of microstructures have made possible the development and assembly of micro-chemical devices. These devices are better than common batch reactors due to the fact that they use minimal amounts of fluids, have high heat and mass transfer rates, and shorter reaction times [27]. In these micro-chemical reactors, multiphase flows are present. It is highly desirable to recognise the characteristics of the multiphase flows in these microstructures in order to properly design, develop and operate them. Knowledge of flow patterns, phase volume fractions, pressure drops, liquid film thicknesses, and internal mixing quality is essential [27, 28].

During fermentation reactions in chemical and biochemical processes, foam is produced. Depending on the conditions of the process, different effects may occur; for example, a loss of sterility may take place as a result of excessive foaming. Also, in order to store the unwanted foam, over-sizing of vessels must occur. This increases the costs of the process, so it is important to monitor and control the different foam phases that may occur during the process [29].

Bubble columns are multiphase reactors which are used in the chemical and biochemical industries. They have advantages over other multiphase reactors, including the simplicity of their construction, good heat and mass transfer rate properties, an absence of mechanical moving parts, high thermal stability, good mixing, low power consumption, and low operational costs. In these reactors, gas is injected into a continuous liquid phase. Applications include oxidation and chlorination reactions, in which kinetically slow gas-liquid reactions take place. The generated bubbles are dependent on: the reactor geometry, the primary gas distribution, the operational conditions, and the physical-chemical properties of the two phases. These parameters affect the size, velocity, shape, and interfacial area of the bubbles. Also, in some applications it is important to quantify the bubble coalescence. Therefore, it is obvious that these parameters must be measured and understood in order to build a representative model of the bubble columns for better operational efficiency [30].

Another device that is used widely in the chemical industry and involves multiphase flow is the riser. Gas and solids usually flow concurrently upward. One example of the use of risers is in Fluid Catalytic Cracking (FCC). The associated type of multiphase flow has a complex behaviour due to the existence of turbulence. This

complexity introduces many difficulties in designing, scaling-up and optimizing the operation of the chemical reactor. Therefore, it is essential to distinguish the physics behind these complex flows and measurements of phase volumetric distributions are important for understanding the behaviour of gas-particle flows encountered in risers [31].

Generally, it is important to be aware of the bubble diameter, phase volume fractions and the mass transfer rates [8, 15 and 32-34] when examining the performance of mass exchangers, absorption processes and chemical reactors such as distillation columns, liquid-liquid-solid fluidized beds and sieve plate reactor towers.

## 1.4 Research aim and objectives

The general aim of the research presented in this thesis is the development of techniques for measuring the local properties of the dispersed phase in bubbly multiphase flows.

The objectives necessary to attain this aim are:

(i) To design a miniature four-sensor local conductance needle probe and associated electronics to measure the local gas velocity vector with minimal error on each orthogonal velocity component (i.e. radial, axial and azimuthal velocity), in bubbly multiphase flow.

(ii) To carry out a sensitivity analysis to determine the influence of errors in time delay measurement and probe dimensional measurement on the measured droplet velocity vector.

(iii) To design and construct a test facility to provide reference measurement of the bubble velocity vector in terms of a polar angle $\alpha$, an azimuthal angle $\beta$ and a velocity magnitude $v$ using two high speed cameras and appropriate image processing. This facility will also be used to quantify the deformation of bubbles caused by impact with the needle probe.

(iv) To quantitatively compare the results of a rotary index dual-sensor needle probe and a four-sensor needle probe with results obtained from the high speed camera reference measurement system.

Techniques for measuring the local properties of multiphase flows enable the characterisation of such multiphase flows for comparison with and validation of numerical models of multiphase flow.

Such techniques can also be used for validating dual plane electrical resistance tomography (ERT) systems [8-9], which are reported to be able to measure the local dispersed phase velocity vector and the local dispersed volume fraction in multiphase flow, but with an unknown level of accuracy.

For the above reasons, an independent method of measuring the local dispersed velocity vector and the local dispersed phase volume fraction with a high degree of accuracy in bubbly gas-liquid flow is very important.

## 1.5 Format of the thesis

It is useful at this stage to describe the format of the thesis which is laid out to present the research in a logical and sequential order. Each chapter is intended to be a

reasonably self-contained description of one area of the research. However, it will occasionally be necessary to refer back to earlier sections of the work.

Chapter 2 Reports the results of background studies carried out for the present investigation. These involve the selection of the measurement principle of the instrument and further detailed research into areas of this measurement principle.

Chapter 3 Reports the design and optimization of the measurement device. This includes the mechanical design and construction of the instrument.

Chapter 4 Discusses the sensitivity of the probe to measure errors in the probe dimensions and errors in the measurement of the relevant time intervals.

Chapter 5 Reports the design and construction of all of the electronic measurement hardware. It also presents the design and construction of the ancillary mechanical and electrical components.

Chapter 6 Presents the software developed for this project, including data acquisition and signal processing.

Chapter 7 Presents the theory used for obtaining reference measurements of the velocity vector. It also presents the theory of image processing and the process of reconstructing the bubble images and camera calibration.

Chapter 8 Describes the experimental set up of the water tank into which air is injected. It also explains the co-ordinate transformations necessary to

define the bubble velocity vector measured by the probe in terms of the tank coordinate system.

Chapter 9 This chapter provides the results of experiments carried out on the 4-sensor probe in the air-water tank.

Chapter 10 This chapter describes an air-water multiphase flow loop.

Chapter 11 All experimental results obtained in the air-water flow loop with and without the swirl are presented. The results obtained are compared with the reference measurements obtained from a high speed camera.

Chapter 12 Conclusions.

Chapter 13 Recommendations for further work.

# CHAPTER 2

## Literature review

Since the beginning of the study of multiphase flow, there have been significant developments in measurement techniques, and various types of measuring devices have been developed. Even though all the equipment/devices have different ways of measuring the properties of the flow, they can all be simply categorised into two groups: non-intrusive (techniques in which the properties of the flow are measured without disturbing the flow) and intrusive (techniques in which the flow is disturbed while the properties of the flow are measured). Both intrusive and non-intrusive techniques can be sub-divided into global and local techniques, listed below.

### 2.1 Non-Intrusive Methods

Non-intrusive methods can be divided into global and local measuring techniques [1-110]. As this project is based on local, intrusive methods of measurementthe detailed information on non intrusive measurement techniques is presented in Appendix A.

### 2.2 Intrusive methods

Although non-intrusive techniques can give the required information that is needed for a process, there are limitations that make them unsuitable for a number of applications. In these situations, intrusive methods are preferred. One of the reasons that intrusive methods are used is that non-intrusive techniques may not give satisfactory results on highly turbulent systems (Christophe et al. [15]); also, in some industrial operating conditions, non-intrusive techniques become ineffective because

of the walls (which need to be transparent in the case of image analysis techniques) and bubble number density (in the case of LDA and PIV); finally, non-intrusive methods are not often easy to apply and install, and they can be very expensive [15]. A further major limitation of non-intrusive methods is their inaccuracy; for example, the poor accuracy of the velocity and volume fraction measurement in multiphase flow using ERT (Lucas et al. [3], Christophe et al. [15]).

As a result of these limitations of non-intrusive systems, intrusive techniques have been developed which are discussed in detail below:

### 2.2.1 Heat transfer probe

Heat transfer probes are also known as hot film anemometers and in multiphase flow can be used for the measurement of local gas volume fraction and liquid volume fractions. They can also be used for measurement of velocity of the continuous phase liquid in liquid continuous phase, and turbulent flow quantities [111-119].

**Figure 2.1 Hot film anemometry probes: one sensor, dual-sensor and three sensors respectively from left to right.**

The sensors of these hot film probes are very small, usually 0.1 μm, and are made up of platinum or nickel films. These films are deposited on thermally insulating substrate, usually quartz. The films are deposited on cathode sputtering to ensure a uniform thickness of the sensing element. A thick layer of conducting material is

connected by sputtering to the ends of the film to supply the electrical heating current. The film is usually coated with a 1–2 μm thick deposited layer of insulating material (quartz). This coating protects the film material from abrasive particles and provides electrical insulation for hot film probes used in liquids. Two or three films can be used for a multi-dimensional flow, as shown in Figure 2.1.

The process of measurement is generally based on the principle of the exchange of heat from the electrically heated probe to the surrounding environment. Thus, the heat transfer coefficient between the probe and the surrounding dispersed phase is given in Equation 2.1 as a Nusselt number $N_u$ (ratio of convective to conductive heat transfer) and depends on the characteristic Reynolds number $\mathrm{Re}$ [117, 119]

$$N_u = A + B \cdot \mathrm{Re}^{-0.5} \qquad \textbf{Equation 2.1}$$

The electric current through the probe is controlled by a Wheatstone bridge interfaced with a regulation amplifier and a high-pass filter [67,119].

The calibration relationship between the voltage $E$ from the Wheatstone bridge (which the current from the probe is passed through) and the liquid velocity is given by King's law [15]:

$$E^2 = A + B \cdot u_e^n \qquad \textbf{Equation 2.2}$$

where, $A$, $B$ and $n$ are coefficients identified by calibration, $E$ is the output voltage from the bridge; $u_e$ is the apparent fluid velocity (whereas the actual velocity is $\vec{u}$, a vector), sensed by the probe. In the case of a non-uniform flow, $u_e$ is the normal component of $u$ with regard to the probe. For the calibration procedure, a Pitot tube is

usually used as a reference measuring technique. Also, due to the fact that the sensor's characteristics can change rapidly, it is recommended that the probe should be calibrated regularly.

The coefficients *A*, *B* and *n* of King's law are dependent not only upon the physical properties (density, viscosity, thermal conductivity) of the fluid near the probe, but also on the geometric characteristics of the sensor. These parameters may also vary with the difference in temperature between the hot film and the fluid [117,119].

Due to their fragile nature, hot film probes are not used in multiphase flows that have solids with high momentum. Also, it is desirable for the temperature in the flow to be uniform. However, care must be taken when they are used, due to the fact that errors in measurements may arise from several factors: flow disturbance due to the probe, calibration curve uncertainty, signal treatment, signal amplification, signal interpretation in turbulent flow, and non-uniform temperature [111,117,119].

Toral et al. [116] used hot wire anemometers in multiphase flow in order to measure the volume fraction of the dispersed phase (air in this case) which was introduced in a tube filled with ethanol. The measurement principle was based on monitoring the different rates of heat dissipation from the probe in vapour and liquid phase. The reference gas volume fraction was determined by using the pressure drop between two pressure tap points (see Chapter 10).

Rensen et al. [120] in 2005 also used a hot wire probe in order to study the bubble-probe interaction, residence time, bubble size (compared with the image captured from high speed cameras) and the arrival and departure bubble velocity. Figure 2.2 shows the schematic diagram of the experimental set up used by Rensen et al. [120].

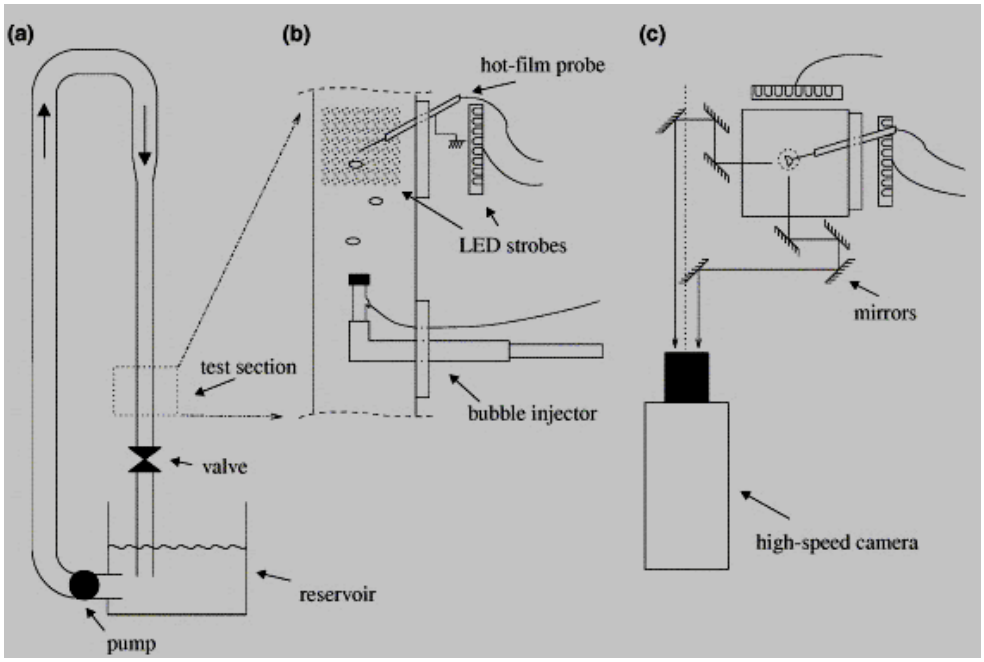


**Figure 2.2 Schematic diagram experiment set-up (a) water channel with circulatory flow (b) Enlargement of the test section (c) optical path for stereoscopic imaging (top view), Rensen et al. [120]**

Rensen et al. [120] describe three types of probe-bubble interaction as follows:-

- Penetrating bubble: - The bubble and probe meet each other and merge. The sensitive part of the probe is then inside the bubble, until the back end of the bubble has passed the probe (see Figure 2.3).
- Bouncing bubble: - The bubble is pulled back under the probe and the bubble leaves the probe on one side (see Figure 2.3).
- Splitting bubble: - The notch that originates from the folding of the bubble becomes deeper, until the back end of the bubble hits the probe. As a consequence, the two bulges break up into two separate bubbles (see Figure 2.3).

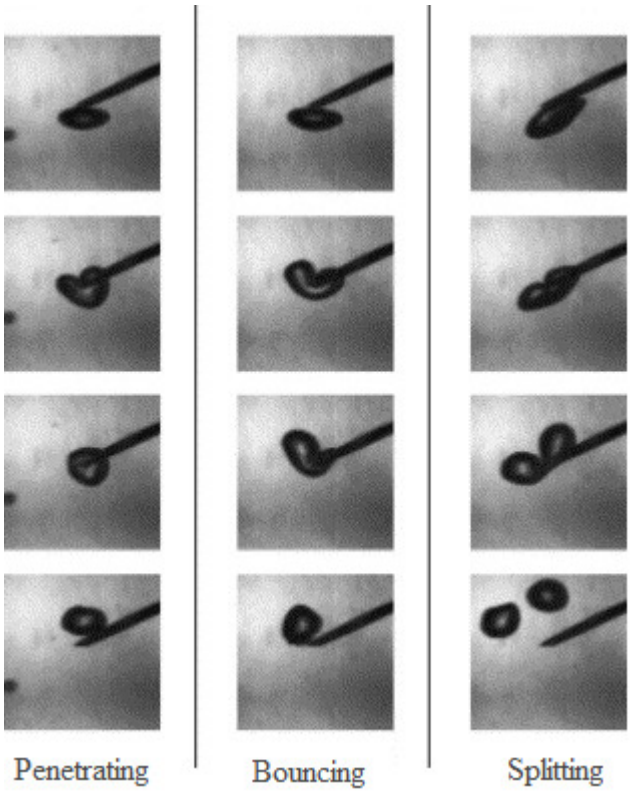


**Figure 2.3 Image sequence of penetrating, bouncing and splitting a bubble as described by Rensen et al. [120]**

Bruun et al. [119], in 1995, describe various types of hot wire probe: S N film probe, X hot film probe and split-film probe. Bruun et al. [119] also describe problems associated with the hot film anemometer such as: electrolysis, cracking of the quartz coating, bubble formation on the probe, temperature drift and probe contamination.

### 2.2.2 Ultrasound probe

Ultrasonic probes were originally developed to be used in the single phase liquid flows (Murakawa et al. [121,122]), in which the pulse echography of ultrasonic beams from an ultrasonic transducer are used to measure the instantaneous velocity profile of the liquid along its measuring line. The advantage of using ultrasonic probes is that they can be used in opaque liquids such as liquid metal and in the presence of magnetic fields. In recent years, these probes have also been used in multiphase

bubbly flow [121,122], in which the ultrasonic pulses are reflected both from the seeding as well as the bubbles in the liquid, so that it is possible to measure the velocity of the bubbles as well as the liquid.

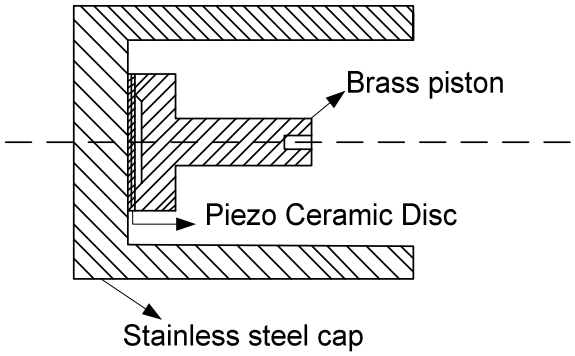


**Figure 2.4 Cross-section of an ultrasound Doppler probe [123].**

In general, the structure of an ultrasound probe consists of a piezo-ceramic disk linked to a damping device included in a metal tube. These probes are able to be used even in aggressive environments; they can resist temperature up to 140°C and pressure to 20MPa. Figure 2.4 shows a diagram of an ultrasound probe [15, 123-124].

The principle of its operation is that acoustic pressure waves are generated from a transducer within the piezo-ceramic disk, causing vibrations. The disk transforms these waves into a voltage signal which, in turn, can be acquired by a computer through a data acquisition card. The frequencies that are used range between 0.2 and 5 MHz. Also, the focal distance of these probes is about 0.2 to 0.3 m; therefore, no disturbance of the flow occurs [15].

There are two types of technique that are used with ultrasound probes. The first uses transmitted wave characteristics such as attenuation in order to make a measurement. In this technique, transmittance $T$ is evaluated through the voltages A (when a bubble is present) and $A_0$ (when bubbles are absent) measured at the receiver probe.

Transmittance $T$ depends on the distance $L$ between the two probes, bubble sauter mean diameter $d_{SM}$, sound dispersion coefficient $S$ and wave characteristics such as frequency f, and celerity c in the liquid medium. Once all these parameters are measured, it is possible to calculate the local interfacial area **A** or the gas volume fractions $\lambda$ using Equation 2.3 as described in [125].

$$\mathbf{A} = \frac{-8\ln(T)}{SL\left(\frac{kd_{SM}}{2}\right)} = \frac{6\lambda}{d_{SM}} \qquad \textbf{Equation 2.3}$$

Where $k = \left(\frac{2\pi}{c}\right) f$

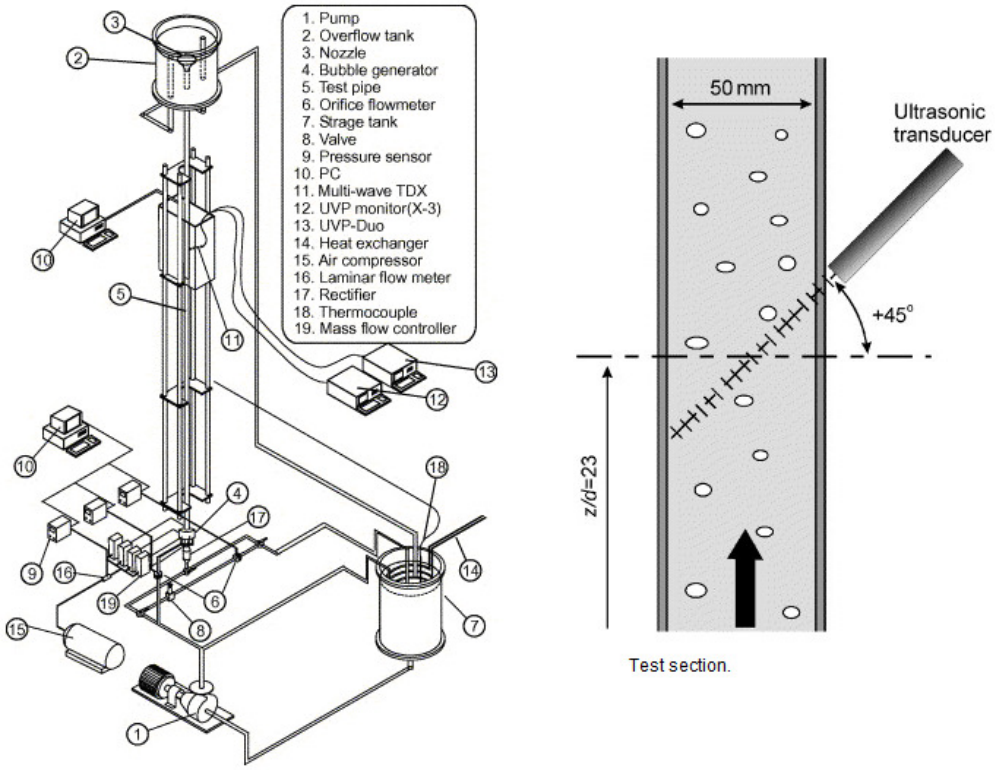


**Figure 2.5 Experimental set up used [ 121,122]**

The second method uses the Doppler technique which is a *pulse echo method*. In other words, in the case of probes that use the Doppler technique, the transmitter and receiver are the same probe (Christophe et al. [15], Murakawa et al. [121] [122]). Due to the fact that gas-liquid interfaces are very good reflectors (acoustic impedance is different in gas and liquid), pulsed signals are emitted into the fluid and their echo is received. Wave characteristics have been altered and these changes correspond to the velocity of the multiphase flow. The frequency of the pulse emission is around 10 kHz. Also, the shorter the pulse, the weaker the echo distortion will be [126].

Murakawa et al. [121, 122] used a similar technique in a multiphase bubbly flow; Figure 2.5 shows the experimental set up they used. In the experiment by Murakawa et al. [121,122], the ultrasonic Doppler method was applied to the bubbly multiphase flow with added seeded particles, with the result that the ultrasonic waves are reflected from both the seeding particles as well as the bubbles. These reflections, captured by the ultrasonic velocity profiler monitor, contain information on the velocities of both phase disperse (bubble in this case) as well as the continuous phase (water). Thus, Murakawa et al. [121] were able to find the velocity of both phases using the phase separation technique.

Later, Murakawa et al. [122] used two different sizes of ultrasonic transducers in order to study the effect of the liquid velocity on the rising velocity of the bubbles.

Figure 2.6 shows the velocity probability density function using 2 MHz and 8 MHz ultrasonic transducers. It was found that, with the 8 MHz ultrasonic transducers, it was only possible to measure the velocity of the liquid, while with 2 MHz ultrasonic transducers, it was possible to measure the velocity of the bubble.

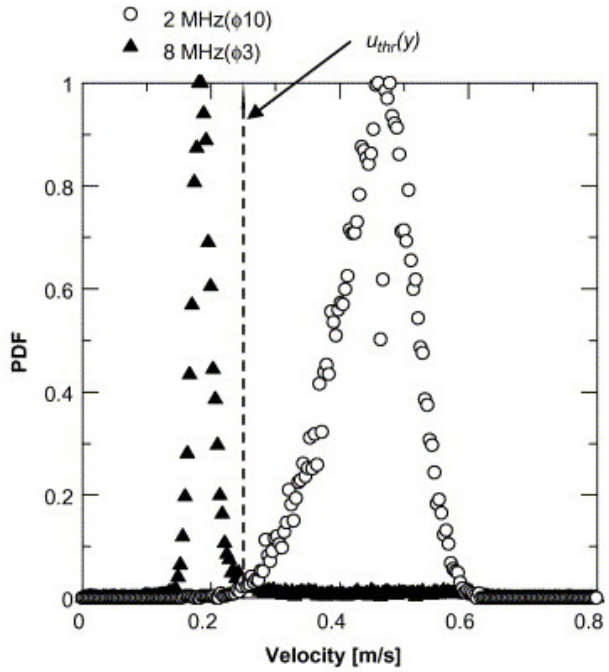


**Figure 2.6 Comparison of the probability density function measured with 2MHz and 8MHz ultrasonic transducers. Murakawa et al. [122]**

Similarly, Wang et al. [127] used a commercially available ultrasonic system, Doppler US2000, in order to measure the gas volume fraction, liquid velocity**,** bubble size, and bubble rise velocity in a bubble column, as shown in Figure 2.7.

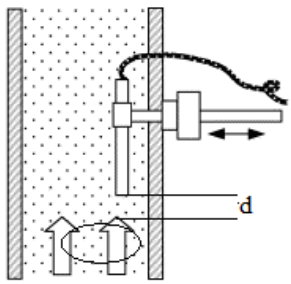


**Figure 2.7 Experimental set up for Wang et al. [127]**

Placing the probe as shown in Figure 2.7 has an advantage: 1) it overcomes the complexity of the ultrasound reflection at the bubble interface which makes the signal difficult to deal with and 2) it also avoids the difficulty of determining the Doppler

angle as the measured velocity, as the DP2000 is directly projected towards the flow direction.

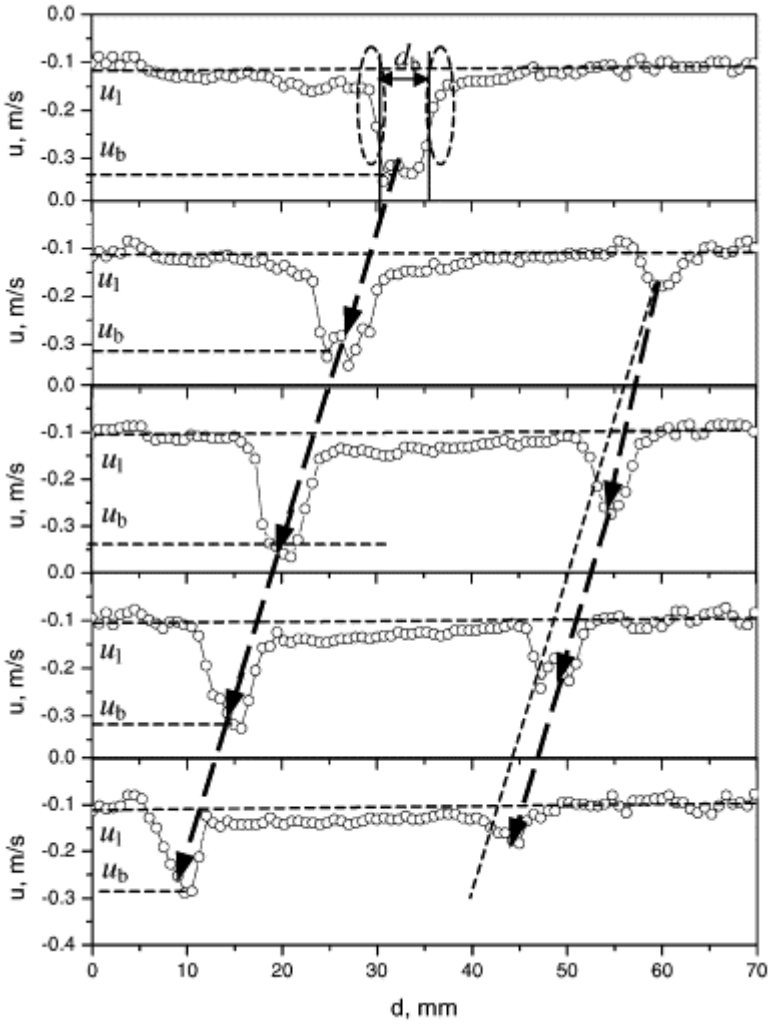


**Figure 2.8 Flow pattern achieved by Wang et al. [127]**

Figure 2.8 shows the sequence profile of the evolution of the bubble signal, as it rises towards the probe, decreasing the distance between the bubble and the probe as the time increases. Thus, Wang et al. [127] recommend a way of calculating the rise velocity of the bubble by dividing the bubble displacement between two sequential profiles by the relevant time interval and then averaging the results.

Using this approach, Wang et al. [127] found good agreement between results in which they found the bubble velocity $U_b$, of 0.32 m/s and the liquid velocity (seeding particles) $U_l$ of 0.12m/s. The bubble slip velocity, given by $U_b$ - $U_l$, is 0.20 m/s, in accordance with the single bubble rise velocity in water.

### 2.2.3 Needle probes

The main characteristic of these probes is that they are thin and they are sharp ended. They are positioned so they face the direction of the flow. Depending on their design, they are able to measure the local dispersed phase volume fraction $\lambda_l$ and local velocity in gas-liquid and liquid-liquid (e.g. oil in water) flows, in the bubbly flow regime. There are two types of needle probes: optical fibre probes and conductive probes. In the literature, the number of tips or the number of needles they use is predominantly one or two [129-140]. With one needle they are able to measure only the local dispersed phase volume fraction; with two needles it is possible to also measure the local dispersed phase velocity. Recently, four and five needle probes have been fabricated [141-156], which also measure vector velocities and bubble shape respectively.

#### ***2.2.3.1 Optical needle probe***

In recent years, optical probes have been frequently used to study the bubbly multiphase flow [129-134]. In these studies, authors used single, dual and four-sensor probes in order to determine the velocity of the dispersed phase, bubble shape and the volume fraction of the dispersed phase.

The principle of optical fibre probes is based on the fact that the critical angle for reflection/refraction changes considerably in the different phases, and is much larger for a water and glass interface than for an air and glass interface. Light is sent through the fibre and, if the tip of the probe is immersed in water, light will leave the fibre, whilst if air or oil is present at the tip of the fibre, the light will be reflected.

Hamad et al. [129-130], in 1997, used a single sensor optical probe in kerosene-water flow to measure the volume fraction of kerosene and compared the results with those acquired from a hot-wire anemometer. Subsequently, in 2002, Hamad et al. [129-130] report implementing a dual-sensor optical probe in kerosene-water flow to measure the local volume fraction, local dispersed phase (kerosene) velocity and the bubble size.

Hamad et al. [129-130] used a five meter long optical probe cable with a 100 μm core diameter and 140 μm cladding diameter. This cladding provides a constant step change in refractive index at the core-cladding interface, which guides the light inside the fibre. In this paper, the author measured the volume fraction of the dispersed phase (kerosene) with an optical probe, using Equation 2.4:

$$\lambda = \lim_{T \to \infty} \left( \frac{\sum T_G}{T} \right) \qquad \textbf{Equation 2.4}$$

where $T$ is total measurement time, $\sum T_G$ is the total time the dispersed phase is present at the selected measuring point and $\lambda$ is the dispersed phase volume fraction. When comparing the results from the optical probe with those from a sampling tube, the author found good agreement between the results.

Hamad et al. [129-130] also reported that the drop size distribution is apparently similar when the volumetric quantity (ratio between the volume of water and the total volume present in the system) is constant and the water flow rate is changed, whereas if the water flow rate is kept constant and the volumetric quantity is increased, results shows that there is a substantial increase in the number of small drops.

S. Guet et al. [130] made a four-sensor probe using fibres with a quartz glass core of 200 μm diameter, having a refractive index of 1.45, a silicon cladding of 380 μm diameter and a protective layer of Teflon of 600 μm diameter. The cladding and Teflon layers were removed from the tip of each sensor. Light was emitted into each fibre by an LED (wavelength of 680 nm) via standard glass fibre connectors and a photodiode was used to detect the reflected light. The collected light was then converted into a voltage output. Figure 2.9 shows the schematic of the four sensor optical probe used by Guet et al. [130].

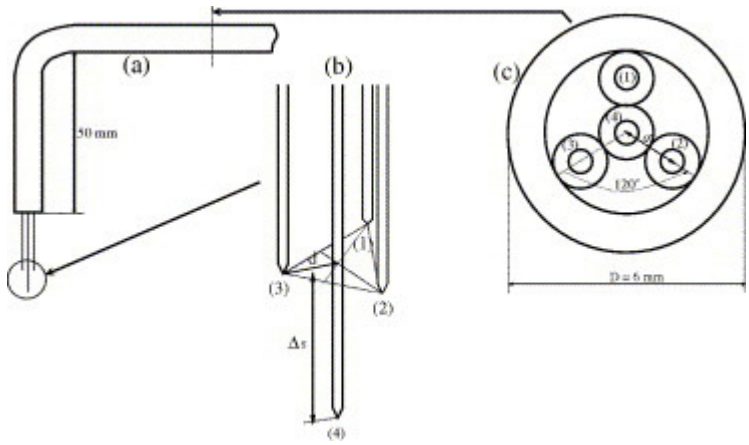


**Figure 2.9 Schematic of four sensor optical probe. Guet et al. [130]**

The author used the optical probe in bubbly gas-water flow to study the bubble shape, the volume fraction profile and the orientation of the bubbles during probe-bubble interaction. In the paper, the author reported that bubbles smaller than 5mm in

diameter accumulate near wall regions to form a wall peaking radial volume fraction profile. As the bubble size increased, the volume fraction profile changed from wall peaking to a centre line peaking volume fraction profile. The author also stated that the orientation angle (angle between the z- axis of the pipe and the velocity vector of the bubble) of the dispersed phase is greater than 0° if the diameter of the bubble is smaller then 5mm, whereas the orientation angle is less then 0° if the bubble is larger than 5mm in diameter.

Julia et al. [131] also used an optical dual-sensor probe to measure the local volume fraction and the trajectory of the dispersed phase in bubbly air-water multiphase flow. The drawback of this study is that the probe was placed just 3.5 cm above the gas injection nozzle. Due to this small degree of separation, bubbles will still be under the influence of the air (gas) pump pressure, thus the chances of receiving the wrong information on velocity are very high. It is also possible, in the case of this small nozzle-probe separation, that the trajectory of the bubble will always be vertically upward as the bubble hits the probe. The author mentions three types of effects that can occur during bubble-probe interaction which can cause an error in measurements. The described effects are: -

Blinding effect: - since the probe detects a disturbed interface position, the local interface deformation during probe impact contributes to the error on the velocity measurement. This leads to the existence of a blind zone or, equivalently, to an effective shape detected by the probe.

Crawling effect: - the whole bubble is decelerated and /or deformed during the interaction.

Drifting effect: - the trajectory of the bubble is altered, leading to either the detection of a smaller chord or to no detection at all.

Although the optical probes described above are capable of measuring the properties of the dispersed phase, they have significant drawbacks, as described below:-

- Probe tips of optical probe are very sensitive to dust.
- The probe must be shaped very precisely, which is very difficult due to the size of the probe and, hence, requires special machining, increasing the overall cost.
- Using a typical optical probe, the reflected light signal is very weak; thus, in order to enhance the signal, a very expensive photo receiver is required. However, for better reflection, a co-axial receiver can be used, but it needs to be finely machined, which is again very expensive.

#### *2.2.3.2 Conductance needle probe*

Given the drawbacks associated with the optical probes described above, in the present investigation it was decided to use a needle conductance probe. Conductance needle probes use metal needles as the sensors. The diameter of the needles is usually smaller than 200μm. They are covered with a non-conductive waterproof layer, except at the tip of the sensor needles. The exposed tips are the actual sensors. The electronic circuit that supports these probes measures the conductance between the tip of the needle and the body of the probe, which is metal. For air-in-water bubbly flow, when the tip is surrounded by water, the measured conductance is 0.05S/m. When a bubble strikes the probe, the tip is surrounded by gas and the measured conductance is very $0.8 \times 10^{-14}$S/m. Hence, measurements can be acquired using the times at which the

bubble surface contacts each sensor. As in the case of optical probes, a one needle probe measures the local dispersed phase volume fraction and a two needle probe measures the local dispersed phase velocity, as well as local dispersed phase volume fractions. In the last few years, four-sensor probes have also been designed and used to measure the local dispersed phase velocity vector. More information regarding conductance probes can be found in [135-140] and in the rest of the thesis, as they are the main subject of the research that is presented here.

It may be helpful to briefly mention some of the problems that occur when needle probes are used. These problems are related to the measurement errors that may occur (see Chapter 3 section 3.2 and Chapter 4). Sources of these errors include: bubble-probe interaction (piercing hydrodynamics), probe orientation in the flow, bubble shape, turbulence, statistical bias (large bubbles are likely to hit the probe more often than small ones), and the signal (and data) processing scheme that is used.

In the current thesis, dual and four-sensor probes have been designed, fabricated and used in a number of experiments. An extensive and detailed description regarding their characteristics will be presented. Also, new designs and signal processing schemes are discussed.

## 2.3 Conductance probe

As discussed in Chapter 1, two phase flows occur in many applications in the chemical, mechanical, gas and petroleum and nuclear industries. The relationships between the phases in gas-liquid flows are very complex and result in different flow patterns, as described in earlier sections. These flow patterns are highly dependent on the flow rates and mean phase volume fractions of the flowing components.

| Author | Sensor material used | Sensor diameter (mm) |
|---|---|---|
| Serizawa et al. 1975 | stainless steel | 0.2 |
| Hills 1974 | tungsten | 0.5 |
| Neal and Bankoff 1963 | stainless steel | 0.75 |
| Kocamustafaogullari et al. 1991 | stainless steel | 0.25 |
| Wu et al. 2000 | stainless steel | 0.089 |
| Hogsett et al.1997 | platinum | 0.127 |
| Sanaullah et al. 1998 | stainless steel | 0.112 |
| Kim et al. 2000 | gold acupuncture needles | 0.13 |
| Herringe and Davis 1976 | stainless steel | 0.08 |
| Panagiotopoulos et al. 2007 | stainless steel | 0.3 |
| Park et al. 1976 | kovar | 1 |
| Rigby et al. 1970 | chromel-alumael | 0.5 |
| Lewis et al. 1983 | stainless steel | 0.315 |
| Yasunishi et al. 1986 | platinum | 0.25 |

**Table 2.1 Summary of probe configurations used by previous researchers**

Within the University of Huddersfield and elsewhere [1-14,135-156], conductance probes have been used to determine the local velocity vector, the local volume fraction and bubble size distribution in gas-liquid flow. A comprehensive list of previous research into conductance probes is given in Table 2.1. However, the probe listed in Table 2.1 was only used to measure the velocity and the volume fraction profile of the bubble with exception to Panagiotopoulos et al. 2007. Panagiotopoulos et al. 2007 used rotary index dual-sensor probe to measure the velocity vector of the bubble (see Chapter 2.6).

These conductance probes detect the passage of interfaces at the tip of each sensor, and use the time delays associated with the passage of these bubble-liquid interfaces

to measure the relevant local dispersed phase properties. These probes are relatively simple to use and have a wide range of application. It is particularly important for them to accurately measure the properties of the dispersed phase because moderate measurement error results in intolerable uncertainty in the estimation of both local gas volume fraction and the local gas axial velocity in gas-liquid flow.

At the beginning of the development of these conductance probes, only one needle (sensor) was used, giving a different signal depending whether the probe was in contact with water or air/gas [144-146].

Bankoff et al. [144] was one of the first to develop the idea of using the conductance probe for the measurement of volumetric gas fraction, bubble frequencies, and local bubble size. The probe that Bankoff used consisted of a 1.25” long 0.033” diameter steel sewing needle welded to the end of a 3” length of 0.033” steel wire. The steel wire was electrically insulated, except at the tip, with a resin varnish as shown in Figure 2.10. A 1/4” S.S tube was used as common ground and the plastic insulation was used to separate needles from the tube, as well as to prevent the water from passing into the tube.

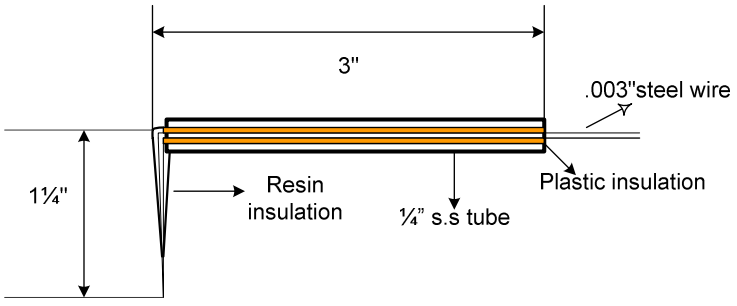


**Figure 2.10 Schematic of probe used by Bankoff et al. [144]**

The author found that, with regard to the smaller bubbles, more bubbles were found at the centre of the tube than the walls near the entrance to the test section. After the flow became fully developed, bubbles were fairly uniformly distributed across the tube cross section. The author also stated that the bubble frequency varies radially and axially in the entrance region, but becomes essentially constant when the flow is fully developed [144].

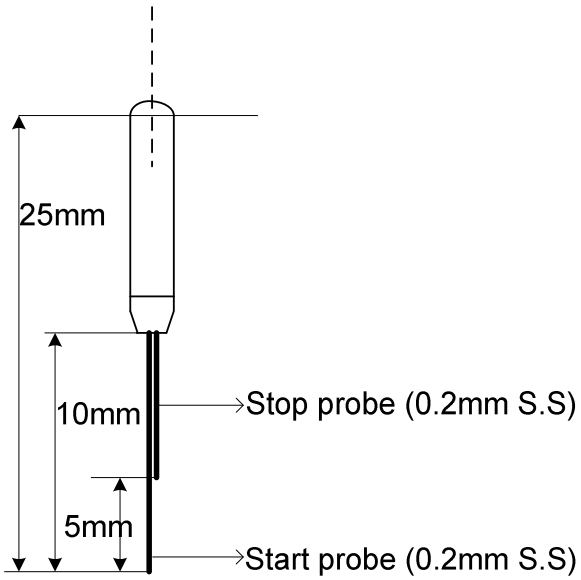


**Figure 2.11 Schematic of Serizawa et al.'s probe [142]**

Later, in 1974, Serizawa et al. [142] developed this idea by introducing an electrical resistance probe consisting of two identical needle sensors, with the needle tips axially separated by 5mm, as shown in Figure 2.11. Each needle sensor was made up of stainless steel wire of 0.2mm diameter, and was insulated electrically except at the tips. The author denoted the upstream sensor as the start sensor and the downstream sensor as the stop sensor. The probe was used to measure local volume fraction (see section 2.4), bubble impact rate, bubble velocity (see section 2.4) and its distribution in a bubbly air-water flow.

Cross-correlation was used to calculate the average time lag of the bubble between the upstream sensor and the downstream sensor. Serizawa et al. [142] stated that the average velocity of the bubbles measured by the cross-correlation technique is about 5% smaller in bubbly flow than that measured by a multichannel technique (technique in which the time to pulse converter was used in order to achieve the time lag from each bubble) due to the shape of the bubble velocity spectrum and bubble – probe interaction effects.

Later, Kocamustafagullari and Wang [145] recommended a 2.5 mm axial sensor separation for the accurate measurement of bubble size and bubble velocity.

Wu et al. [146-148] used a double-sensor probe made up of stainless steel wire of 89 µm diameter, insulated with 5 µm thick insulation resin, so as to make only the tips of both sensors electrically conductive. The axial sensor separation between front and rear sensor was 2.65mm, as shown in Figure 2.12.

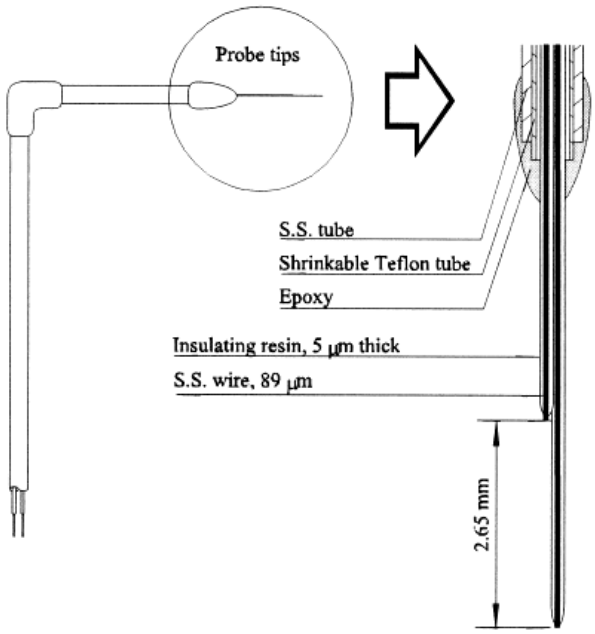


**Figure 2.12 Double sensor conductance probe. Wu et al. [146-148]**

Wu et al. [146] used the probe to investigate the effects of the axial sensor separation on velocity measurement with spherical and elliptical bubbles in air-water flow. They stated that "The measurable velocity may approach infinity if the ratio of the sensor separation to the diameter of the measured bubbles is smaller then the maximum relative fluctuation of the bubble velocity." They therefore suggested using a sensor separation greater than one half of the bubble diameter for effective elimination of the singularity problem. Wu et al. [146-148] also stated that, if the sensor spacing is 0.5 to 2 times the bubble diameter, the calibration factor (ratio of true mean bubble velocity to the mean measurable value) is almost independent of the sensor spacing. This conclusion conflicts with the results found by Kataoka et al. [149], who stated that if the sensor separation was smaller than 0.2 of the measured bubble diameter, there is little effect on the calibration factor.

Wu et al. [146] also proposed a sampling rate greater then 2000 KHz for the spherical shaped bubble.

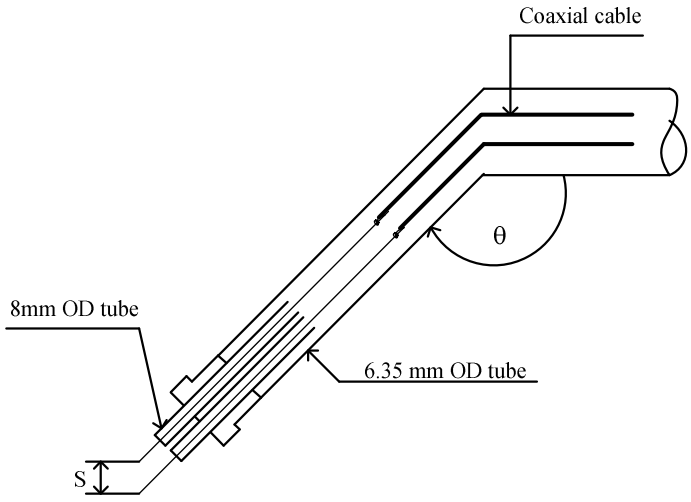


**Figure 2.13 Sanaullah et al.'s dual-sensor probes**

Sanaullah et al. [150] used a two-needle inclined sensor (at θ = 90°, 110° and 145°), made of Teflon coated stainless steel wire with a 5 mm tip distance (S in Figure 2.13), for the validation and comparison of the results that they previously acquired using a vertical sensor probe (θ = 90°). Sanaullah et al. [150] also studied the effect of probe inclination θ on the measured bubble size, bubble frequency and local void fraction. They found that the calculated parameter was much closer to the reference values at θ = 110° than at θ = 90° or 145°.

## 2.4. Theory of the dual-sensor conductance probe

The basic purpose of a dual-sensor conductance probe is to measure the local volume fraction and the local velocity of the dispersed phase at a point in the cross section of a bubbly two-phase flow. Many researchers, including Serizawa et al. [142], Herringe et al. [152] and Wu et al. [146-147], have successfully used dual-sensor probes to measure variations in the local electrical impedance of the multiphase mixture and, hence, to determine the local volume fraction and local velocity distribution of the dispersed phase in the cross section (as described below).

The volume fraction of the dispersed phase can be measured by one sensor, but for the measurement of the velocity of the dispersed phase it is necessary to use a dual-sensor probe. The operation of the dual-sensor conductance probe is based on changes of the electrical conductance in a multiphase flow. When the tip of each sensor is exposed to a mixture of two phases, the conductance between the probe tip and the common ground (sensor body) is measured. Due to the large difference in conductance between the water and the air, the conductance signal falls sharply when a bubble passes over the sensor.

Assume that a dual-sensor probe is positioned vertically and faces the direction of a vertical bubbly air-water flow (see Figure 2.14), and the surface of an air bubble makes contact with the front sensor for the first time at time $t_{1f}$ and the last time at $t_{2f}$. Before proceeding, it is important to note that, in [2], Mishra et al. showed that in multiphase flows the bubbles of the dispersed phase (gas-liquid) have an oblate spheroid shape as they move in the liquid, and that the plane of symmetry is normal to the direction of motion. Furthermore, it is also assumed that the bubble surface makes first contact with the rear sensor at time $t_{1r}$ and last contact at time $t_{2r}$. Figure 2.14 shows the bubble striking the sensors at the contact times described above.

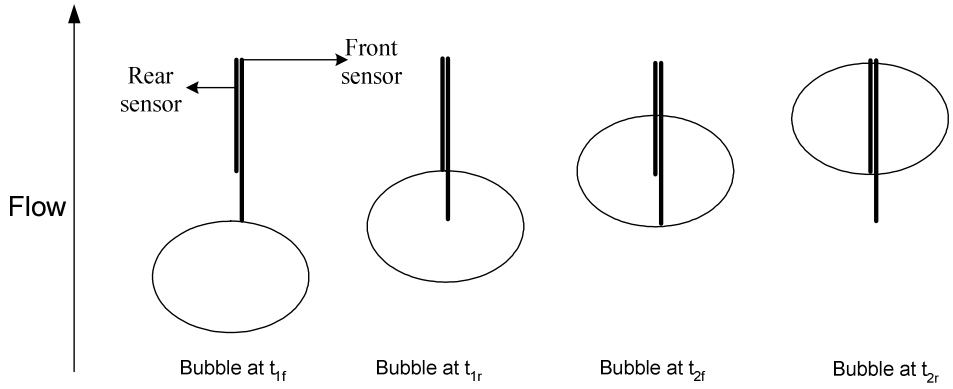


**Figure 2.14 Bubble strikes dual-sensor probe at different time intervals.**

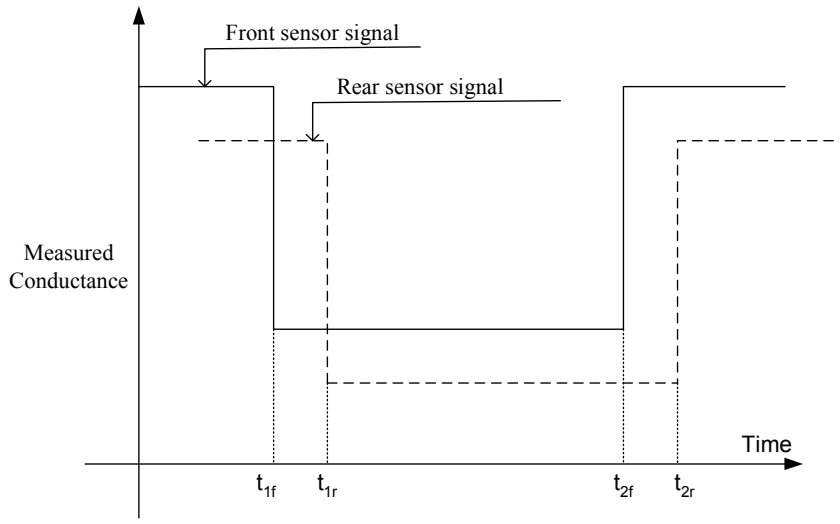


**Figure 2.15 Ideal signal obtained from a bubble striking a dual-sensor probe.**

Based on the above, when the bubble strikes the front sensor, the measured conductance will fall sharply as the tip of the sensor is immersed in air (which is a very low conductivity material) instead of water (which has high conductivity). As long as the tip of the sensor stays in the bubble's interior, the measured conductance stays low. When the bubble leaves the front sensor, the measured conductance will sharply rise, since water will surround the sensor's tip. The same events happen with the rear sensor. Figure 2.15 shows the conductance changes for both sensors and the times of the occurrences.

Suppose $N$ bubbles hit both the front and the rear sensors during a sampling period $T$. For the $i^{th}$ bubble, two time intervals $\delta t_{1,i}$ and $\delta t_{2,i}$ may be defined as follows:

$$\delta t_{1,i} = t_{1r,i} - t_{1f,i} \qquad \textbf{Equation 2.5}$$

and

$$\delta t_{2,i} = t_{2r,i} - t_{2f,i} \qquad \textbf{Equation 2.6}$$

The mean local axial bubble velocity $v$ at the position of the probe is then given by:

$$v = \frac{2s}{N}\sum_{i=1}^{N}\frac{1}{\left(\delta t_{1,i} + \delta t_{2,i}\right)} \qquad \textbf{Equation 2.7}$$

where $s$ is the axial distance between the tips of the sensors. If the bubbles have a plane of symmetry normal to their direction of motion, then use of Equation 2.7 minimises the errors in the calculated value of $v$ due to the effects of the curvature of any bubbles that hit the probe 'off centre', as demonstrated by Steinemann and Buchholz [137]. This is made clearer in Figure 2.16, which shows the typical

arrangement for a probe – bubble interaction. Figure 2.16 shows that when both (front and rear) probes hit the upper surface, the front sensor hits first and then the rear sensor after $\delta t_1$ seconds; which is given by Equation 2.8

$$\delta t_1 = \delta t^* + \Delta t_1 \qquad \textbf{Equation 2.8}$$

similarly, when hitting the bottom surface of the bubble, the rear sensor hits first and then the front sensor after $\delta t_2$ seconds, as shown in Equation 2.9.

$$\delta t_2 = \delta t^* - \Delta t_2 \qquad \textbf{Equation 2.9}$$

where $\delta t^* = \frac{s}{v}$ , and if $\Delta t_1 = \Delta t_2$

$$\frac{\delta t_1 + \delta t_2}{2} = \delta t^* \qquad \textbf{Equation 2.10}$$

Thus, using Equation 2.10 compensates for the time intervals in hitting the probe.

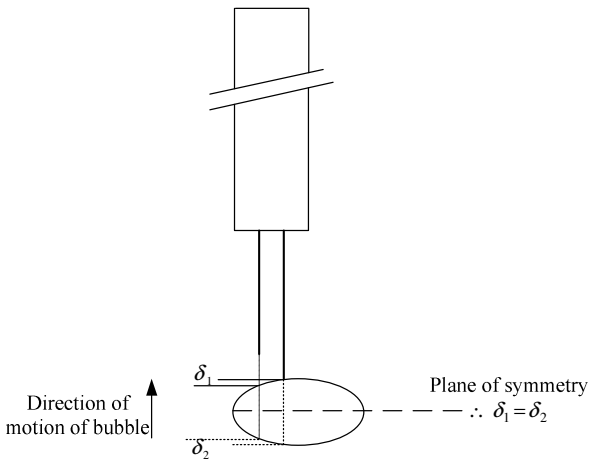


**Figure 2.16 Typical bubble-probe interaction**

The local volume fraction $\lambda_l$ of the bubbles at the position of the probe can be estimated from the conductance signal from either the front or the rear sensor. In the case whereby the front sensor's signal is considered, then $\lambda_l$ can be calculated by [146]:

$$\lambda_l = \frac{1}{T}\sum_{i=1}^{N}\left(t_{2f,i} - t_{1f,i}\right) \qquad \textbf{Equation 2.11}$$

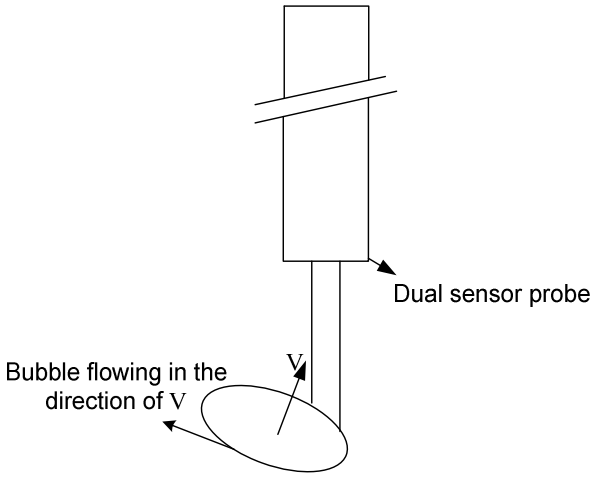


**Figure 2.17 Typical bubble-probe interactions with lateral velocity component showing singularity problem**

It is important to mention that in real, as opposed to ideal, vertical upward air-water flows, the velocities of the air bubbles are not purely axial; they also have small lateral components. In [146] it is shown that these lateral velocity components can cause the surface of the bubble to strike both sensors at almost the same time, which Wu et al. [146] described as a singularity problem, as shown in Figure 2.17. This will make the values of $\delta t_{1,i}$ *and* $\delta t_{2,i}$ very small. Since $\delta t_{1,i}$ *and* $\delta t_{2,i}$ are in the denominator of Equation 2.7, the outcome will be a very large value for $v$, which will not correspond to reality. Therefore, Wu et al. [146] stated that one way of minimising the effect of this problem in typical vertical bubbly multiphase flows is to make the

axial sensor separation *s* in the range between 0.5d and 2d, where d is the diameter of the bubble. As stated earlier, Wu said that, if $0.5d \leq s \leq 2d$, the measured bubble velocity fluctuation will be independent of the axial sensor separation.

## 2.5. Theory of the four-sensor probe

This section describes previous work on the four sensor conductance probe, including the associated mathematical model. As described in section 2.4, the local dual-sensor conductance probe has been widely used to obtain distributions of local gas velocity and gas volume fraction in multiphase flow. However, a dual-sensor probe is restricted to measuring the axial bubble velocity. Thus, a four-sensor probe was introduced to enable measurements of the vector velocity (magnitude and direction) of the dispersed bubbles in bubbly flow.

Prior to describing the model and the analysis of the four-sensor probe, it is proper to present the assumptions and conditions that should be taken into account before the model is applied.

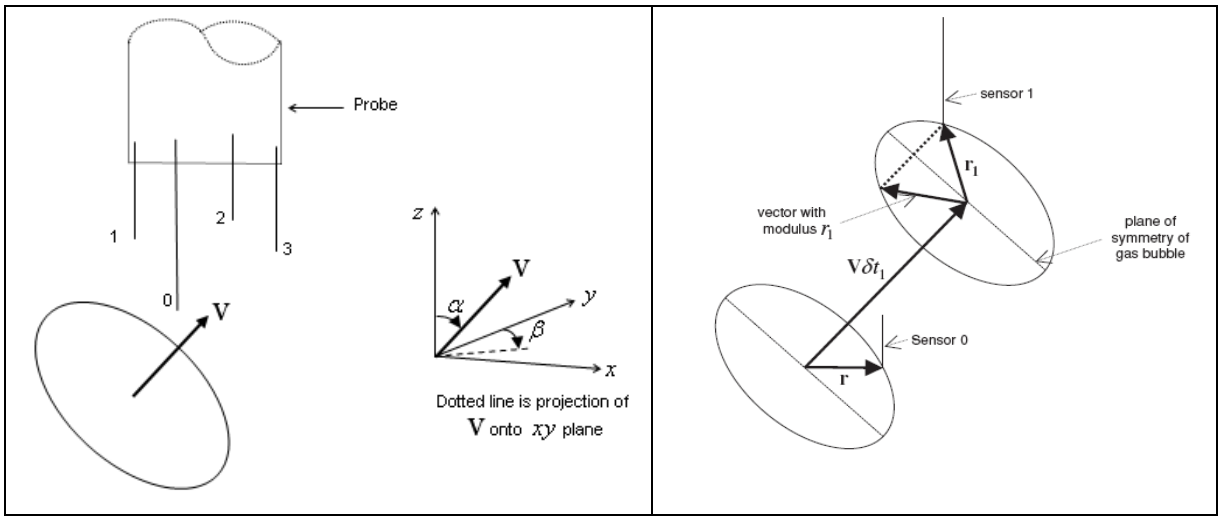


**Figure 2.18 (A): Bubble with vector velocity moving across the four-sensor probe. (B): motion of bubble between front sensor 0 and rear sensor 1.**

The four-sensor probe and the corresponding model are applicable to bubbly multiphase flows, where the continuous phase is a conducting liquid and the dispersed phase is a non-conductive gas or liquid. In the current research, the probe and its model were relevant to air-water bubbly flows.

The assumptions that were made for the development of the model are as follows:

1. Each bubble has a plane of symmetry normal to its direction of motion. Such bubble shapes include spheres and oblate spheroids. [NB:- As reported in [1-2], gas bubbles of the dispersed phase are flattened in their direction of motion due to their velocity relative to the continuous phase. Experimental observations reported in [1-2] showed that bubbles with small diameters (about 4mm) had spherical shapes, while bubbles with bigger diameters (about 8mm) tended to have oblate spheroid shapes.]
2. Each gas bubble strikes the front sensor ‘0’ first and then the rear sensors, as shown in Figure 2.18.
3. The surface of each gas bubble hits all four sensors twice. The first time is when the gas bubble initially contacts a sensor. The second time is when the gas bubble leaves the sensor.
4. The sensors do not alter the gas bubble’s properties or characteristics (shape and vector velocity).
5. When a gas bubble strikes the probe, the sensor output signals resemble the ideal signals shown in Figure 2.19 [note that the bubble hits the first sensor 0 first].

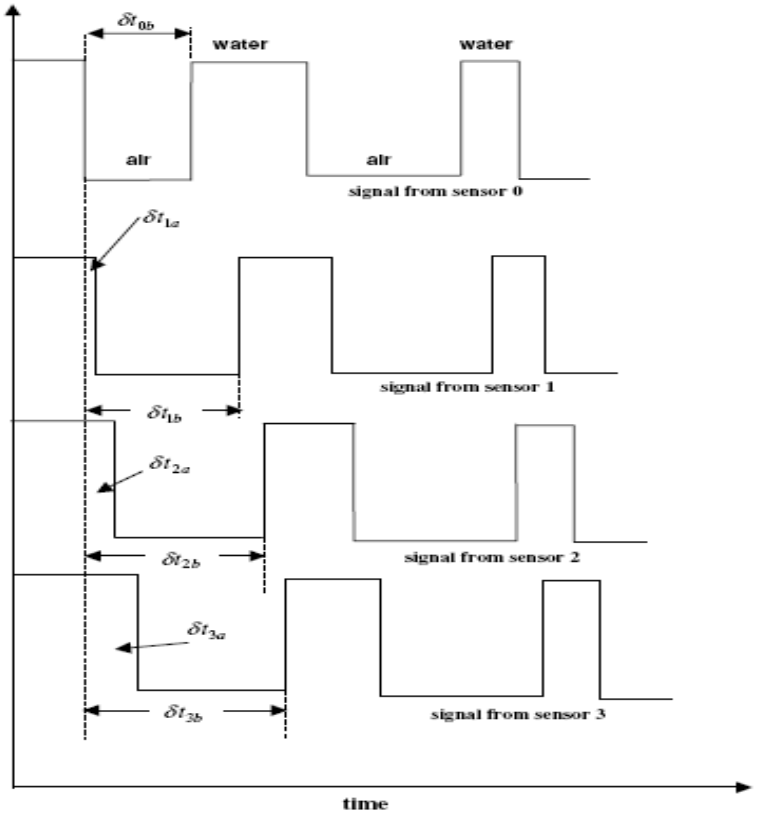


**Figure 2.19 Ideal signals from the four-sensor probe**

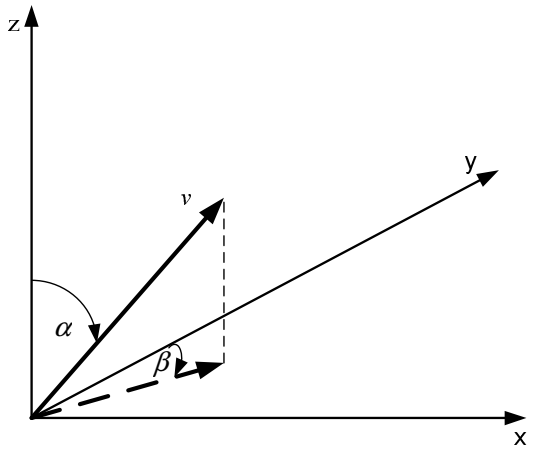


**Figure 2.20 Velocity vector representations**

The velocity vector **V** of a bubble can be represented mathematically by Equation 2.12 using the coordinate system shown in Figure 2.16.

$$\mathbf{V} = v\left(\sin\alpha\sin\beta\,\mathbf{i} + \sin\alpha\,\cos\beta\,\mathbf{j} + \cos\alpha\,\mathbf{k}\right) \qquad \textbf{Equation 2.12}$$

or

$$\mathbf{V} = v \cdot \hat{n}_v \qquad \textbf{Equation 2.13}$$

where $\alpha$ is the polar angle between the z-axis and the vector **V**, $\beta$ is the azimuthal angle between the y-axis and the projection of vector **V** onto the x-y plane, $v$ is the magnitude of the vector **V**, $\hat{n}_v$ is the unit vector in the direction of **V**, and **i, j, k** are unit vectors in the direction of the *x, y*, and *z* axes respectively. So, in order to find the velocity vector of a bubble, it is necessary to find the three parameters that define it. These are the polar angle ($\alpha$), the azimuthal angle ($\beta$), and the velocity magnitude ($v$).

### 2.5.1 A model for determining the bubble velocity vector from seven time delays

This section is based on work by Lucas et al. [1] and Mishra et al. [2]. Let us assume that a bubble moves with a velocity vector **V** (which can be described by Equations 2.20 and 2.21) relative to the coordinate system shown in Figure 2.20 and strikes the four-sensor probe. Also, let us take the case where the bubble strikes the front sensor (which has 0 as an index) and then strikes one of the rear sensors (with 1 as an index) as shown in Figure 2.18B.

When the bubble strikes front sensor 0 for the first time, a position vector **r** can be defined between the geometrical centre of the bubble and the point that contacts the sensor (see Figure 2.18 b). This position vector can be expressed as $\mathbf{r} = r\,\hat{n}_i$, where $\hat{n}_i$ is a unit vector. After some time, $\delta t_1$ the bubble strikes rear sensor 1, which is located

at $x_1, y_1, z_1$ with respect to the front sensor. The position vector $\mathbf{r_1}$ of this point of contact with sensor 1 relative to the centre of the gas bubbles can be given by:

$$\mathbf{r_1} = (\mathbf{r} + x_1\,\mathbf{i} + y_1\,\mathbf{j} + z_1\,\mathbf{k} - \mathbf{V}\,\delta t_1) \qquad \textbf{Equation 2.14}$$

Equation 2.14 can be expanded to derive the following expression for $r_1{}^2$, where $r_1$ the magnitude of is $\mathbf{r_1}$:

$$(\mathbf{r} + x_1\,\mathbf{i} + y_1\,\mathbf{j} + z_1\,\mathbf{k} - \mathbf{V}\,\delta t_1).(\mathbf{r} + x_1\,\mathbf{i} + y_1\,\mathbf{j} + z_1\,\mathbf{k} - \mathbf{V}\,\delta t_1) = r_1^2 \qquad \textbf{Equation 2.15}$$

Expanding the bracket in Equation 2.15, and writing $\mathbf{V} = v\,\hat{n}_v$ and $\mathbf{r} = r\,\hat{n}_i$ gives:

$$\begin{aligned} &r^2 + r\,x_1(\hat{n}_i\,.\mathbf{i}) + r\,y_1(\hat{n}_i\,.\mathbf{j}) + r\,z_1(\hat{n}_i\,.\mathbf{k}) - r\,v\delta t_1(\hat{n}_i.\hat{n}_v) + r\,x_1(\hat{n}_i\,.\mathbf{i}) \\ &+ x_1^2 - x_1 v\delta t_1(\hat{n}_v\,.\,\mathbf{i}) + ry_1(\hat{n}_i\,.\mathbf{j}) + y_1^2 - y_1 v\delta t_1(\hat{n}_v\,.\mathbf{j}) + r\,z_1(\hat{n}_i\,.\mathbf{k}) \\ &+ z_1^2 - z_1 v\delta t_1(\hat{n}_v\,.\mathbf{k}) - r\,v\delta t_1(\hat{n}_v\,.\hat{n}_i) - v\,x_1\delta t_1(\hat{n}_v\,.\mathbf{i}) - vy_1\delta t_1(\hat{n}_v\,.\mathbf{j}) \\ &- vz_1\delta t_1(\hat{n}_v\,.\mathbf{k}) + v^2\delta t_1^2 = r_1^2 \end{aligned} \qquad \textbf{Equation 2.16}$$

Equation 2.16 can be rearranged into following quadratic equation

$$\begin{aligned} &v^2\delta t_1^2 - 2v\delta t_1\{r(\hat{n}_i\,.\hat{n}_v) + 2x_1(\hat{n}_v\,.\,\mathbf{i}) + 2y_1(\hat{n}_v\,.\mathbf{j}) + 2z_1(\hat{n}_v\,.\mathbf{k})\} + \\ &\{x_1^2 + y_1^2 + z_1^2 + 2\,r\,x_1(\hat{n}_i\,.\,\mathbf{i}) + 2\,r\,y_1(\hat{n}_i\,.\,\mathbf{j}) + 2\,r\,z_1(\hat{n}_i\,.\,\mathbf{k}) + r^2 - r_1^2\} = 0 \end{aligned} \qquad \textbf{Equation 2.17}$$

The solution for the above quadratic equation can be written as:

$$\delta t_1 = \frac{-b \pm \sqrt{b^2 - 4ac}}{2a} \qquad \textbf{Equation 2.18}$$

where

$$a = v^2 \qquad \textbf{Equation 2.19}$$

$$b = -v\left(2r\left(\hat{n}_i.\hat{n}_v\right) + 2x_1 2x_1\left(\hat{n}_v \,.\, \mathbf{i}\right) + 2y_1\left(\hat{n}_v \,.\mathbf{j}\right) + 2z_1\left(\hat{n}_v \,.\mathbf{k}\right)\right) \qquad \textbf{Equation 2.20}$$

and

$$c = \left(x_1^2 + y_1^2 + z_1^2 + 2r\,x_1\left(\hat{n}_i \,.\mathbf{i}\right) + 2r\,y_1\left(\hat{n}_i \,.\mathbf{j}\right) + 2r\,z_1\left(\hat{n}_i \,.\mathbf{k}\right) + r^2 - r_1^2\right) \qquad \textbf{Equation 2.21}$$

Equation 2.18 has two solutions for time delays which are given as

$$\delta t_{1a} = \frac{-b - \sqrt{b^2 - 4ac}}{2a} \qquad \textbf{Equation 2.22}$$

$$\delta t_{1b} = \frac{-b + \sqrt{b^2 - 4ac}}{2a} \qquad \textbf{Equation 2.23}$$

The first solution $\delta t_{1a}$ is the time interval between the first contact of the bubble with front sensor 0 and the first contact of the bubble with rear sensor 1. The second solution $\delta t_{1b}$ is the time interval between the first contact of the bubble with front sensor 0 and the last contact of the bubble with rear sensor 1. Based on the assumption that the bubbles have a plane of symmetry normal to their direction of motion (see Figure 2.18), it is valid to conclude that $r_1$ is the same for the first and last contacts of the gas bubble with the rear sensor. Therefore, with reference to Figure 2.18, the terms $a, b$ and $c$ have the same values for the first and last contacts and Equations 2.30 and 2.31 can be combined into:

$$\delta t_{1a} + \delta t_{1b} = -\frac{b}{a} \qquad \textbf{Equation 2.24}$$

Applying Equations 2.28 and 2.29 to Equation 2.24, the result is:

$$\delta t_{1a} + \delta t_{1b} = \frac{\left(2r\left(\hat{n}_i . \hat{n}_v\right) + 2x_1\left(\hat{n}_v . \mathbf{i}\right) + 2y_1\left(\hat{n}_v . \mathbf{j}\right) + 2z_1\left(\hat{n}_v . \mathbf{k}\right)\right)}{v} \qquad \textbf{Equation 2.25}$$

Using the same procedure for the other two rear sensors, the corresponding equations are:

$$\delta t_{2a} + \delta t_{2b} = \frac{\left(2r\left(\hat{n}_i . \hat{n}_v\right) + 2x_2\left(\hat{n}_v . \mathbf{i}\right) + 2y_2\left(\hat{n}_v . \mathbf{j}\right) + 2z_2\left(\hat{n}_v . \mathbf{k}\right)\right)}{v} \qquad \textbf{Equation 2.26}$$

$$\delta t_{3a} + \delta t_{3b} = \frac{\left(2r\left(\hat{n}_i . \hat{n}_v\right) + 2x_3\left(\hat{n}_v . \mathbf{i}\right) + 2y_3\left(\hat{n}_v . \mathbf{j}\right) + 2z_3\left(\hat{n}_v . \mathbf{k}\right)\right)}{v} \qquad \textbf{Equation 2.27}$$

Looking at Equations 2.33-2.35, it can be observed that there are three equations with four unknowns, which are $r, v, \hat{n}_i, \hat{n}_v$. This problem can be overcome by considering the time interval $\delta t_{0b}$, which is the time between the first and last contact of the bubble with the front sensor only. Therefore, applying the same concept that was used for deriving Equations 2.33-2.35 to the front sensor, another equation is produced, which is:

$$\delta t_{0a} + \delta t_{0b} = \frac{\left(2r\left(\hat{n}_i . \hat{n}_v\right) + 2x_0\left(\hat{n}_v . \mathbf{i}\right) + 2y_0\left(\hat{n}_v . \mathbf{j}\right) + 2z_0\left(\hat{n}_v . \mathbf{k}\right)\right)}{v} \qquad \textbf{Equation 2.28}$$

But $x_0 = y_0 = z_0 = 0$ (since the origin of the coordinate system is the tip of the front sensor). So, Equation 2.28 can be written as:

$$\delta t_{0a} + \delta t_{0b} = \frac{2r\left(\hat{n}_i . \hat{n}_v\right)}{v} \qquad \textbf{Equation 2.29}$$

However, since timing starts when the bubble hits the front sensor for the first time, we may write that $\delta t_{0a} = 0$.

Substituting Equation 2.29 for Equations 2.25, 2.26 and 2.27 gives

$$\delta t_{11} = \frac{\left(2x_1(\hat{n}_v \,.\, \mathbf{i}) + 2y_1(\hat{n}_v \,.\, \mathbf{j}) + 2z_1(\hat{n}_v \,.\, \mathbf{k})\right)}{v} \qquad \textbf{Equation 2.30}$$

$$\delta t_{22} = \frac{\left(2x_2(\hat{n}_v \,.\mathbf{i}) + 2y_2(\hat{n}_v \,.\mathbf{j}) + 2z_2(\hat{n}_v \,.\mathbf{k})\right)}{v} \qquad \textbf{Equation 2.31}$$

$$\delta t_{33} = \frac{\left(2x_3(\hat{n}_v \,.\, \mathbf{i}) + 2y_3(\hat{n}_v \,.\mathbf{j}) + 2z_3(\hat{n}_v \,.\mathbf{k})\right)}{v} \qquad \textbf{Equation 2.32}$$

Where, $\delta t_{11} = \delta t_{1a} + \delta t_{1b} - \delta t_{0b}$ **Equation 2.33**

$$\delta t_{22} = \delta t_{2a} + \delta t_{2b} - \delta t_{0b} \qquad \textbf{Equation 2.34}$$

$$\delta t_{33} = \delta t_{3a} + \delta t_{3b} - \delta t_{0b} \qquad \textbf{Equation 2.35}$$

With reference to Figure 2.18, $\hat{n}_v$ can be written as

$\hat{n}_v = \left(\sin\alpha\sin\beta\ \mathbf{i} + \sin\alpha\cos\beta\,\mathbf{j} + \cos\alpha\mathbf{k}\right)$. From Equations 2.34 - 2.35 the final equations that describe the vector velocity of a bubble that hits a four-sensor probe are derived:

$$x_1 \sin\alpha \sin\beta + y_1 \sin\alpha\cos\beta + z_1 \cos\alpha = \frac{v\delta t_{11}}{2} \qquad \textbf{Equation 2.36}$$

$$x_2 \sin\alpha\sin\beta + y_2 \sin\alpha\cos\beta + z_2 \cos\alpha = \frac{v\delta t_{22}}{2} \qquad \textbf{Equation 2.37}$$

$$x_3 \sin\alpha\sin\beta + y_3 \sin\alpha\cos\beta + z_3 \cos\alpha = \frac{v\delta t_{33}}{2} \qquad \textbf{Equation 2.38}$$

This results in three Equations 2.44-2.46, with three unknown variables. Solving these three equations gives the polar angle $\alpha$, the azimuthal angle $\beta$, and the magnitude $v$ of the velocity of the bubble.

$$\tan\beta = \frac{\left(\frac{z_1}{\delta t_{11}} - \frac{z_2}{\delta t_{22}}\right)\left(\frac{y_1}{\delta t_{11}} - \frac{y_3}{\delta t_{33}}\right) - \left(\frac{z_1}{\delta t_{11}} - \frac{z_3}{\delta t_{33}}\right)\left(\frac{y_1}{\delta t_{11}} - \frac{y_2}{\delta t_{22}}\right)}{\left(\frac{z_1}{\delta t_{11}} - \frac{z_3}{\delta t_{33}}\right)\left(\frac{x_1}{\delta t_{11}} - \frac{x_2}{\delta t_{22}}\right) - \left(\frac{z_1}{\delta t_{11}} - \frac{z_2}{\delta t_{22}}\right)\left(\frac{x_1}{\delta t_{11}} - \frac{x_3}{\delta t_{33}}\right)}$$

**Equation 2.39**

$$\tan\alpha = \frac{\left(\frac{z_2}{\delta t_{22}} - \frac{z_1}{\delta t_{11}}\right)}{\left(\frac{x_1}{\delta t_{11}} - \frac{x_2}{\delta t_{22}}\right)\sin\beta - \left(\frac{y_1}{\delta t_{11}} - \frac{y_2}{\delta t_{22}}\right)\cos\beta}$$

**Equation 2.40**

From the measured sensor co-ordinates $x_i$, $y_i$, $z_i$ and the measured time intervals $\delta t_{ii}$ for the bubble, the azimuthal angle $\beta$ for a particular bubble is calculated using Equation 2.30 and polar angle $\alpha$ is calculated using Equation 2.40. Once the value of $\beta$ and $\alpha$ is calculated, $v$ is calculated using any one of Equations 2.44-2.46.

However the procedure to calculate $\beta$ and $\alpha$ is somewhat complicated, for any value of $\tan\beta$, there are two possible values of $\beta$ which can either be positive or negative that lie between $0^o$ and $360^o$. Lets assume $\beta_1$ as a positive value for the value of $\tan\beta$ [i.e. $\beta_1$ will lie between $0^o$ and $90^o$ (first quadrant) and between $180^o$ and $270^o$ (third quadrant)] and $\beta_2$ as a negative value for the value of $\tan\beta$ [ i.e. $\beta_2$ will lie between $90^o$ and $180^o$ (second quadrant) and between $270^o$ and $360^o$ (fourth quadrant)].

If $\beta_1$ is substituted into Equation 2.40 then we get two possible values for $\alpha$, as $\alpha_1$ and $\alpha_2$. Similarly, when $\beta_2$ is substituted into Equation 2.40 then we get two further possible values for $\alpha$ denoted as $\alpha_3$ and $\alpha_4$. These four values of $\alpha$ thus calculated will all lie in different quadrants. From the definition of $\alpha$ shown in Figure 2.18 (in which $\alpha$ can only lie between $0^o$ and $180^o$) the values of $\alpha$ that lie in quadrants three and four can therefore be rejected. For the experiments described in this thesis, the bubble velocity vector $\mathbf{V}$ always makes an acute angle with the increasing z-axis of the probe co-ordinate system; hence the value of $\alpha$ arising from Equation 2.40 that lies in the second quadrant ($90^o$ to $180^o$) can also be rejected. The remaining value of $\alpha$, which lies in the first quadrant ($0^o$ to $90^o$) is chosen as the 'correct' polar angle $\alpha_{meas}$, as measured by the four-sensor probe. The value of $\beta$ which gives correct $\alpha_{meas}$ is selected as the 'correct' azimuthal angle $\beta_{meas}$ as measured by the four-sensor probe.

### 2.5.2 Comments on the model

From Equations 2.44-2.48, it is obvious that, in order to calculate the bubble vector velocity $\mathbf{V}$ in the probe coordinate system, the dimensions of the probe must be measured and so must the time delays $\delta t_{ii}$ (see Equations 2.41 - 2.43). Note that the dimensions of the probe are the $x_i, y_i$ and $z_i$, distances of the tips of the rear sensors from the tip of the front sensor in the probe coordinate systems (see Figure 2.18).

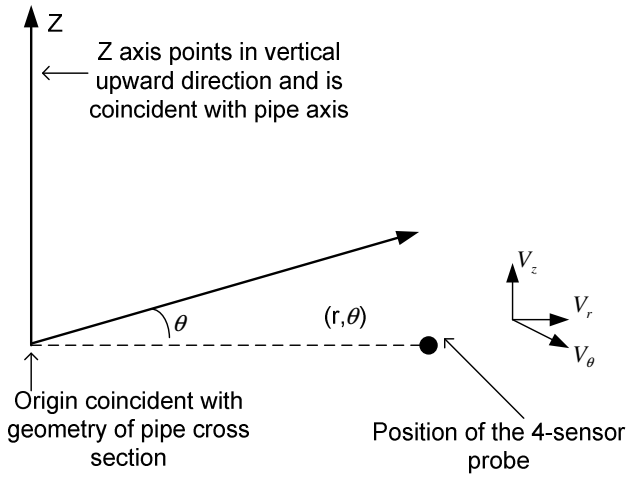


**Figure 2.21 Cylindrical coordinate system for pipe. The large black dot represents the position of the four-sensor probe.**

Also, since the velocity magnitude, the polar angle $\alpha$, and the azimuthal angle $\beta$ are known, the velocity components of the bubble in the coordinate systems of a circular pipe can be computed using Equations 2.49 - 2.51 (see Figure 2.21 and Chapter 7.2 for details). Equations 2.49 - 2.51 assume that the z-axis of the probe coordinate system is parallel to the z-axis of the pipe coordinate systems and the y-axis of the probe coordinate system is parallel to a pipe radius.

$$V_\theta = v \sin\alpha \sin\beta \qquad \textbf{Equation 2.41}$$

$$V_r = v \sin\alpha \cos\beta \qquad \textbf{Equation 2.42}$$

$$V_z = v \cos\alpha \qquad \textbf{Equation 2.43}$$

In Equations 2.41 - 2.43, $V_\theta$ is azimuthal velocity, $V_r$ is the radial velocity, and $V_z$ is the axial velocity. Based on these definitions, it is obvious that a positive axial velocity means that the bubbles go upwards (if the probe faces the bubble's direction), a positive radial velocity means that the bubbles move away from the centre of the

pipe, and a positive azimuthal velocity means that the bubbles have a clockwise motion (when viewed facing the oncoming flow). The bubble velocity vector measured by the probe can also be transformed into the coordinate systems of the rectangular cross sectional tank, even when the probe is tilted or rotated to the relative tank coordinate systems. A more detailed analysis can be found in Chapter 7.

It is important to mention that the mean local volume fraction of the dispersed phase $\lambda_l$ can be calculated by:

$$\lambda_l = \frac{1}{T}\sum_{n=1}^{N}(\delta t_{0b})_n \qquad \textbf{Equation 2.44}$$

Where $T$ is the total time of the sampling process, and $N$ is the number of bubbles that strike the front sensor.

## 2.6 The rotary index dual-sensor probe

Panagiotopoulos et al. [11] used a rotary index dual-sensor probe in order to simulate a four-sensor probe by rotating the rear sensor with respect to the front sensor. Using this formation, it is obvious that the frontal area is much smaller than that of the traditional four-sensor probe, thus it causes fewer disturbances to the flow. Hence, the main objective of using this type of probe was to investigate the retarding effect of the probe on the bubble. These rotary index dual-sensor probes are also much easier to fabricate than a four-sensor probe. The main disadvantage of the rotary index dual-sensor probe is that these probes can only be used in steady flow where the air bubbles all have the same trajectory, size and shape and the same velocity vector and orientation when they strike the probe [11].

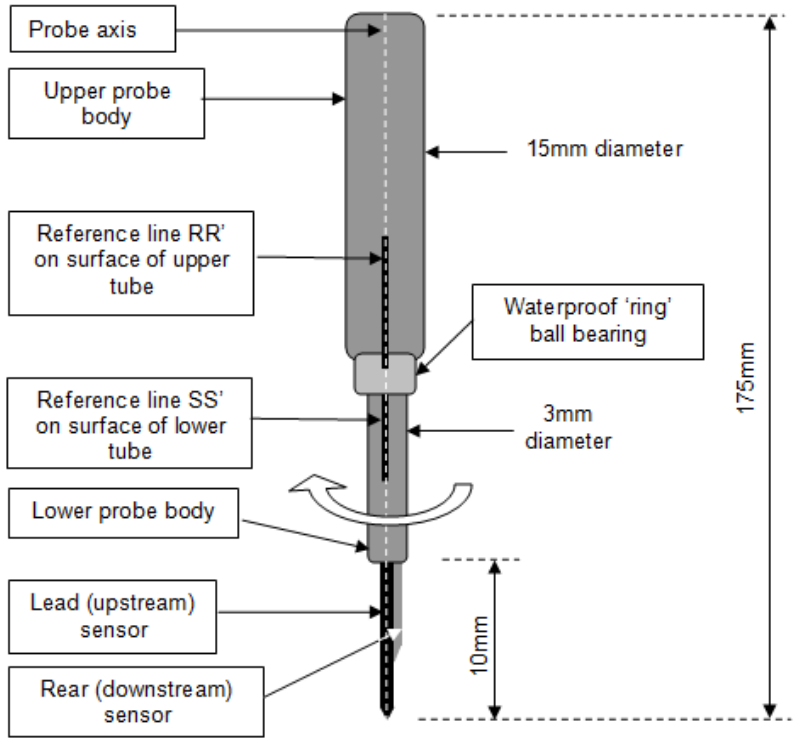


**Figure 2.22 The rotary index dual-sensor probe (not to scale). Panagiotopoulos et al. [11]**

The rotary index dual-sensor probe described by Panagiotopoulos et al. [11] (see Figure 2.22) consisted of an upper part and a lower part which were connected using a waterproof ball bearing. The upper part of the probe was clamped onto a platform, whereas the lower part of the probe contains two acupuncture needles coated with insulating film. The insulating film was removed from the tips of the needles so as to make them conductive to allow them to work as sensors in bubbly air-water two-phase flow.

For the simulated four-sensor probe, as described by Panagiotopoulos et al. [11], with an axial sensor separation of 1.1765mm between the upstream and downstream sensors, the effective x, y and z coordinates, in the probe coordinate system, of the three simulated rear sensor are give in Table 2.2 below.

| | x (mm) | y(mm) | z(mm) |
|---|---|---|---|
| Sensor 1 | 0 | 0.7326 | 1.1765 |
| Sensor 2 | 0.6344 | -0.3663 | 1.1765 |
| Sensor 3 | -0.6344 | -0.3663 | 1.1765 |

**Table 2.2 Probe dimensions measured by Panagiotopoulos et al. [11]**

These probe dimensions can be compared with the probe dimensions of the conventional four-sensor probe given by Lucas et al. [1], as shown in Table 2.3. From the dimensions given in Table 2.2, the effective cross-sectional area of this rotary index dual-sensor probe is much smaller, at 1.67mm$^2$, as compared to the dimension in Table 2.2 which is 6.60mm$^2$; this reduction lessens the retarding effect of the probe on the bubble. Also, while simulating a rotary index dual-sensor as a four-sensor probe, the bubble does not see the full area of the rotary index dual-sensor probe. The bubble only sees two sensors at a time which means the retarding effect of the probe on the bubble is even smaller.

| | x (mm) | y(mm) | z(mm) |
|---|---|---|---|
| Sensor 1 | -0.702 | 0.999 | 1.084 |
| Sensor 2 | 0.254 | 1.486 | 1.067 |
| Sensor 3 | 0.81 | 1.081 | 1.153 |

**Table 2.3 Probe dimensions measured by Lucas et al. [1]**

From Table 2.2 it is also clear that the front (upstream) sensor of the rotary index dual-sensor lies in between the three simulated rear sensors, ensuring that the bubble always hits the front sensor. From Table 2.3, it is clear that, in the case of the conventional four-sensor probe described by Lucas et al.[1], the front sensor does not lie in between the three rear sensors, meaning it is likely that the bubble does not necessarily always hit the front sensor first. The effect is described in Chapter 3.

Lucas et al. [1] also introduced a calibration factor *K* to compensate for the retarding effect of the probe on the bubble as follows:

$$K\,\overline{u}_{g.probe} = \overline{u}_{g.ref} \qquad \textbf{Equation 2.45}$$

Where $\overline{u}_{g.probe}$ is the mean axial gas velocity, obtained by probe and $\overline{u}_{g.ref}$ is the mean axial gas reference velocity.

For the conventional four-sensor probe, Lucas et al. [1] found a calibration factor *K* of 1.2 with a variation of up to ±20%, whereas from the rotary index dual-sensor probe it was found that the calibration factor is approximately 0.94. This result shows that the frontal area of the probe plays a significant role in reducing the velocity of the bubble when the probe interacts with the bubble. However, only disadvantage of this method is it requires three sets of reading for each experiment.

# CHAPTER 3

# Probe Fabrication

## 3.1 Fabrication manufacturing and steps of manufacturing the probes

A dual-sensor probe can measure gas volume fraction, axial bubble velocity and local bubble frequencies in a bubbly gas-liquid flow, but it cannot measure the local velocity vector of the dispersed bubble in such flows. To measure the local velocity vector of the dispersed bubbles, a four-sensor probe is needed, as described earlier in Chapter 2.

For accurate measurement of the local bubble velocity vector, it is important that the frontal area of the fabricated four-sensor probe is as small as possible (see Chapter 2.6). Since the bubble strikes each sensor twice, it is important that the probe has a minimal effect on the bubble shape and velocity vector. Due to certain physical circumstances, listed below, the manufacture of the four-sensor probe is not straightforward.

1. As the probe is fabricated by hand, the accuracy of the positioning of the needles is limited by human factors especially associated with the eye and with hand movement. It is difficult both to place the needles in the correct position and also to measure the position of the needle tops with great accuracy (see section 3.4 and Chapter 4 for measurement and the sensitivity of the dimension).

2. The smaller the dimensions of the probe, the higher the sampling rate (maximum sampling frequency was made 50 KHz to limit the size of data to be able to process in considerable amount of time) is needed in order to acquire a reliable and representative signal from each sensor.

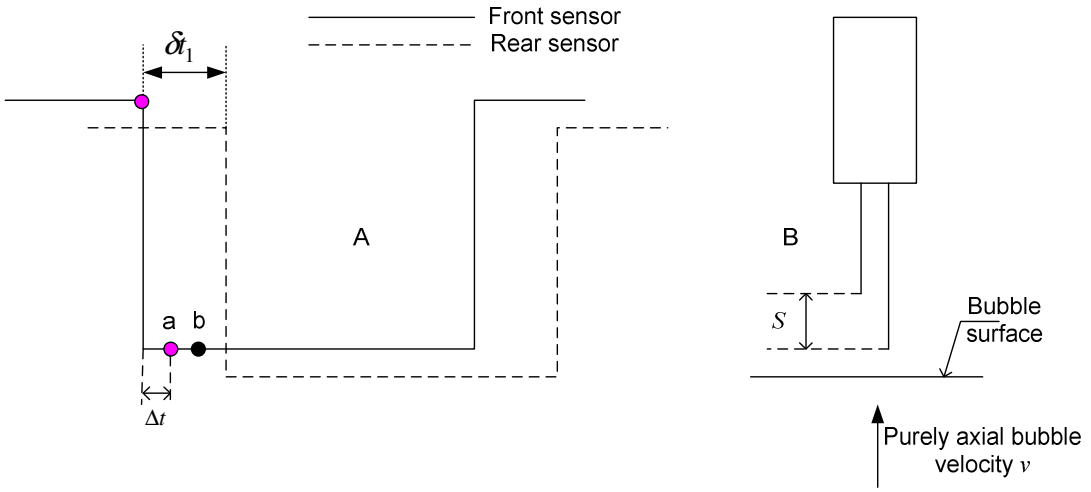


**Figure 3.1 (A) Typical signal from a dual-sensor probe where "a" is time taken at sampling frequency 40 KHz and "b" is time taken at sampling frequency 20 KHz (B) Dual-sensor probe**

For example, if the data are sampled at the frequency ( $fs$ ) with a dual-sensor probe, Figure 3.1 shows the ideal output from the dual-sensor probe. The time taken ( $\Delta t$ ) to sample single data is given by Equation 3.1.

$$\Delta t = \frac{1}{fs} \qquad \textbf{Equation 3.1}$$

Equation 3.2 gives the actual local gas velocity $v_{,true}$ .

$$v_{,true} = \frac{s}{\delta t_1} \qquad \textbf{Equation 3.2}$$

Measured time delay = $\delta t_1$

Measured time delay can be in the range of $\delta t_1$ to $\delta t_1 + \frac{1}{fs}$

Hence measured local gas velocity $v_{,meas}$ can be in the range from Equation 3.3 to 3.4.

$$v_{,meas} = \frac{s}{\delta t_1} \quad \textbf{Equation 3.3}$$

$$v_{,meas} = \frac{s}{\delta t_1 + \frac{1}{fs}} \quad \textbf{Equation 3.4}$$

Therefore, as the sampling frequency increases, the difference between $v_{,true}$ and $v_{,meas}$ tends towards zero.

### 3.1.1 Fabrication of a new design four-sensor probe (PN1)

The process in this section describes the fabrication technique for the early version of the four-sensor probe (denoted by PN1 in this thesis) used during this research. The purpose of fabricating a new design of the four-sensor probe PN1 was to overcome the existing problems with the four-sensor probe (denoted by PN0) used by Lucas et al. [1], i.e. to bring the calibration factor *K* closer to unity, which was 1.2 with a possible error of ±20%, as previously suggested by Lucas et al. [1]. The reason behind this higher value of *K* factor was believed to be due to the frontal cross-section area of the probe itself, which causes the deformation of the bubble during probe-bubble interaction. Therefore, the fabrication of the new four-sensor probe concentrated on reducing the frontal cross-sectional area of the probe. In order to achieve this goal, a new ceramic guide, available on the market, was used (see Figure 3.2).

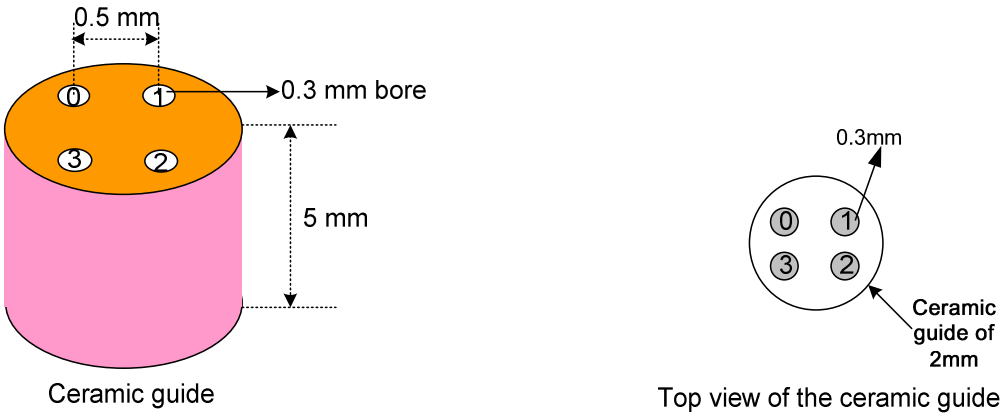


**Figure 3.2 New ceramic guide used for PN1**

The new ceramic guide has an outer diameter of 2 mm and contains four holes of 0.3 mm in diameter which are 0.5mm apart from each other (see Figure 3.2).

The components and materials chosen for fabricating the four-sensor probes PN1 were as follows:

- Stainless steel acupuncture needles as sensing electrodes (50mm x 0.3mm).
- Stainless steel tubing as the support and the common electrode (5 mm O/D, 2.1mm I/D).
- Resin based two component glue for bonding the parts.
- Waterproof paint and insulating silicon paint for needles.
- 30 AWG silver-plated copper wire for connecting needles to the measurement system.
- Silver loaded conducting paint for connecting wire to the needles.
- 4 hole ceramic guide (see Figure 3.2.)

The reason for using acupuncture needles was that they have a very small diameter (0.3mm), they are rigid, and have a straight, uniform shape. The small needle

diameter is an advantage due to the fact that it minimises the interaction between the sensor and the bubble, affecting the bubble's characteristics and dynamics as little as possible. The rigidity and the uniform shape of the needles give the advantage of assembling a sensor with uniform characteristics.

The stainless steel tube of 5mm diameter was used to hold the sensors and also act as the common electrode. The tube was bent at an angle of $90^0$ (see Figure 3.3) in order to make it easy to mount in the pipe, and also for the probe measurement (see Chapter 3.3). Finally, the tube was connected with the traverse mechanism, a device that will be described in Chapter 10.

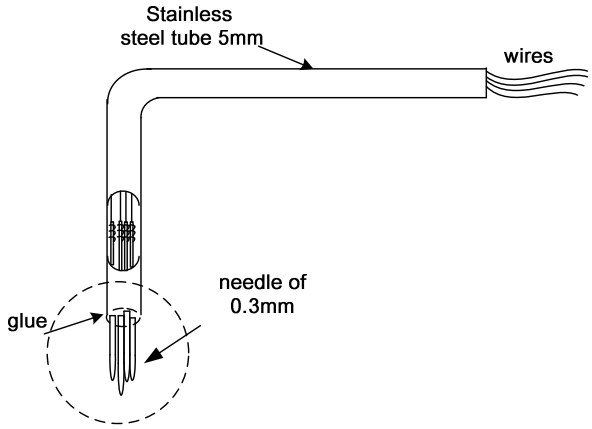


**Figure 3.3 Schematic of four-sensor probe PN1**

Initially two types of coatings were used to insulate the needles, except at their tips: a waterproof paint, and an insulating varnish. The waterproof paint electrically isolates the needles from the water. The insulating varnish creates an additional insulating layer. Due to the fact that the varnish coating was difficult and time consuming to apply to the sensors, this technique was abandoned and silicon coating was applied instead. This method was easier and less time consuming, but concentration was

needed in order to make the paint thickness uniform along the needles. The performance of the probe was not changed because of this alteration.

*3.1.1.1 Steps of fabrication of a four-sensor probe*

Step 1: Cut stainless steel tube, needles and wire to length; use different colour wire.

Step 2: To achieve close lateral needle spacing, bend the blunt end of three needles (see Figure 3.4) so as to allow sufficient space for the wire to be connected to the needles.

**Figure 3.4 Bent acupuncture needles used for four-sensor probe PN1**

Step 3: Clean needles of dust and grease and remove the first few millimetres of wire insulation and twist around the blunt end of the needles.

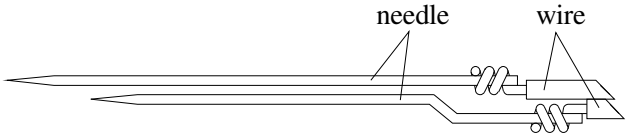


**Figure 3.5 Two out of four needles showing the conductive wire twisted around the blunt ends.**

Step 4: Apply conducting paint to glue together the wire-needle connections; thus, the wire connects firmly with the needles.

Step 5: Clean needles and apply a thin layer of silicon paint on all conducting areas (needle and conducting paint); while painting silicon, it is important to ensure that the

paint is as smooth as possible to avoid any deformation of the bubble passing over the sensor.

Step 6: Remove insulation from tips of needles with fine sandpaper to make it electrically conductive.

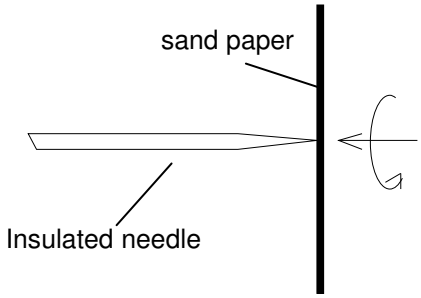


**Figure 3.6 Sandpaper used to remove insulation from the tips of the sensor.**

Step 7: The prepared needles were then glued onto a ceramic guide. While applying glue to the needles, it was ensured that one out of the four needles was placed forward of the others, as shown in Figure 3.7. The distance between the tip of the front sensor and the tips of all the rear sensors was made approximately equal to 1-2 mm i.e. $z_1 = z_2 = z_3 =$ 1-2 mm. The tip of this upstream needle was defined as the front sensor (marked as '0' in Figure 3.2). The origin of the coordinate system was made coincident with the position of the front sensor, whilst the $z$-axis of the probe coordinate system was parallel to the axis of the probe (this axis was vertical for vertically mounted probes such as those described in [1]). The $x$ and $y$ axes are chosen arbitrarily, but are orthogonal to each other and to the $z$-axis.

Step 8: Insert needle assembly into stainless steel tube of 5mm diameter, used as a common electrode, and bond them with two component glue. Also glue far end of the

tube where the wires come out for strain relief of the needles (see Figure 3.7). Finally the tube was bent to 90° (see Figure 3.3).

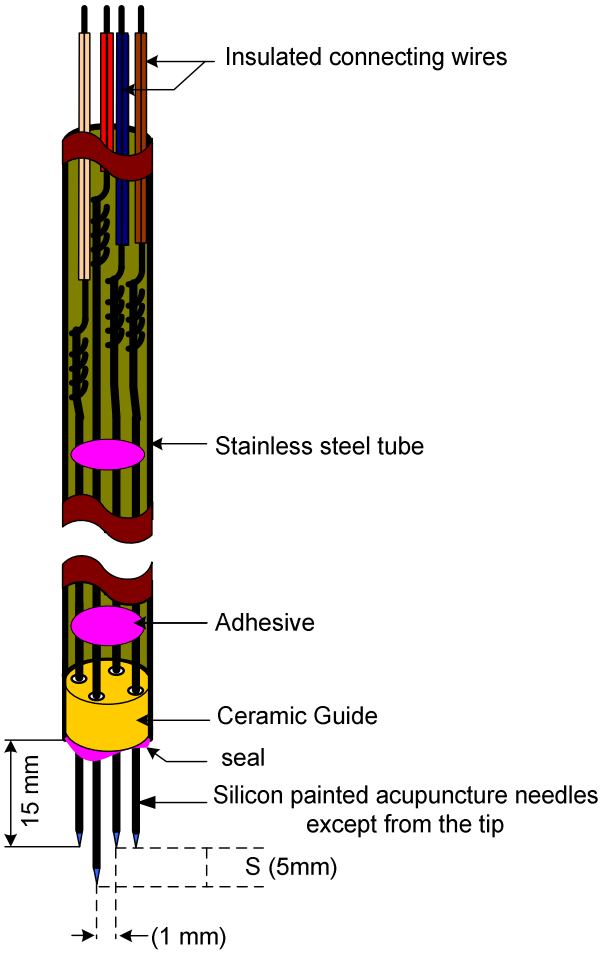


**Figure 3.7 Cross section schematic of a four-sensor probe PN1.**

Step 9: Measure probe dimensions (see Chapter 4).

The spatial locations of rear sensors 1, 2 and 3 can be defined using this probe coordinate system. Suppose that an approaching bubble has velocity vector **V** relative to the probe coordinate system, as shown in Figure 2.18 (further details are in Chapter 7.2).

A digital microscope was used to measure the probe (see later section 3.3 for details). The measurements were carried out with reference to Figure 2.18 (see Chapter 7.2 for further details of the probe coordinate system).

| | *x* (mm) | *y* (mm) | *z* (mm) |
|---|---|---|---|
| Sensor 1 | -0.702 | 0.999 | 1.084 |
| Sensor 2 | 0.254 | 1.486 | 1.067 |
| Sensor 3 | 0.810 | 1.081 | 1.153 |

**Table 3.1 Measured dimensions of a typical probe (PN1) with a new type of ceramic guide.**

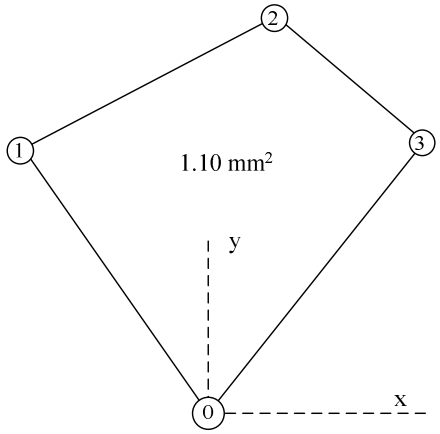


**Figure 3.8 Sketch of the frontal view of the probe PN1 based on the dimensions in Table 3.1 with sensor 0 being at coordinate (0, 0, 0)**

Table 3.1 shows the dimensions of one of the many newly built probes (PN1) using the new type of ceramic guide. Figure 3.8 shows a sketch of the frontal view of the probe based on the dimensions provided in Table 3.1 with the front sensor '0' as the coordinate (0, 0, 0). These dimensions show the frontal area of the probe is approximately 1.10 $mm^2$. The newly made probe PN1 (described above) was compared with the probe (PN0) used by Lucas et al. [1].

| | *x* (mm) | *y* (mm) | *z* (mm) |
|---|---|---|---|
| Sensor 1 | 1.384 | -0.988 | 1.200 |
| Sensor 2 | 0.263 | -1.713 | 0.640 |
| Sensor 3 | -0.988 | -1.318 | 1.800 |

**Table 3.2 Probe dimensions of the PN0 probe**

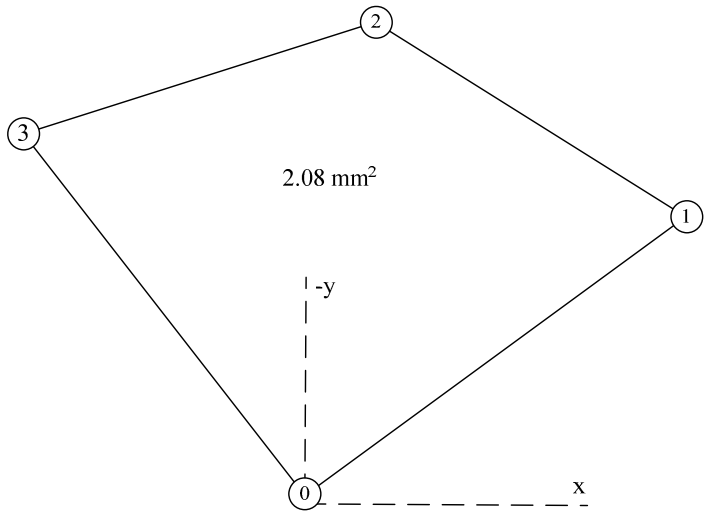


**Figure 3.9 Sketch of the frontal view of the PN0 probe based on the dimensions in Table 3.2 with sensor 0 being at coordinate (0, 0, 0)**

Table 3.2 shows the probe dimensions used by Lucas et al. [1] and Figure 3.9 shows the frontal view of the previous probe (PN0) drawn from the probe dimensions provided in Table 3.2. From the dimensions given in Table 3.2, the frontal area of the previous probe PN0 was found to be approximately 2.08mm$^2$. Thus the overall frontal area of the new probe PN1 was reduced by about 50% compared with the previous probe PN0 using the new ceramic guide. Thus the new probe can be expected to reduce the retarding effect caused by the bubble probe interaction. Although the frontal area of the newly fabricated probe was significantly reduced, initial investigations suggested that there was no improvement in calibration factor *K*, which was believed to be due to the applied paint on the acupuncture needles. Therefore, it

was decided to design another new probe (described as PN2 in this thesis) with an even smaller frontal area, as well as using thinner needles, so as to minimise the effect on the bubble during bubble-probe interaction, which is described in section 3.2.

## 3.2 Miniature four-sensor probe (PN2)

The previous results (Chapter 2), from the four-sensor probe used by Lucas et al. [1] and the rotating index dual sensor probe developed by Panagiotopoulos et al. [11], and the above discussion suggest that the rotating dual sensor probe has a much smaller retarding effect on the bubbles than an equivalent conventional four-sensor probe, which implies that, when designing a four-sensor probe, the issue of probe intrusiveness must be addressed. Thus, new ideas for fabricating the four-sensor probe were considered, including the following two options:-

**Option one**: - The first option is to sputter coat gold onto a substrate and then remove the track from the sensor using a method such as lithography, etching, laser beam machining or electrical discharge machining.

**Option two**: - Another possible method is to use Teflon (PTFE) coated needles with a diameter of 0.15mm in conjunction with a centred hole ceramic guide, as shown in Figure 3.10. This ceramic guide contains six holes of 0.3mm diameter with one hole in the centre (see Figure 3.10). From the five outer holes, three outer holes are chosen (with an additional hole in the centre) in such a way that the three outer holes form an isosceles triangle.

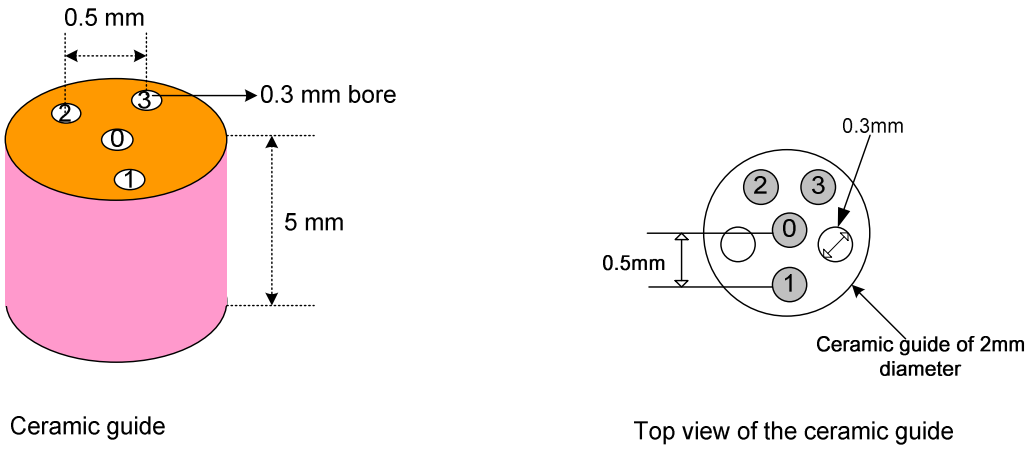


**Figure 3.10 Ceramic guides with a hole in the centre used for PN2 probe**

From the above two options, option two was chosen for this research, as although the proposed first method might be feasible, the process was found to be very complicated and expensive.

### 3.2.1 Advantages of a miniature new probe PN2

This section describes the advantages of the newer version of probe PN2 made with Teflon coated needles over the older probe PN1 made with acupuncture needles.

1. There is a smoother insulating layer on the needles: the Teflon coating was already applied by the factory using non conductive Teflon; hence, it was not necessary to paint the needles again. Since the non conductive Teflon was applied in the factory, the surface of the needles is much smoother than the hand painted probe PN1.
2. Fewer 'obstacles' on the probe's surface: due to the smoother layer on probe PN2 there are less obstacles during bubble–probe interaction as compared with PN1.
3. Smaller overall frontal area: compare the new probe PN2 with probe PN1 made from conventional acupuncture needles and the new type of ceramic

guide (centred hole ceramic) as shown in Figure 3.10. This ceramic guide contains six holes of 0.3mm diameter with one hole in the centre (see Figure 3.10). From the five outer holes, three outer holes are chosen (with an additional hole in the centre) in such a way that the three outer holes form an isosceles triangle.

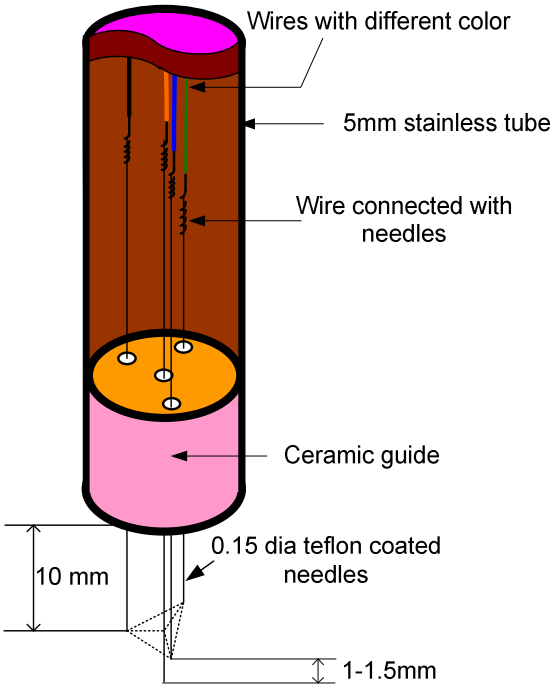


**Figure 3.11 Cross-sectional view of miniaturised four-sensor probe PN2 with a new ceramic guide (hole in the centre of Figure 3.10) and Teflon coated needles.**

The centre hole was used for the front (upstream) sensor, sensor'0', and the other three holes were used for the rear (downstream) sensors '1','2' and '3', as shown in Figure 3.11. The rear sensors were placed approximately 1mm behind the front sensors, which is the axial sensor separation making $z_1 \approx z_2 \approx z_3 \approx$1-1.5 mm. The four-sensor probes PN2 fabricated from the above method have two important advantages:

A. Using this technique to place the sensors, there is a higher possibility that the bubble will always hit the front sensor first followed by the rear sensor (see advantage number 5 for details) which allows the data to be collected during a shorter period of time (sampling time), thus making the data file smaller which means it can be processed faster.

B. Another advantage of using this technique is the reduction of the frontal area of the probe itself. Table 3.3 shows the typical dimensions of the rear probe with respect to the front probe.

| | *x* (mm) | *y* (mm) | *z* (mm) |
|---|---|---|---|
| sensor 1 | 0.0233 | 0.7471 | 0.7965 |
| sensor 2 | 0.4128 | -0.6322 | 0.9535 |
| sensor 3 | -0.4767 | -0.6149 | 0.8605 |

**Table 3.3 Measured dimensions of the PN2 probe**

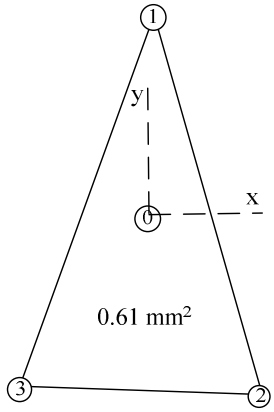


**Figure 3.12 Sketch of the frontal view of PN2 probe based on the dimensions in Table 3.3 and sensor 0 being at coordinate (0, 0, 0)**

From the above table it can be seen that the frontal area of probe PN2 is approximately equal to 0.61mm$^2$, which is half of the area of probe

PN1 and four times smaller than PN0 described in the previous section (see Figures 3.8 and 3.9); this can also be verified by Figure 3.12, which is a sketch of the frontal view of the rear sensor based on the coordinates given in Table 3.3, with the front sensor, sensor'0', placed as coordinate (0, 0, 0).

4. Less deformation of bubbles due to interaction with the probe: due to probe PN2 possessing a smaller frontal area and smoother needles, there is less deformation of the bubble during bubble-probe interaction.
5. More bubbles hit the front sensor first: the new layout of probe PN2 ensures that the probes are arranged in an isosceles triangle, where the three rear sensors are placed on the three corners of the triangle with the front sensor in the middle of the triangle, as shown in Figure 3.13.

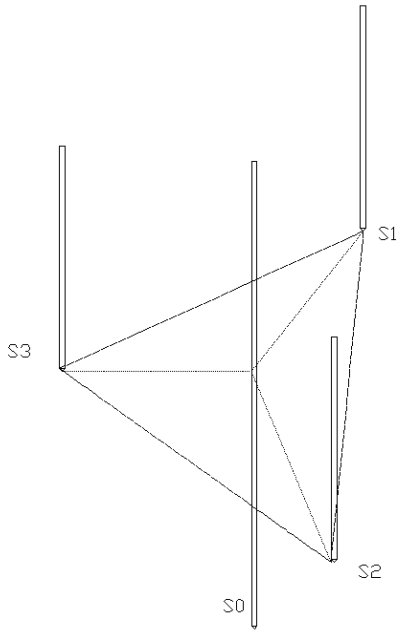


**Figure 3.13 Layout of probe PN2**

Therefore, it is more likely that the bubble will hit the front sensor before hitting any other sensors, which is the basic assumption of the mathematical model, no matter which direction the bubble is flowing. Whereas in the older designs [1, 2], namely probes PN0 and PN1, there is a high possibility of the bubble hitting the rear sensor before hitting the front sensor if it is flowing in a different direction (see Figure 3.14). This situation results in lots of bubbles being ignored during signal processing because they don't hit the front sensor first, thus causing a longer sampling time and increasing the amount of data to be processed (see Chapter 6 for details).

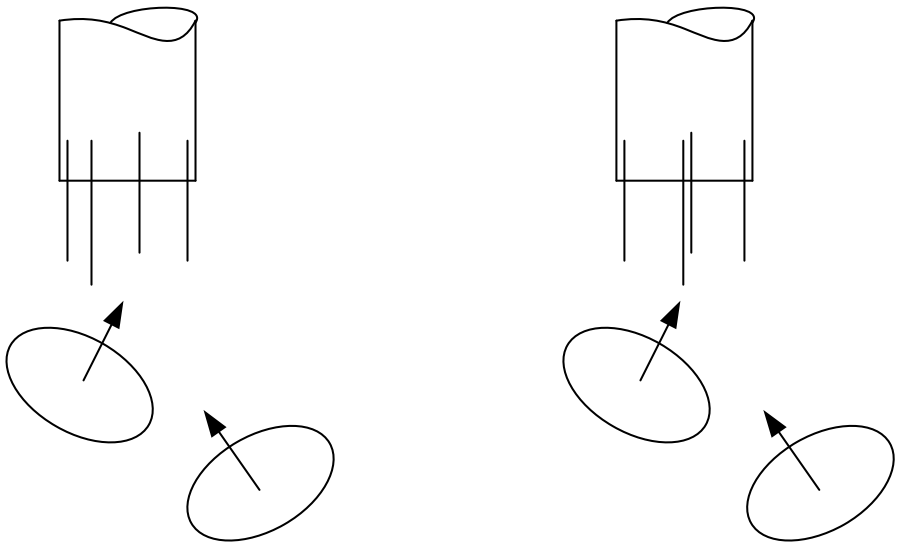

**Figure 3.14 Showing the general idea of hitting the probe using conventional (left) and new probe designs (right)**

### 3.2.2 Steps for manufacturing probe PN2

- Cut the Teflon coated needles, stainless tube and wire to length; use different colour wires.

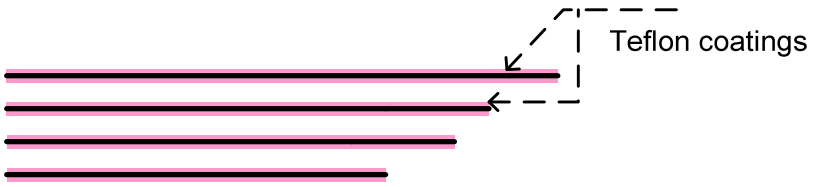


**Figure 3.15 Teflon coated needles cut to different lengths**

- To prevent the wires from touching each other, cut the Teflon coated needles to a different length.
- Scratch the Teflon from the tip of the needles so as to make them conductive in order to connect the wire.

**Figure 3.16 Scratched Teflon coating in order to make needles conductive**

- Apply the conductive paint to glue together the wire-needles connections; thus, the wire connects firmly with the needles.

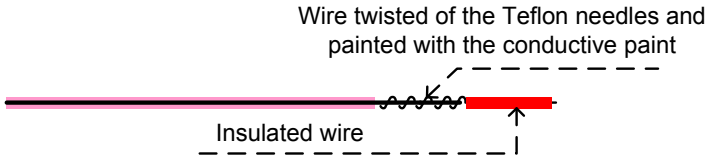


**Figure 3.17 Wire twisted and glued on the scratched needle**

- Place and glue the needles in the four holes of the ceramic guide, denoted by '0', '1', '2' and '3', as shown in Figure 3.10.
- Insert the needle assembly into the stainless steel tube and bond them with two-component glue. Also glue the far end of the tube where the wires come

out in order to relieve the strain on the needles. Ensure the needle at the centre of ceramic '0' is approximately 1- 2 mm longer than the remaining three needles; this is the front sensor of the four-sensor probe.

- Bend the stainless steel tube at 90° facing away from front sensor '0', as shown in Figure 3.18.

The probe constructed by following the above procedure was measured again with a digital microscope using the probe coordinate scheme referred to in Figure 2.18. The positions $(x_1, y_1, z_1), (x_2, y_2, z_2), (x_3, y_3, z_3)$ of sensors 1, 2 and 3 with respect to sensor 0 are shown in Table 3.3. Figure 3.19 shows the probe under the microscope, ready to be measured, which has a magnification of 40 times that of the true probe (see Chapter 3.3 for the detailed procedure for measuring probes).

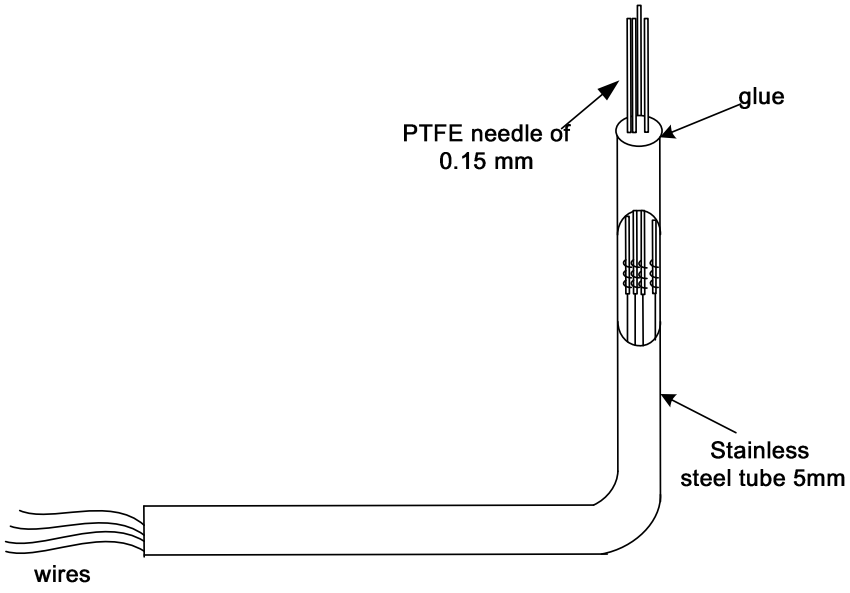


**Figure 3.18 Miniature four-sensor probe PN2 with the probe holder**

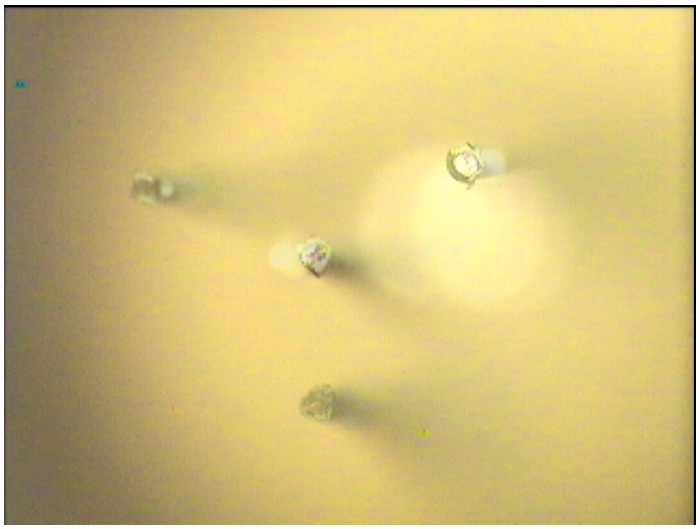

**Figure 3.19 Measurement of a probe PN2 under a digital microscope**

## 3.3 Measurement of a probe

In Chapter 2, Equations 2.44 - 2.48 suggest that the calculation of the velocity vector of the bubble is highly dependent on two variables i.e. the time intervals $\delta t_{ii}$ and the probe dimensions $x_i$, $y_i$ *and* $z_i$ (where $i$ = 1, 2 and 3).

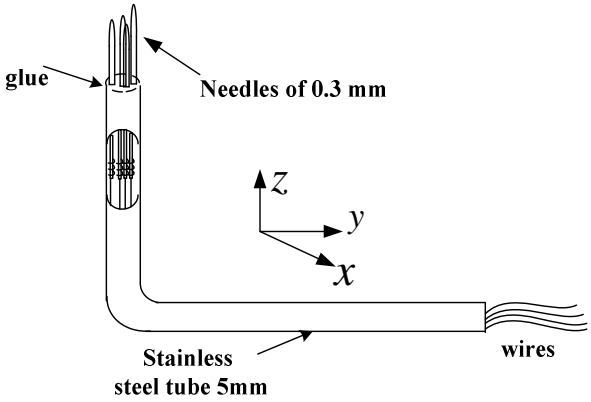


**Figure 3.20 Schematic of a four-sensor probe PN0**

Thus, this section describes the method used to measure the dimension of the probe. Within the University of Huddersfield, in earlier days, the sensors in four-sensor PN0

probes were placed in a rectangular position (see section 3.1.1), where the front sensor was normally placed 2.5 mm upstream of the rear sensors. The probe body (5mm stainless tube) was bent 90° away from the front sensor perpendicular to the front sensor '0', which was marked as the $y$ axis of the probe, as shown in Figure 3.20.

Further details on the probe axis definition are provided in Chapter 7. These PN0 probes were measured using a shadowgraph.

In the present study, the probes were measured using a commercially available digital stereo microscope shown in Figure 3.21, MOTIC DM-143B. The microscope has a magnification range of up to 40X, and the viewing head can be rotated to 360° and consists of a two mega pixel CMOS digital camera.


**Figure 3.21 Digital stereo microscope MOTIC DM-143B used to measure the probe dimensions**

In order to measure the probe dimensions it is important to align the axes of the microscope $X_c$, $Y_c$ and $Z_c$ with the axes of the probe $x, y$ *and* $z$. In order to align these axes, a holder for the probe was designed, as shown in Figure 3.22.

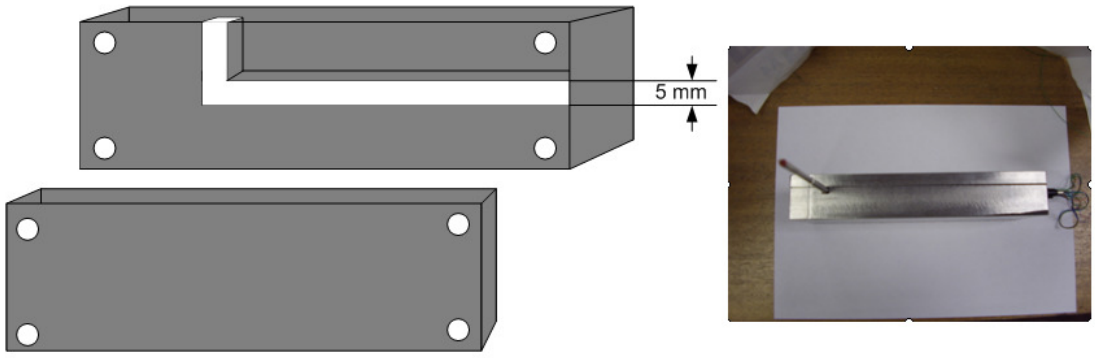


**Figure 3.22 Probe holder**

The holder was made from a metal block 200 mm long, 90 mm wide and 25 mm thick and in the centre a groove of 5mm was made where the probe can be placed, as shown in Figure 3.22. In order to keep the probe fixed during the measurement process, the holder was covered and fixed with another block of metal.

Figure 3.23 shows the schematic of the probe holder in place under the microscope, where it defines the axis of the probe and the camera. $x, y$ *and* $z$ denote the axes of the probe, whereas $X_c$, $Y_c$ and $Z_c$ denote the axes of the microscope. The $x$ axis of the probe co-ordinate system is defined as being parallel to section BB of the probe holder. The $z$ axis of the probe co-ordinate system is defined as being parallel to section AA of the probe holder and orthogonal to $y$ axis. The origin of the probe coordinate system is the tip of the front sensor '0'. The $x$ axis of the probe coordinate system is orthogonal to both the $y$ and $z$ axes. Similarly, $Z_c$ is defined as the vertical pillar of the digital microscope and is intended to be parallel to $z$ axis and $Y_c$, as the

base of microscope is intended to be parallel to $y$ axis. The axis $X_c$ of the microscope coordinate system is orthogonal to both $Z_c$ and $Y_c$ axes.

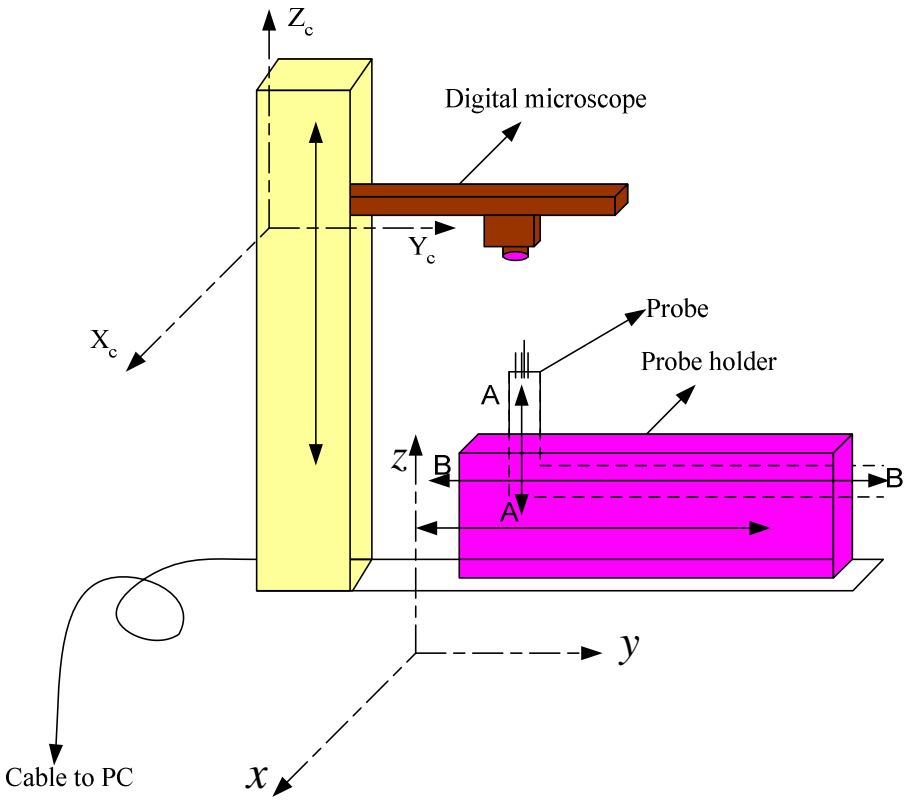


**Figure 3.23 Schematic of the probe with the probe holder in place under the microscope**

### 3.3.1 Measurement of probe PN1

In order to measure the probe, it is important to ensure that the probe axes $x, y$ *and* $z$ are respectively parallel to the microscope axes $X_c$, $Y_c$ and $Z_c$. To carry out this process, the microscope was placed on a smooth table and levelled both vertically and horizontally with the help of spirit levels. Then, the probe that was mounted in the probe holder, which was placed in front of the microscope as shown in Figure 3.18. The spirit levels were used again to ensure that the probe was parallel and level.

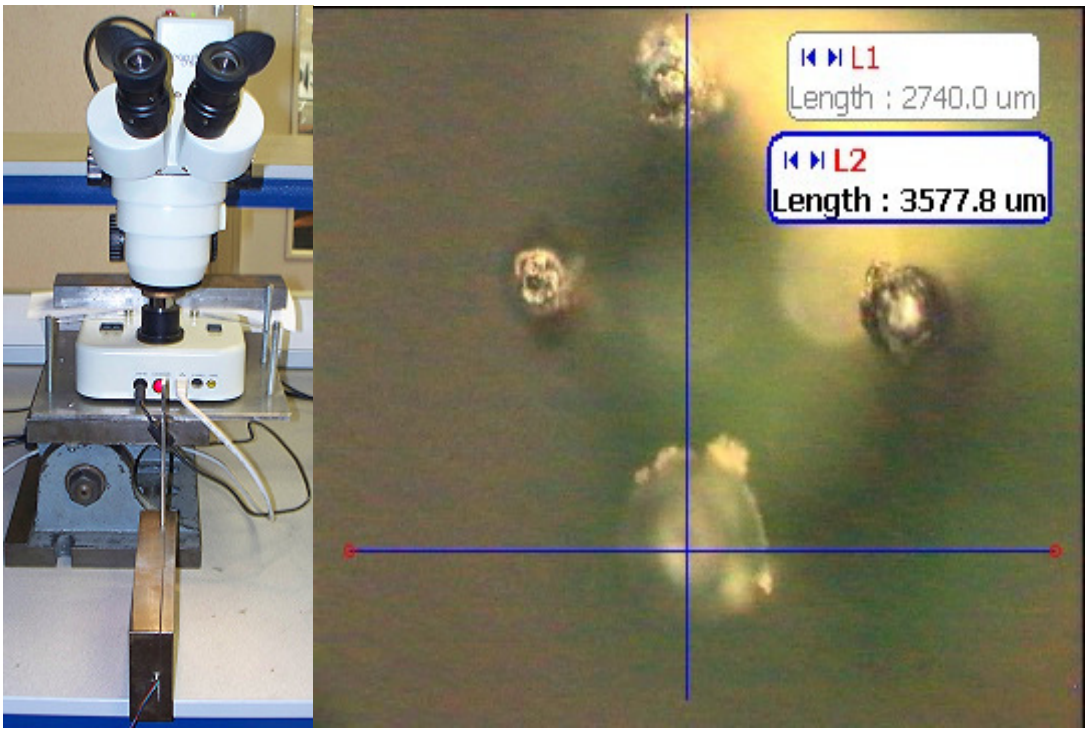


**Figure 3.24 Probe PN1 under the microscope (left) positioned to measure $(x_i, y_i)$ (right) 40X magnified image captured by the microscope**

Once the probe was positioned, the microscope was focused in between the front and rear sensor and the image was captured with a magnification of 40X the original probe, as shown in Figure 3.24 (right). The captured image was then measured using inbuilt measuring software. The software makes it possible to draw line; the X and Y axis was drawn over front sensor '0' and the point of intersection was regarded as coordinate (0, 0). The distance between each rear sensor and the front sensor was measured to obtain the distance $(x_i, y_i)$ dimensions of each sensor with respect to the front sensor.

For the measurement of the Z dimensions, the probe was placed under the microscope in a horizontal position parallel to $X_c$, as shown in Figure 3.25. The above procedure was repeated again to find the dimension $z_i$ of the probe, only this time the reference

line was drawn perpendicular to the front sensor '0', making it parallel to $y$ axis and $Y_c$.

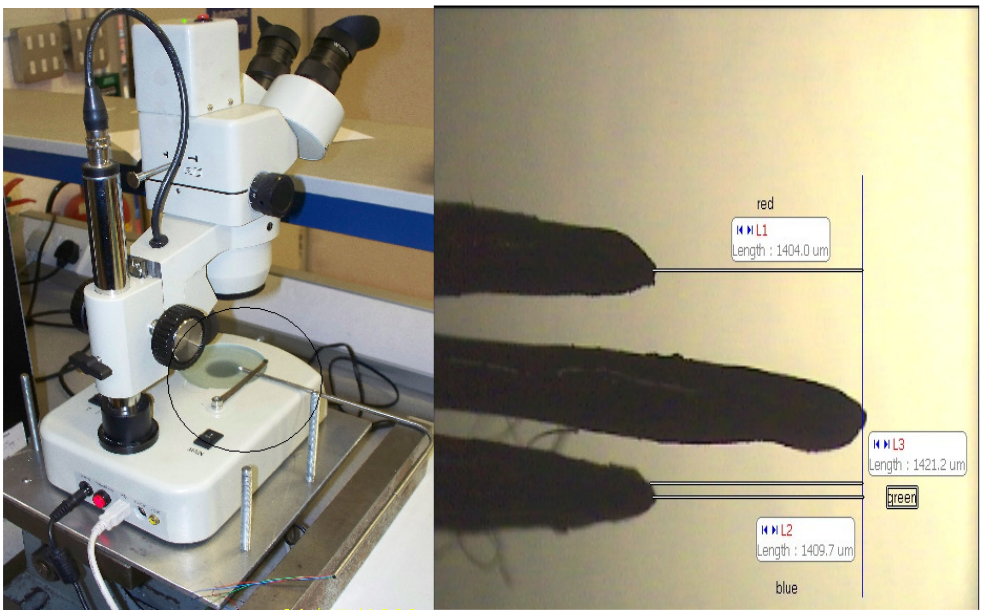


**Figure 3.25 Positioning of PN1 probe under the microscope (left) probe under the microscope magnified 40X to measure $z_i$**

The method described above to measure the dimension of the local probes was not necessarily always accurate, as the captured image was focussed neither on the front nor on the rear sensor; thus, it was necessary to make an assumption as to where the centre of the tip of the sensor was placed.

### 3.3.2 Measurement of the new miniaturised probe PN2

To overcome the uncertainty of allocating the tips of the front and rear sensors, a new approach was introduced. In this new technique, two images were captured; the first image was captured with the focus on the front sensor and the next image was captured with the focus on the rear sensor, as shown in Figure 3.26. Figure 3.26 (left) is the captured image that was focused on the front sensor, whereas Figure 3.26 (right)

is the captured image that was focused on the rear sensor. Before capturing the images, the probe was mounted in the same way as described in section 3.3.1.

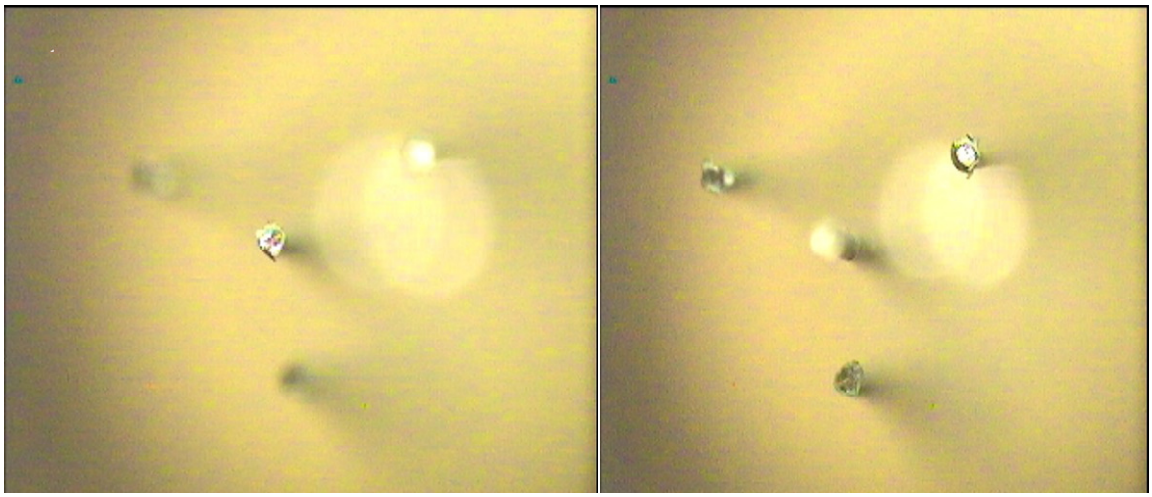

**Figure 3.26 Microscopes capturing the image of front (left) and rear (right) sensors of the PN2 probe**

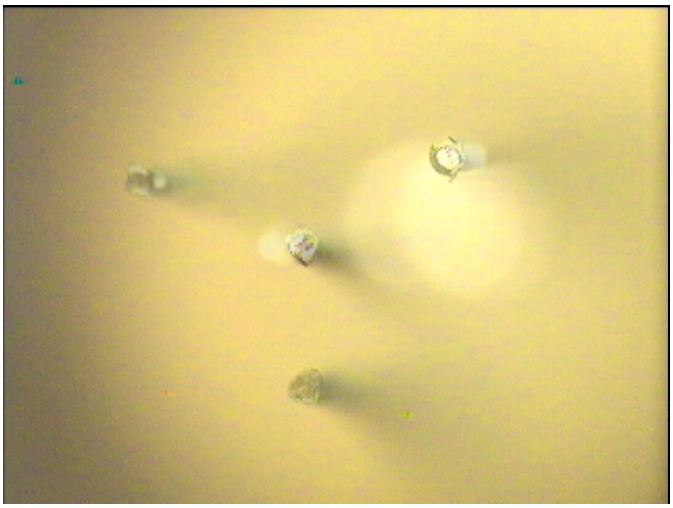

**Figure 3.27 Image of the combined front and rear sensors in Figure 3.26**

Next, the captured images were combined using the commercially available software MOTIC PLUS, making the entire sensor visible and clear. The software allows similar pictures to be combined, as it detects the edge of both provided pictures and overlaps them on top of one another. Figure 3.27 shows the front and rear sensors

combined. When comparing Figure 3.27 to Figure 3.24 (right), it is clear that the method of taking the images with a combined front and rear sensor gives a much clearer image of all four sensors.

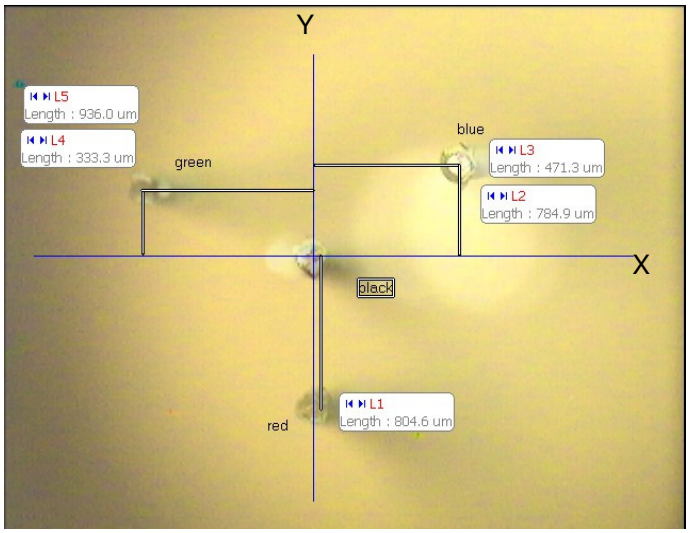


**Figure 3.28 Measuring $x_i$ and $y_i$ of the combined image of the PN2 probe**

Due to the clarity of the image of all four sensors it was possible to measure probe dimensions with greater accuracy. Figure 3.28 shows the measurement of the captured image. In the figure, the blue lines denote X and Y axes parallel to the axes of microscope $X_c$ and $Y_c$. The intersection of these two lines was on the tip of the front sensor, '0', which was in the centre in this case and was described as coordinate (0, 0). Once the line was plotted, the measurement of the distance between all the three rear sensors and the X and Y axes was carried out, as shown in Figure 3.28, which is $(x_i, y_i)$ of probe PN2.

To measure the $z_i$ of probe PN2, the probe was placed in the horizontal position, making the probe $x$ axis parallel to the X axis of the microscope $X_c$. Once the image was captured, the reference line was plotted perpendicular to the front sensor, '0', as shown in Figure 3.29, making the line parallel to $Y_c$ as well as $y$ axis. Once the line

was plotted, the distance between all the rear sensors to the line was measured to achieve the $z_i$ of each rear sensor with respect to the front sensor.

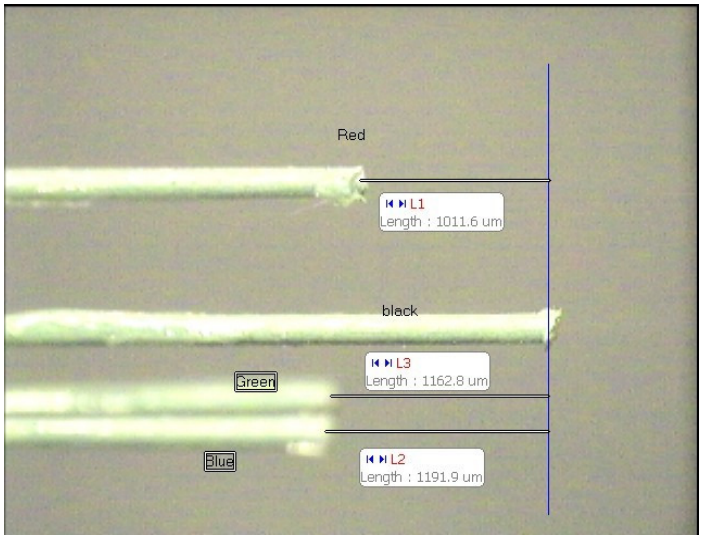


**Figure 3.29 Probe PN2 under the microscope to measure $z_i$**

The measurement process was carried out twice for each probe, once before capturing data and once after data capture, to ensure that the dimension of the probe hadn't been affected by the bubble-probe interaction.

# CHAPTER 4

## Sensitivity Analysis

It can be seen from Equations 2.47 and 2.48 in Chapter 2 that the calculation of the polar angle $\alpha$ and the azimuthal angle $\beta$ are highly dependent on the measured probe dimensions $x_i, y_i \text{ and } z_i$ and the measured time delays $\delta t_{ii}$ (where $i$ = 1, 2 and 3). Thus, in this chapter an effort is made to analyse the sensitivity of the calculated polar angle $\alpha_c$ and the calculated azimuthal angle $\beta_c$ to errors in the measured probe dimensions $x_{i,meas}, y_{i,meas} \text{ and } z_{i,meas}$ and to the measured time intervals $\delta t_{ii,meas}$ during the bubble-probe interaction. For comparison purposes, an analysis was carried out using two different reference polar angles with $\alpha_t$ = 0° and $\alpha_t$ = 30°, keeping the reference azimuthal angle $\beta_t$ constant at 0° in both cases (N.B. when $\alpha_t = 0° \; \beta_t$ does not have any physical meaning).

### 4.1 Effect on polar angle $\alpha$ and azimuthal angle $\beta$ due to the errors in the measured probe dimensions

It can be seen from Equations 2.44 - 2.46 that, when polar angle $\alpha$ is equal to zero, the terms $x_i \sin\alpha \sin\beta$ and $y_i \sin\alpha \cos\beta$ $(i = 1, 2 \text{ and } 3)$ are both equal to zero, making the polar angle $\alpha$ and the azimuthal angle $\beta$ only dependent on $z_i$ and $\delta t_{ii}$. Therefore, a series of MATLAB simulations were carried out with various values of $z_i$ and $\delta t_{ii}$ ($\pm 10\%$ of error was introduced in real values of $z_i$ and $\delta t_{ii}$). In order to proceed with the analysis, probe dimensions were chosen as shown in Table 4.1.

| $i$ | 1 | 2 | 3 |
|---|---|---|---|
| $x_{i,t}$ | 0 | 0.4 | -0.4 |
| $y_{i,t}$ | 0.5 | -0.3 | -0.3 |
| $z_{i,t}$ | 1 | 1 | 1 |

**Table 4.1 Assumed probe dimensions in mm**

### 4.1.1 Effect on the calculated polar angle $\alpha_c$ and azimuthal angle $\beta_c$ due to the error in $z_{1,meas}$

1. Select the probe dimensions $x_{i,t}$ , $y_{i,t}$ and $z_{i,t}$ from Table 4.1.
2. Calculate $\delta t_{ii,t}$ $(i=1,2 \text{ and } 3)$ using Equations 2.44 – 2.46, assuming reference polar angle $\alpha_t$ equals 0° or 30°, azimuthal angle $\beta_t$ equals 0° and the velocity of the bubble $v_t$ equals 0.5 ms$^{-1}$.
3. Using the value of $\delta t_{ii,t}$ calculated in step 2 and the correct values of $x_{i,t}$ and $y_{i,t}$ and for $z_{2,t}$ and $z_{3,t}$, $z_{1,meas}$ is varied from 0.9 mm to 1.1 mm in steps of 0.01 mm in order to calculate new values for $\alpha_c$ and $\beta_c$.
4. The intention is to show the effect on the calculated values of $\alpha_c$ and $\beta_c$ of the measurement errors from -10% to +10% in the value of $z_{1,meas}$ .

Figure 4.1 shows the effect on the calculated polar angle $\alpha_c$ and azimuthal angle $\beta_c$ due to the measurement error in $z_{1,meas}$. It can be seen that the calculated polar angle $\alpha_c$ increases as the assumed value of $z_{1,meas}$ decreases below its true value of 1mm. It also shows that if the assumed value of $z_{1,meas}$ increases, the calculated polar angle $\alpha_c$ also increases. The error in $\alpha_c$ reaches 7.2° when the error in the measured value of $z_{1,meas}$ is both ±10% .

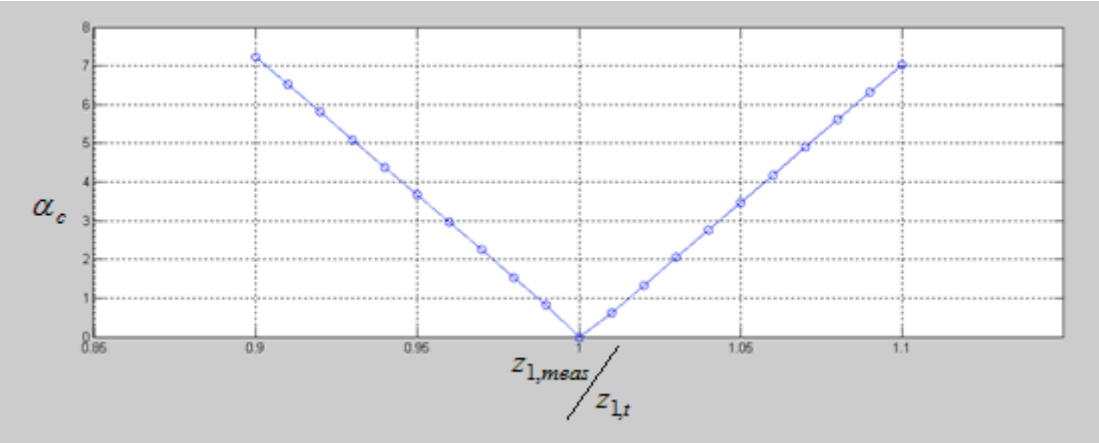


**Figure 4.1 Variation of calculated polar angle $\alpha_c$ with the error in $z_{1,meas}$ using reference polar angle $\alpha_t$ = 0° and $\beta_t = 0°$**

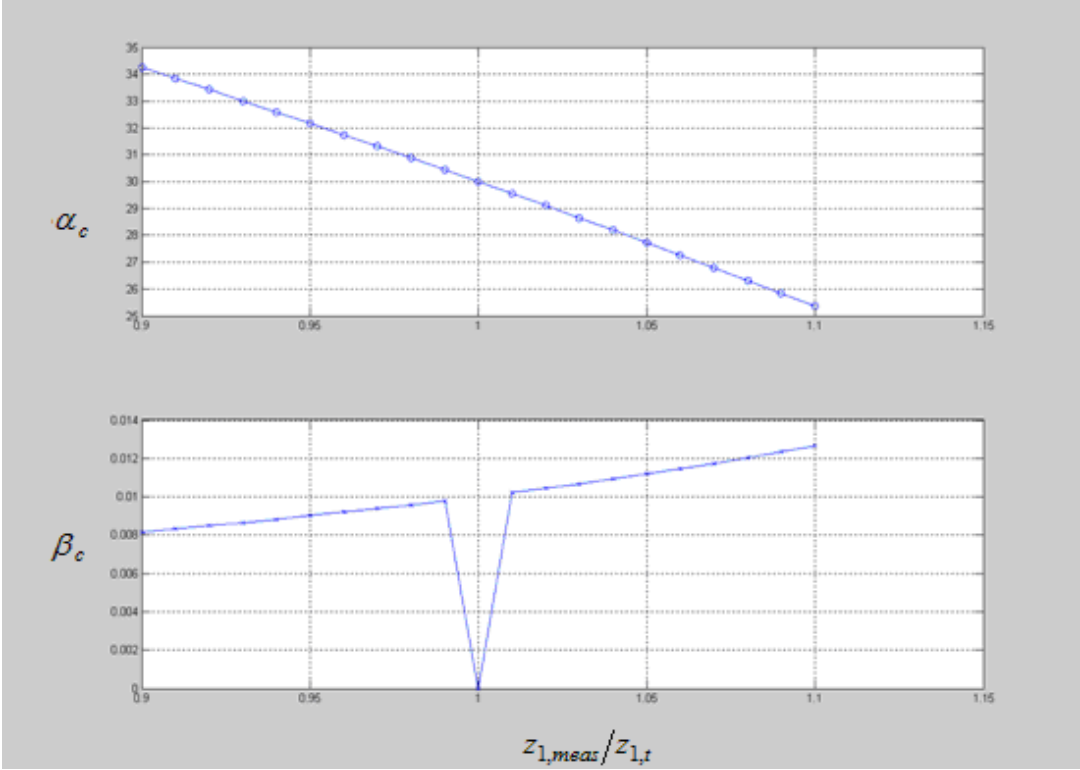


**Figure 4.2 Variation of calculated polar angle $\alpha_c$ and azimuthal angle $\beta_c$ with the error in $z_{1,meas}$ using reference polar angle $\alpha_t$ = 30° and $\beta_t = 0°$**

Similarly, Figure 4.2 shows the effect on the calculated polar angle $\alpha_c$ and azimuthal angle $\beta_c$ when the measurement error in $z_{1,meas}$ is ±10% for the reference polar angle

$\alpha_t$ = 30° and azimuthal angle $\beta_t$ = 0°. The figure suggests that, as the assumed value of $z_{1,meas}$ decreases below its true value of 1mm, $\alpha_c$ increases gradually to 34.2°; whereas, if the assumed value of $z_{1,meas}$ increases, $\alpha_c$ decreases to 25.2°. Figure 4.2 also shows that there is very little variation (0.008 – 0.012) in $\beta_c$ for the variation -10% to +10% in the value of $z_{1,meas}$.

### 4.1.2 Effect on the calculated polar angle $\alpha_c$ and azimuthal angle $\beta_c$ due to the error in $z_{2,meas}$

1) Select the probe dimensions $x_{i,t}$ , $y_{i,t}$ and $z_{i,t}$ from Table 4.1.
2) Calculate $\delta t_{ii,t}$ using Equations 2.44 – 2.46, assuming reference polar angle $\alpha_t$ equals 0° or 30°, azimuthal angle $\beta_t$ equals 0° and velocity of the bubble $v_t$ equals 0.5 ms$^{-1}$.
3) Using the value of $\delta t_{ii,t}$ calculated in step 2 and the correct values of $x_{i,t}$ and $y_{i,t}$ and for $z_{1,t}$ and $z_{3,t}$, $z_{2,meas}$ is now varied from 0.9 mm to 1.1 mm in steps of 0.01 mm in order to calculate new values for $\alpha_c$ and $\beta_c$.
4) The intention is to show the effect on the calculated values of $\alpha_c$ and $\beta_c$ due to the measurement error from -10% to +10% in the value of $z_{2,meas}$.

Figure 4.3 shows the effect on the calculated polar angle $\alpha_c$ of the error in $z_{2,meas}$. The figure shows that, as $z_{2,meas}$ decreases below its true value of 1mm, the calculated polar angle $\alpha_c$ increases. Similarly, if $z_{2,meas}$ increases, polar angle $\alpha_c$ increases

again. The error in $\alpha_c$ reaches up to 8° when the error in the measured value of $z_{2,meas}$ is both -10% and +10%.

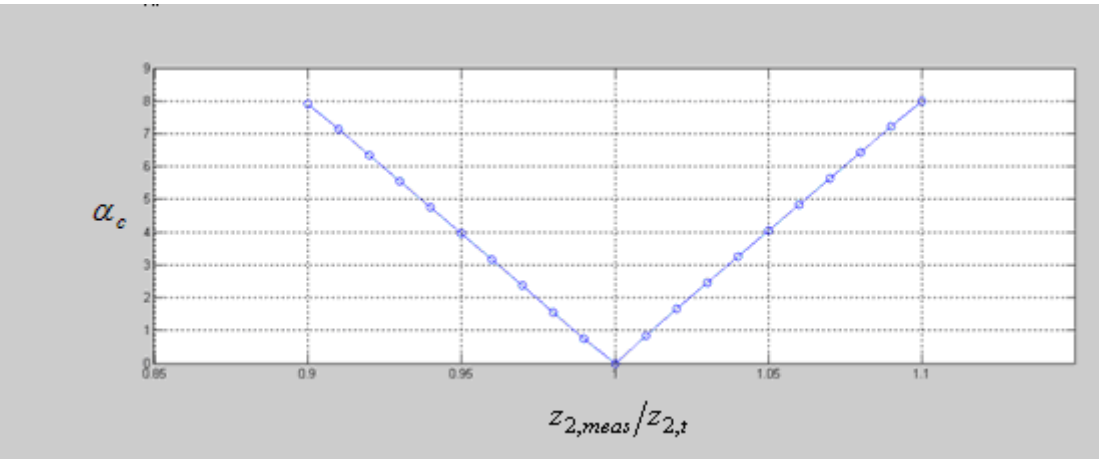


**Figure 4.3 Variation of calculated polar angle $\alpha_c$ with the error in $z_{2,meas}$ using reference polar angle $\alpha_t$ = 0 and $\beta_t = 0°$**

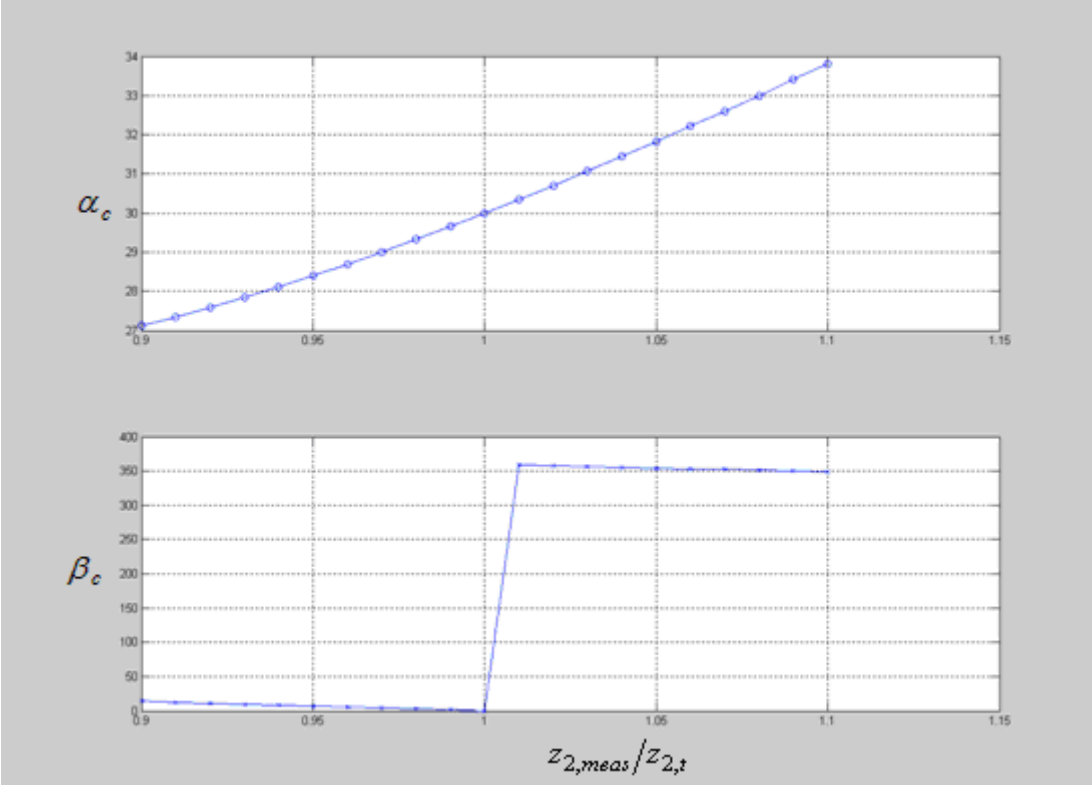


**Figure 4.4 Variation of calculated polar angle $\alpha_c$ and azimuthal angle $\beta_c$ with the error in $z_{2,meas}$ using reference polar angle $\alpha_t$ = 30 and $\beta_t = 0°$**

Similarly, Figure 4.4 above shows the effect on the calculated polar angle $\alpha_c$ and azimuthal angle $\beta_c$ when the measurement error in $z_{2,meas}$ is ±10% for the reference polar angle $\alpha_t$ = 30° and azimuthal angle $\beta_t$ = 0°. The figure suggests that, as the assumed value of $z_{2,meas}$ decreases below its true value of 1mm, $\alpha_c$ decreases gradually to 27°; whereas, if $z_{2,meas}$ increases $\alpha_c$ also increases to 34° . Figure 4.4 also shows that there is very little variation in $\beta_c$ for the variation -10% ( $\beta_c$ increases slightly up to 10°); however, $\beta_c$ reaches 350° when $z_{2,meas}$ increases above its true value of 1mm.

### 4.1.3 Effect on the calculated polar angle $\alpha_c$ and azimuthal angle $\beta_c$ due to the error in $z_{3,meas}$

1) Select the probe dimensions $x_{i,t}$ , $y_{i,t}$ and $z_{i,t}$ from Table 4.1.
2) Calculate $\delta t_{ii,t}$ using Equations 2.44 – 2.46, assuming polar angle $\alpha_t$ equals 0° or 30°, azimuthal angle $\beta_t$ equals 0° and velocity of the bubble $v_t$ equals 0.5 $ms^{-1}$.
3) Using the value of $\delta t_{ii,t}$ calculated in step 2 and the correct values of $x_{i,t}$ and $y_{i,t}$ and for $z_{1,t}$ and $z_{2,t}$ , $z_{3,meas}$ is now varied from 0.9 mm to 1.1 mm in steps of 0.01 mm in order to calculate new values for $\alpha_c$ and $\beta_c$ .
4) The intention is to show the effect on the calculated values of $\alpha_c$ and $\beta_c$ due to the measurement error from -10% to +10% in the value of $z_{3,meas}$.

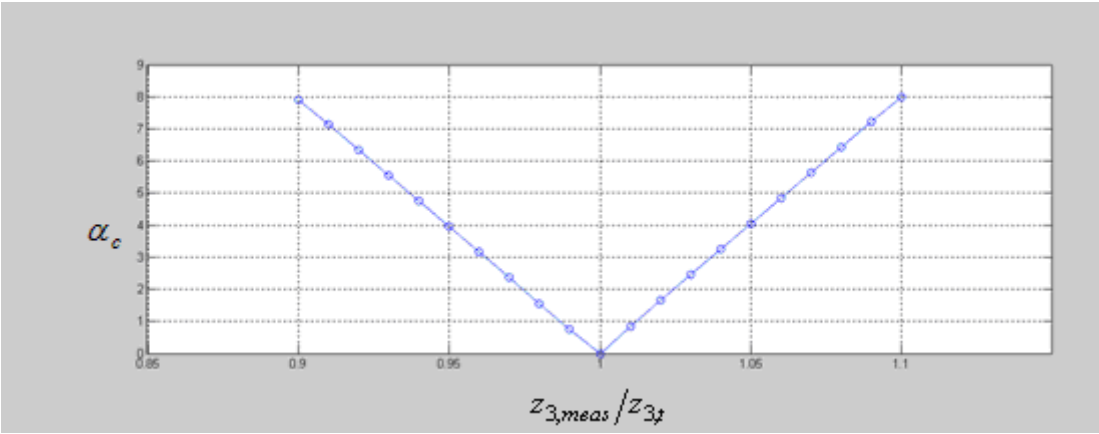


**Figure 4.5 Variation of calculated polar angle $\alpha_c$ with the error in $z_{3,meas}$ using reference polar angle $\alpha_t$ = 0 and $\beta_t = 0°$**

Figure 4.5 above shows the effect on calculated polar angle $\alpha_c$ due to the error in $z_{3,meas}$. The figure shows that, as $z_{3,meas}$ decreases below its true value of 1mm, polar angle $\alpha_c$ increases. Similarly, if $z_{3,meas}$ increases, polar angle $\alpha_c$ increases again. The increment of polar angle $\alpha_c$ reaches 8° when the error in the measured value of $z_{3,meas}$ is -10% and +10% of $z_{3,meas}$.

Similarly, Figure 4.6 shows the effect on polar angle $\alpha_c$ and azimuthal angle $\beta_c$ when the measurement error in $z_{3,meas}$ is ±10% for the reference polar angle $\alpha_t = 30°$ and azimuthal angle $\beta_t = 0°$. The figure suggests that, as $z_{3,meas}$ decreases below its true value of 1mm, $\alpha_c$ also decreases gradually to 27°, whereas if the assumed value of $z_{3,meas}$ increases, $\alpha_c$ also increases to 34°. Figure 4.6 also shows that $\beta_c$ reaches 300° for a variation of -10%; however, $\beta_c$ changes only slightly ($\beta_c$ increases up to 10°) when $z_{3,meas}$ is increased by +10%.

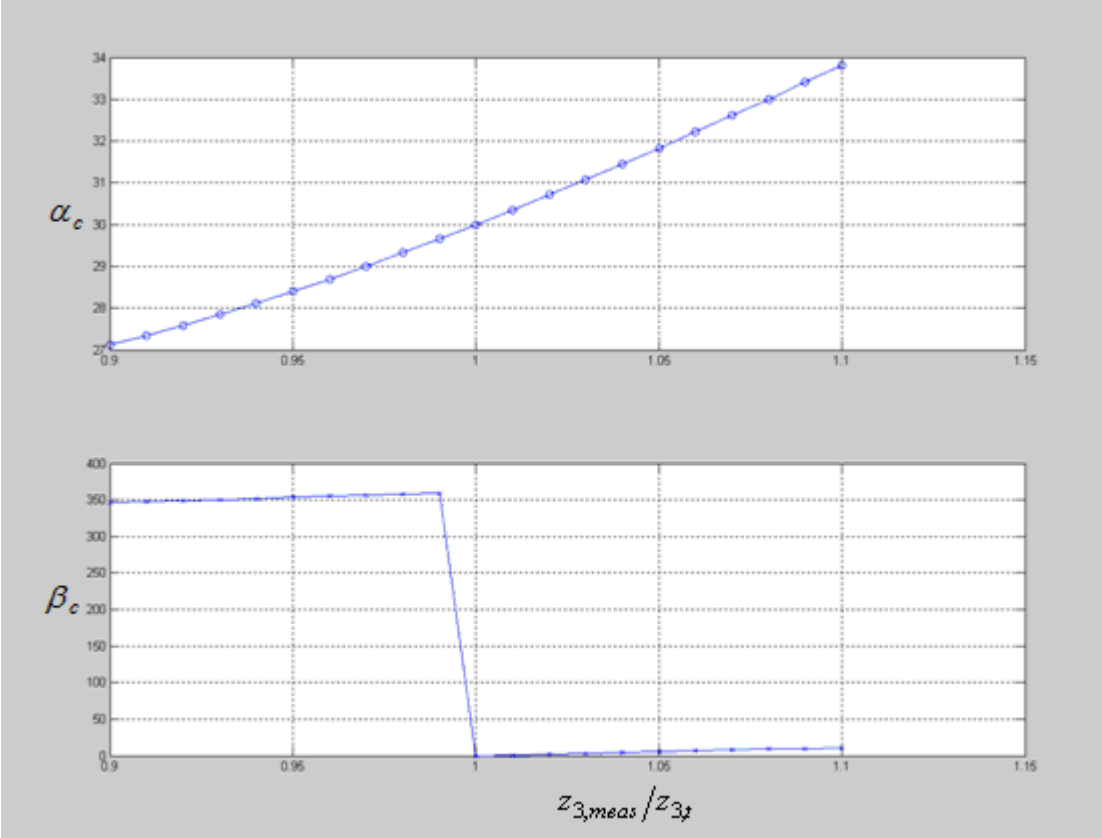


**Figure 4.6 Variation of calculated polar angle $\alpha_c$ and azimuthal angle $\beta_c$ with the error in $z_{3,meas}$ using reference polar angle $\alpha_t$ = 30 and $\beta_t = 0°$**

### 4.1.4 Effect on the calculated polar angle $\alpha_c$ and azimuthal angle $\beta_c$ due to the error in $z_{2,meas}$ (increasing) and $z_{3,meas}$ (increasing)

1. Select the probe dimensions $x_{i,t}$ , $y_{i,t}$ and $z_{i,t}$ from Table 4.1.
2. Calculate $\delta t_{ii,t}$ using Equations 2.44 – 2.46, assuming polar angle $\alpha_t$ equals 0° or 30°, azimuthal angle $\beta_t$ equals 0° and velocity of the bubble $v_t$ equals 0.5 ms$^{-1}$.
3. Using the value of $\delta t_{ii,t}$ calculated in step 2 and the correct values of $x_{i,t}$ and $y_{i,t}$ for $z_{1,t}$ , $z_{2,meas}$ is varied from 1 mm to 1.1 mm and $z_{3,meas}$ from 1 mm to 1.1 mm in steps of 0.01 mm in order to calculate new values for $\alpha_c$ and $\beta_c$.

4. $z_{2,meas}$ and $z_{3,meas}$ are altered in such a way that, when $z_{2,meas}$ is changed by 1%, $z_{3,meas}$ is changed from 1% to 10% again, $z_{2,meas}$ is changed by 2% and $z_{3,meas}$ is changed from 1% to 10%; the process continues until $z_{2,meas}$ changes to 10%, making a total of 100 data points.
5. The intention is to show the effect on the calculated values of $\alpha_c$ and $\beta_c$ due to the measurement error in the value of $z_{2,meas}$ and $z_{3,meas}$.

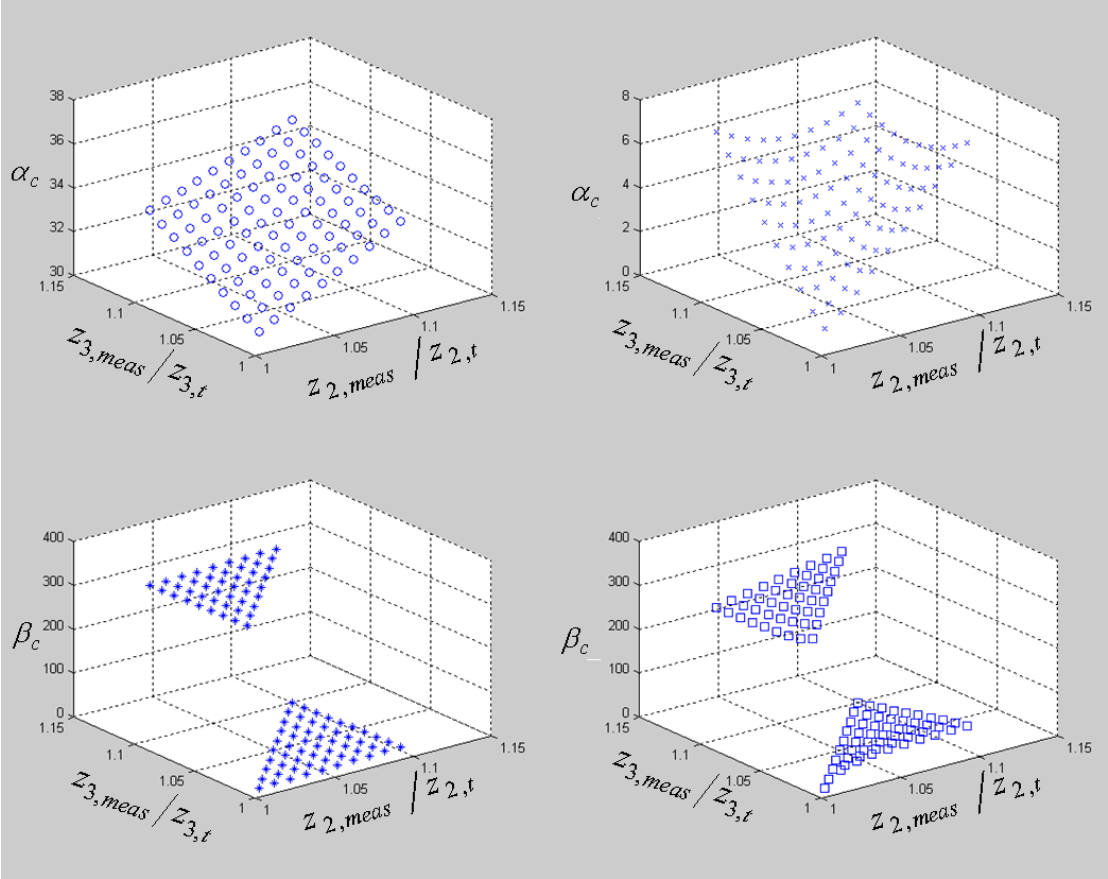


**Figure 4.7 Effect on polar angle $\alpha_c$ and azimuthal angle $\beta_c$ due to the error in $z_{2,meas}$ (increasing) and $z_{3,meas}$ (increasing), polar angle $\alpha_t$=30° (left) polar angle $\alpha_t$=0° (right) $\beta_t = 0°$**

Figure 4.7 shows the effect on the calculated polar angle when the reference polar angle $\alpha_t$ is 30° (top left) or when the reference polar angle $\alpha_t$ is 0° (top right) and

azimuthal angle when $\alpha_t$ is 30° (bottom left) or when $\alpha_t$ is 0° (bottom right) due to the error discussed above. The figure on the top left shows the variation in the calculated polar angle $\alpha_c$ when the reference polar angle $\alpha_t$ = 30°, where the calculated polar angle $\alpha_c$ increases when increments were made in $z_{2,meas}$ and $z_{3,meas}$ and this rise in the value of $\alpha_c$ reaches 35° when the measurement error in both $z_{2,meas}$ and $z_{3,meas}$ is 10% of their true value of 1mm.

Similarly, the bottom left figure shows the variation of azimuthal angle $\beta_c$ when the reference polar angle is 30°, which shows that azimuthal angle $\beta_c$ is always close to the reference azimuthal angle $\beta_t$ which is 0° (taking 360° equivalent to 0°). When calculated, azimuthal angle $\beta_c$ was found to be a maximum of 10° when $z_{2,meas}$ is increased by 10% of its true value and $z_{3,meas}$ is increased by 1% of its true value.

Similarly, Figure 4.7 on the right shows the variation in polar angle $\alpha_c$ and azimuthal angle $\beta_c$ (top and bottom respectively), while reference polar angle $\alpha_t$ and azimuthal angle $\beta_t$ are both 0°. The results shows that the calculated polar angle $\alpha_c$ reaches a maximum of 7° when the measurement error in both, $z_{2,meas}$ and $z_{3,meas}$, is increased by 10% of their true value of 1mm. As mentioned earlier, the model used suggests that azimuthal angle $\beta_c$ is not relevant in terms of $\alpha_t$=0°.

### 4.1.5 Effect on the calculated polar angle $\alpha_c$ and azimuthal angle $\beta_c$ due to the error in $z_{2,meas}$ (increasing) and $z_{3,meas}$ (decreasing)

1. Select the probe dimensions $x_{i,t}$, $y_{i,t}$ and $z_{i,t}$ from Table 4.1.

2. Calculate $\delta t_{ii,t}$ using Equations 2.44 – 2.46, assuming polar angle $\alpha_t$ equals 0° or 30°, azimuthal angle $\beta_t$ equals 0° and velocity of the bubble $v_t$ equals 0.5 $ms^{-1}$.
3. Using the value of $\delta t_{ii,t}$ calculated in step 2 and the correct values of $x_{i,t}$, and $y_{i,t}$ and $z_{1,t}$ , $z_{2,meas}$ is varied from 1mm to 1.1mm and $z_{3,meas}$ from 0.9 mm to 1mm in steps of 0.01mm in order to calculate new values for $\alpha_c$ and $\beta_c$.
4. $z_{2,t}$ and $z_{3,meas}$ are altered in such a way that, when $z_{2,meas}$ is changed by 1%, $z_{3,meas}$ is changed from -1% to -10% again, $z_{2,meas}$ is changed by 2% and $z_{3,meas}$ is changed from -1% to -10%; the process continues until $z_{2,meas}$ changes to 10%, making a total of 100 data points.
5. The intention is to show the effect on the calculated values of $\alpha_c$ and $\beta_c$ due to the measurement error from +1% to +10% in the value of $z_{2,meas}$ and -1% to -10% in the value of $z_{3,meas}$.

Figure 4.8 shows the effect on the calculated polar angle when the reference polar angle $\alpha_t$ is 30° (top left) or when the reference polar angle $\alpha_t$ is 0° (top right) and azimuthal angle when $\alpha_t$ is 30° (bottom left) or when $\alpha_t$ is 0° (bottom right) due to the error discussed above. The figure on the top left shows the variation in polar angle $\alpha_c$ when the reference polar angle $\alpha_t$ = 30°, where the calculated polar angle $\alpha_c$ increases with the increments made in $z_{2,meas}$ and $z_{3,meas}$ and this rise in the value of $\alpha_c$ increases to 34° when $z_{2,meas}$ is increased by 10% and $z_{3,meas}$ is reduced by 10% of its true value of 1mm.

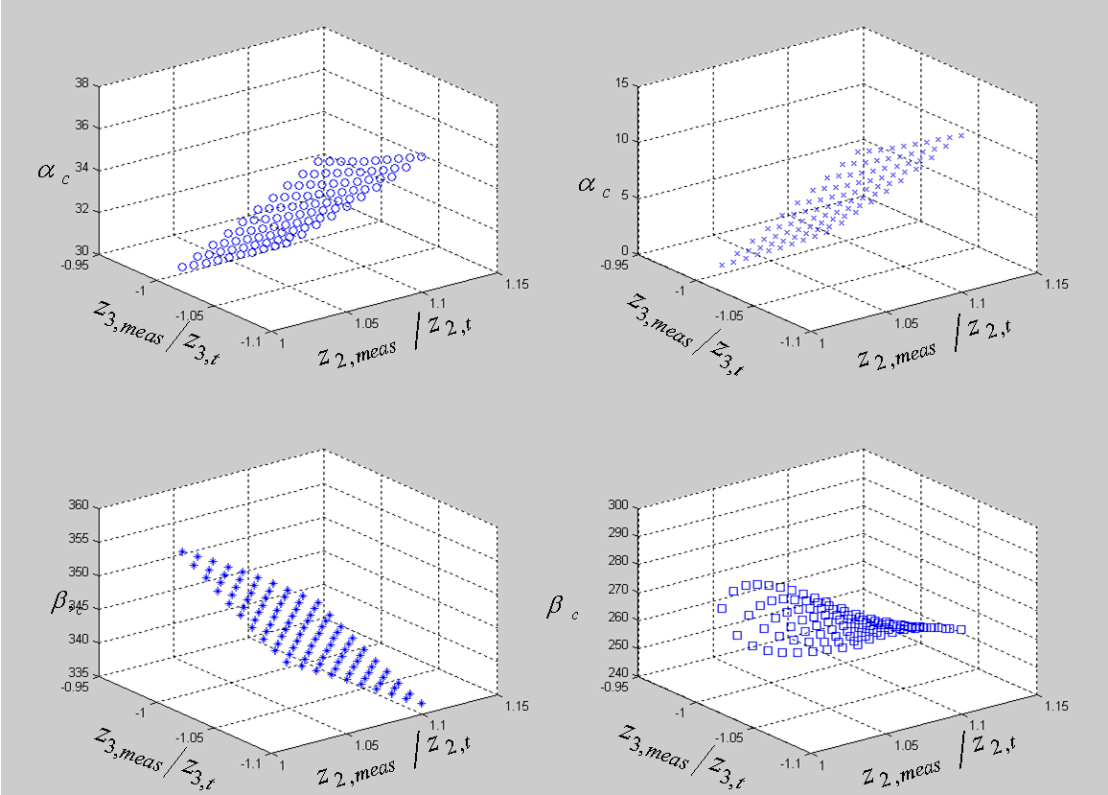


**Figure 4.8 Effect on the calculated polar angle $\alpha_c$ and azimuthal angle $\beta_c$ due to the error in $z_{2,meas}$ (increasing) and $z_{3,meas}$ (decreasing), polar angle $\alpha_t$=30° (left) polar angle $\alpha_t$=0° (right) $\beta_t = 0°$**

Similarly, the bottom left figure shows the calculated value of azimuthal angle $\beta_c$ when $\alpha_t$ is 30°, which shows that azimuthal angle $\beta_c$ is always close to $\beta_t$ which is 0° (taking 360° equivalent to 0°). When calculated, azimuthal angle $\beta_c$ was found to be at a minimum of 340° when $z_{2,meas}$ is increased by 9% and $z_{3,meas}$ is decreased by -10% of its true value of 1mm. Similarly, Figure 4.8 on the right shows the variation in the calculated polar angle $\alpha_c$ and azimuthal angle $\beta_c$ (top and bottom respectively), while reference polar angle $\alpha_t$ and azimuthal angle $\beta_t$ are both 0°. Results show that the $\alpha_c$ reaches up to 14° when both $z_{2,meas}$ and $z_{3,meas}$ are at their most extreme.

### 4.1.6 Effect on the calculated polar angle $\alpha_c$ and azimuthal angle $\beta_c$ due to the error in $z_{2,meas}$ (decreasing) and $z_{3,meas}$ (increasing)

1. Select the probe dimensions $x_{i,t}$ , $y_{i,t}$ and $z_{i,t}$ from Table 4.1.
2. Calculate $\delta t_{ii,t}$ using Equations 2.44 – 2.46, assuming polar angle $\alpha_t$ = 0° or 30°, azimuthal angle $\beta_t$ = 0° and velocity of the bubble $v_t$ = 0.5ms$^{-1}$.
3. Using the value of $\delta t_{ii,t}$ calculated in step 2 and the correct values of $x_{i,t}$ and $y_{i,t}$ for $z_{1,t}$ , $z_{2,meas}$ is varied from 0.9 mm to 1 mm and $z_{3,meas}$ from 1 mm to 1.1 mm in steps of 0.01 mm in order to calculate new values for $\alpha_c$ and $\beta_c$.
4. $z_{2,meas}$ and $z_{3,meas}$ are altered in such a way that when $z_{2,meas}$ is changed by 1%, $z_{3,meas}$ is changed from -1% to -10% again, $z_{2,meas}$ is changed by 2% and $z_{3,meas}$ is changed from 1% to 10%; the process continues until $z_{2,meas}$ changes to 10%, making a total of 100 data points.
5. The intention is to show the effect on the calculated values of $\alpha_c$ and $\beta_c$ due to the measurement error from -1% to -10% in the value of $z_{2,meas}$ and +1% to +10% $z_{3,meas}$.

Figure 4.9 shows the effect on the calculated polar angle when the reference polar angle $\alpha_t$ is 30° (top left) or when the reference polar angle $\alpha_t$ is 0° (top right) and azimuthal angle when $\alpha_t$ is 30° (bottom left) or when $\alpha_t$ is 0° (bottom right) due to the error discussed above.. The figure on the top left shows the variation in the calculated polar angle $\alpha_c$ when the reference polar angle $\alpha_t$ = 30°, where polar

angle $\alpha_c$ gradually decreases until $\alpha_c$ reaches 27° when $z_{2,meas}$ is decreased by 1% and $z_{3,meas}$ is increased by 10% from its true value of 1mm.

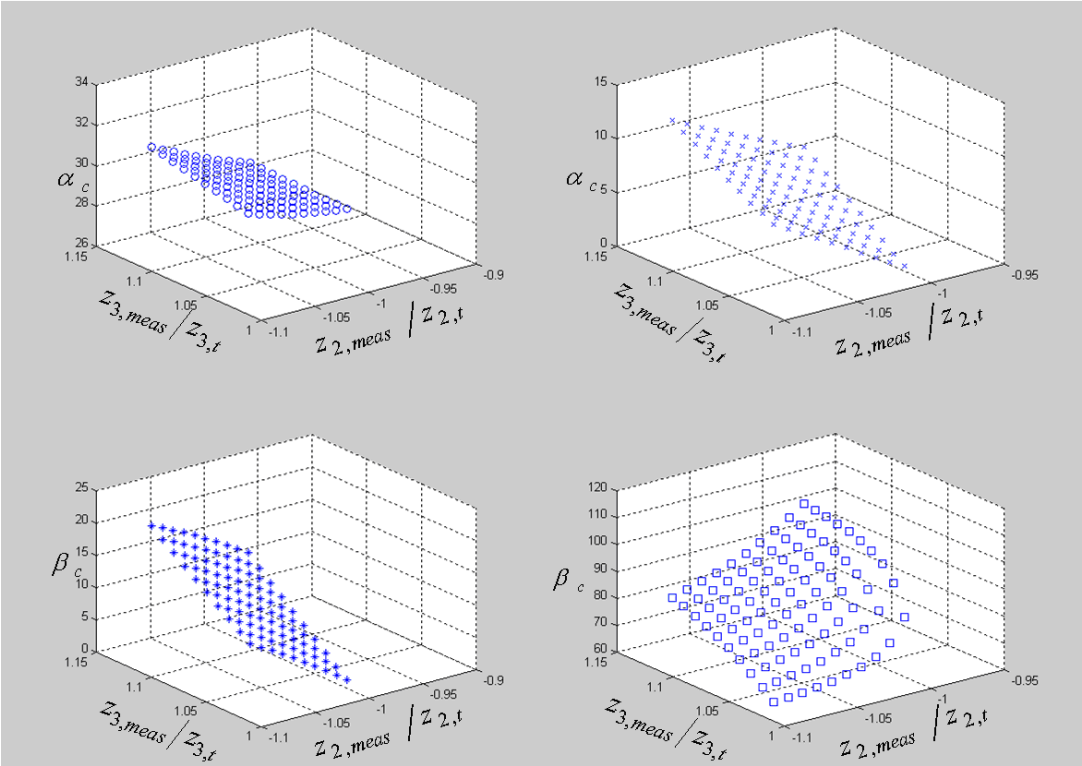


**Figure 4.9 Effect on the calculated polar angle $\alpha_c$ and azimuthal angle $\beta_c$ due to the error in $z_{2,meas}$ (decreasing) and $z_{3,meas}$ (increasing), polar angle $\alpha_t$=30° (left) polar angle $\alpha_t$=0° (right) $\beta_t$ = 0°**

Similarly, the bottom left figure shows the variation of calculated azimuthal angle $\beta_c$ when $\alpha_t$ = 30°, which shows that the calculated azimuthal angle $\beta_c$ is always close to the reference azimuthal angle $\beta_t$ which is 0°. Calculated azimuthal angle $\beta_c$ was found to be at a maximum of 24° when the measurement error in $z_{2,meas}$ is decreased by 10% and $z_{3,meas}$ is increased by 10%. Figure 4.9 on the right shows the variation in calculated polar angle $\alpha_c$ and azimuthal angle $\beta_c$ (top and bottom respectively) while reference polar angle $\alpha_t$ and azimuthal angle $\beta_t$ are both 0°. Results show that the

polar angle reaches 14° when the measurement error in $z_{2,meas}$ is decreased by 10% and $z_{3,meas}$ is increased by 10%.

### 4.1.7 Effect on the calculated polar angle $\alpha_c$ and azimuthal angle $\beta_c$ due to the error in $z_{2,meas}$ (decreasing) and $z_{3,meas}$ (decreasing)

1. Select the probe dimensions $x_{i,t}$ , $y_{i,t}$ and $z_{i,t}$ from Table 4.1.
2. Calculate $\delta t_{ii,t}$ using Equations 2.44 – 2.46, assuming polar angle $\alpha_t$ = 0° or 30°, azimuthal angle $\beta_t$ = 0° and velocity of the bubble $v_t$ = 0.5 ms$^{-1}$. .
3. Using the value of $\delta t_{ii,t}$ calculated in step 2 and the correct values of $x_{i,t}$ , and $y_{i,t}$ and $z_{1,t}$ , $z_{2,meas}$ is varied from 0.9 mm to 1 mm and $z_{3,meas}$ from 0.9 mm to 1 mm in steps of 0.01 mm to calculate new values for $\alpha_c$ and $\beta_c$.
4. $z_{2,meas}$ and $z_{3,meas}$ are altered in such a way that, when $z_{2,meas}$ is changed by -1%, $z_{3,meas}$ is changed from -1% to -10% again, $z_{2,meas}$ is changed by -2% and $z_{3,meas}$ is changed from -1% to -10%; the process continues until $z_{2,meas}$ changes to -10%, making a total of 100 data points.
5. The intention is to show the effect on the calculated values of $\alpha_c$ and $\beta_c$ due to the measurement error in the value of $z_{2,meas}$ and $z_{3,meas}$.

Figure 4.10 shows the effect on the calculated polar angle when the reference polar angle $\alpha_t$ is 30° (top left) or when the reference polar angle $\alpha_t$ is 0° (top right) and azimuthal angle when $\alpha_t$ is 30° (bottom left) or when $\alpha_t$ is 0° (bottom right) due to the error discussed above due to the error discussed above. The figure on the top right shows the variation in the polar angle $\alpha_c$ when the

reference polar angle $\alpha_t$ = 30°, where the calculated polar angle $\alpha_c$ gradually decreases as increments are made in $z_{2,meas}$ and $z_{3,meas}$ and the decrease continues until $\alpha_c$ reaches 22°, when both $z_{2,meas}$ and $z_{3,meas}$ are decreased by 10% from their true value of 1mm.

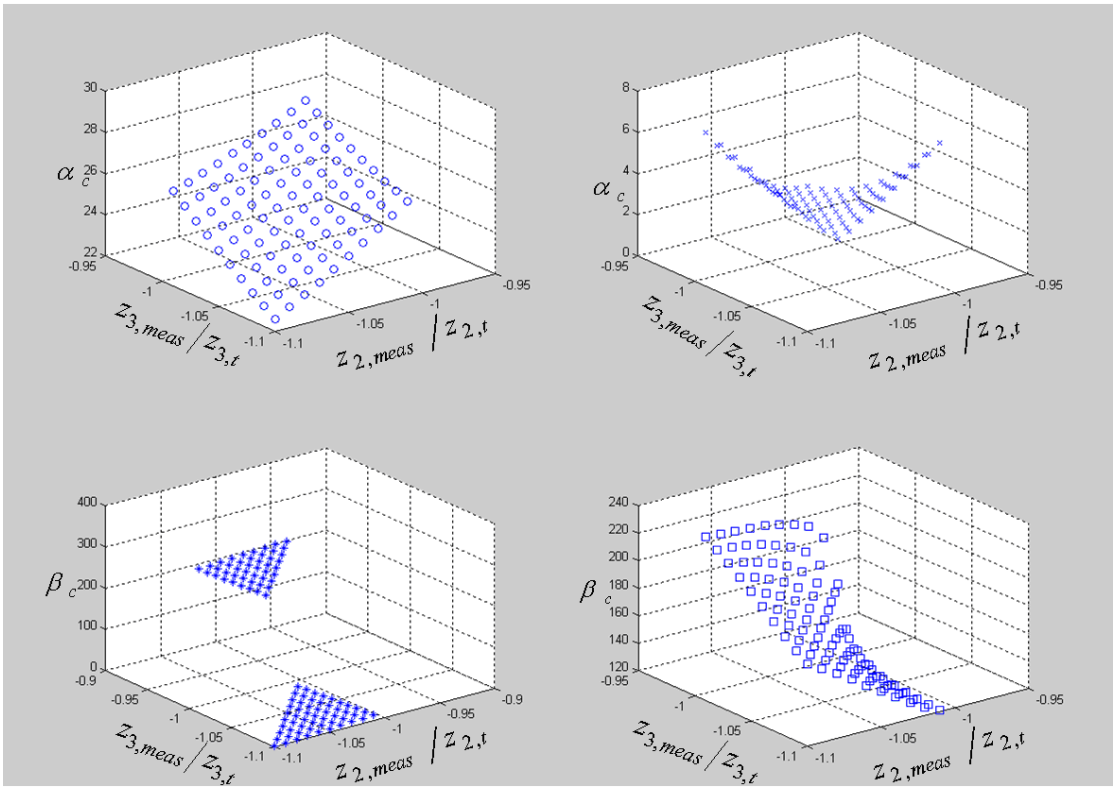


**Figure 4.10 Effect on the calculated polar angle $\alpha_c$ and azimuthal angle $\beta_c$ due to the error in $z_{2,meas}$ (decreasing) and $z_{3,meas}$ (decreasing), polar angle $\alpha_t$=30° (left) polar angle $\alpha_t$=0° (right) $\beta_{,t}$ = 0°**

Similarly, the bottom left figure shows a variation of the calculated azimuthal angle $\beta_c$ when the reference polar angle $\alpha_t$ is 30°, which shows that the calculated azimuthal angle $\beta_c$ is always close to the reference azimuthal angle $\beta_t$ which is 0° (taking 360° as equivalent to 0°). Calculated azimuthal angle $\beta_c$ was found to be at a maximum of 347° when $z_{2,meas}$ is decreased by 10% and $z_{3,meas}$ is reduced by 1% of its true value.

Similarly, Figure 4.10 on the right shows a variation in the calculated polar angle $\alpha_c$ and azimuthal angle $\beta_c$ (top and bottom respectively), while the reference polar angle $\alpha_t$ and the azimuthal angle $\beta_t$ are both 0°. Results shows that the calculated polar angle $\alpha_c$ reaches up to 7° when both $z_{2,meas}$ and $z_{3,meas}$ are decreased by 10%.

## 4.2 Effect on the calculated polar angle $\alpha_c$ and azimuthal angle $\beta_c$ due to the errors in the measured time intervals $\delta t_{ii,meas}$ (where *i* = 1, 2 and 3)

This section will focus on how the calculated polar angle $\alpha_c$ and azimuthal angles $\beta_c$ are affected by the error in measurement of $\delta t_{ii,meas}$ (where $i$ = 1, 2 and 3). As discussed in the previous section, this section will also introduce an error of ± 10% in the true value of $\delta t_{ii,t}$, where $\delta t_{ii,t}$ is calculated with dimensions $x_{i,t}$, $y_{i,t}$ and $z_{i,t}$ given in Table 4.1 and reference parameters given below:

Velocity magnitude $v_t = 0.5\text{ms}^{-1}$

Azimuthal angle $\beta_t = 0°$

Polar angle $\alpha_t$ = 0° or 30°

The analysis was carried out with the error introduced in the individual $\delta t_{ii,meas}$, as well as the error in multiple $\delta t_{ii,meas}$ (see section 4.2.4).

### 4.2.1 Effect on the calculated polar angle $\alpha_c$ and azimuthal angle $\beta_c$ due to the error in time intervals $\delta t_{11,meas}$

1. Select the probe dimensions $x_{i,t}$ , $y_{i,t}$ and $z_{i,t}$ from Table 4.1.
2. Calculate $\delta t_{ii,t}$ using Equations 2.44 – 2.46, assuming $\alpha_t$ equals 0° or 30°, azimuthal angle $\beta_t$ equals 0° and velocity of the bubble $v_t$ equals 0.5 ms$^{-1}$.
3. Using the true values of $x_{i,t}$ , $y_{i,t}$ , $z_{i,t}$ and the value of $\delta t_{33,t}$ and $\delta t_{22,t}$ calculated in step 2, $\delta t_{11,meas}$ is varied from 0.9 mm to 1.1 mm in steps of 0.01 mm and a new $\alpha_c$ and $\beta_c$ are calculated.
4. The intention is to show the effect on the calculated values of $\alpha_c$ and $\beta_c$ due to the measurement error from -10% to +10% in the true value of $\delta t_{11,meas}$.

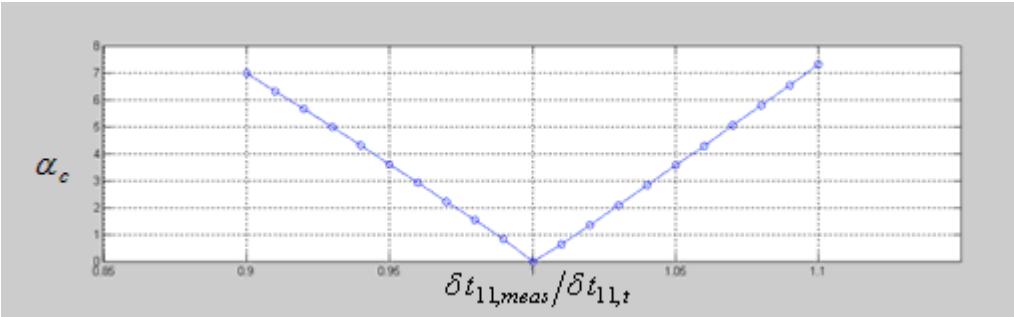


**Figure 4.11 Variation of the calculated polar angle $\alpha_c$ with the error in $\delta t_{11,meas}$ using reference polar angle $\alpha_t$ = 0° and $\beta_t$ = 0°**

Figure 4.11 shows the effect on the calculated polar angle $\alpha_c$ ($\alpha$=0°) due to the error in $\delta t_{11,meas}$. The figure shows that, as $\delta t_{11,meas}$ decreases from its true value, the calculated polar angle $\alpha_c$ increases. Similarly, if $\delta t_{11,meas}$ increases, the calculated polar angle $\alpha_c$ increases again. The increment of the calculated polar angle $\alpha_c$ reaches 7.2° (supposed to be 0°) for either side of ±10% of true value of $\delta t_{11,meas}$.

Similarly, Figure 4.12 below shows the effect on the calculated polar angle $\alpha_c$ and azimuthal angle $\beta_c$ when the error in $\delta t_{11,meas}$ is ±10% for the reference polar angle

$\alpha_t$ = 30° and azimuthal angle $\beta_t$ = 0°. The figure suggests that, as $\delta t_{11,meas}$ decreases from its true value, $\alpha_c$ decreases gradually to 24°, whereas if $\delta t_{11,meas}$ is increased, $\alpha_c$ increases to 35°. Figure 4.12 also shows that there is very little variation (0.008° – 0.012°) in $\beta_c$ for the variation -10% to +10% in the value of $\delta t_{11,meas}$.

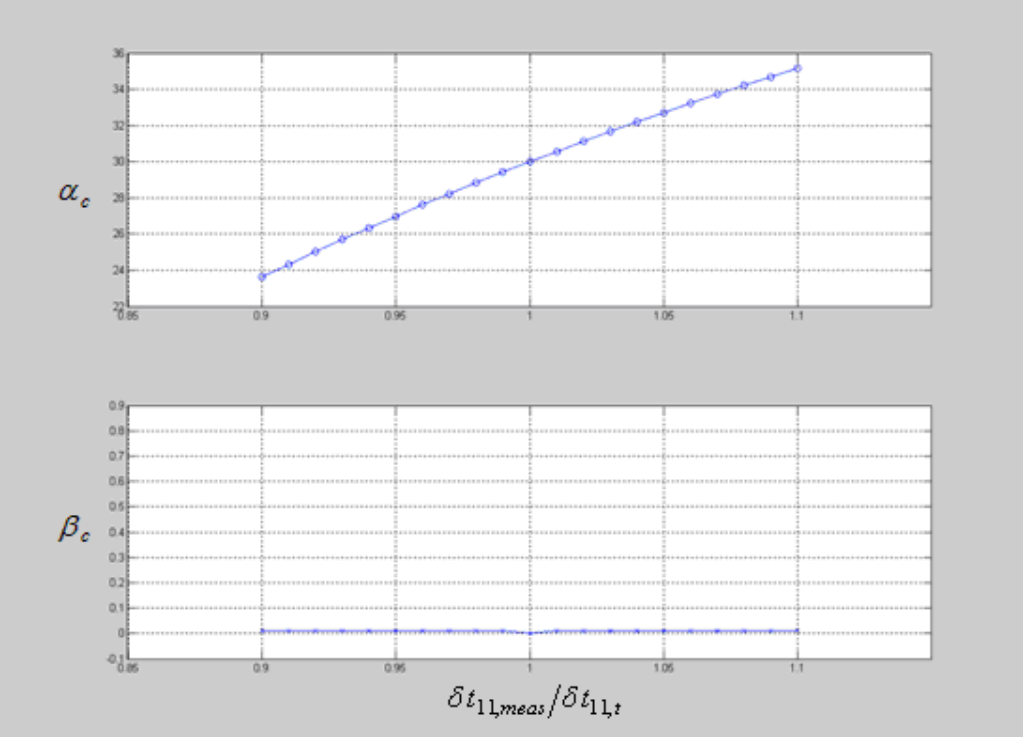


**Figure 4.12 Variation of the calculated polar angle $\alpha_c$ and azimuthal angle $\beta_c$ with the error in $\delta t_{11,meas}$ using reference polar angle $\alpha_t$ = 30° and $\beta_t$ = 0°**

### 4.2.2 Effect on the calculated polar angle $\alpha_c$ and azimuthal angle $\beta_c$ due to the error in time intervals $\delta t_{22,meas}$

1. Select the probe dimensions $x_{i,t}$, $y_{i,t}$ and $z_{i,t}$ from Table 4.1.
2. Calculate $\delta t_{ii,t}$ using Equations 2.44 – 2.46, assuming polar angle $\alpha_t$ = 0° or 30°, azimuthal angle $\beta_t$ = 0° and velocity of the bubble $v_t$ = 0.5 ms$^{-1}$.

3. Using the true values of $x_{i,t}$, $y_{i,t}$, $z_{i,t}$ and the value of $\delta t_{33,t}$ and $\delta t_{11,t}$ calculated in step 2, $\delta t_{22,meas}$ is varied from 0.9 mm to 1.1 mm in steps of 0.01 mm and a new $\alpha_c$ and $\beta_c$ is calculated.
4. The intention is to show the effect on the calculated values of $\alpha_c$ and $\beta_c$ due to the measurement error from -10% to +10% in the true value of $\delta t_{22,meas}$.

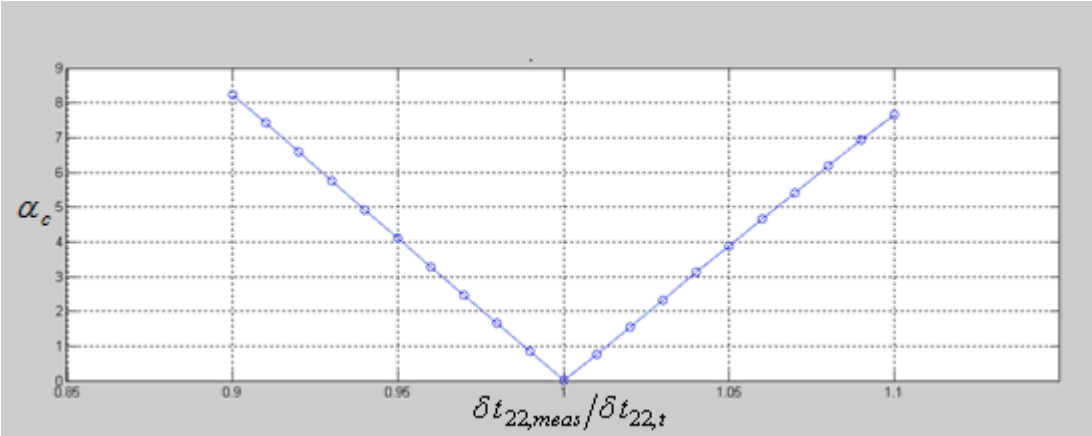


**Figure 4.13 Variation of the calculated polar angle $\alpha_c$ with the error in $\delta t_{22,meas}$ using reference $\alpha_t$ = 0° and $\beta_t$ =0°**

Figure 4.13 shows the effect on the calculated polar angle $\alpha_c$ and the azimuthal angle $\beta_c$ due to the error in $\delta t_{22,meas}$. Figure 4.13 shows that, as $\delta t_{22,meas}$ decreases from its true value, the calculated polar angle $\alpha_c$ increases. Similarly, if $\delta t_{22,meas}$ is increased, the calculated polar angle $\alpha_c$ increases again. The increment of $\alpha_c$ reaches 8° (supposed to be 0°) when the error is ±10% of true value of $\delta t_{22,meas}$.

Figure 4.14 shows the effect on the calculated polar angle $\alpha_c$ and azimuthal angle $\beta_c$ when the measurement error in $\delta t_{22,meas}$ is ±10%. The figure suggests that, as the $\delta t_{22,meas}$ decreases from its true value, $\alpha_c$ increases gradually to 33°, whereas if

$\delta t_{22,meas}$ increases from its true value, $\alpha_c$ decreases gradually to 27.5°. Figure 4.14 also shows that there is very little variation in $\beta_c$ resulting from the variation when the error in $\delta t_{22,meas}$ is decreased by 10% from its true value ($\beta_c$ increases slightly up to 10°). However, $\beta_c$ reaches almost 350° (10° offset while 360° = 0°) when the error in $\delta t_{22,meas}$ is increased by 10%.

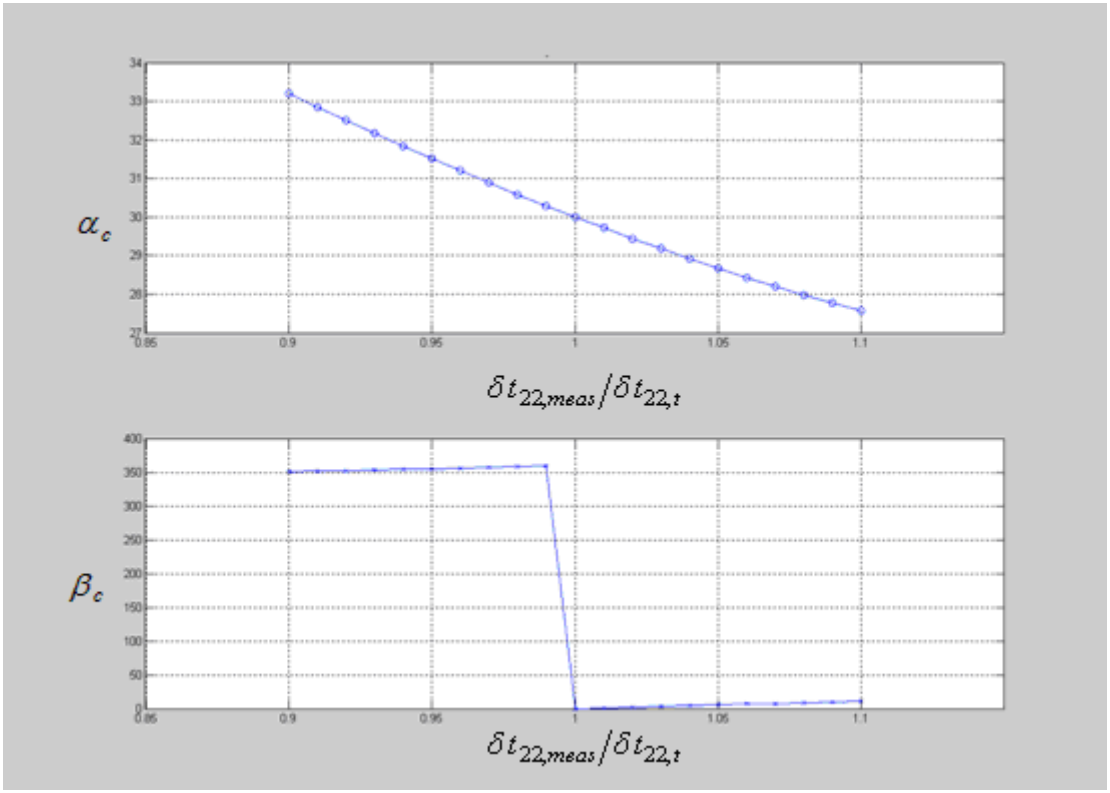


**Figure 4.14 Variation of the calculated polar angle $\alpha_c$ and azimuthal angle $\beta_c$ with the error in $\delta t_{22,meas}$ using reference $\alpha_t$ = 30° and $\beta_t$ =0°**

### 4.2.3 Effect on the calculated polar angle $\alpha_c$ and azimuthal angle $\beta_c$ due to the error in time intervals $\delta t_{33,meas}$

1. Select the probe dimensions $x_{i,t}$ , $y_{i,t}$ and $z_{i,t}$ from Table 4.1.

2. Calculate $\delta t_{ii,t}$ using Equations 2.44 – 2.46, assuming polar angle $\alpha_t$ equals 0° or 30°, azimuthal angle $\beta_t$ equals 0° and velocity of the bubble $v_t$ equals 0.5 ms$^{-1}$.
3. Using the true values of $x_{i,t}$, $y_{i,t}$, $z_{i,t}$ and the value of $\delta t_{11,t}$ and $\delta t_{22,t}$ calculated in step 2, $\delta t_{33,meas}$ is varied from 0.9 mm to 1.1 mm in steps of 0.01 mm and a new $\alpha_c$ and $\beta_c$ are calculated.
4. The intention is to show the effect on the calculated values of $\alpha_c$ and $\beta_c$ due to the measurement error from -10% to +10% in the true value of $\delta t_{33,meas}$.

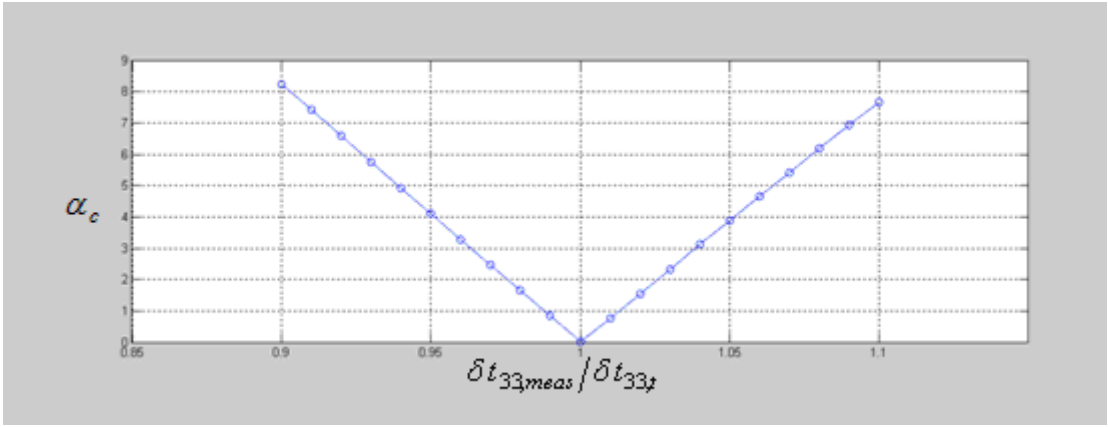


**Figure 4.15 Variation of the calculated polar angle $\alpha_c$ with the error in $\delta t_{33,meas}$ using reference $\alpha_t$ = 0° and $\beta_t$ =0°**

Figure 4.15 shows the effect on the calculated polar angle $\alpha_c$ due to the error in $\delta t_{33,meas}$. The figure shows that, as $\delta t_{33,meas}$ decreases from its true value, the calculated polar angle $\alpha_c$ increases. Similarly, if $\delta t_{33,meas}$ is increased from its true value, polar angle $\alpha_c$ increases again. The increment of polar angle $\alpha_c$ reaches 8° (supposed to be 0°) when the error is ±10% of true value of $\delta t_{33,meas}$.

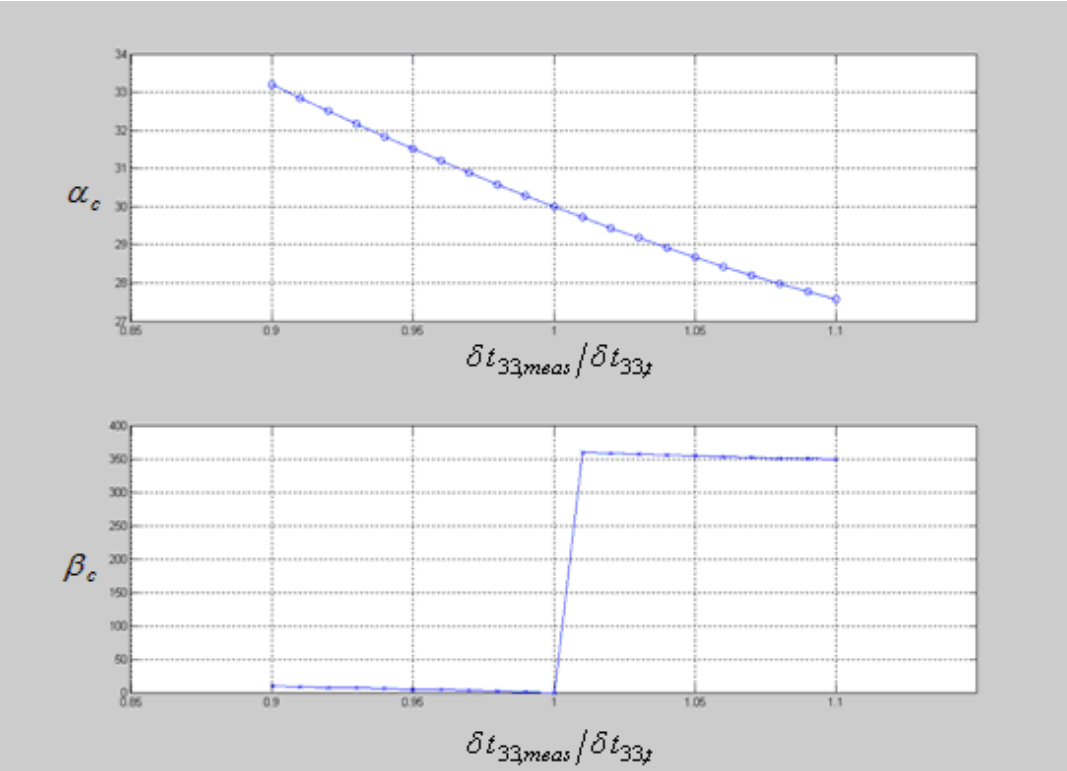


**Figure 4.16 Variation of the calculated polar angle $\alpha_c$ and azimuthal angle $\beta_c$ with the error in $\delta t_{33,meas}$ using reference $\alpha_t = 30°$ and $\beta_t = 0°$**

Similarly, Figure 4.16 shows the effect on the calculated polar angle $\alpha_c$ and azimuthal angle $\beta_c$ when the measurement error in $\delta t_{33,meas}$ is ±10% from its true value for the reference polar angle $\alpha_t = 30°$ and azimuthal angle $\beta_t = 0°$. The figure suggests that, as $\delta t_{33,meas}$ decreases from its true value $\alpha_c$ increases gradually to 33°, whereas if $\delta t_{33,meas}$ is increased from its true value, $\alpha_c$ decreases gradually to 27.5° for the 10% error in $\delta t_{33,meas}$. Figure 4.16 also shows that $\beta_c$ reaches 350° when the error is increased by 10% in $\delta t_{33,meas}$. However, $\beta_c$ shows only a small change (increases slightly up to 10°) when the error in $\delta t_{33,meas}$ is increased by 10% of its true value.

### 4.2.4 Effect on the calculated polar angle $\alpha_c$ and azimuthal angle $\beta_c$ due to the error in multiple time intervals $\delta t_{ii,meas}$

In this section, the effect on the calculated polar angle $\alpha_c$ and azimuthal angle $\beta_c$ due to the error in the multiple time intervals $\delta t_{ii,meas}$ was investigated. Firstly, $\delta t_{ii,t}$ is calculated from the dimensions given in Table 4.1 with the reference velocity of 0.5ms$^{-1}$, azimuthal angle 0° and polar angle 0° and 30°. Once all the time intervals $\delta t_{ii,t}$ are calculated, an error of ± 10% is introduced in two time intervals out of three, keeping one constant. For example, keeping $\delta t_{11,t}$ constant, $\delta t_{22,meas}$ and $\delta t_{33,meas}$ are changed to ± 10%. For simplicity, four conditions are introduced.

Condition 1: both the time intervals are increased by 10%, for example if $\delta t_{11,t}$ is constant, $\delta t_{22,meas}$ increases by 1% and $\delta t_{33,meas}$ increases from 1% to 10%, again $\delta t_{22,meas}$ increases by 2% and $\delta t_{33,meas}$ increases from 1% to 10%. The process continues until $\delta t_{22,meas}$ reaches 10%.

Condition 2: keeping the first time interval constant, the second time interval is increased by 1% to 10%, while the third time interval is decreased by 1% to 10% (taking $\delta t_{11,t}$, $\delta t_{22,t}$ and $\delta t_{33,t}$ as the first, second and third time intervals respectively). For example, if $\delta t_{11,t}$ is constant, $\delta t_{22,meas}$ increases by 1% and $\delta t_{33,meas}$ decreases from 1% to 10%, again $\delta t_{22,meas}$ increases by 2% and $\delta t_{33,meas}$ decreases from 1% to 10%. The process continues until $\delta t_{22,meas}$ reaches 10%.

Condition 3: keeping the first time interval constant, the second time intervals are decreased by 1% to 10%, while the third time interval is increased by 1% to 10%

(taking $\delta t_{11,t}$, $\delta t_{22,t}$ and $\delta t_{33,t}$ as the first, second and third time intervals respectively). For example, if $\delta t_{11,t}$ is constant, $\delta t_{22,meas}$ decreases by 1% and $\delta t_{33,meas}$ increases from 1% to 10%, again $\delta t_{22,meas}$ decreases by 2% and $\delta t_{33,meas}$ increases from 1% to 10%. The process continues until $\delta t_{22,meas}$ reaches -10%.

Condition 4: both the time intervals are decreased by 1% to 10%, for example if $\delta t_{11,t}$ is constant, $\delta t_{22,meas}$ decreases by 1% and $\delta t_{33,meas}$ decreases from 1% to 10%, again $\delta t_{22,meas}$ decreases by 2% and $\delta t_{33,meas}$ decreases from 1% to 10%. The process continues until $\delta t_{22,meas}$ reaches -10%.

*4.2.4.1 Effect on the calculated polar angle $\alpha_c$ and azimuthal angle $\beta_c$ using Condition 1*

Figure 4.17 shows the effect on the calculated polar angle $\alpha_c$ and azimuthal angle $\beta_c$ due to the error in the measured time intervals $\delta t_{ii,meas}$ as shown in Condition 1 (described above). The variation in red denotes constant $\delta t_{11,meas}$, with errors in $\delta t_{22,meas}$ and $\delta t_{33,meas}$. The data in black is the constant $\delta t_{22,meas}$ and errors in $\delta t_{33,meas}$ and $\delta t_{11,meas}$. The data in blue is constant $\delta t_{33,meas}$ with the errors in $\delta t_{11,meas}$ and $\delta t_{22,meas}$.

In Figure 4.17, the top half (the left is the calculated polar angle $\alpha_c$ and the right is the azimuthal angle $\beta_c$) of the figure is the effect on the polar angle and azimuthal angle calculated with reference to the polar angle $\alpha_t = 0°$, whereas the bottom half

(the left is the calculated polar angle $\alpha_c$ and the right is the azimuthal angle $\beta_c$) is calculated with reference to the polar angle $\alpha_t = 30°$.

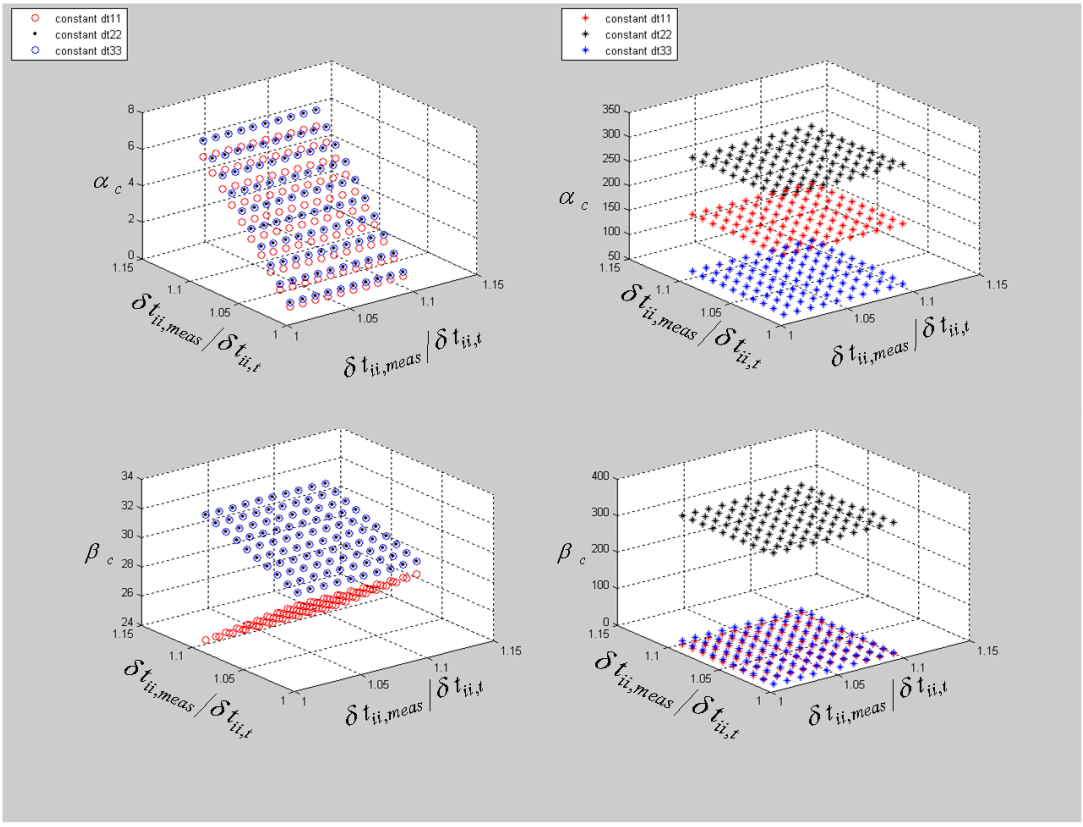


**Figure 4.17 Variation of the calculated polar angle $\alpha_c$ and azimuthal angle $\beta_c$ due to the errors described in Condition 1**

Figure 4.17 suggests that the calculated polar angle $\alpha_c$, in the case of $\alpha_t = 0°$, rises to 7° with all constant time intervals. Figure 4.17 also shows that when reference polar angle $\alpha_t = 30°$ and when $\delta t_{11,meas}$ is equal to $\delta t_{11,t}$, as the error increases, the calculated polar angle $\alpha_c$ decreases gradually until it reaches 24°; whereas, when $\delta t_{22,meas}$ and $\delta t_{33,meas}$ are constant, the calculated polar angle $\alpha_c$ increases gradually to 33° as the error increases. Calculated azimuthal angle $\beta_c$ in each case shows very small variation, as it is either close to 0° or 360°

*4.2.4.2 Effect on the calculated polar angle $\alpha_c$ and azimuthal angle $\beta_c$ using Condition 2*

Figure 4.18 shows the effect on the calculated polar angle $\alpha_c$ and azimuthal angle $\beta_c$ due to the error in time intervals $\delta t_{ii,meas}$ as per Condition 2 (as described above). The variation in red denotes constant $\delta t_{11,meas}$, with errors in $\delta t_{22,meas}$ and $\delta t_{33,meas}$. The data in black is the constant $\delta t_{22,meas}$ and errors in $\delta t_{33,meas}$ and $\delta t_{11,meas}$. The data in blue is constant $\delta t_{33,meas}$ with the errors in $\delta t_{11,meas}$ and $\delta t_{22,meas}$.

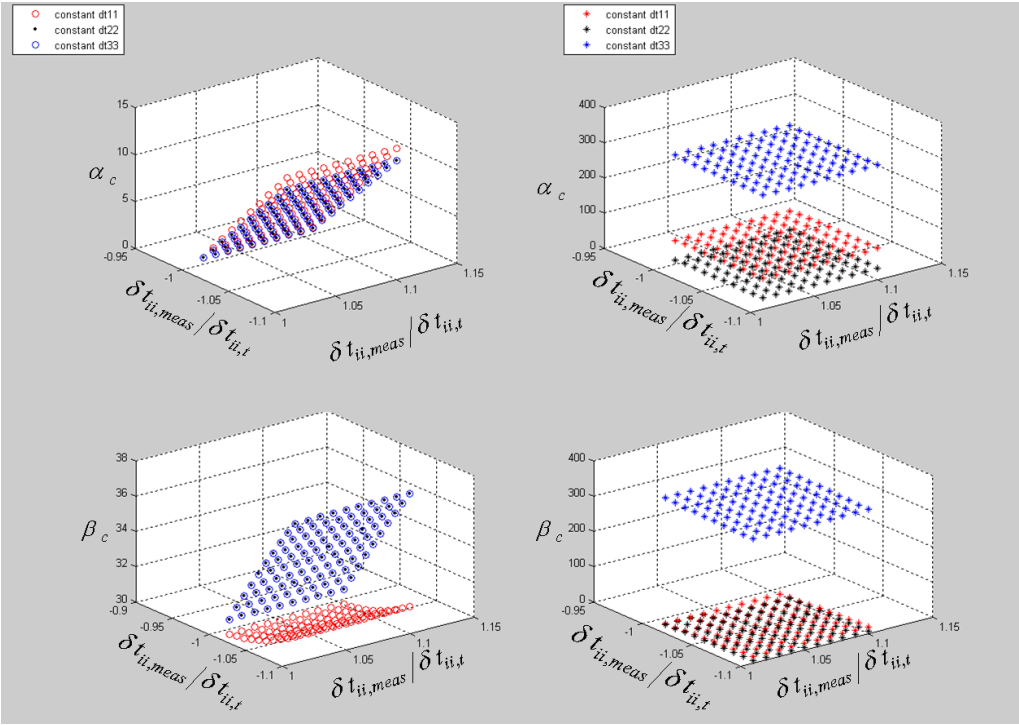


**Figure 4.18 Variation of the calculated polar angle $\alpha_c$ and azimuthal angle $\beta_c$ due to the error described in Condition 2**

In Figure 4.18, the top half (the left is the calculated polar angle $\alpha_c$ and the right is the azimuthal angle $\beta_c$) of the figure shows the effect on the calculated polar angle and azimuthal angle calculated with reference to polar angle $\alpha_t = 0°$, whereas the

bottom half (the left is the calculated polar angle $\alpha_c$ and the right is the azimuthal angle $\beta_c$) is calculated with reference to the polar angle $\alpha_t$ = 30°. Figure 4.18 suggests the calculated polar angle $\alpha_c$, in the case of $\alpha_t$ = 0°, rises to 10° with all constant time intervals. The figure also shows that, when polar angle $\alpha_t$ = 30° and when $\delta t_{11,meas}$ is constant, as the error increases the calculated polar angle $\alpha_c$ slightly increases until it reaches 33°; whereas when $\delta t_{22,meas}$ and $\delta t_{33,meas}$ are constant, the calculated polar angle $\alpha_c$ increases gradually to 36° as the error increases. Calculated azimuthal angle $\beta_c$ in each case shows a very small variation, as it is either close to 0° when $\delta t_{11,meas}$ and $\delta t_{22,meas}$ are constant or 360° when $\delta t_{33,meas}$ is constant.

*4.2.4.3 Effect on the calculated polar angle $\alpha_c$ and azimuthal angle $\beta_c$ using Condition 3*

Figure 4.19 shows the effect on the calculated polar angle $\alpha_c$ and azimuthal angle $\beta_c$ due to the error in time intervals $\delta t_{ii,meas}$ as shown in Condition 3 (described above). The variation in red denotes constant $\delta t_{11,meas}$, with errors in $\delta t_{22,meas}$ and $\delta t_{33,meas}$. The data in black is the constant $\delta t_{22,meas}$ and errors in $\delta t_{33,meas}$ and $\delta t_{11,meas}$. The data in blue is constant $\delta t_{33,meas}$ with the errors in $\delta t_{11,meas}$ and $\delta t_{22,meas}$. In Figure 4.19, (the left is the calculated polar angle $\alpha_c$ and the right is the azimuthal angle $\beta_c$) of the figure is the effect on the polar angle and azimuthal angle calculated with reference to the polar angle $\alpha_t$ = 0°, whereas the bottom half (the left is the calculated polar angle $\alpha_c$ and the right is the azimuthal angle $\beta_c$) is calculated with reference to the polar angle $\alpha_t$ = 30°. The figure suggests that the calculated polar angle $\alpha_c$, in

case of $\alpha_t = 0°$, rises up to 6° with all constant time intervals. Figure 4.19 also shows that, when reference polar angle $\alpha_t = 30°$ and when $\delta t_{11,meas}$ is constant, as the error increases the calculated polar angle $\alpha_c$ increases gradually until it reaches 34°, whereas when $\delta t_{22,meas}$ and $\delta t_{33,meas}$ are constant, the calculated polar angle $\alpha_c$ decreases gradually to 27° as the error increases. Calculated azimuthal angle $\beta_c$ in each case shows a very small variation, as it is either close to 0° when $\delta t_{33,meas}$ is constant or 360° when $\delta t_{11,meas}$ and $\delta t_{22,meas}$ are constant.

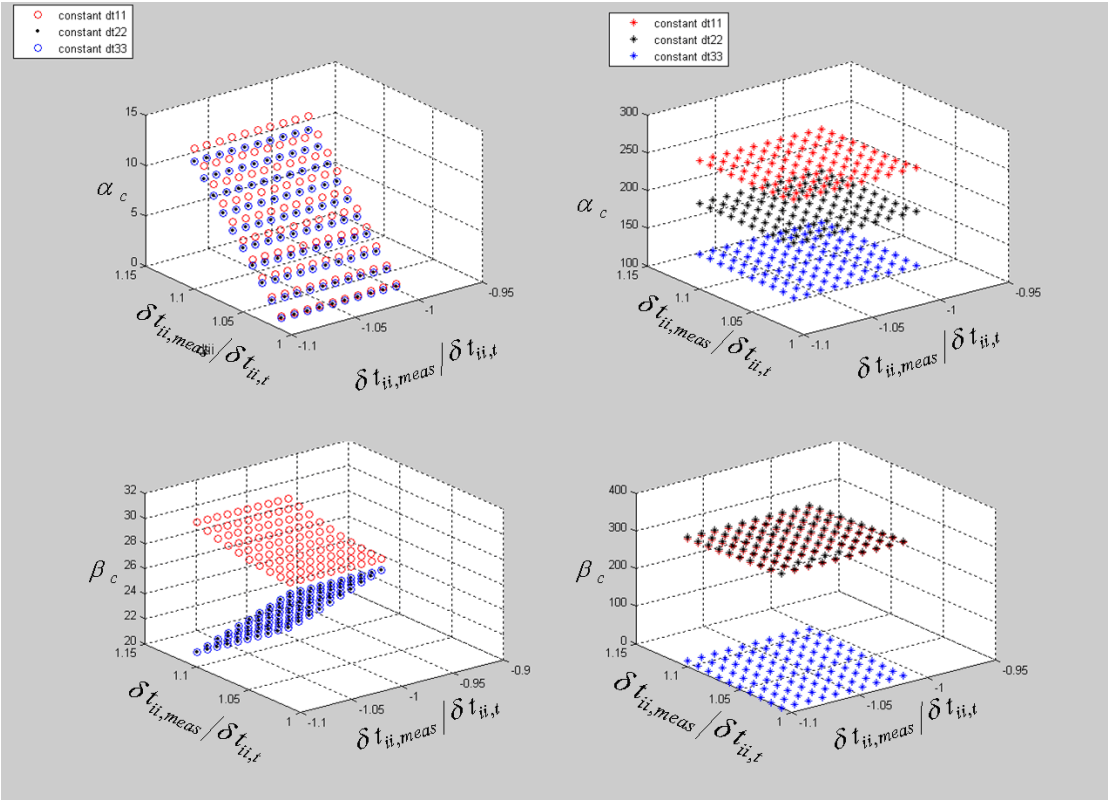


**Figure 4.19 Variation of the calculated polar angle $\alpha_c$ and azimuthal angle $\beta_c$ due to the error described in Condition 3**

*4.2.4.4 Effect on the calculated polar angle $\alpha_c$ and azimuthal angle $\beta_c$ using Condition 4*

Figure 4.20 shows the effect on the calculated polar angle $\alpha_c$ and azimuthal angle $\beta_c$ due to the error in the measured time intervals $\delta t_{ii,meas}$, as shown in Condition 4 (as described above). The variation in red denotes constant $\delta t_{11,meas}$, with errors in $\delta t_{22,meas}$ and $\delta t_{33,meas}$. The data in black is the constant $\delta t_{22,meas}$ and errors in $\delta t_{33,meas}$ and $\delta t_{11,meas}$. The data in blue is constant $\delta t_{33,meas}$ with the errors in $\delta t_{11,meas}$ and $\delta t_{22,meas}$.

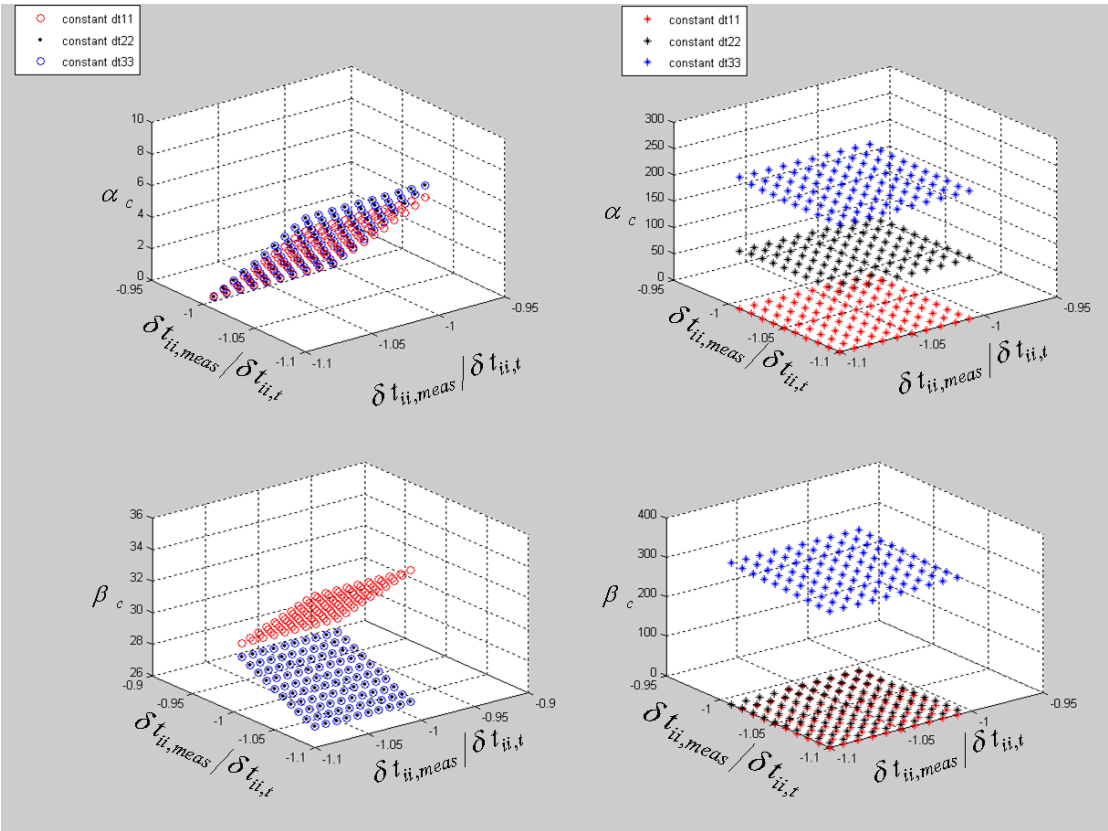


**Figure 4.20 Variation of the calculated polar angle $\alpha_c$ and azimuthal angle $\beta_c$ due to the error described in Condition 4**

In Figure 4.20, the top half (the left is the calculated polar angle $\alpha_c$ and the right is the azimuthal angle $\beta_c$) of the figure is the effect on the polar angle and azimuthal angle calculated with reference to the polar angle $\alpha_t = 0°$, whereas the bottom half (the left is the calculated polar angle $\alpha_c$ and the right is the azimuthal angle $\beta_c$) is calculated with reference to the polar angle $\alpha_t = 30°$.

Figure 4.20 suggests the calculated polar angle $\alpha_c$ , in case of $\alpha_t = 0°$, rises up to 7° with all constant time intervals. Figure 4.20 also shows that, when reference polar angle $\alpha_t = 30°$ and when $\delta t_{11,meas}$ is constant, as the error increases the calculated polar angle $\alpha_c$ slightly increases until it reaches 33°, whereas when $\delta t_{22,meas}$ and $\delta t_{33,meas}$ are constant, the calculated polar angle $\alpha_c$ decreases gradually to 27° as the error increases. Calculated azimuthal angle $\beta_c$ in each case shows a very small variation, as it is either close to 0° when $\delta t_{11,meas}$ and $\delta t_{22,meas}$ are constant or 360° when $\delta t_{33,meas}$ is constant.

### 4.3 Conclusion

In this chapter, the sensitivity of the 'z' dimensions of the four-sensor probe and the time intervals were analysed. The analysis was carried out with the introduced error of ± 10% in the single variable, as well as the multiple variable. In order to check the effect of the error, the results were analysed in reference polar angle 0° and 30°. The results show that even a small error in the measurement of probe and time intervals for the calculation showed a big difference in the polar angle when the reference polar angle is 0°.

However, when the reference polar angle is 30° (or when the probe is tilted by 30°), the calculation shows a great difference in the reference and the measured values, due to the error in the 'z' dimensions as well as in time intervals $\delta t_{ii}$. These results show good agreement with the results presented by Sanaullah et al. [150], where the author states that the probe has less effect on the bubble when it is tilted by 20° (polar angle). The author also states that the effect of the probe rises as the probe's inclination becomes closer to 55° (polar angle).

# CHAPTER 5

## Measurement Electronics

### 5.1 DC circuitry

Figure 5.1 shows the basic circuit design that is required for the four-sensor probe to measure the conductance of air or water. The complete circuit is based on a non-inverting amplifier and a regulated DC voltage source.

In Figure 5.1, $SR1$ is the resistance between the relevant sensor tip and the probe body (common electrode). The output voltage $V_{amp}$ from the operational amplifier in the circuit is given by:

$$V_{amp} = V_{in}\left\{1+\frac{RF1}{SR1}\right\} \qquad \textbf{Equation 5.1}$$

The working principle of the circuit is that when the tip of the given sensor is immersed in water, the value of $SR1$ is very small compared to the feedback resistor $RF1$ (which is typically > 1.5 MΩ). Thus, $V_{amp}$ saturates at the positive supply voltage of the operational amplifier (+15 V). When the tip of the sensor is immersed in a bubble, the circuit becomes open loop, making the value of $SR1$ higher than $RF1$ and making the quantity $\frac{RF1}{SR1}$ close to zero so that $V_{amp}$ approaches $V_{in}$, which is typically +5 volts. Thus, as each of the four sensors is immersed successively in water and air, output signals similar to those shown in Figure 5.2 are obtained. Note that the variable resistor $OR1$ was used to fine tune the output voltage $V_{out}$, to cover the full range of analogue to digital converters of the data acquisition system that was used.

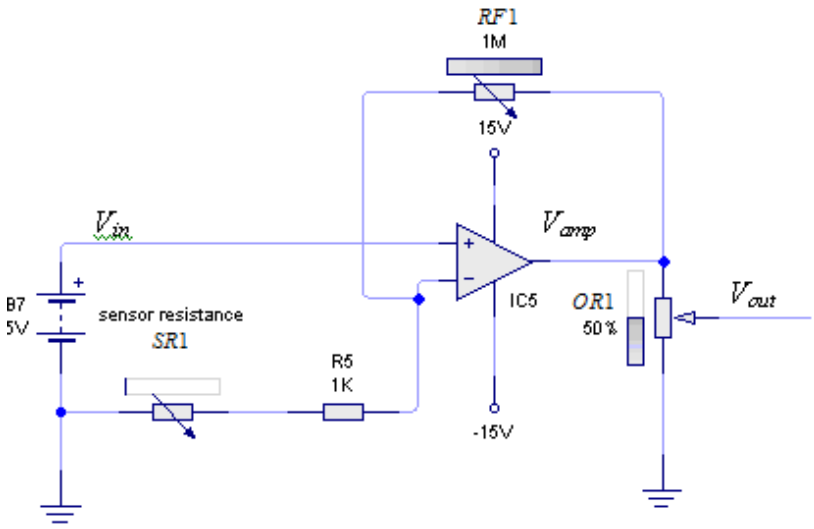


**Figure 5.1 D C circuit**

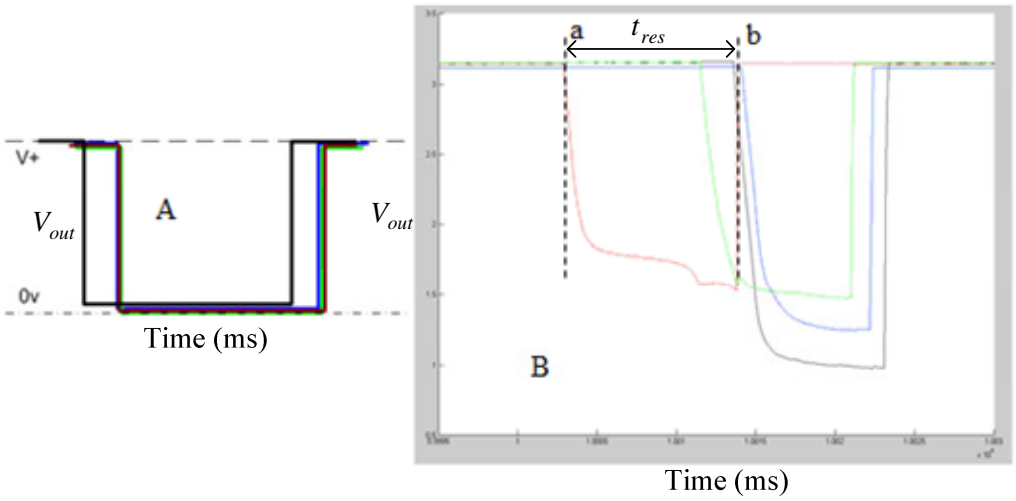


**Figure 5.2 (A) Typical output from four-sensor probe DC circuit.**

**(B) Output from four-sensor probe.**

Four separate circuits were made for the four-sensor probe, as described above. Figure 5.2 (A) shows the ideal output signal from the four sensors of a four-sensor probe, and Figure 5.2 (B) is the experimental output from the probe when a gas bubble (in water) passes over it. In Figure 5.2 (B), the red coloured signal is from the front sensor while the other coloured signals are from the three rear sensors. The time lag between the front and the rear sensors (time interval between the drop in signal level between the

front and rear sensors) depends on the axial separation between the front and the rear three sensors. The time interval from when the signal from a given sensor drops and rises again (e.g. from point 'a' to point 'b' in Figure 5.2 B) depends on the size of the bubble (diameter '*d*' of the bubble) and the bubble velocity. This residence time $t_{res}$ of the bubble on the sensor can be approximated by $t_{res} = \frac{d}{v}$ for the bubble travelling with velocity $v$ parallel to the probe axis which strikes the given sensor centrally.

When using the DC excitation circuit, the disadvantage of electrolysis caused by the DC source should not be forgotten. Electrolysis is a process whereby a DC current is applied across two electrodes, one of which is a negative electrode and the other is a positive electrode. The negative terminal is referred to as the cathode, and the positive terminal is referred to as the anode. Negatively charged electrons flow through the wiring of the circuit from cathode to anode, which results in corrosion of the anode; thus, solid corrosive residue forms on its surface.

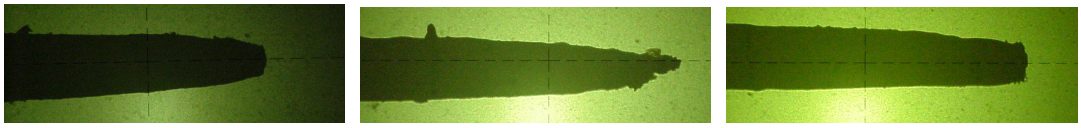

**Figure 5.3 Sensor tip – before electrolysis (left), after electrolysis (middle), and after cleaning (right). Images are from a shadow-graph.**

Due to this electrolysis process (in the present study the probe holder and the sensor tip work as the electrodes for electrolysis), the performance of the sensors can be degraded because particles from the insulation may become loose as a result of the corrosion. Also, the tiny particles that exist in the flow will attract to the tips of the sensors because they are electrically charged. This will result in the sensor tips becoming partially or completely covered by a non-conducting film of dirt and the

acquired signal's characteristics will be altered, creating errors in the signal processing scheme. The solution to this problem is to clean the tips of the probe whenever it is observed that the probe's performance starts to deteriorate. The sensor tip can be cleaned using very fine emery paper. Figure 5.3 shows stages of the tip of a sensor affected by the electrolysis and the improved sensor tip after the cleaning procedure is applied.

## 5.2 AC circuitry

Another way to measure the conductance of air or water without causing the electrolysis process is to use AC excitation instead of DC. The working principle of this type of circuit is similar to that of the DC circuit, where the conductance value increases and decreases as the sensor tip is immersed in water or air respectively. The only difference is that this circuit uses an AC source instead of DC, as shown in Figure 5.4.

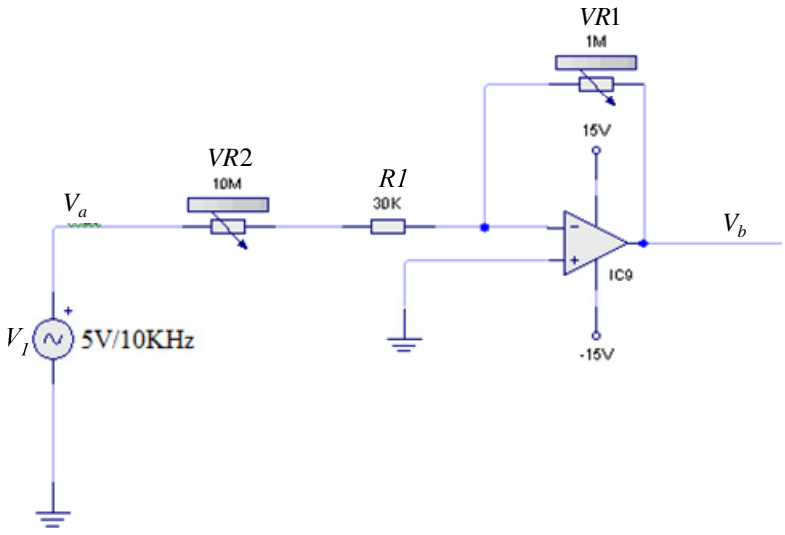


**Figure 5.4 Basic AC circuit**

An investigation was carried out with AC excitation as a possible alternative to DC excitation. The complete circuit was based on inverting an amplifier and regulated

voltage source, as shown in Figure 5.4. A 10 kHz AC 5V peak-to-peak signal was applied as an excitation signal, as shown in Figure 5.5 (simulated signal). Four identical circuits (as shown in Figure 5.4) were made for a four-sensor probe. For each circuit *VR2* was replaced with the relevant sensor. The circuit was also designed and simulated in the software "Proteus" for comparison purposes.

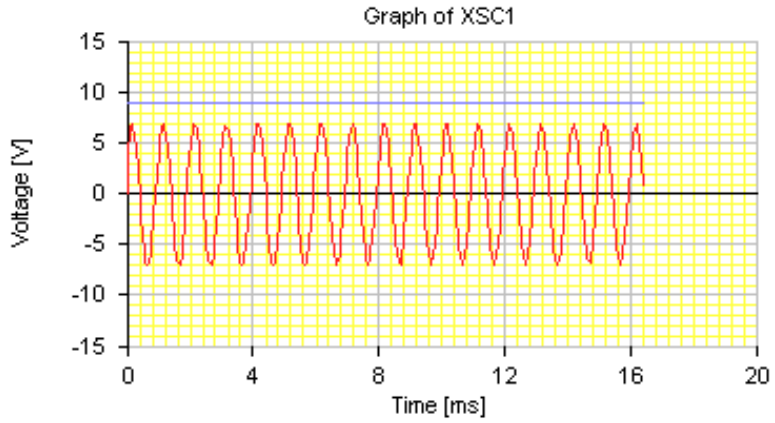


**Figure 5.5 Simulated input signal**

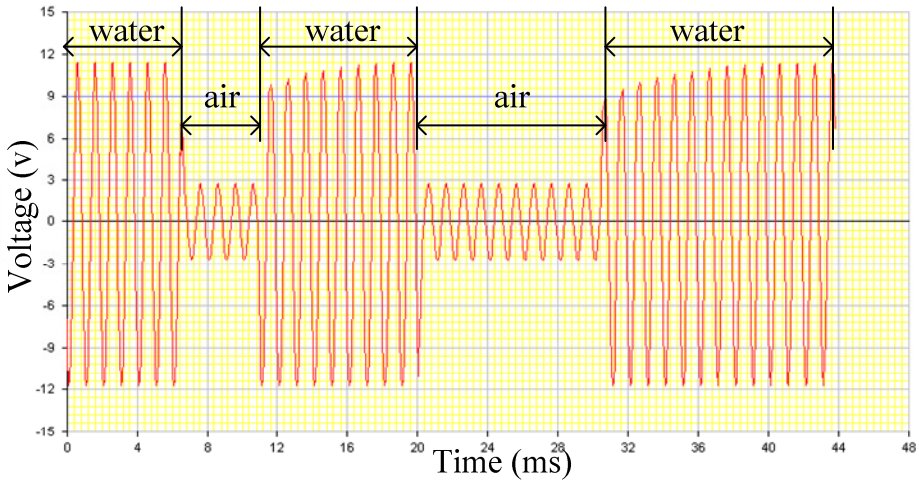


**Figure 5.6 Output signal**

Figure 5.6 shows the simulated output signal from the circuit as the sensor is immersed in air and water. The increased amplitude denotes that the sensor was in contact with the water, making the resistance value of the sensor (*VR*2) smaller than

$VR1$. The output of circuit $V_b$ (output of inverting amplifier) is given by Equation 5.2 so when the sensor is immersed in water, the value of $V_b$ is greater than $V_a$.

$$V_b = -V_a\left(\frac{VR1}{(VR2+R1)}\right) \qquad \textbf{Equation 5.2}$$

However, when the tip of the sensor is immersed in a bubble, the circuit becomes open loop, making the value of $VR2$ higher than $VR1$ and making the quantity $\frac{VR1}{(VR2+R1)}$ close to zero so that $V_b$ approaches $V_a$, as shown in Figure 5.6. The amplified output $V_b$ is then passed through the rectifier in conjunction with an active low pass filter (Figure 5.7) to convert the output from AC to DC for easy signal processing. The cut-off frequency $f_c$ for the low-pass filter is calculated as Equation 5.3.

$$f_c = \frac{1}{2\pi R_9 C_3} \qquad \textbf{Equation 5.3}$$

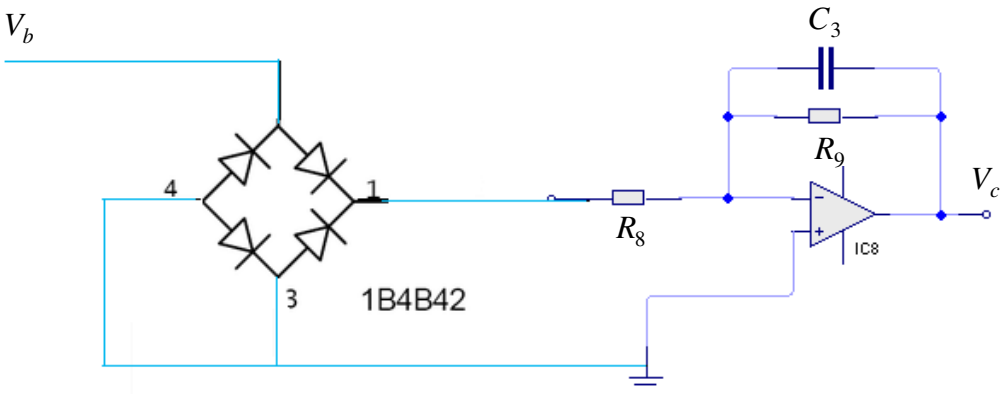


**Figure 5.7 Low-pass filter**

Figure 5.8 (A) shows the "Proteus" generated simulated output signal from the low-pass filter, and (B) shows the output signal from a built circuit. Both of the signals show similar characteristics, with noise on the rising level and slow decay on the

falling edge of the signal.

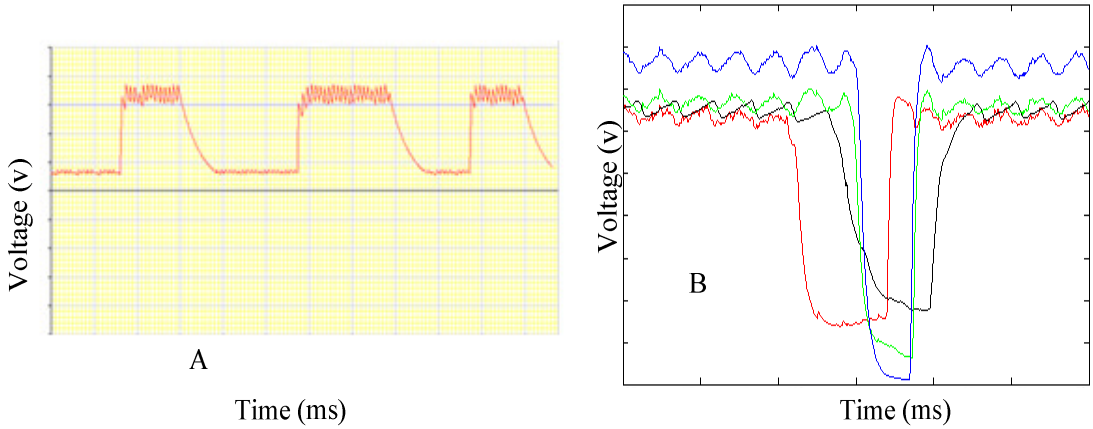


**Figure 5.8 Output signal after low – pass filter is: A) simulated B) experimental**

From the signals obtained using the DC circuit (Figure 5.2) or the AC circuit (Figure 5.8), it is necessary to measure the time intervals $\delta t_{ii}$ ($i$ = 1, 2 and 3). From the calculated values of $\delta t_{ii}$ and the measured probe dimensions (see Chapter 3.3), it is possible to calculate the polar angle $\alpha$, azimuthal angle $\beta$ and the velocity magnitude $v$ of a bubble using Equations 2.48, 2.47 and 2.46 respectively, as described in Chapter 2.

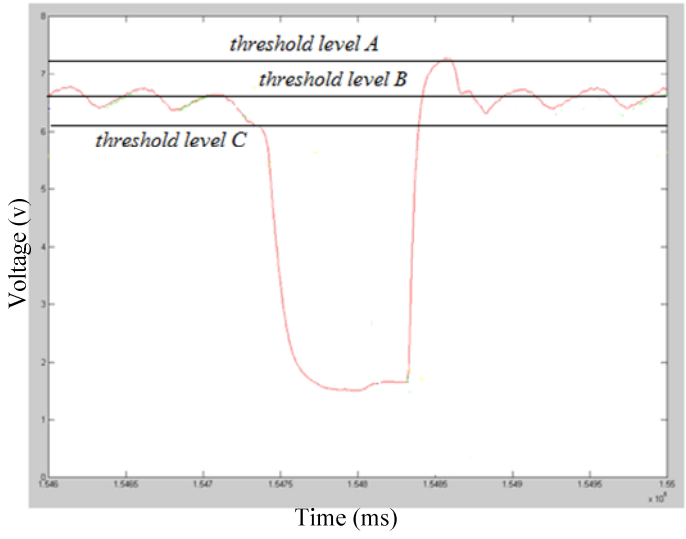


**Figure 5.9 Various levels of threshold**

Although it is possible to calculate the velocity vector from the signal obtained using an AC source, it is extremely likely that the calculated velocity vector might not be very accurate. The presence of the rectifier and the low-pass filter in the circuit causes a high level of noise (see Figure 5.8) in the signal and, as a result, it will force the use of a lower value of threshold, as shown in Figure 5.9.

In Figure 5.9, three different threshold levels are presented; in an ideal situation, the threshold level is placed where it just contacts the rising or falling edge of the signal. "Threshold level *A"* shows there is only contact with the rising edge of the signal, resulting in the data processing software ignoring this type of signal (see Chapter 6).

"Threshold level *B"* shows that, although it contacts both the rising and the falling edge of the signal, the threshold level touches the rising and the falling edge very often and the measured time interval between the rising and the falling edges is likely to be ambiguous; again, the software will avoid this bubble (see Chapter 6).

"Threshold level *C*", however, fulfils the required criteria as it touches the falling edge and the rising edge of the bubble at approximately the correct times, but this level itself is very low for the threshold value and the measured times at which the bubble's surface contacts the sensor are likely to be incorrect. Hence, by using this lower value of threshold, it is more likely that the wrong times for the falling edge and rising edge will be chosen, giving incorrect values for $\delta t_{ii}$, and ultimately an incorrect bubble velocity vector.

Despite the possibility of electrolysis, it was decided to carry out experiments with DC source circuits. To overcome the problem of electrolysis, it was decided to replace the probe when any of the original sensors stopped working.

## 5.3 Trigger circuitry

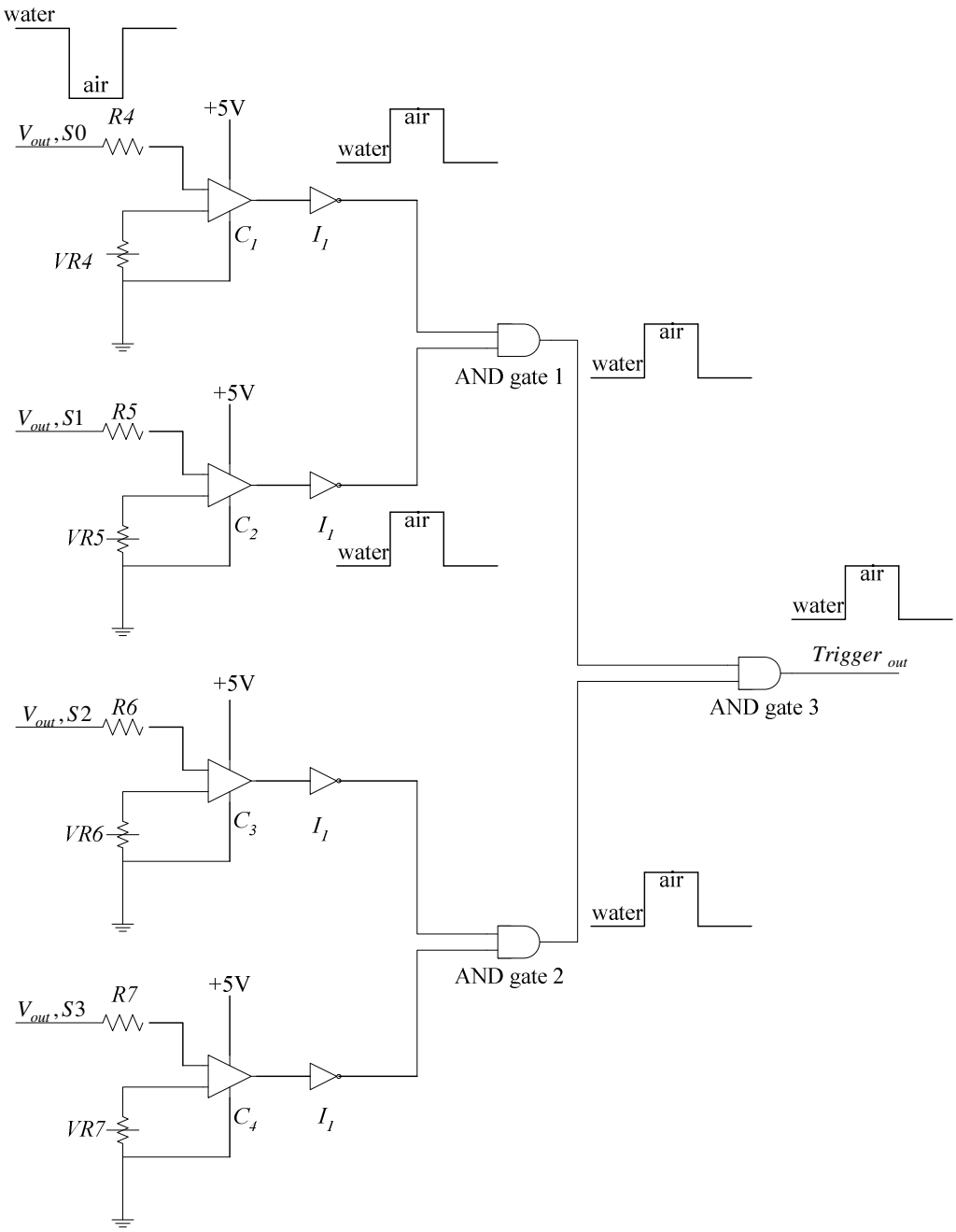


**Figure 5.10 Trigger circuit for four-sensor probe**

A trigger signal was used in the bench test experiments to stop high speed cameras (see Chapter 7) from capturing the images. The trigger circuit was also used to stop the data acquisition card (see Chapter 6) from collecting the data. The trigger signal was used as a mid-trigger for the high speed cameras (see Chapter 7). The velocity

vector calculated from the high speed camera was used as a reference with which to compare the velocity vector calculated from the four-sensor probe. Therefore, it was important to ensure that the velocity vector measured from the probe is from the same bubble that was captured and measured by the high speed camera. Hence, it is important that the trigger signal was generated by a bubble that strikes all four sensors of the probe.

In order to fulfil the above criteria, the signal obtained from each sensor ($V_{out}$) from the DC source circuit, as described in Chapter 5.1, was passed on from a comparator (*C1*) in conjunction with an inverter (*I1*) and AND gates, as shown in Figure 5.10. A trigger circuit was made such that the trigger is only received if a bubble strikes all four sensors. Figure 5.10 shows the trigger circuit for the four–sensor probe, where three different AND gates were used.

The outputs from the two individual sensors ($V_{out,}S0$ and $V_{out,}S1$ ) from the DC source circuit were passed through AND gate 1. The output from AND gate 1 will become high (+5v) only if a bubble touches sensor '0' (*S0*) as well as sensor '1' (*S1*); however, if a bubble touches only one sensor or touches none then the output from AND gate 1 stays low (0v). Similarly, the outputs from the remaining two sensors ($V_{out,}S2$ and $V_{out,}S3$ ) were passed through AND gate 2.

The output from AND gate 2 will become high (+5v) only if a bubble touches sensor '2' (*S2*) as well as sensor '3' (*S3*); however, if a bubble touches only one sensor or touches none then the output from AND gate 2 stays low (0v). The outputs from the above two AND gates were again passed through AND gate 3. When either one or both outputs from AND gate 1 and AND gate 2 is low, the output from AND gate 3 will also be low. The output from AND gate 3 only becomes high when both the

outputs from AND gate 1 and AND gate 2 are high. This output from AND gate 3 is used as the trigger signal. Figure 5.11 shows the output trigger signal generated by a four-sensor probe.

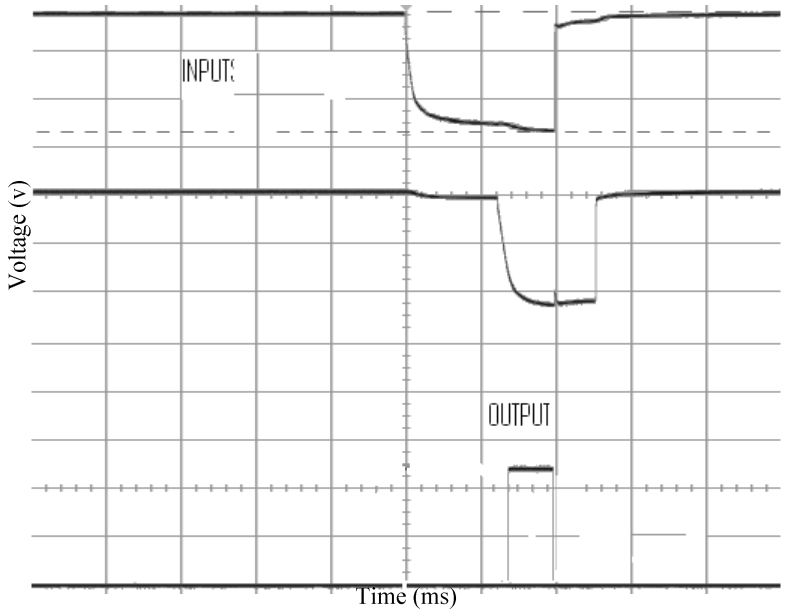


**Figure 5.11 Trigger output**

# CHAPTER 6

# Software Developments

## 6.1 Data acquisition

This chapter will discuss the software that has been developed in order to be used in this project. This software includes programs used to collect the data and also to process the collected data. In order to acquire the data from the circuits (see Chapter 5) which were connected to the four-sensor probe, a data acquisition card (DAQ 2006 purchased from ADLINK technology) was used. The DAQ 2006 can sample 250ks/s (kilo sample / second) simultaneously with four analogue input channels. The DAQ 2006 also contains analogue and digital trigger inputs, which were required to trigger the DAQ 2006 to prevent it from collecting data.

In order to communicate between the computer and the DAQ 2006, C++ and Visual Basic software was used (for detailed software listings see Appendix B). In this project, the data was collected by two different methods. In the first method, the data was collected continuously for a certain period of time, allowing numerous bubbles to hit all four-sensors. This was named the Continuous Data Collection.

In another method the data was collected from only one bubble that hit all four sensors and was named the Single Bubble Data Collection. Both these methods are described in detail later in this chapter.

### 6.1.1 Continuous Data Collection

In this process, data was collected for a certain period of time (max 180 seconds). For

this purpose, Visual Basic code was used to communicate with the DAQ2006 from the computer. The basic code format is shown below and Figure 6.1 shows the block diagram for data collection (for further details see Appendix B). A program named "asynchronous double buffer mode and scan channels to file" was used to collect the data; the program allows the collected data to be recorded straight to a designated file.

card = D2K_Register_Card(DAQ_2006, card_number); ///( resister DAQ2006)

- Register the DAQ card once the card is detected by the software.

D2K_AI_AsyncDblBufferMode (card, **1**); // (Analogue input Asynchronous double buffer (buffer fills one at a time) mode)

- Once the card is detected, call the function Analogue input Asynchronous double buffer mode; this function allows the analogue data to be input with a double buffer, which allows two samples of data to be scanned or read at a time.

D2K_AI_ContBufferSetup (card, ai_buf, data_size, &BufId);

- Set up the first buffer.

D2K_AI_ContBufferSetup (card, ai_buf2, data_size, &BufId); //(DAQ2006 Analogue input continuous buffer2 setup)

- Set up the second buffer.

D2K_AI_ContScanChannelsToFile (card, channel, BufId, data_size/(channel+1), ScanIntrv, SampIntrv, ASYNCH_OP);

- Call function D2K_AI_ContScanChannelsToFile, which allows all four channels to be scanned continuously, and store the scanned data to the specific file in the directory.

```
do {

D2K_AI_AsyncDblBufferHalfReady(card, &HalfReady, &fstop);
```

- Call the function DAQ2006 Analogue input Asynchronous double buffer half ready; half ready is always either 0 or 1

```
} while (!HalfReady);
```

- Function helps to scan the second data when the first data is halfway through being scanned by the first buffer. The remaining half of the first data is scanned by the second buffer.

```
D2K_AI_AsyncClear(card, &startPos, &count); // (DAQ2006 Analogue input Asynchronous clear card)
```

- Once the data are stored in the file, this function clears the data from the card and the card is ready to collect another set of data.

```
D2K_Release_Card (card);
```

- Function helps to release DAQ2006.

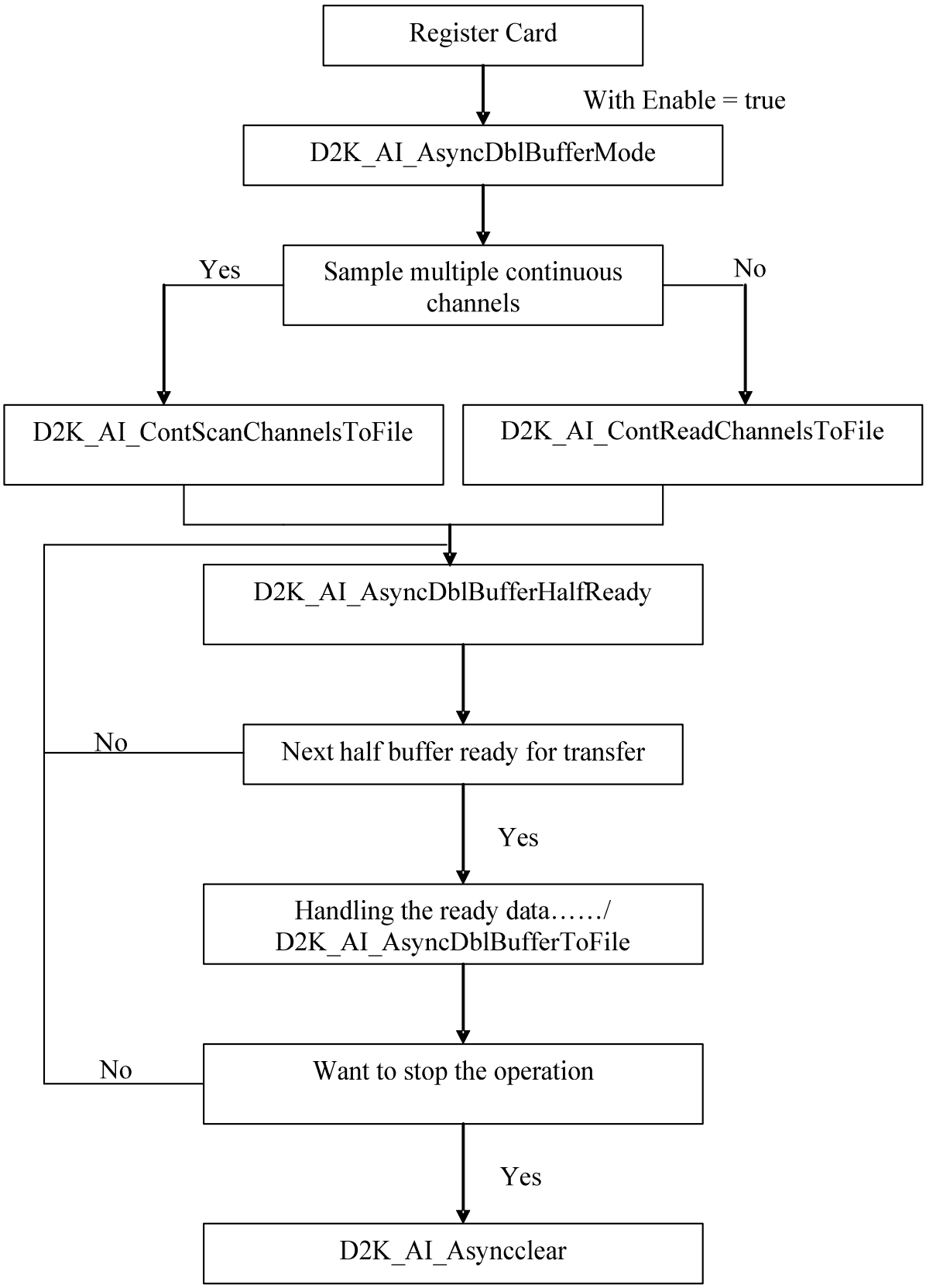


**Figure 6.1 Block diagram for continuous data collection**

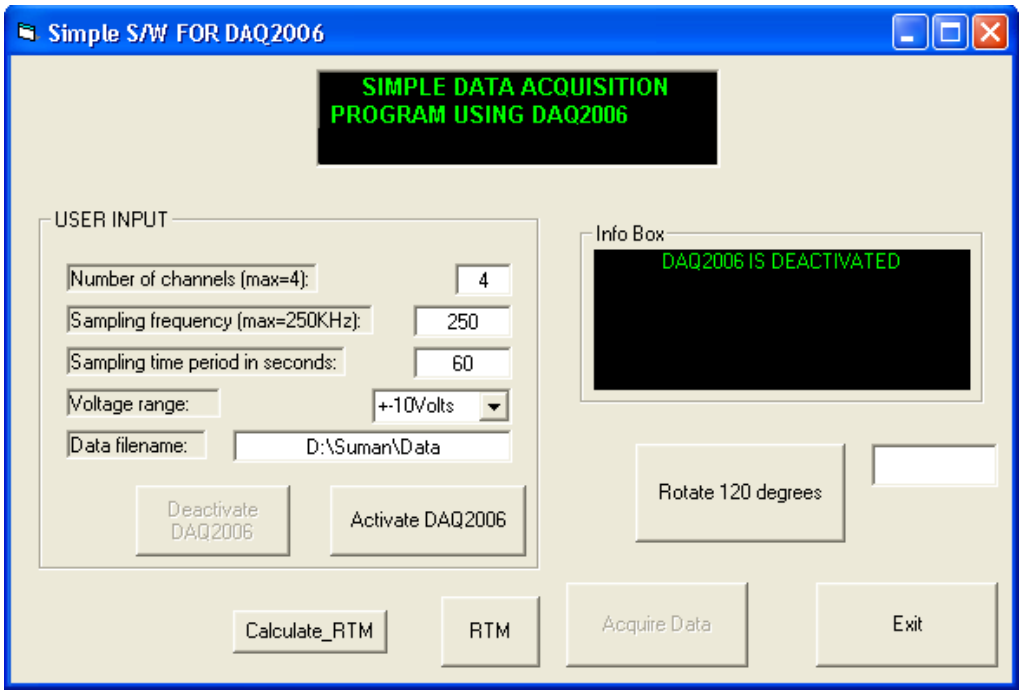


**Figure 6.2 EXE windows for continuous data collection**

Figure 6.2 above shows the execution window for collecting the data, where it is possible to:

1. Input channels: the number of sensors to be scanned; in this case it is either two or four (i.e. software can be used with dual-sensor or four-sensor probes).
2. Sampling frequency: this is the parameter which decides how fast it is necessary to read the signal. The maximum sampling frequency is 250 kHz (for four channels simultaneously). Sampling frequency is chosen depending on the frequency at which the bubbles collide with the probe and the sensor separation. The faster the bubble frequency, the higher the sampling frequency. Also, the smaller the sensor separation, the higher the sampling frequency needed, as described earlier in Chapter 3.
3. Sampling time period: this is the parameter which governs for how long samples are collected. The maximum sampling time period which can be

chosen is 180 seconds; the lower the bubble frequency, the higher the sampling time period needed. The sampling time period is chosen to ensure that at least 30 or more bubbles touch all four sensors of the probe within that period of time.

4. Voltage range: the range of the voltage can be chosen up to ±10 V. There is no particular rule to decide what voltage should be chosen, except that the chosen voltage range must be greater than that of the output voltage from the circuit.
5. Data file name: specifies the directory and path to which the collected data can be saved.

### 6.1.2 Single Bubble Data Collection

This data collection process is similar to that described above in section 6.1.1. The only difference in this method is that there is no sampling time period; instead, a trigger signal was used which was generated by a bubble that hits all four sensors of the probe (see Chapter 5). The trigger signal was used as a mid-trigger on the DAQ 2006 so that it is possible to see the output from the four sensors resulting from this bubble. The mid-trigger signal was also used on the cameras so that the cameras could be used to obtain a reference velocity vector for the same bubble. This process is carried out in order to find the local velocity vector of a single bubble. Thus, the results can be compared with the results obtained from the Continuous Data Collection and can also be used to compare the bubble velocity vector measured by the probe with the velocity vector obtained from high speed cameras (see Chapter 9). Visual C++ was used as a programming language. The basic code format is detailed below and Figure 6.3 shows the block diagram for data collection (for further details see Appendix B):

[Example Code Fragment]

```
card = D2K_Register_Card(DAQ_2006, card_number);

D2K_AI_CH_Config (card, channel, range )

D2K_AI_Config (card, 0, DAQ2K_AI_TRGMOD_PRE|
    DAQ2K_AI_TRGSRC_ExtD| DAQ2K_AI_TrgPositive, 0, 0, 0, 1);

D2K_AI_AsyncDblBufferMode (card, 0); //non-double-buffered AI

D2K_AI_ContBufferSetup (card, ai_buf, data_size, &BufId);

D2K_AI_ContScanChannels (card, channel, BufId, data_size/(channel+1),
    ScanIntrv, SampIntrv, ASYNCH_OP); or

D2K_AI_ContReadChannel(card, channel, BufId, data_size, ScanIntrv,
SampIntrv, ASYNCH_OP)

do { D2K_AI_AsyncCheck(card, &bStopped, &count);

} while (!bStopped);

D2K_AI_AsyncClear(card, &startPos, &count);

D2K_Release_Card(card);
```

The code described here is similar to that described in section 6.1.1 (see section 6.1.1 for a detailed explanation of the code), except in this case the function that allows the external positive trigger signal to be introduced is called “D2K_AI_Config (card, 0, DAQ2K_ AI_TRGMOD_PRE| DAQ2K_AI_TRGSRC_ExtD| DAQ2K_AI_Trg Positive, 0, 0, 0, 1)”.

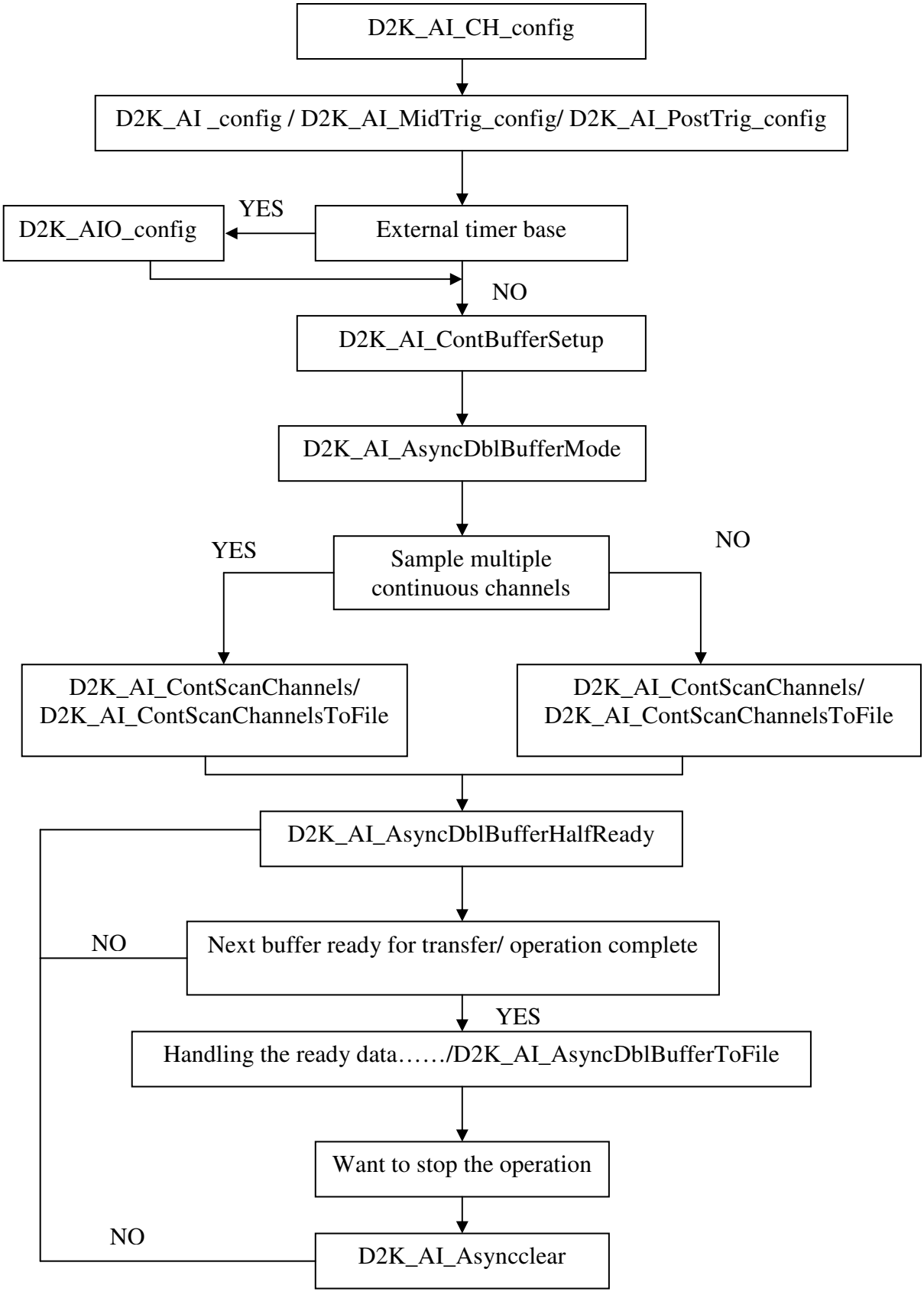


**Figure 6.3 Block diagram for single bubble data collection**

## 6.2 Signal processing for analysis of the collected data

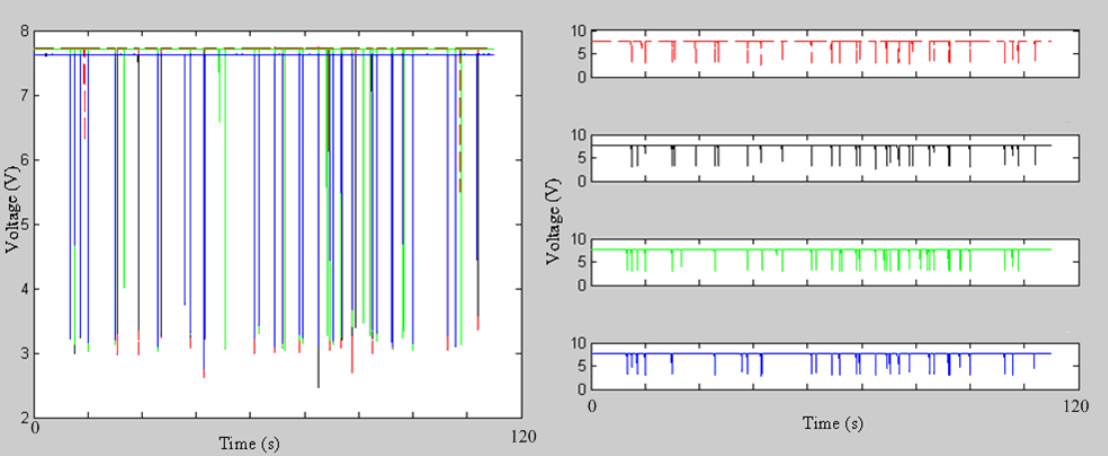


**Figure 6.4 (Left) raw signals from the four-sensor probe over 120 seconds time, (right) raw signal from the individual sensors.**

New signal processing software was written in 'MATLAB' in order to analyse the collected data. Figure 6.4 (left) shows the raw signal from the four sensors during a specific period (0 - 120s) of time and Figure 6.4 (right) shows the extracted raw signals for each sensor. Figure 6.5 show the sensor signals, extracted (40 - 40.1s) from Figure 6.4, for a particular bubble. In order to calculate the bubble velocity vector, it is important that the bubble touches all four sensors on the probe twice without any deformation of the bubble being caused. From Figure 6.5 it can be seen that the signals are different from the ideal signals (Figure 2.29). Using the mathematical model, the time intervals (see Chapter 2) must be calculated from these probe signals.

In some cases it is possible that the bubble only touches some of the sensors. In other cases two different bubbles might hit the probe at approximately the same time. In both these cases it will not be possible to calculate the correct bubble velocity vector.

Therefore, in order to minimize these errors, various signal processing methods were

implemented to extract the required information from the raw signals, as discussed below.

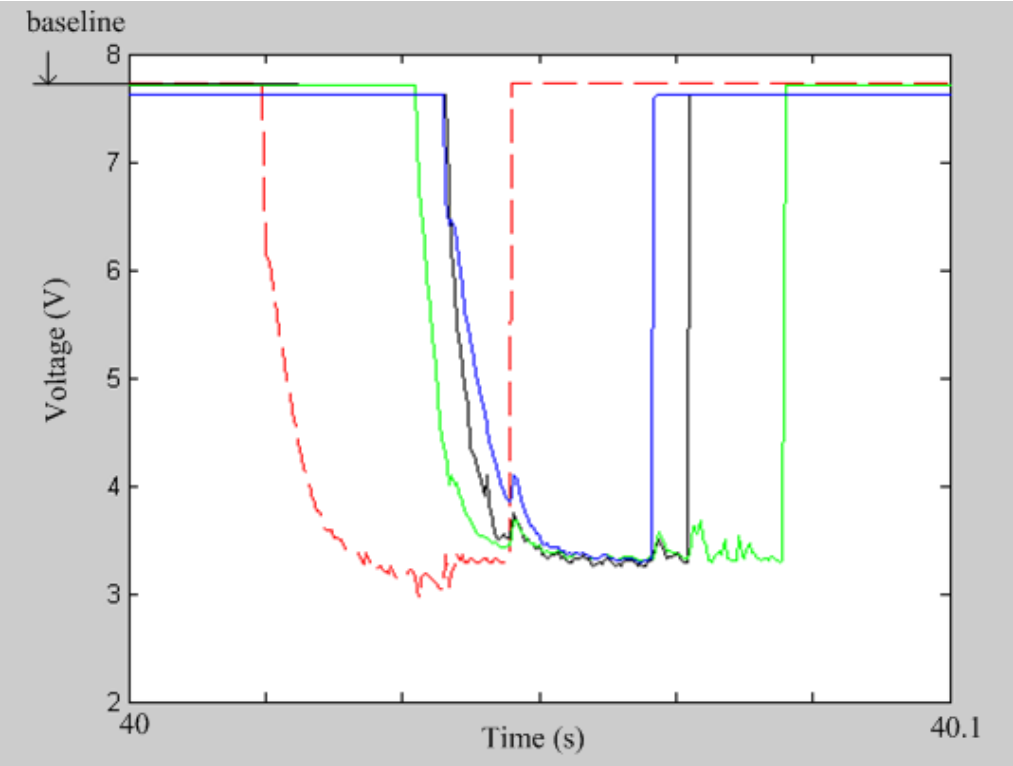


**Figure 6.5 Raw signals from an individual bubble**

### 6.2.1 Evolution of signal processing

Data are collected by the probe with a sampling frequency of 20 - 40 KHz. These data are used to find the relevant time intervals of sensor signals $\delta t_{ia}$ and $\delta t_{ib}$ (where $i$ = 1, 2 and 3, see Equation 2.22 and 2.23 in Chapter 2). For accurate measurement of the velocity vector of the bubble, it is important that the signals (four signals from four sensors) are generated by the same bubble. Therefore, the most important factors for the software to pick up are the falling and rising edges of the sensor signals caused by the same bubble. It is also a requirement that each bubble touches sensor 0 first followed by the three rear sensors. The following signal processing conditions were used to ensure that a group of sensor signals, from which $\delta t_{ia}$ and $\delta t_{ib}$ ($i$ =1, 2 and 3)

were determined, were all produced by the same bubble.

#### 6.2.1.1 Voltage threshold

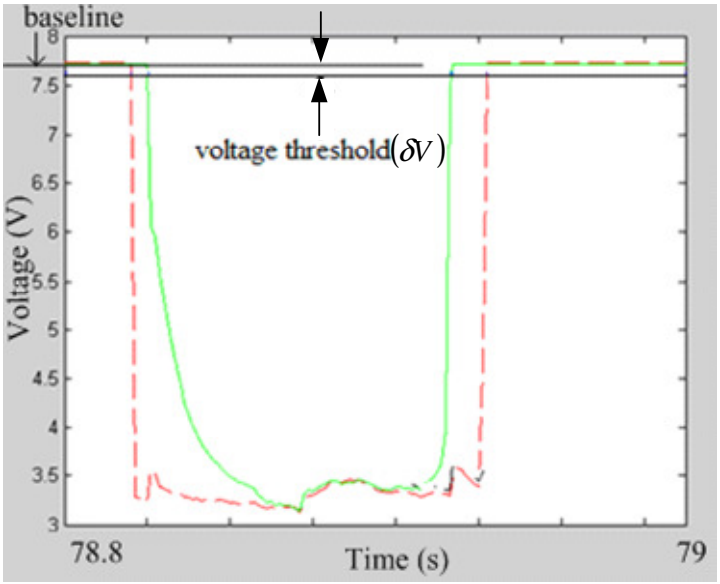


**Figure 6.6 Baseline and voltage threshold for the front sensor signal**

Voltage threshold is a small value of voltage below the baseline (see Figure 6.6) at which the corresponding bubble surface touches the sensor. From the raw signals (Figure 6.5), it can be seen that the rising and falling edges of the signals obtained from each sensor are not purely vertical, as they would be in the case of the ideal signal (see Figure 2.29). Additionally, for each sensor signal, the times at which the signal leaves or rejoins the baseline may not actually represent the contact times between the sensor and the bubble surface. This may be due to a small reduction in the sensor's conductance just before the bubble actually touches the sensor, due to the bubble partially blocking the flow of electrical current through the water from the sensor tip to the earthed probe body. For a similar reason, the sensor conductance may not return to its baseline value until a short time after the bubble has ceased to be in contact with the sensor. In [2], the transient response of a four-sensor probe has been

analysed and it has been shown that the time intervals $\delta t_{ia}$ and $\delta t_{ib}$ ($i$ =1, 2 and 3) are relatively insensitive to the choice of the threshold voltage values.

In order to find the effect of the threshold voltage values on the velocity vector of the bubble, a small experiment was carried out using the camera to film the $z_T$ axis of the tank (see Chapter 7). Two lines separated by a distance of 23mm (in the Z direction) were drawn on the wall of the tank and a high speed camera was used to record the time interval for a given bubble to pass from the first to the second mark. The time interval between successive frames from the camera is equal to 0.004s. Using video processing software, it was possible to count the number of frames it took for a given bubble to pass between the two lines. The mean reference velocity $v_{z,ref}$ in ms$^{-1}$of the bubbles (approximately 5mm in diameter) in the 'Z' direction is then given by

$$v_{z,ref} = \frac{23\times10^{-3}}{\overline{N}_f \times 0.004} \qquad \textbf{Equation 6.1}$$

Where $\overline{N}_f$ is the mean number of frames that the bubble takes to pass between the two lines. The mean value of the bubble velocity in the Z direction was 0.24m/s.

Different threshold voltage values were used to measure the velocity component of the bubble in the Z direction using the probe signals and the mathematical model in Chapter 2 (N.B. this is straightforward when the $z$ axis of the probe coordinate system is in the Z direction, but requires the use of mathematical transformations when the $z$ axis of the probe is inclined with respect to the $z_T$ axis of the tank [4, 11]). The threshold voltage value $\delta V$ was varied from 0.2V to 2.0V for each sensor signal from the respective baseline of each signal. The increment was made in an order of 0.1V. Figure 6.7 shows the velocity of the bubble in the Z direction, as measured by the

probe.

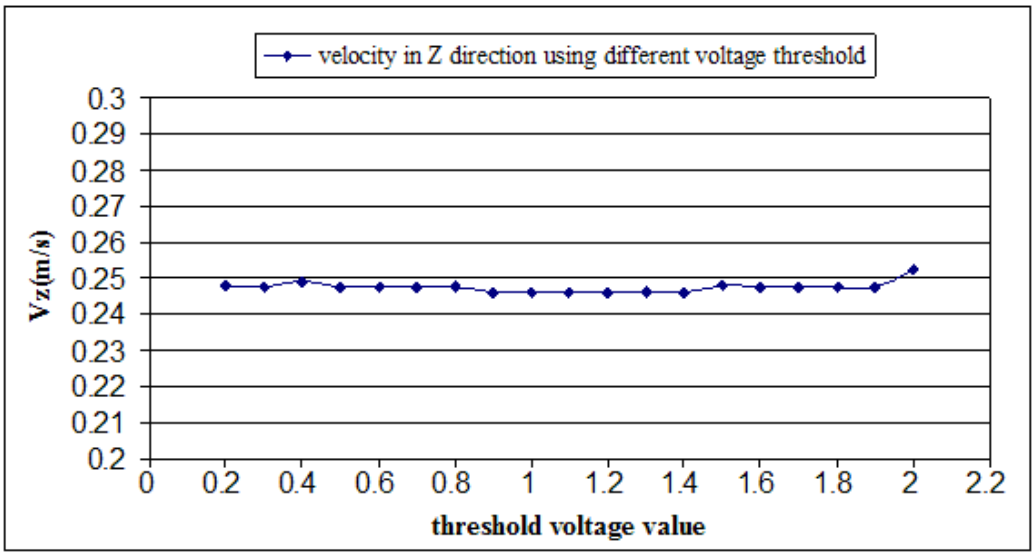


**Figure 6.7 The velocity of the bubble in the Z direction using the different threshold voltage values**

It can be seen from Figure 6.7 that, for the different threshold voltage values, the velocities of the bubbles in the 'Z' direction measured by the probe are very close to the reference value 0.24m/s. In fact, the mean value in Figure 6.7 is 0.248m/s and the standard deviation is 0.00128m/s. Varying the threshold voltage value from 0.2V to 1.5V makes very little difference to the calculated probe velocity in the Z direction. [N.B. another possible method for choosing the threshold voltage is based on a comparison of the mean local volume fraction measured by the probe with the local volume fraction measured using an alternative technique (such as a differential pressure measurement [1])]. From the results shown above, it is believed that the relative insensitivity of the velocity measured by the probe in the Z direction to the choice of threshold voltage is a major advantage of the probing technique described in this project. The voltage threshold value used in this research is 0.3V from the baseline of each signal for all four sensor signals.

#### 6.2.1.2 Ignoring signals with small time intervals and small voltage changes by introducing a time threshold ($t_{thres}$) and voltage level threshold ($V_{l,thres}$) respectively

Most of the probes touch the bubble at its centre and it is important that the bubble touches all four sensors twice. There can, however, be some circumstances when one or two sensors touch only the edge of the bubble, causing confusion during the signal processing. It is more likely that, when the a sensor hits the edge of the bubble, the time interval between the falling and the rising edge for that sensor will be very small as compared to when the sensor hits the centre of the bubble. Such small time intervals will result in a higher velocity, ultimately resulting in an incorrect bubble velocity vector. This effect can be clearly been seen in the signal in the form of a small time interval, as shown in Figure 6.8. Figure 6.8 shows two different signals where the bubble hits all four sensors. The signal on the left shows that one of the sensors hits the edge of the bubble, whereas the signal on the right shows that two sensors hit the edge of the bubble, causing the time interval between the falling edge and rising edge to be very small as compared to the other signal in which the sensors hit the bubble at the centre. Thus, in order to achieve correct results, it is important to delete (ignore) this type of signal which has a small time interval. Therefore, a time threshold ($t_{thres}$) is introduced, which is 0.1 times the average residence time ($t_{res}$) of each signal, within the software to ignore all the signals with a time interval which is less than the time threshold.

$$t_{thres} = 0.1 \frac{\sum t_{res}}{N} \qquad \textbf{Equation 6.1}$$

where N is the total number of bubbles hitting all four sensors.

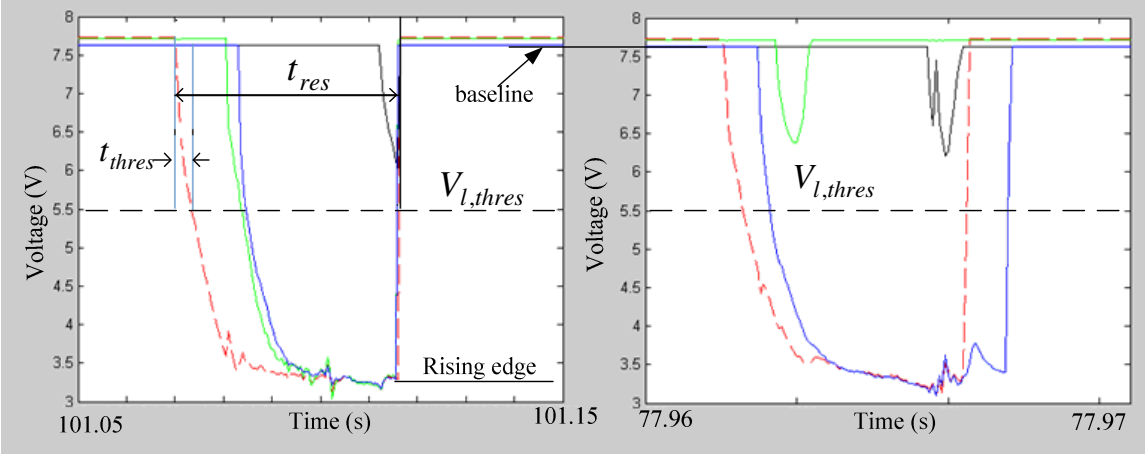


**Figure 6.8 (Left) one sensor hitting the edge of the bubble, (right) two sensors hitting the edge of the bubble**.

In some cases, as shown in Figure 6.8, the voltage drop from the signal associated with a particular sensor is much smaller than for the other three sensors, suggesting that the bubble is only grazing the probe's surface. In order to ignore this type of situation, another voltage level threshold ($V_{l,thres}$) is applied which is normally half of the average voltage level i.e. baseline to the rising edge, as shown in Figure 6.8. The two situations discussed above often happen together.

#### 6.2.1.3 Ignoring bubbles which do not strike all four sensors

It is only possible to measure the bubble velocity vector when the bubble hits all four sensors. It is also important that the bubble hits the first sensor '0' first and only then hits the rear three sensors, but sometimes a signal from only three or less sensors rather than four sensors is achieved, as shown in Figure 6.9 (left). Therefore, in order to ignore such signals, a new dummy time threshold ($t_{dummy}$) is introduced. A dummy time threshold is the average time between the falling edge and the rising edge of the front sensor '0'. Software is used to check if all the falling edges from the three rear

sensors are within $t_{dummy}$, as well as the number of falling edges. If the number of falling edges within $t_{dummy}$ is less or more than three, the signals are ignored.

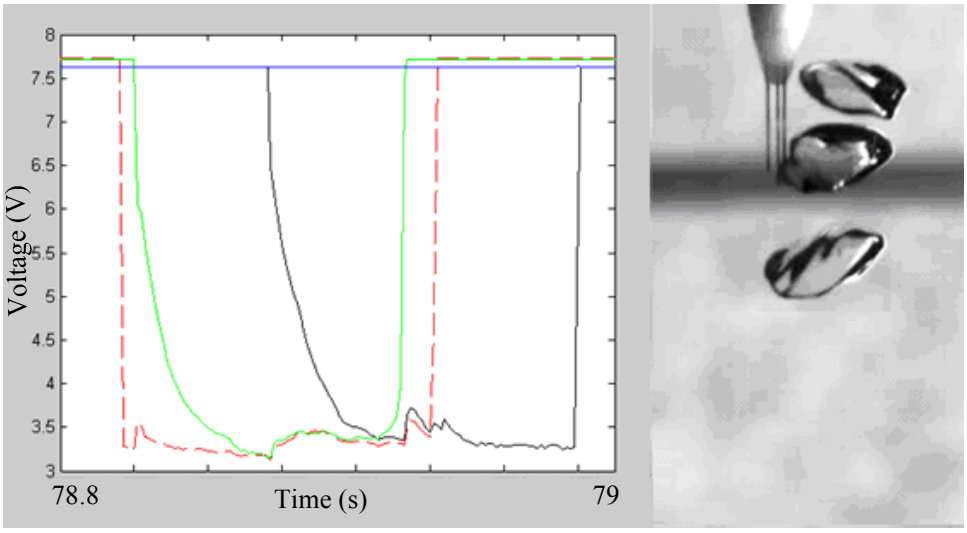


**Figure 6.9 (Left) signal from four-sensor probe with one signal missing (right) image of bubble at three different positions in its trajectory.**

In previous work, Mishra et al. [1] mentioned that if a bubble touches the front sensor of the four-sensor probe first it is more likely that bubble's surface will touch all four sensors twice. However, this depends upon the relative sizes of the frontal area of the probe and the bubble. Consequently, under some circumstances, the bubble's surface will not touch all of the four sensors twice. For example, Figure 6.9 (right) shows the same bubble at three different positions in its trajectory captured by a high speed camera.

In some cases, it is also possible that the first bubble touches front sensor '0' and one or two of the other rear sensors and a second bubble touches the remaining rear sensor. However, if the axial sensor separation between the front sensor '0' and the other three rear sensors is small (normally between 1 to 1.5mm for the probes used in this investigation), it is extremely unlikely that any of the probe's sensors will miss

the bubble.

### 6.2.2 Calculations of polar angle $\alpha$ and azimuthal angle $\beta$ and velocity magnitude $v$

After the signal processing and extraction of the valid signals from the invalid ones, $\delta t_{ii}$ for the individual bubbles are calculated. With the collected $\delta t_{ii}$ values and the measured probe dimensions $x_i, y_i, z_i$ (where $x_i, y_i, z_i$ are the probe coordinates of the rear sensors with respect to the front sensor, which are measured using a digital microscope, see Chapter 4.2) it is possible to calculate the azimuthal angle $\beta$ by using Equation 2.39, polar angle $\alpha$ by using Equation 2.40 and, once $\alpha$ and $\beta$ are found, it is possible to find the velocity magnitude $v$ by using any of these three Equations 2.36-2.38. However, this procedure is somewhat complicated and the process of calculating $\alpha$ and $\beta$ is described in detail in section 2.5.1.

Before calculating $\alpha$ and $\beta$ the following steps are carried out:-

Step 1:- Call the stored data collected by DAQ2006.

Step 2: - Check if the data contains all four signals or not (visual check)

Step 3:- Introduce voltage threshold (section 6.2.1.1)

Step 4: - Calculate $\delta t_{ii}$

Step 5: - Check if the signals are for the same bubbles or not, i.e. falling edge of the rear three sensors should be in between the falling and rising edge of the signal from front sensor '0', by introducing dummy time threshold $t_{dummy}$ (section 6.2.1.3).

Step 6: - Ignore the signals which contain signals from different bubbles and those missing signals from the bubble (section 6.2.1.3).

Step 7: - Ignore the signals with a small time interval by introducing time threshold $t_{thres}$ (section 6.2.1.2).

Step 8: - Ignore the signals with a small voltage by introducing voltage level threshold $V_{thres}$ (section 6.2.1.2).

Step 9: - Check if any signals remain.

Step 10:- Calculate $\alpha$ and $\beta$

Figure 6.10 shows the steps and the signal process used in this research, in the block diagram. From the figure, it can be seen that polar angle $\alpha$ and azimuthal angle $\beta$ are calculated in two ways, which are described below.

#### 6.2.2.1 Averaging individual $\alpha$ and $\beta$

In this process, $\alpha$ and $\beta$ of the individual bubbles are calculated as described in section 2.5.1 and the average is calculated as a mean $\alpha$ and $\beta$ .

#### 6.2.2.2 Calculation of $\alpha$ and $\beta$ by Average of $\delta t_{ii}$

In this process, first the collected $\delta t_{ii}$ are averaged and from the averaged $\delta t_{ii}$ $\alpha$ and $\beta$ are calculated as in section 2.5.1 using Equations 2.48 and 2.47.

The results of both the above conditions are described in detail in Chapter 10. The block diagram below shows the signal processing scheme, as discussed above.

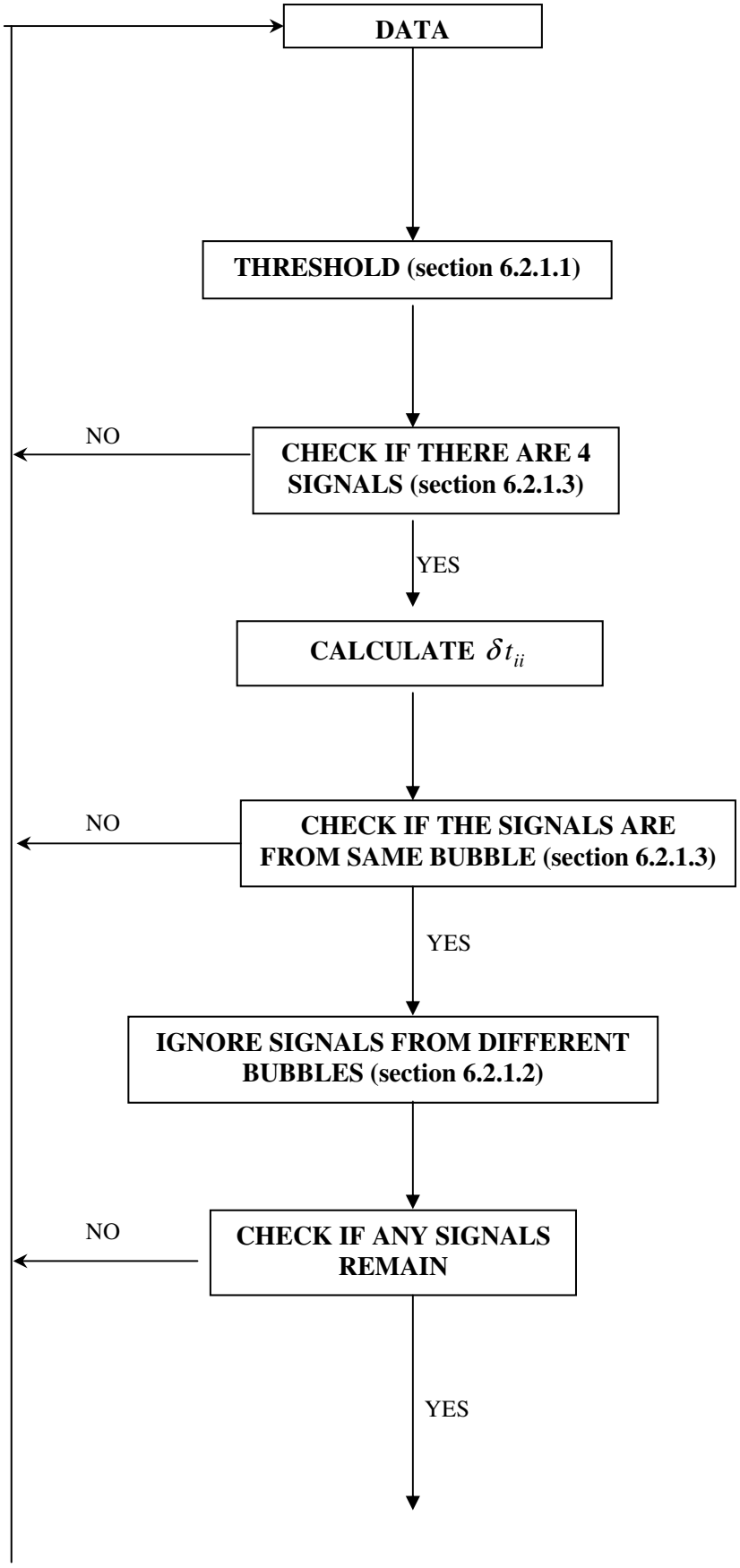
DATA
THRESHOLD (section 6.2.1.1)
NO
CHECK IF THERE ARE 4 SIGNALS (section 6.2.1.3)
YES
CALCULATE $\delta t_{ii}$
NO
CHECK IF THE SIGNALS ARE FROM SAME BUBBLE (section 6.2.1.3)
YES
IGNORE SIGNALS FROM DIFFERENT BUBBLES (section 6.2.1.2)
NO
CHECK IF ANY SIGNALS REMAIN
YES

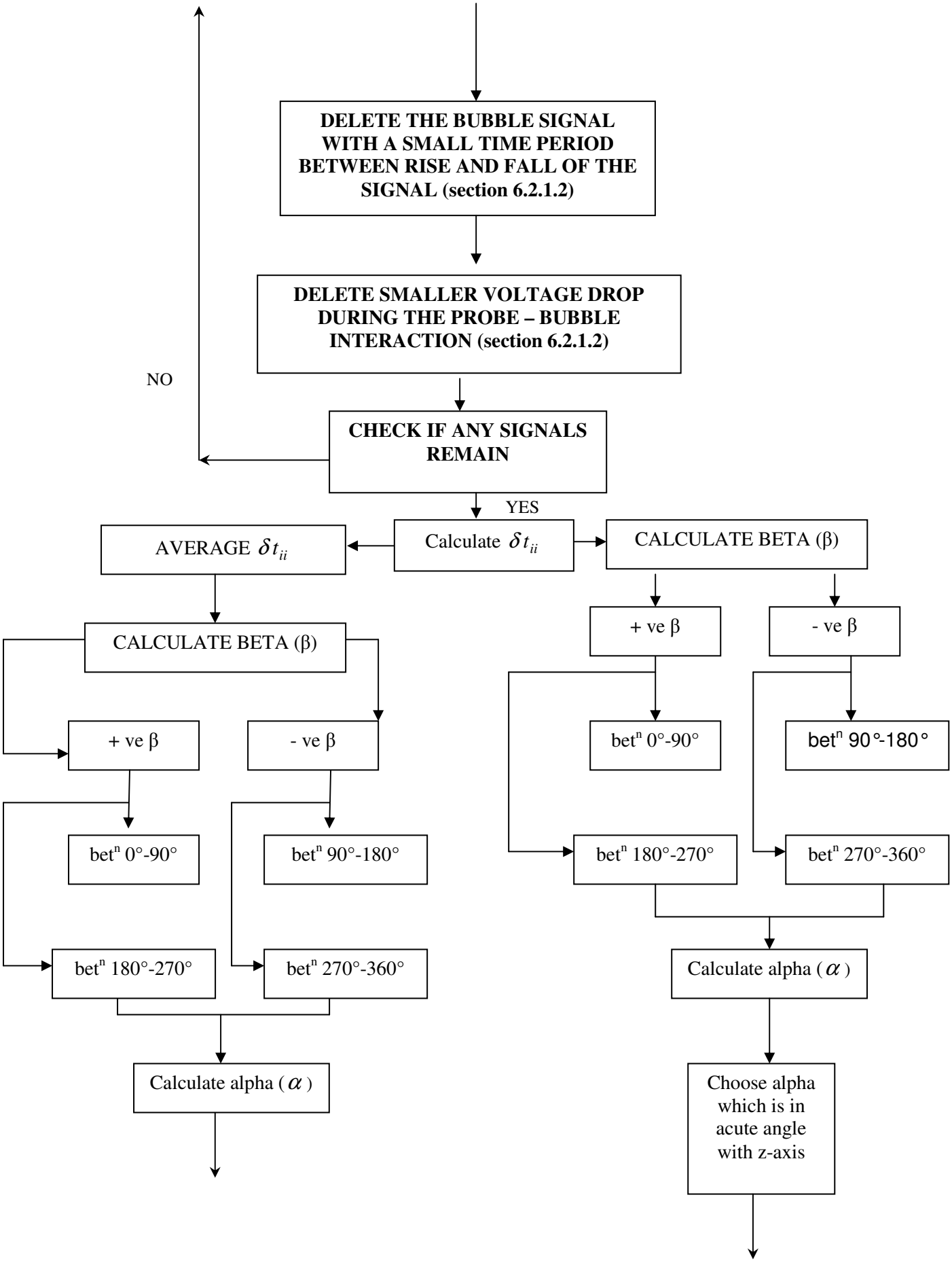
DELETE THE BUBBLE SIGNAL WITH A SMALL TIME PERIOD BETWEEN RISE AND FALL OF THE SIGNAL (section 6.2.1.2)
DELETE SMALLER VOLTAGE DROP DURING THE PROBE – BUBBLE INTERACTION (section 6.2.1.2)
NO
CHECK IF ANY SIGNALS REMAIN
YES
Calculate $\delta t_{ii}$
AVERAGE $\delta t_{ii}$
CALCULATE BETA (β)
CALCULATE BETA (β)
+ ve β
- ve β
+ ve β
- ve β
bet^n 0°-90°
bet^n 90°-180°
bet^n 0°-90°
bet^n 90°-180°
bet^n 180°-270°
bet^n 270°-360°
bet^n 180°-270°
bet^n 270°-360°
Calculate alpha ( $\alpha$ )
Calculate alpha ( $\alpha$ )
Choose alpha which is in acute angle with z-axis

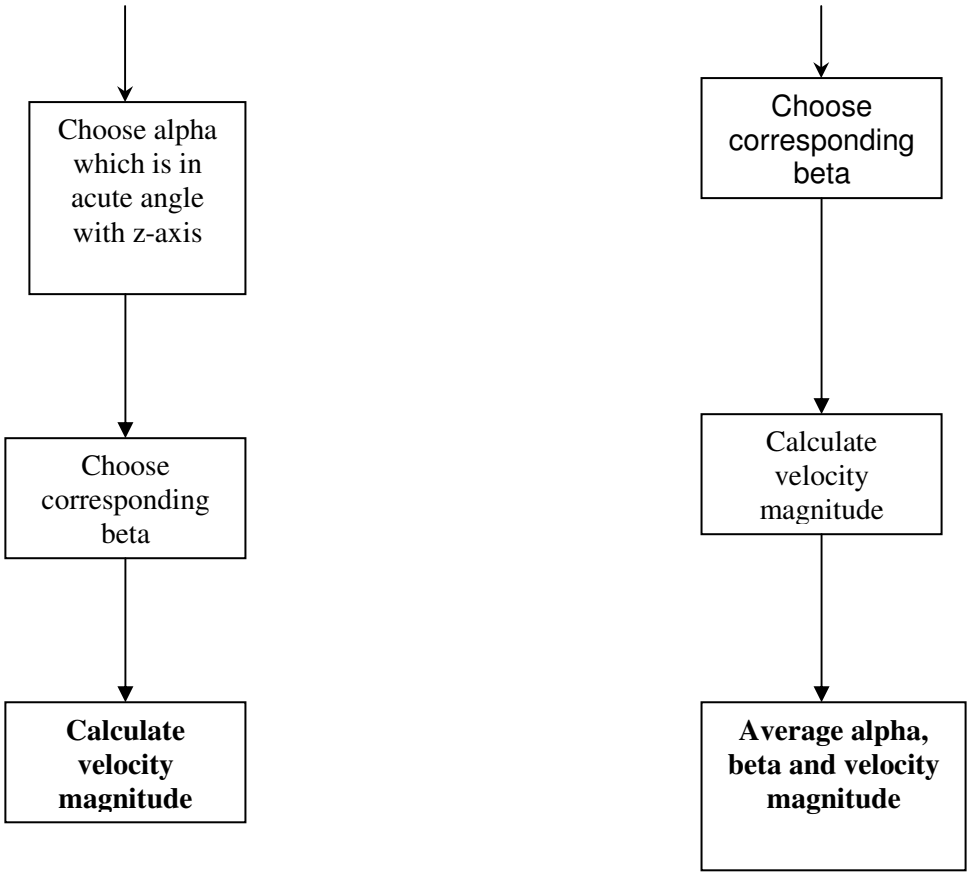


**Figure 6.10 Block diagram for signal processing and calculating $\alpha$ and $\beta$ from the collected data**

# CHAPTER 7

## Image Processing

### 7.1 Introduction

In this chapter, a model is described which enables the reference velocity vector of an individual bubble, relative to the coordinate system ($x_T, y_T, z_T$) of the tank, to be determined from images taken by two orthogonal high speed cameras, as shown in Figure 7.1. The images were captured by both the cameras simultaneously at a speed of 250 frames per second.

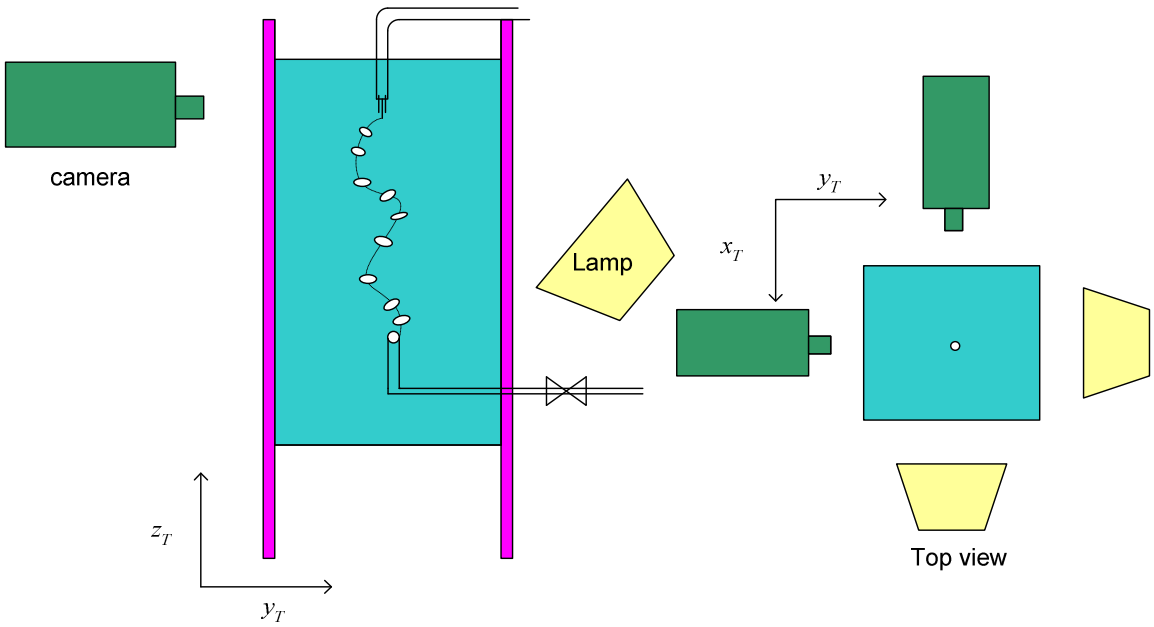


**Figure 7.1 Experimental set up for the tank experiments**

The aim of using high speed cameras was to compare the velocity vector calculated by the probe with the velocity vector calculated by the cameras. Therefore, it is important that the data collected by DAQ 2006 was from the same bubble as that captured by the cameras.

In order to ensure the cameras capture the same bubble that hits all four sensors of the probe, the trigger system described in Chapter 5 was used to capture images from the cameras as well as capturing data from the probe via DAQ 2006. The mid-trigger system was used to trigger both the cameras and DAQ 2006. The mid- trigger stops the cameras recording shortly after receiving the trigger and allows 20 frames of captured images to be saved before and after receiving the trigger (21 frames with the trigger signal i.e. 10 frames before and after the trigger signal is received by each camera). The same trigger was also used to stop the DAQ 2006 collecting data.

## 7.2 Synchronizing the cameras

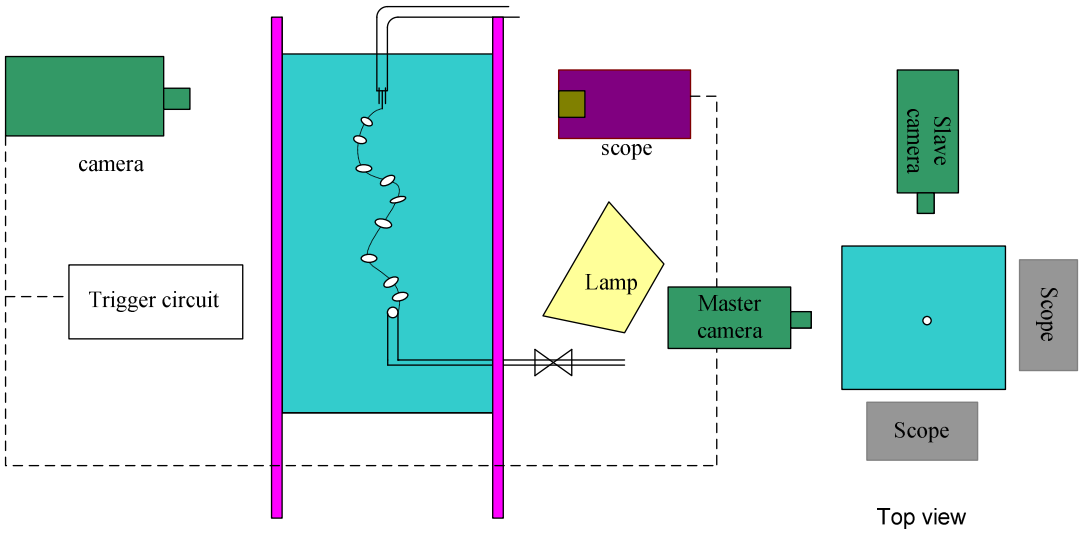


**Figure 7.2 Camera set up with the oscilloscope**

During the processing of the captured images, it was found that the cameras have a delay in their trigger time i.e. the trigger signal received by the first camera was at the $10^{th}$ frame and the second camera received the same trigger at the $11^{th}$ frame, out of 21 saved frames. To avoid errors in calculating the velocity vector when using the cameras, it is important to know which frame from each camera captures a picture of the bubble at the same instance in time. Any differences in the timing of the images

from each camera will cause errors in the calculated reference bubble velocity vector obtained from the cameras.

Thus, to avoid any miscalculation, a pair of analogue oscilloscopes was placed in front of each camera, as shown in Figure 7.2. Both the cameras were synchronized by the inbuilt function 'master' and 'slave', so that both could be controlled by the master camera. All the cameras and the scopes were given the trigger signal, which stops the cameras, and in the meantime the scopes indicate the trigger signal voltage level.

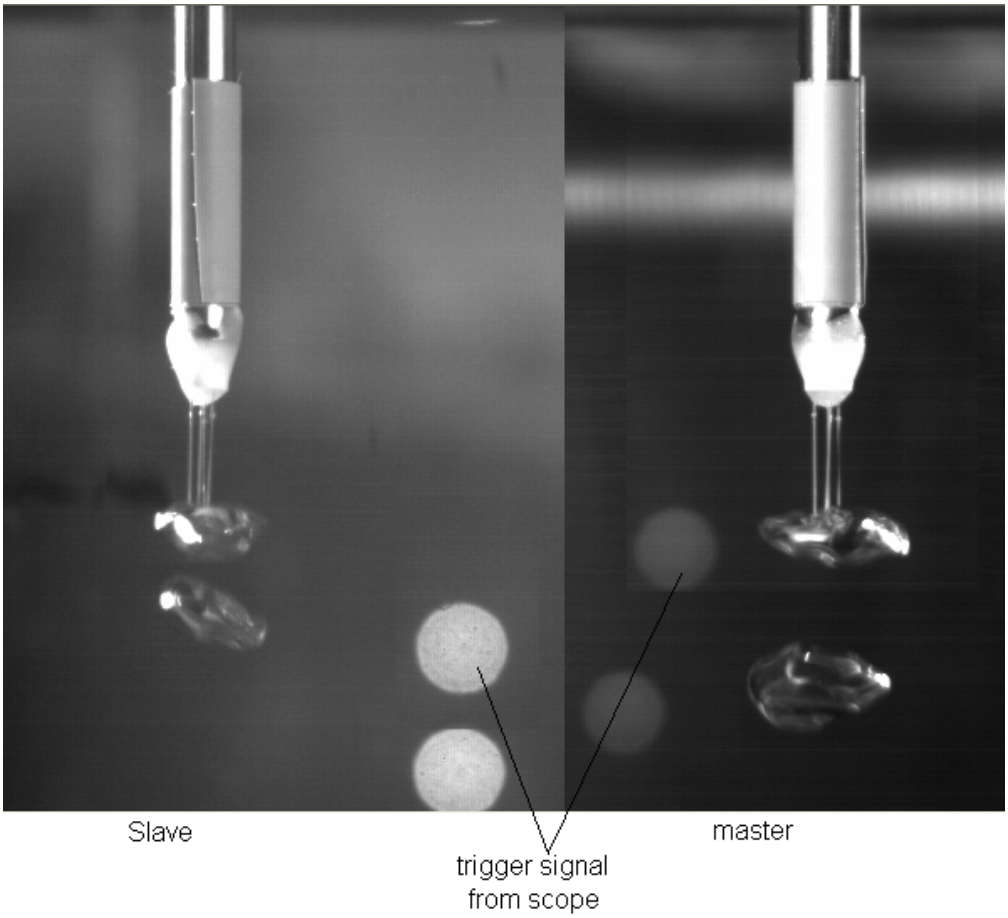


**Figure 7.3 Two consecutive frames from 'slave' (left) and 'master' (right) cameras with trigger signal from the scope in the background. The two white dots are the trigger signal on the oscilloscope; the lower positioned dot means the trigger signal has not yet been received. The higher dot means the trigger signal has been received.**

With regard to the above system, when capturing the images, the cameras will depict the bubble that strikes all four sensors of the probe. Since the trigger signal is generated by a bubble which hits all four sensors and is connected to both the cameras, as well as to the scopes, the cameras will also capture the trigger signal displayed on the scopes, as shown in Figure 7.3. On the left hand side of Figure 7.3, two consecutive frames from the 'slave' camera are shown, where the two white dots are the trigger signal on the oscilloscope. It can be seen that the trigger level stays low until the bubble hits all four sensors. A similar situation can be seen in the figure on the right hand side (from the 'master' camera). Therefore, from these displayed trigger level signals, the correct frame corresponding to the moment at which the bubble hits all four sensors can be obtained from both cameras. Any time delay between the two cameras can be eliminated by counting from the frame where the trigger signal first rises, as seen by each camera.

In order to process these images, ten frames from either side of the trigger signal were saved from both of the cameras. Thus, the captured images are processed according to the model described below.

The model described below enables mathematical expressions to be obtained for the shape of a given bubble. Although the model is able to provide a reference velocity for any part of the bubble (e.g. the geometric centre of the upper or lower surface and the centre of gravity), it was subsequently found that, due to oscillations of the bubble's surface, the most reliable reference velocity was that of the centre of gravity (COG) of the bubble.

The analysis presented in this section is applied to images taken by the 'master' camera, which is orthogonal to the $x_T, z_T$ plane of the tank coordinate system, and by

the 'slave' camera which is orthogonal to the $y_T, z_T$ plane of the tank coordinate system (see Figures 7.1 and 7.2).

The camera images were pre-processed using MATLAB software, as described step by step below:

1 Extract the individual frame from the saved images.
2 Extract the first frame.
3 Convert the frame to 'grayscale' from 'RGB' image (combined Red, Green and Blue).
4 Introduce the edge detection function for the clear visualization of the bubble (see Figure 7.4).
5 Identify the coordinate of every black dot at the border of the bubble. These points are defined as the edge of the bubble.
6 From the above identified coordinate points, the major axis of the bubble is calculated, which is the longest distance between any two points in the border. This calculation was performed automatically in MATLAB, where the distance between every pair of points on the border was calculated and the coordinates of the points with the longest distance between them is picked. These points are identified as $(x_1, z_1)$ and $(x_2, z_2)$ in the $x_T - z_T$ plane (master camera) as the major axis of the particular bubble, as shown in Figure 7.4.
7 The centre of gravity (COG) of the bubble is defined as the centre of the major axis, which is defined as $(x_c, z_c)$, as shown in Figure 7.4.

A similar process for the other frames of the same bubble is carried out. The above

mentioned process is also conducted for the images captured by the camera placed in the $y_T - z_T$ plane (slave camera). In the next section, an analysis of a bubble image from the master camera is described in detail. A similar analysis of the bubble image from the slave camera was undertaken.

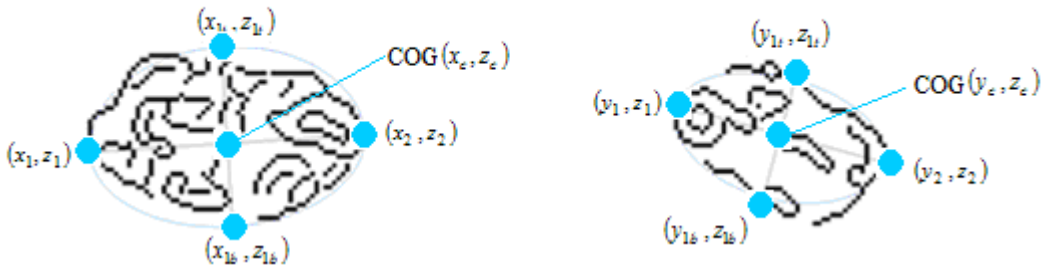


**Figure 7.4 Frames from $x_T - z_T$ plane on the left and $y_T - z_T$ plane on the right from the cameras after image processing**

## 7.3 Theory behind image processing

It is assumed that the bubble image from the master camera (orthogonal to the $x_T, z_T$ plane) is in the shape of two semi-ellipses with a common major axis of length $a_T$ (see Figure 7.5). The bubble centre of gravity (COG) is at the centre of this major axis, which is assumed to be the longest possible chord between any two boundary points of the bubble. Assume that points $(x_1, z_1)$ and $(x_2, z_2)$ represent the end points of the major axis. The bubble centre of gravity then has coordinates $(x_c, z_c)$ where

$$(x_c, z_c) = \frac{(x_2 - x_1)}{2}, \frac{(z_2 - z_1)}{2} \qquad \textbf{Equation 7.1}$$

The slope $m_1$ of the major axis is given by

$$m_1 = \frac{(z_2 - z_1)}{(x_2 - x_1)}$$ **Equation 7.2**

The slope $m_2$ of the minor axis of the semi-ellipse that forms the top half of the bubble is obtained from the relationship $m_1 m_2 = -1$. From this calculated value of $m_2$, it is now possible to initially assume that the semi-ellipse defining the top half of the bubble passes through point $\mu$ where the coordinates of $\mu$ are the intersection of the line of slope $m_2$ (which passes through the centre of the major axis) and the upper boundary of the bubble image. From the coordinates of $\mu$ it is now possible to make an initial guess of the length $b_T$ of the minor axis for the semi-ellipse defining the top of the bubble.

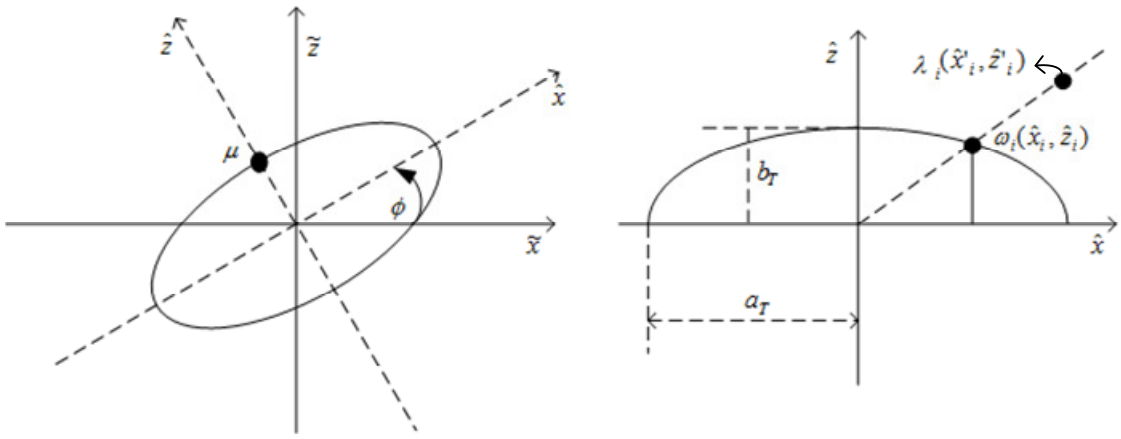


**Figure 7.5 Coordinate systems and notations used in processing the bubble images for the cameras.**

At this stage, it is helpful to define a new coordinate system $(\tilde{x}, \tilde{z})$ such that $\tilde{x} = x - x_c$ and $\tilde{z} = z - z_c$ (see Figure 7.5). Suppose that the major axis of the ellipse makes an angle $\phi$ with the increasing $\tilde{x}$ axis, as shown in Figure 7.5 [NB: $\phi$ is measured anticlockwise relative to the increasing $\tilde{x}$ axis). Another new coordinate

system $(\hat{x},\hat{z})$ may be defined such that $\hat{x} = \tilde{x}\cos\phi + \tilde{z}\sin\phi$ and $\hat{z} = -\tilde{x}\sin\phi + \tilde{z}\cos\phi$. In the $(\hat{x},\hat{z})$ coordinate system, the equation for the initial guess of the semi-ellipse forming the top half of the bubble is (for positive $\hat{z}$ only)

$$\frac{\hat{x}^2}{{a_T}^2} + \frac{\hat{z}^2}{{b_T}^2} = 1 \qquad \textbf{Equation 7.3}$$

The curve of the semi-ellipse created from Equation 7.3 is not necessarily the best fit for the boundary points for the top half of the bubble image obtained from the master camera, so it is necessary to use least squares curve-fitting to minimize the distance of the boundary points in the bubble image from the calculated bubble boundary. This curve-fitting is carried out in the $\hat{x},\hat{z}$ coordinate system, where the origin is at the COG of the bubble, where the $\hat{x}$ axis coincides with the bubble major axis and where the $\hat{z}$ axis coincides with the minor axis of the top part of the bubble. Let us define a point $\omega_i$ with coordinates $(\hat{x}_i, \hat{z}_i)$ which lie on the boundary of the upper part of the image of the bubble (Figure 7.5). A line may also be defined with gradient $\hat{m}_i$ from the COG of the ellipse to $\omega_i$. This line intersects the boundary of the calculated ellipse at point $\lambda_i$ with coordinates $(\hat{x}'_i, \hat{z}'_i)$ (Figure 7.5). $\hat{x}'_i$ and $\hat{z}'_i$ may be calculated as follows. Equation 7.4 gives

$$\left(\frac{{\hat{x}'_i}^2}{{a_T}^2}\right) + \left(\frac{{\hat{z}'_i}^2}{{b_T}^2}\right) = 1 \qquad \textbf{Equation 7.4}$$

But there is also the relationship that $\hat{z}'_i = \hat{m}_i \hat{x}'_i$ which gives

$$\hat{x}'_i = \sqrt{\frac{{a_T}^2 {b_T}^2}{({b_T}^2 + {\hat{m}_i}^2 {a_T}^2)}}$$

and

$$\hat{z}'_i = m_i \sqrt{\frac{a_T{}^2 b_T{}^2}{(b_T{}^2 + \hat{m}_i{}^2 a_T{}^2)}} \qquad \textbf{Equation 7.5}$$

The distance from the COG to $\lambda_i$ is $s_i$ and the distance from the COG to $\omega_i$ is $r_i$

where $r_i = \sqrt{(\hat{x}_i)^2 + (\hat{z}_i)^2}$ and $s_i = \sqrt{(\hat{x}'_i)^2 + (\hat{z}'_i)^2}$ **Equation 7.6**

An error term $\varepsilon_i$ may be defined such that $\varepsilon_i = (s_i - r_i)^2$ **Equation 7.7**

A total error term $\varepsilon$ can now be defined such that $\varepsilon = \sum_{i=1}^{N} \varepsilon_i$ **Equation 7.8**

where $N$ is the number of individual points (pixels) on the upper part of the bubble boundary in the image from the master camera. Equation 7.8 is used to calculate $\varepsilon$ for different values of $b_T$. By minimising $\varepsilon$, the best value for $b_T$ can be found, which is the length of the minor axis of the semi-ellipse, which defines the upper part of the bubble boundary in the image from the master camera. A similar procedure is followed to find the best value for $b_B$, the length of the minor axis of the semi-ellipse for the bottom part of the bubble image from the master camera. The whole procedure is then repeated for the image from the slave camera. Once optimum values for the major and minor axes of all of the relevant semi-ellipses have been found, the appropriate ellipse equations are transformed back into the $(x_T, y_T, z_T)$ coordinate system.

For successive images of the bubble from the master camera, separated by a time interval $\delta t$, it is possible to calculate bubble velocity components $v_{xT}$ and $v_{zT,1}$

where

$$v_{xT} = \frac{\delta x_T}{\delta t}$$ **Equation 7.9**

and

$$v_{zT,1} = \frac{\delta z_{T1}}{\delta t}$$ **Equation 7.10**

where $\delta x_T$ and $\delta z_{T1}$ are the displacements of the bubble COG in the $x_T$ and $z_T$ directions respectively, as viewed by the master camera. Similarly, for the slave camera, it is possible to define bubble velocity components $v_{yT}$ and $v_{zT,2}$ where

$$v_{yT} = \frac{\delta y_T}{\delta t}$$ **Equation 7.11**

and

$$v_{zT,2} = \frac{\delta z_{T2}}{\delta t}$$ **Equation 7.12**

A reference bubble velocity vector $\mathbf{V_{bt}}$ obtained using both the master camera and slave camera can now be defined relative to the tank where

$$\mathbf{V_{bt}} = v_{xT}\mathbf{i}_T + v_{yT}\mathbf{j}_T + v_{zT}\mathbf{k}_T$$ **Equation 7.13**

and where $v_{zT} = \frac{(v_{zT,1} + v_{zT,2})}{2}$ **Equation 7.14**

and $\mathbf{i}_T, \mathbf{j}_T$ **and** $\mathbf{k}_T$ are unit vectors parallel to the $x_T, y_T$ and $z_T$ direction

respectively.

The reference bubble velocity vector $\mathbf{V_{bt}}$ (measured using cameras 1 and 2) enables a comparison with the bubble velocity vector relative to the tank, as measured by the four-sensor probe $\mathbf{V_{btp}}$, as described in the next chapter. To compare the velocity vector measured by the four-sensor probe, the reference bubble velocity vector $\mathbf{V_{bt}}$ of the bubble crossing the probe was calculated for each experiment presented in Chapter 9.

## 7.4 Calibration of cameras

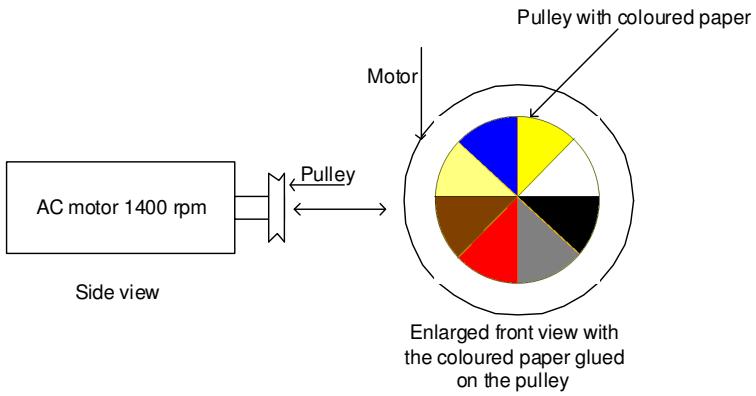


**Figure 7.6 Disc for calibrating the cameras**

Even though the factory specification stated that the frame rate of the camera is 250 frames per second, to maximise the precision of the calculation of the velocity vector of the bubble, it was decided that the cameras should be calibrated to determine the actual frame rates of the cameras. The calibration was carried out using a coloured circle attached to a pulley and the pulley itself was directly coupled onto the shaft of an AC motor rated 1400 rpm, as shown in Figure 7.6.

The image of the coloured paper was captured by both the cameras with the motor rotating at its full speed. The rotational speed of the disk was measured by a

tachometer, and found to be 1400 rpm, i.e. 70 revolutions in three seconds (three seconds was chosen for simplicity, as one second makes 23.3 revolutions and the decimal place adds an unnecessary complication). The images captured from both cameras were extracted with software called 'Virtual Dub'. The software also allows the extracted images to be counted frame by frame. Thus, numbers of frames were counted while the coloured disc made 70 full rotations. The number of frames was found to be 738. These counted frames give the actual frame rate for the camera. Therefore, the calibrated frame rate of the camera is 246 per second for both the cameras (738 is the frame rate for three seconds). Hence, the actual time interval for each frame is 0.0041 seconds.

# CHAPTER 8

# Bench Test Rig Experimental Set Up

## 8.1 Relationship between the probe and tank coordinates

### 8.1.1 Positioning the probe to vary the velocity vector of the bubbles relative to the probe for a purely vertical bubble air-water flow.

The origin of the probe coordinate system (see Figure 2.18) defined by Lucas et al.[1] for the four-sensor probe corresponds with the position of the lead sensor, with the $z$-axis parallel to the axis of the probe where this is vertically mounted. The $x$ and $y$ axes are orthogonal to each other and to the $z$-axis, and are parallel with the top of the probe holder.

The spatial locations of rear sensors 1, 2 and 3 can be defined using this probe coordinate system. Suppose that an approaching bubble has velocity vector $\mathbf{V}$, relative to the probe coordinate system, as shown in Figure 2.18. $\mathbf{V}$ makes a polar angle $\alpha$ with respect to the $z$-axis. Furthermore, the projection of $\mathbf{V}$ onto the x-y plane gives rise to a line that makes an azimuthal angle $\beta$ to the $y$-axis (in the direction shown in Figure 2.18). According to the theory outlined in section 2.5 and Lucas et al. [1], in order to determine the effectiveness of the four-sensor probe in measuring the velocity vector $\mathbf{V}$ of a bubble, it is necessary to subject the probe to bubbles approaching with a wide range of values of $\mathbf{V}$. Since it is not practical to change the direction of the air bubbles, it becomes necessary that the position of a probe can be rotated or tilted. One way to change the probe's position is to mount it

horizontally at the top of the column on a hinged platform, as shown in Figure 8.1. The hinged platform is able to tilt and rotate the probe, making it possible to change the direction of $\mathbf{V}$ relative to the probe coordinate system, as described below.

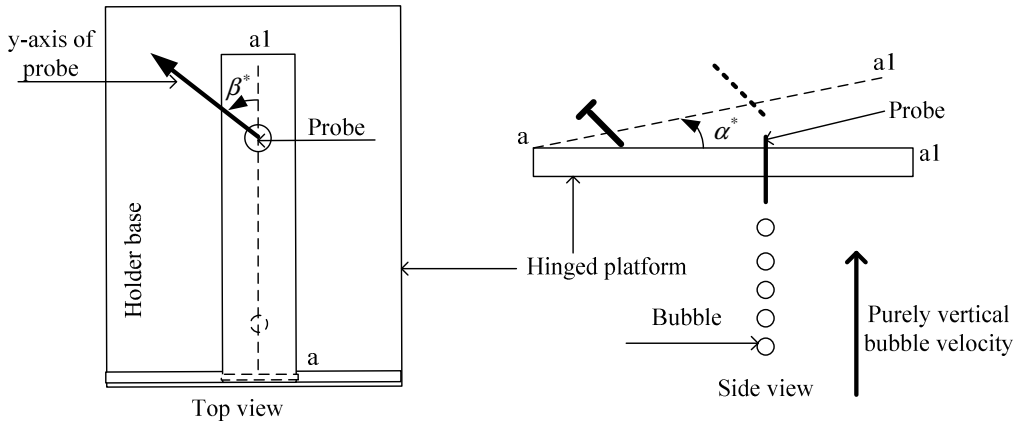


**Figure 8.1 Schematic of how the probe is moved in order to the change the vector velocity of bubbles relative to the probe.**

According to the theory outlined by Pradhan et al. [13], the $y$-axis of the probe coordinate system is parallel with the centreline a-a1 of the hinged platform, with the increasing $y$-axis in the direction from a to a1, when using a four-sensor probe mounted horizontally on a hinged platform at the top of the column. As the hinged platform is rotated through angle $\alpha^*$ (in the direction shown in Figure 8.1), the velocity vector $\mathbf{V}$ of the approaching bubbles will now make a polar angle $\alpha$ relative to the $z$-axis of the probe where $\alpha = \alpha^*$. If the $y$-axis of the probe coordinate system is now rotated counter clockwise (as viewed from above) through an angle $\beta^*$ relative to the line a-a1, the projection of the velocity vector $\mathbf{V}$ (of the bubbles approaching the probe) onto the x-y plane will make an azimuthal angle $\beta$ relative to the $y$-axis where $\beta = \beta^*$. By varying the angles $\alpha^*$ and $\beta^*$, the direction of $\mathbf{V}$ relative to the probe coordinate system can be varied for the purposes of testing or

calibrating a four-sensor probe. The magnitude $v$ of the bubble velocity vector cannot easily be changed, since this is a function of the rise velocity of air bubbles through stationary water; however, small variations in $v$ could be achieved by varying the size of the air bubbles via manipulation of the air injection system.

In the present investigation, reference measurement of the inclination angle $\alpha^*$ of the hinged platform was made using an inclinometer. Reference measurement of angle $\beta^*$ was made using a simple protractor system.

### 8.1.2 Transformation of the Bubble Velocity Vector measured by the probe into the Tank Coordinate System for the bubble where the rise velocity is not purely vertical.

In order to investigate the accuracy of the four-sensor probe (described in section 2.5) which can measure the bubble velocity vector, a series of experiments were carried out in which the probe coordinate system is orientated at different angles relative to an approaching stream of bubbles and, hence, makes different angles relative to the tank coordinate system [11]. Initially assume that the $x, y, z$ axes of the probe coordinate system are respectively parallel to the $x_T, y_T, z_T$ axes of the tank coordinate system. Let the probe be rotated through an angle $\alpha^*$ about the $x$-axis and $\beta^*$ about the $z$-axis, as described in section 8.1.1.

Therefore, a new direction of the probe $x$-axis in the tank coordinate system is given by $\mathbf{i}_T \cos\beta^*$ in $x_T$ direction, $\mathbf{j}_T \sin\beta^* \cos\alpha^*$ in $y_T$ direction and $\mathbf{k}_T \sin\beta^* \sin\alpha^*$ in $z_T$ direction.

Similarly, the new direction of the probe in $y$-axis in the tank coordinate system is given by $-\mathbf{i}_T \sin\beta^*$ in $x_T$ direction, $\mathbf{j}_T \cos\beta^* \cos\alpha^*$ in $y_T$ direction and $\mathbf{k}_T \cos\beta^* \sin\alpha^*$ in $z_T$ direction.

Also, the new direction of the probe in $z$-axis in the tank coordinate system is given by 0 in $x_T$ direction, $-\mathbf{j}_T \sin\alpha^*$ in $y_T$ direction and $\mathbf{k}_T \cos\alpha^*$ in $z_T$ direction.

Where $\mathbf{i}_T, \mathbf{j}_T, \mathbf{k}_T$ are the unit vectors in the directions of the $x_T, y_T, z_T$ axes of the tank coordinate system, let $\mathbf{i}, \mathbf{j}, \mathbf{k}$ be the unit vectors in the new directions of the $x, y, z$ axes of the probe (which has undergone rotations $\alpha^*$ and $\beta^*$ as described above). $\mathbf{i}, \mathbf{j}, \mathbf{k}$ can now be given by the following expressions

$$\mathbf{i} = \cos\beta^* \mathbf{i}_T + \sin\beta^* \cos\alpha^* \mathbf{j}_T + \sin\beta^* \sin\alpha^* \mathbf{k}_T \qquad \textbf{Equation 8.1}$$

$$\mathbf{j} = -\sin\beta^* \mathbf{i}_T + \cos\beta^* \cos\alpha^* \mathbf{j}_T + \cos\beta^* \sin\alpha^* \mathbf{k}_T \qquad \textbf{Equation 8.2}$$

$$\mathbf{k} = -\sin\alpha^* \mathbf{j}_T + \cos\alpha^* \mathbf{k}_T \qquad \textbf{Equation 8.3}$$

Suppose a bubble which strikes the probe is measured by the probe to have a polar angle $\alpha$ and an azimuthal angle $\beta$ relative to the probe coordinate system and a velocity magnitude $v$. Then, the velocity vector $\mathbf{V}$ of the bubble relative to the probe coordinate system is given by

$$\mathbf{V} = v(\sin\alpha \sin\beta \mathbf{i} + \sin\alpha \cos\beta \mathbf{j} + \cos\alpha \mathbf{k}) \qquad \textbf{Equation 8.4}$$

Substituting for $\mathbf{i}, \mathbf{j}, \mathbf{k}$ from Equations 8.1, 8.2 and 8.3 in Equation 8.4

$$\mathbf{V} = (v)\sin\alpha \sin\beta \left(\cos\beta^* \mathbf{i}_T + \sin\beta^* \cos\alpha^* \mathbf{j}_T + \sin\beta^* \sin\alpha^* \mathbf{k}_T\right)$$

$$+\sin\alpha\cos\beta\left(-\sin\beta^{*}\mathbf{i}_T+\cos\beta^{*}\cos\alpha^{*}\mathbf{j}_T+\cos\beta^{*}\sin\alpha^{*}\mathbf{k}_T\right)$$

$$+\cos\alpha\left(-\sin\alpha^{*}\mathbf{j}_T+\cos\alpha^{*}\mathbf{k}_T\right) \qquad \textbf{Equation 8.5}$$

$$\mathbf{V}=(v)\sin\alpha\sin\beta\cos\beta^{*}\mathbf{i}_T+\sin\alpha\sin\beta\sin\beta^{*}\cos\alpha^{*}\mathbf{j}_T+\sin\alpha\sin\beta\sin\beta^{*}\sin\alpha^{*}\mathbf{k}_T$$

$$-\sin\alpha\cos\beta\sin\beta^{*}\mathbf{i}_T+\sin\alpha\cos\beta\cos\beta^{*}\cos\alpha^{*}\mathbf{j}_T+\sin\alpha\cos\beta\cos\beta^{*}\sin\alpha^{*}\mathbf{k}_T$$

$$-\cos\alpha\sin\alpha^{*}\mathbf{j}_T+\cos\alpha\cos\alpha^{*}\mathbf{k}_T \qquad \textbf{Equation 8.6}$$

$$\mathbf{V}=(v)\sin\alpha\sin\beta\cos\beta^{*}\mathbf{i}_T-\sin\alpha\cos\beta\sin\beta^{*}\mathbf{i}_T \qquad \textbf{Equation 8.7}$$

$$+\sin\alpha\cos\beta\cos\beta^{*}\cos\alpha^{*}\mathbf{j}_T+\sin\alpha\sin\beta\sin\beta^{*}\cos\alpha^{*}\mathbf{j}_T-\cos\alpha\sin\alpha^{*}\mathbf{j}_T$$

$$+\cos\alpha\cos\alpha^{*}\mathbf{k}_T+\sin\alpha\cos\beta\cos\beta^{*}\sin\alpha^{*}\mathbf{k}_T+\sin\alpha\sin\beta\sin\beta^{*}\sin\alpha^{*}\mathbf{k}_T$$

It may now be written that the bubble velocity vector $\mathbf{V_{btp}}$ relative to the tank coordinate system, as measured by the probe, is given by Equation 8.8.

$$\mathbf{V_{btp}}=v\,(\boldsymbol{\eta}_{\mathbf{btp}}) \qquad \textbf{Equation 8.8}$$

where $\boldsymbol{\eta}_{\mathbf{btp}}$ is a unit vector given by

$$\boldsymbol{\eta}_{\mathbf{btp}}=(\sin\alpha\sin\beta\cos\beta^{*}-\sin\alpha\cos\beta\sin\beta^{*})\mathbf{i}_T$$

$$+(\sin\alpha\sin\beta\sin\beta^{*}\cos\alpha^{*}+\sin\alpha\cos\beta\cos\beta^{*}\cos\alpha^{*}-\cos\alpha\sin\alpha^{*})\mathbf{j}_T$$

$$+(\sin\alpha\sin\beta\sin\beta^{*}\sin\alpha^{*}+\sin\alpha\cos\beta\cos\beta^{*}\sin\alpha^{*}+\cos\alpha\cos\alpha^{*})\mathbf{k}_T \qquad \textbf{Equation 8.9}$$

As described in Chapter 7.4, the calculation of $\mathbf{V_{btp}}$ from Equation 8.8 can be compared with the reference bubble velocity vector $\mathbf{V_{bt}}$ measured by camera 1 and camera 2, as described in Chapter 7.3 and defined in Equation 7.13.

## 8.2 Experimental apparatus and setup for the bench test rig

In order to carry out the measurements on the dispersed bubbles in the multi-phase air-water flow using the four-sensor probes, experiments were carried out on a bench test rig as well as in an air-water flow loop. Both of these test rigs, as well as the flow loop, consist of various types of reference measurement device and control systems. In the bench test rig, high speed cameras were used for the reference measurement of the bubble velocity vector (see Chapter 7). This chapter is therefore intended to describe in detail the above-mentioned items in the bench test rig.

### 8.2.1 Bench Test Rig

For the purpose of the experiments, a 750mm high water tank of square cross section was designed and built from Perspex sheets of 6mm thickness. The tank's overall dimensions were 100mm x 100mm x 750mm high. For the injection of bubbles of different sizes (1mm - 5mm diameter), a series of removable injectors were made and placed at the base of the tank, as shown in Figure 8.2 left. Each injector was made up of stainless steel tube, as shown in Figure 8.3, which was connected to the tank using pressure tap screws in order to prevent leakage of water from the joints. In this current experiment, two injectors with 6mm external diameters and internal diameters of 3.5 mm and 5mm respectively were used.

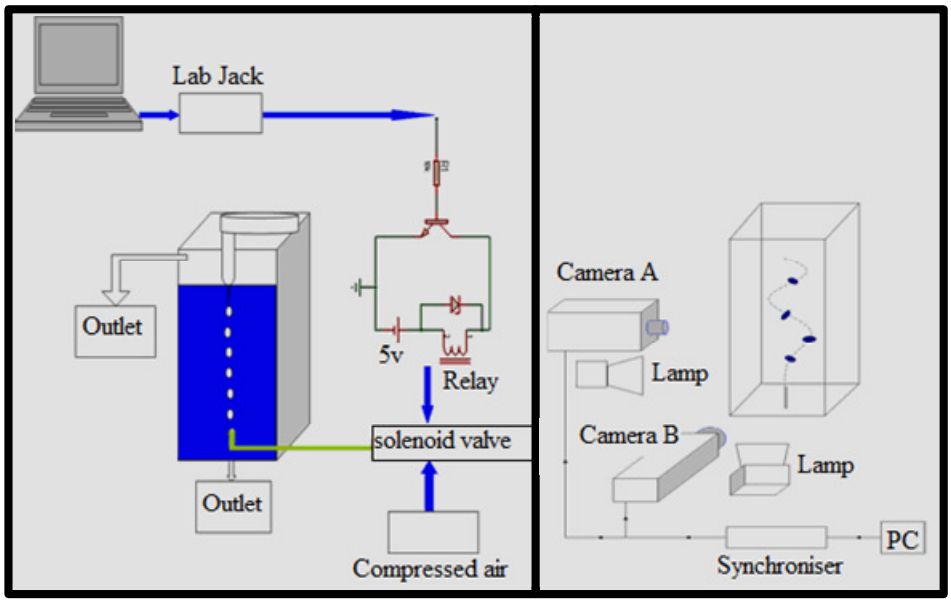


**Figure 8.2 Bench test rig with the bubble injector set up (left). High speed camera to obtain a 3-D image (right).**

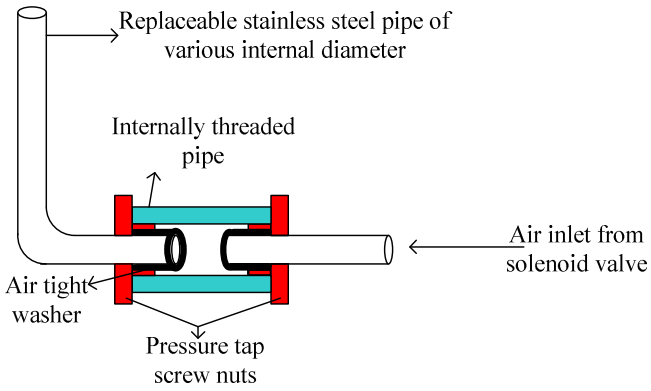


**Figure 8.3 Assembly diagram of the air inlet for the bench test rig**

Initially, a small air pump was used as the source of the air-bubbles, but due to its poor performance, pressurized air from the university compressor was used. This air supply was controlled by using a manual valve regulator and a solenoid valve. The solenoid valve was controlled by software via a data acquisition and control card for the precision flow of the bubbles. Software was written in MATLAB and developed in such a way that the opening and closing time of the valve could be altered as necessary, to give the appropriate bubble size and structure. During the experiments

described in Chapter 9, it was observed that the bubble size varied with the opening time of the solenoid valve; the longer the opening time, the bigger the bubbles. The assumption was made that the above situation had occurred due to the diameter of the solenoid valve itself, which is 1/2 inch. Thus, to overcome the issue, a small manual pipe valve was used to control the air that passed from the solenoid valve, allowing the bubble diameter to be approximately 5mm.

In order to vary the velocity vector $\mathbf{V}$ of the bubbles relative to the probe coordinate system, a new probe holder platform was designed, as shown in Figure 8.1. The platform consists of a metal base with a slotted hole in the middle for the probe to go through. It was then fixed to two rotating holders, one of which was used for varying $\beta^*$ and the other for varying $\alpha^*$. The detailed description of the transformation of the bubble velocity vector measured by the probe into the tank coordinate system for the bubble is described earlier in section 8.1.1. In this particular experiment, the data was collected using the values of $\alpha^*$ of 0°,10°,20° and 30° and values of $\beta^*$ of 0°, 90°, 180° and 270°. Since the bubble rise velocity was expected to be close to vertical, these values of $\alpha^*$ and $\beta^*$ were expected to approximate values of $\alpha$ and $\beta$ that the bubble velocity vector makes relative to the probe coordinate system.

Two high speed cameras (model *trouble shooter 250*), with a capability of 250 frames per second, were also placed orthogonal to each other, as shown in Figure 8.2). The cameras were interlinked with each other as master and slave, so that both the cameras could be controlled by the master camera (see Chapter 7). These cameras enabled the determination of the reference velocity vector $\mathbf{V_{bt}}$ of each individual bubble, relative to tank coordinate system ( $x_T$ , $y_T$ , $z_T$ ), as explained in Chapter 7.3.

# CHAPTER 9

## Tank Experimental Results

This section presents the results of the experimental testing carried out using the local four-sensor probe. The results presented below are from the experiments conducted using the bench test rig. This section also describes the reference measurements carried out with the high speed orthogonal cameras which include measurements of the bubble shape, the trajectories of single bubbles and the bubble velocity magnitude.

### 9.1 Image processing

Image processing involved the use of two high speed cameras placed orthogonally, as described in Chapter 7. These camera images were used in order to obtain the reference bubble velocities for the bench test experiments. The images were further used to obtain the bubble shape, size, and the trajectory of a single bubble as they passed over the local four-sensor probe.

#### 9.1.1 Reference velocity measurement

For the calculation of the reference bubble velocity, the images were first captured as described in Chapter 7. Ten frames from the captured images were saved before and after the trigger points. In order to establish a reference dimension, a mark 15mm wide was placed on the body of the probe using insulation tape, as shown in Figure 7.3 and 9.1.

Captured images were extracted using 'MATLAB' software to find the longest possible chord corresponding to the major axis of the bubble. The centre of the major

axis was calculated and assumed to be the centre of gravity (COG) of the particular bubble at a particular frame.

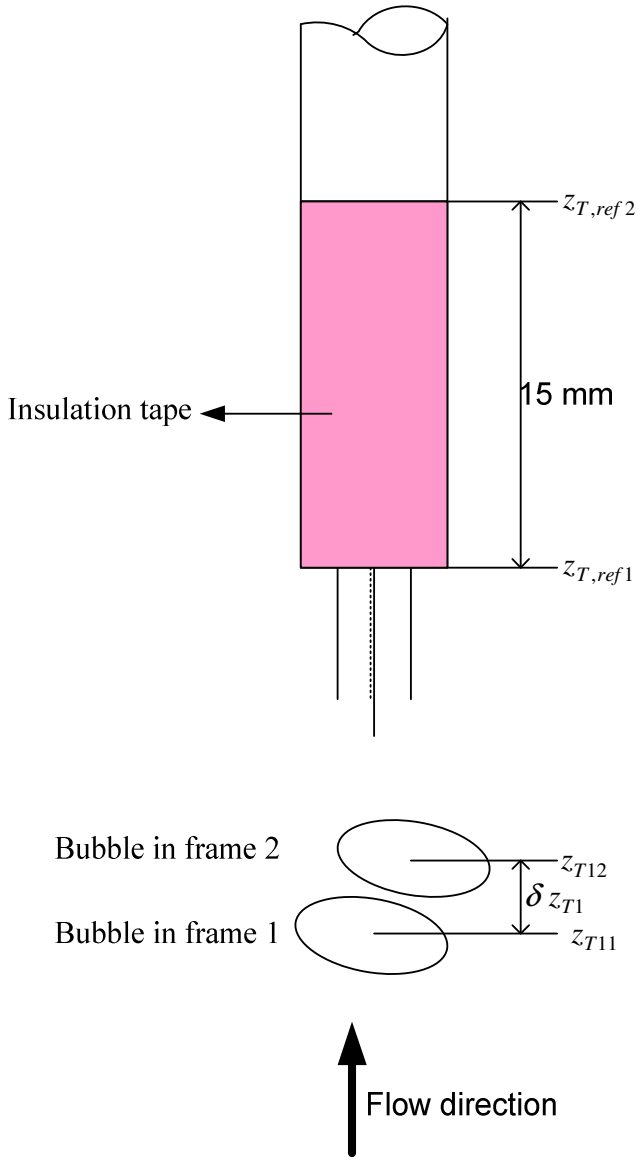


**Figure 9.1 Calculation of the distance travelled by a bubble between two frames in $(x_T, z_T)$ plane using the reference distance of 15mm marked by using insulation tape**

From the extracted COG the distance travelled between two different frames was calculated. This distance was calculated by comparing the coordinate of the $z$-axis

with the coordinate of the mark placed on the probe body, as shown in Figure 9.1. Let $z_{T12}$ and $z_{T11}$ be the coordinate of the COG of a bubble in frames 2 and 1 respectively as measured by the camera in the $x_T, z_T$ plane of the tank coordinate system. Let $z_{T,ref2}$ and $z_{T,ref1}$ be the top and the bottom coordinates of the 15 mm insulation tape. Therefore, the distance travelled by a bubble between two frames is $\delta z_{T1}$, as given by Equation 9.1.

$$\delta z_{T1} = \left(z_{T12} - z_{T11}\right) \qquad \textbf{Equation 9.1}$$

With the known coordinates and the reference length of the insulation tape used, the actual distance $\hat{\delta} z_{T1}$ travelled by a bubble between the two successive frames is given by Equation 9.2.

$$\hat{\delta} z_{T1} = \left( \frac{0.015}{z_{T,ref2} - z_{T,ref1}} \right) \delta z_{T1} \qquad \textbf{Equation 9.2}$$

Chapter 7 details the calibration of the cameras, which established a frame rate of 246 frames per second; therefore, one frame corresponds to an elapsed time of 4.06ms. As the time taken for each frame and the distance travelled by the bubble in each frame has been established, it is possible to calculate the reference bubble velocity of the bubble in the tank coordinate system. The results presented in Table 9.1 are only from the COG of the bubble.

Table 9.1 shows the velocity magnitude for a free rising single bubble measured for 21 frames using high speed cameras. Three set of identical experiments were carried out to observe the difference between the velocity of a single bubble and a stream of bubbles. Each experiment shows the calculated velocity between the successive 21

frames captured by the camera. The average test results of the 21 frames shows that the velocity of the bubble is 0.24m/s, which is very close to the axial rising velocity, as shown by Sam et al. [159].

| Frame No | Velocity (m/s) | | |
|---|---|---|---|
| | **Set 1** | **Set 2** | **Set 3** |
| 1-2 | 0.33 | 0.19 | 0.31 |
| 2-3 | 0.25 | 0.30 | 0.13 |
| 3-4 | 0.30 | 0.20 | 0.33 |
| 4-5 | 0.16 | 0.13 | 0.21 |
| 5-6 | 0.20 | 0.30 | 0.43 |
| 6-7 | 0.28 | 0.32 | 0.21 |
| 7-8 | 0.24 | 0.22 | 0.15 |
| 8-9 | 0.25 | 0.32 | 0.34 |
| 9-10 | 0.24 | 0.18 | 0.16 |
| 10-11 | 0.38 | 0.37 | 0.24 |
| 11-12 | 0.12 | 0.10 | 0.18 |
| 12-13 | 0.24 | 0.34 | 0.29 |
| 13-14 | 0.25 | 0.21 | 0.25 |
| 14-15 | 0.27 | 0.24 | 0.26 |
| 15-16 | 0.15 | 0.11 | 0.26 |
| 16-17 | 0.20 | 0.29 | 0.17 |
| 17-18 | 0.21 | 0.26 | 0.40 |
| 18-19 | 0.29 | 0.25 | 0.16 |
| 19-20 | 0.19 | 0.26 | 0.18 |
| 20-21 | 0.19 | 0.29 | 0.21 |
| **average** | **0.24** | **0.24** | **0.24** |

**Table 9.1 Velocity magnitude of the individual bubble from the camera**

Table 9.2 shows the average bubble velocity of 21 frames of a bubble when rising as a stream of rising bubbles. The high speed cameras were used to calculate the velocity of bubbles when the probe was tilted at various polar angles $\alpha^*$. These calculated bubble velocities were used as reference velocities in later experiments for calculating velocity vector using the four-sensor probe. The velocity was calculated between each subsequent frame from the images that were captured just before collecting the data using the four–sensor probe, when the probe was tilted at a certain polar angle $\alpha^*$ and the calculated velocity was used as a reference velocity for the particular $\alpha^*$

as presented in section 9.2. $\alpha^*$ and $\beta^*$ are defined as follows. The $z$ axis of the probe is initially parallel to the $z_T$ of the tank and the $y$ axis of the probe is initially parallel to the $y_T$ axis of the tank. The bubble is allowed to be purely in $z_T$ direction. The probe is then tilted by $\alpha^*$ and rotated by $\beta^*$ (as described in Chapter 8.2). The bubble velocity vector now makes a polar angle $\alpha^*$ and azimuthal angle $\beta^*$ relative to the probe coordinate system (see Figure 2.18).

| | Tests carried for various polar angle $\alpha^*$ (by tilting the probe by angle $\alpha^*$ ) | | | |
|---|---|---|---|---|
| $\alpha^*$ | 0° | 5° | 10° | 20° |
| **Average bubble velocity of 21 frames** | **0.38** | **0.34** | **0.41** | **0.35** |

**Table 9.2 Velocity magnitude for an individual bubble picked from the stream of bubbles when the probe is tilted at various polar angles**

From Table 9.2 it can be seen that the velocity is different for various $\alpha^*$. Although, the velocity of the bubble is unaffected by the position of the probe, the variation of the bubble velocity is due to the fact that the experiments were carried out on various days and at various times and also the fact that the frequency of the bubble was controlled manually; thus, it was impossible to maintain an equal frequency of the bubble.

Thus, calculated velocities were used as a reference velocity for each polar angle $\alpha^*$. These results show the velocity as being somewhat different from the ideal shown in Table 9.1. The reason behind this could be due to the stream of bubbles from the injector causing a wake effect. The effect is also verified by the study of Celata et al. 2004 [60] and Tsuge et al. [161], who suggest that the larger the bubble diameter, the greater the wake effect. Celata et al [60] also suggests the increase of velocity with

frequency is inversely related to bubble size, until it becomes negligible for a bubble diameter smaller then 1.2mm. Therefore, based on those previous research papers, the existence of a reasonable amount of wake effect in these experiments can also be expected.

### 9.1.2 Bubble trajectory

In Figure 9.2, a diagram shows the trajectory of the centre of gravity of a bubble injected into the base of a water tank in which the four-sensor probe was mounted (the injector was 500mm below the probe). The diagram shows the bubble trajectory in a plane parallel to the $x_T$, $z_T$ plane of the water tank, as measured by camera 1, and parallel to the $y_T$, $z_T$ plane, as measured by camera 2. Also shown in Figure 9.4 are the outline shapes of the bubbles, as viewed in the $x_T$, $z_T$ and $y_T$, $z_T$ planes for each of the bubble positions [note that in Figure 9.2, the linear scale used for the bubble shapes is different from that used for the bubble trajectories, where the vertical scale was expanded to match the scale of each bubble]. From results such as those shown in Figure 9.2, the initial simplifying assumption was made that the velocity vector $\mathbf{V_{bt}}$ of each bubble relative to the tank was purely in the vertical direction. Given this simplifying assumption, the angles $\alpha^*$ and $\beta^*$ by which the probe is rotated relative to the tank coordinate system (see Chapter 3 and [11]) now represent 'reference values' for the polar and azimuthal angles of the bubble velocity vector $\mathbf{V_{bp}}$ relative to the probe coordinate system. Thus $\alpha_{ref} = \alpha^*$ and $\beta_{ref} = \beta^*$.

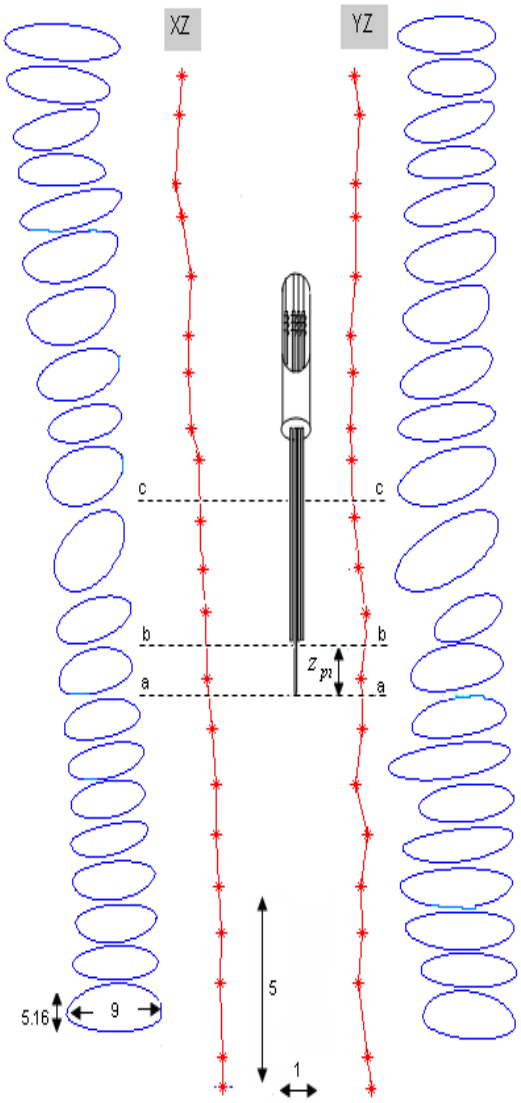


**Figure 9.2 The path of a single bubble as measured by camera 1 ( $x_T$ , $z_T$ ) and camera 2 ( $y_T$ , $z_T$ ). Also shown are the corresponding bubble shapes at each point on the two trajectories. All dimensions are in mm. The scale shown for the lower left bubble applies to all bubbles. The other scale applies to both trajectories and also to the probe. Line cc is the position of the upper surface of a bubble when the lower surface leaves the probe**

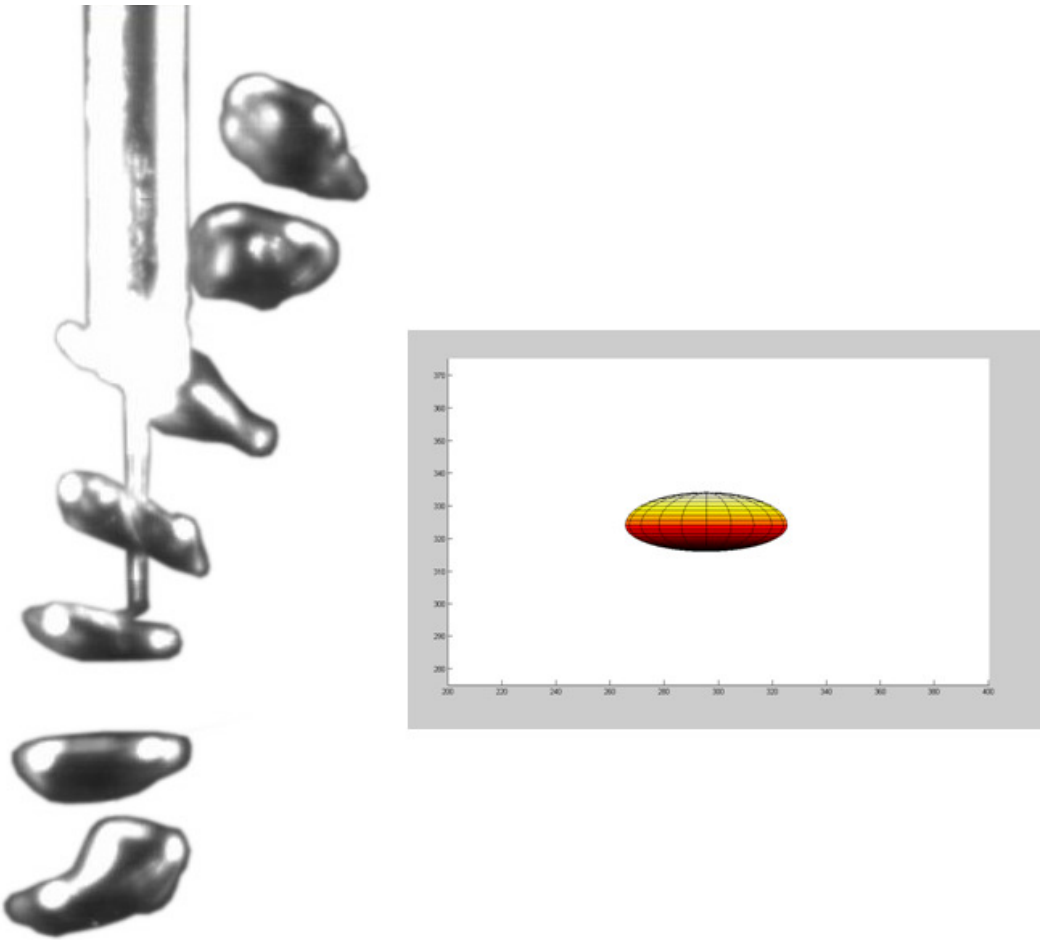

**Figure 9.3 Image of single bubble at different stages passing through the local four-sensor probe (left) and a reconstruction of a single bubble (right)**

## 9.2 Bench test rig

The experiments on the bench test rig were carried out using the tank with the set-up shown in Figure 8.2, as discussed earlier in Chapter 8. In order to measure the conductance from the probe, the dc-circuit, as described in Chapter 5, was used. The DAQ-2006, as described in Chapter 6, was used to collect the data. The data were collected with a probe made up of Teflon coated needles. Teflon-coated needles with a diameter of 0.15mm and 0.25mm were used to investigate the best size of needles for future use, in terms of deformation and the rigidity of the needles themselves. The experiments were also carried out with two different sizes of bubble and two different

dimensions of $z_i$ ( $i$ =1,2 and 3, $z_i$ is the distance between the tip of front sensor and the rear sensor) categorized as longer $z_i$ with dimensions between 1.5 – 2.5 mm, and short $z_i$, with dimensions between 1- 1.5 mm. In this section, various sets of processed results are presented from the Teflon-coated probe, collected from different sets of experiments, as listed below.

For each experiment, calibration factor *K* was also calculated which was introduced by Lucas et al. [1] after finding $v_{meas}$ is always less than $v_{ref}$ with $v_{meas}$ being typically 80% of the $v_{ref}$, which led the author to make an assumption that the cause was due to the retarding effect of the probe-bubble interaction. Thus, the author introduced calibration factor *K*, which is given by:

$$K\, v_{meas} = v_{ref} \qquad \textbf{Equation 9.3}$$

The initial experiment results, gathered from the painted 0.3mm diameter acupuncture needles, indicate that the velocity vector measured shows a big error. This could be due to the probe size, as well as the roughness of the sensors due to the painting. It could also have been due to the effect of the overall area of the probe. Hence, in this section, only the results from the Teflon coated probes are presented. The data were collected using two different diameters of Teflon coated needles, 0.15mm and 0.25mm. These results are presented and discussed below in detail.

### 9.2.1 Experiment 1

The experiment was carried out using Teflon coated needles of 0.25mm diameter, with a bubble size of 10mm and probe dimensions as shown in Table 9.3, where $x_1$ = -0.26 mm , $y_1$ = 0.68 mm , $z_1$= 1.70 mm , $x_2$ = 0.63 mm, $y_2$ = -0.66 mm, $z_2$ = 1.76

mm, $x_3$ = -0.24 mm, $y_3$ = -0.65 mm , $z_3$ = 1.59 mm. The tests were carried out using two reference polar angles $\alpha_{ref}$ 0° and 10° in a stream of rising bubbles. For comparison purposes, two data sets were collected for $\alpha_{ref}$ = 0° and for $\alpha_{ref}$ = 10° the data were collected at various reference azimuthal angles $\beta_{ref}$. All the data were collected at a sampling frequency of 10 KHz for 120 seconds.

| | 1 | 2 | 3 |
|---|---|---|---|
| $x$ | -0.26 mm | 0.63 mm | -0.24 mm |
| $y$ | 0.68 mm | -0.66 mm | -0.65 mm |
| $z$ | 1.70 mm | 1.76 mm | 1.59 mm |

**Table 9.3 Probe dimensions for Experiment 1**

| | $\alpha_{ref}$ | $\beta_{ref}$ | $v_{ref}$ | $\alpha_{meas}$ | $\beta_{meas}$ | $v_{meas}$ | $\delta t_{11}$ | $\delta t_{22}$ | $\delta t_{33}$ | NOB |
|---|---|---|---|---|---|---|---|---|---|---|
| Test | (deg) | (deg) | ($ms^{-1}$) | (deg) | (deg) | ($ms^{-1}$) | (s) | (s) | (s) | |
| 1 | 0 | N/A | 0.38 | **18.97** | **-** | **0.24** | 0.011482 | 0.016046 | 0.012991 | 14 |
| 2 | 0 | N/A | 0.38 | **24.04** | **-** | **0.24** | 0.011983 | 0.015875 | 0.011642 | 6 |
| 3 | 10 | 0 | 0.41 | **11.91** | **119.17** | **0.27** | 0.011303 | 0.013861 | 0.011531 | 9 |
| 4 | 10 | 90 | 0.41 | **31.87** | **101.91** | **0.24** | 0.010497 | 0.016040 | 0.011041 | 17 |
| 5 | 10 | 270 | 0.41 | **38.44** | **242.14** | **0.25** | 0.010136 | 0.009709 | 0.012425 | 19 |

**Table 9.4 Results with reference polar angle 0°,and 13° at various azimuthal angles**

| Test | $\varepsilon_{abs,\alpha}$ (deg) | $\varepsilon_{abs,\beta}$ (deg) | $\varepsilon_v$ (%) | $K$ |
|---|---|---|---|---|
| 1 | 18.97 | NA | -36.84 | 1.58 |
| 2 | 24.04 | NA | -36.84 | 1.58 |
| 3 | 1.91 | 119.17 | -34.15 | 1.52 |
| 4 | 21.87 | 11.91 | -41.46 | 1.71 |
| 5 | 28.44 | -27.86 | -39.02 | 1.64 |
| | $\bar{\varepsilon}_{abs,\alpha}$ | $\bar{\varepsilon}_{abs,\beta}$ | $\bar{\varepsilon}_v$ | Average |
| | **19.05** | **34.41** | **-37.66** | **1.61** |
| | **9.11** | **50.97** | **2.45** | |
| | $\sigma_{abs,a}$ | $\sigma_{abs,\beta}$ | $\sigma_v$ | |

**Table 9.5 Errors in the values of polar angle, azimuthal angle and velocity magnitude of the results presented in Table 9.4**

Table 9.4 shows results of measured polar angle $\alpha_{meas}$, azimuthal angle $\beta_{meas}$ and velocity magnitude $v_{meas}$ for the reference polar angle $\alpha_{ref}$ = 0º and 10 ° calculated with various reference azimuthal angles $\beta_{ref}$ . However when $\alpha_{ref}$ = 0º, the value of $\beta_{meas}$ is meaningless. The reference velocity $v_{ref}$ = 0.38 m/s when $\alpha_{ref}$ = 0º and $v_{ref}$ = 0.41 m/s when $\alpha_{ref}$ = 10º. Table 9.4 also shows the average time interval $\delta t_{ii}$ (*i*=1, 2 and 3) and the total number of bubbles (NOB) that hit all four sensors.

Table 9.5 shows the error analysis of the results tabulated in Table 9.4. Table 9.5 shows the mean absolute error $\varepsilon_{abs,\alpha}$ of the measured polar angle $\alpha_{meas}$ and mean absolute error $\varepsilon_{abs,\beta}$ of the measured azimuthal angle $\beta_{meas}$. The table also presents the percentage error in $\varepsilon_v$ in $v_{meas}$ which is defined as

$$\varepsilon_v = \frac{v_{meas} - v_{ref}}{v_{ref}} 100 \qquad \textbf{Equation 9.4}$$

Table 9.5 shows that the mean value $\bar{\varepsilon}_{abs,\alpha}$ of the absolute error in $\varepsilon_{abs,\alpha}$ is equal to 19.05º and the standard deviation $\sigma_{abs,a}$ of $\varepsilon_{abs,\alpha}$ is equal to 9.11º. The mean value $\bar{\varepsilon}_{abs,\beta}$ of the absolute error in $\varepsilon_{abs,\beta}$ is equal to 34.41º and the standard deviation $\sigma_{abs,\beta}$ of $\varepsilon_{abs,\beta}$ is 50.97º. The mean value $\bar{\varepsilon}_v$ of the percentage error in the bubble velocity magnitude is -37.66%. The standard deviation $\sigma_v$ of $\varepsilon_v$ is 2.45%. Table 9.5 also shows that calibration factor $K$ is 1.61. The results show that, although the miniature four-sensor probe can be used to calculate the polar angle $\alpha$ and azimuthal angle $\beta$ of the bubble velocity vector, this may lead to a large error for the following reasons.

- Sensor diameter:- The bigger the diameter of the sensor needles, the higher the possibility of deformation of the bubble during probe-bubble interaction, leading it to calculate incorrect time intervals. This, in turn, gives us an incorrect velocity vector.
- Dimensions of $z_i$:- The longer the separation between the front and rear sensors, the longer it takes for the bubble to hit the rear sensor, allowing enough time for the bubble to deform and thus provide incorrect time intervals. This, in turn, gives us an incorrect velocity vector. Wu et al. [146-148] recommended the probe spacing is 0.5 to 2 times the size of the bubble diameter.
- Bubble size: - The bigger the size of the bubble, the greater the possibility of deformation of the bubble during probe-bubble interaction, leading to incorrectly calculated time intervals. This, in turn, gives us an incorrect velocity vector.
- Sampling frequency: - The smaller the dimensions of the probe, the higher the sampling rate that is needed in order to acquire a reliable and representative signal from each sensor (see section 3.1).

Hence, in the later tests, the above parameters will be carefully examined one by one in order to achieve the best possible results from the defined parameters.

### 9.2.2 Experiment 2

The second experiment was carried out using Teflon coated needles of 0.25mm diameter, with a bubble size of 10 mm and the probe dimensions shown in Table 9.6 where $x_1$ = -0.10 mm , $y_1$ = 0.51 mm , $z_1$= 0.99 mm , $x_2$ = 0.27 mm, $y_2$ = -0.64 mm, $z_2$ = 1.18 mm, $x_3$ = -0.24 mm, $y_3$ = -0.78 mm , $z_3$ = 1.11 mm with a smaller $z_i$ as

compared to Experiment 1. The tests were again carried out on two reference polar angles $\alpha_{ref}$ 0° and 10°. For comparison purposes, two sets of data were collected for both $\alpha_{ref}$ = 0° and for $\alpha_{ref}$ = 10° the data were collected at various reference azimuthal angles $\beta_{ref}$ at a sampling frequency of 10 KHz for 120 seconds in a stream of rising bubbles.

| | 1 | 2 | 3 |
|---|---|---|---|
| $x$ | -0.10 | 0.27 | -0.24 |
| $y$ | 0.51 | -0.64 | -0.78 |
| $z$ | 0.99 | 1.18 | 1.11 |

**Table 9.6 Probe dimensions for Experiment 2**

| | $\alpha_{ref}$ | $\beta_{ref}$ | $v_{ref}$ | $\alpha_{meas}$ | $\beta_{meas}$ | $v_{meas}$ | $\delta t_{11}$ | $\delta t_{22}$ | $\delta t_{33}$ | NOB |
|---|---|---|---|---|---|---|---|---|---|---|
| Test | (deg) | (deg) | ($ms^{-1}$) | (deg) | (deg) | ($ms^{-1}$) | (s) | (s) | (s) | |
| 1 | 0 | N/A | 0.38 | **10.01** | **N/A** | **0.37** | 0.00691 | 0.00969 | 0.00875 | 20 |
| 2 | 0 | N/A | 0.38 | **2.90** | **N/A** | **0.38** | 0.00661 | 0.00822 | 0.00799 | 18 |
| 3 | 10 | 0 | 0.41 | **15.13** | **310.22** | **0.30** | 0.00676 | 0.00641 | 0.00667 | 19 |
| 4 | 10 | 0 | 0.41 | **14.51** | **5.48** | **0.29** | 0.00732 | 0.00667 | 0.00601 | 9 |
| 5 | 10 | 180 | 0.41 | **16.64** | **210.42** | **0.29** | 0.00575 | 0.00858 | 0.00893 | 28 |
| 6 | 10 | 180 | 0.41 | **21.92** | **171.16** | **0.28** | 0.00510 | 0.00945 | 0.00922 | 15 |
| 7 | 10 | 270 | 0.41 | **15.31** | **256.7** | **0.28** | 0.00679 | 0.00792 | 0.00849 | 4 |
| 8 | 10 | 270 | 0.41 | **14.23** | **257.79** | **0.29** | 0.00663 | 0.00770 | 0.00818 | 5 |

**Table 9.7 Results for reference polar angle 0° and 13° at various azimuthal angles**

Table 9.7 shows results of measured polar angle $\alpha_{meas}$, azimuthal angle $\beta_{meas}$ and velocity magnitude $v_{meas}$ for the reference polar angle $\alpha_{ref}$ = 0º and 10 º calculated with various reference azimuthal angles $\beta_{ref}$. Table 9.7 also shows the average time interval $\delta t_{ii}$ ( $i$ =1,2 and 3) and the total number of bubbles (NOB) that hit all four sensors.

| Test | $\varepsilon_{abs,\alpha}$ (deg) | $\varepsilon_{abs,\beta}$ (deg) | $\varepsilon_V$ (%) | $K$ |
|---|---|---|---|---|
| 1 | 10.01 | NA | -2.63 | 1.03 |
| 2 | 2.90 | NA | 0.00 | 1.00 |
| 3 | 5.13 | 49.78 | -26.83 | 1.37 |
| 4 | 4.51 | 5.48 | -29.27 | 1.41 |
| 5 | 6.64 | 30.42 | -29.27 | 1.41 |
| 6 | 11.92 | -8.84 | -31.71 | 1.46 |
| 7 | 5.31 | -13.30 | -31.71 | 1.46 |
| 8 | 4.23 | -12.21 | -29.27 | 1.41 |
| | $\bar{\varepsilon}_{abs,\alpha}$ | $\bar{\varepsilon}_{abs,\beta}$ | $\bar{\varepsilon}_V$ | Average |
| | **6.33** | **8.55** | **-22.59** | **1.32** |
| | **2.89** | **20.94** | **12.38** | |
| | $\sigma_{abs,a}$ | $\sigma_{abs,\beta}$ | $\sigma_V$ | |

**Table 9.8 Errors in the values of polar angle, azimuthal angle and velocity magnitude of the results presented in Table 9.7**

Table 9.8 shows that the mean value $\bar{\varepsilon}_{abs,\alpha}$ of the absolute error in $\varepsilon_{abs,\alpha}$ is equal to 6.33º and the standard deviation $\sigma_{abs,a}$ of $\varepsilon_{abs,\alpha}$ is equal to 2.89º. The mean value $\bar{\varepsilon}_{abs,\beta}$ of the absolute error in $\varepsilon_{abs,\beta}$ is equal to 8.55º and the standard deviation $\sigma_{abs,\beta}$ of $\varepsilon_{abs,\beta}$ is 20.94º. The mean value $\bar{\varepsilon}_V$ of the percentage error in the bubble velocity magnitude is -22.59%. The standard deviation $\sigma_V$ of $\varepsilon_V$ is 12.38%. Table 9.8 also shows that calibration factor $K$ is 1.32.

### 9.2.3 Experiment 3

In order to conduct the next experiment, the Teflon coated 0.15 mm diameter needles (a smaller sensor needle diameter than the ones used in the previous two experiments) were used as sensors to avoid the errors that exist in the above two experiments. This experiment was conducted again with a larger bubble (10 mm) and longer $z_i$. The data were collected for 60 seconds at a sampling rate of 10 KHz and Table 9.9 shows the dimensions of the probe used to collect the data where $x_1$ = -0.30 mm, $y_1$ = 0.43

mm, $z_1$= 2.61 mm, $x_2$ = 0.15 mm, $y_2$ = -0.30 mm, $z_2$ = 2.57 mm, $x_3$ = -0.20 mm, $y_3$ = -0.50 mm, $z_3$ = 2.58 mm

| | 1 | 2 | 3 |
|---|---|---|---|
| $x$ | -0.30 | 0.15 | -0.20 |
| $y$ | 0.43 | -0.30 | -0.50 |
| $z$ | 2.61 | 2.57 | 2.58 |

**Table 9.9 Probe dimensions Experiment 3**

| | $\alpha_{ref}$ | $\beta_{ref}$ | $v_{ref}$ | $\alpha_{meas}$ | $\beta_{meas}$ | $v_{meas}$ | $\delta t_{11}$ | $\delta t_{22}$ | $\delta t_{33}$ | NOB |
|---|---|---|---|---|---|---|---|---|---|---|
| Test | (deg) | (deg) | ($ms^{-1}$) | (deg) | (deg) | ($ms^{-1}$) | (s) | (s) | (s) | |
| 1 | 5 | 0 | 0.34 | **11.99** | **351.11** | **0.34** | 0.015540 | 0.014385 | 0.014219 | 57 |
| 2 | 5 | 0 | 0.34 | **21.48** | **279.34** | **0.34** | 0.015162 | 0.013825 | 0.014558 | 21 |
| 3 | 5 | 90 | 0.34 | **9.85** | **211.80** | **0.37** | 0.013741 | 0.013977 | 0.014270 | 40 |
| 4 | 5 | 90 | 0.34 | **11.10** | **200.53** | **0.31** | 0.015910 | 0.016416 | 0.016741 | 19 |
| 5 | 5 | 90 | 0.34 | **8.37** | **227.20** | **0.33** | 0.015349 | 0.015356 | 0.015668 | 17 |
| 6 | 5 | 180 | 0.34 | **16.74** | **213.91** | **0.31** | 0.015938 | 0.016494 | 0.017128 | 38 |
| 7 | 5 | 180 | 0.34 | **18.28** | **218.04** | **0.32** | 0.015142 | 0.015627 | 0.016320 | 33 |
| 8 | 5 | 270 | 0.34 | **21.91** | **268.95** | **0.32** | 0.015803 | 0.014676 | 0.015549 | 31 |
| 9 | 5 | 270 | 0.34 | **18.48** | **257.22** | **0.33** | 0.015100 | 0.014471 | 0.015220 | 45 |
| 10 | 10 | 0 | 0.41 | **10.43** | **307.76** | **0.33** | 0.016257 | 0.015199 | 0.015385 | 16 |
| 11 | 10 | 0 | 0.41 | **16.96** | **353.65** | **0.35** | 0.015034 | 0.013545 | 0.013302 | 29 |
| 12 | 10 | 90 | 0.41 | **12.34** | **176.83** | **0.34** | 0.014500 | 0.015318 | 0.015473 | 13 |
| 13 | 10 | 90 | 0.41 | **12.36** | **164.00** | **0.34** | 0.014257 | 0.015147 | 0.015187 | 24 |
| 14 | 10 | 180 | 0.41 | **29.43** | **212.13** | **0.31** | 0.013960 | 0.015113 | 0.016186 | 25 |
| 15 | 10 | 270 | 0.41 | **32.68** | **265.01** | **0.28** | 0.016423 | 0.014889 | 0.016373 | 30 |

**Table 9.10 Results for reference polar angle 5° and 10° at various azimuthal angles**

Table 9.10 shows results of measured polar angle $\alpha_{meas}$, azimuthal angle $\beta_{meas}$ and velocity magnitude $v_{meas}$ for the reference polar angle $\alpha_{ref}$ = 5º and 10 º calculated with various reference azimuthal angles $\beta_{ref}$. The reference velocity $v_{ref}$ = 0.34 m/s when $\alpha_{ref}$ = 5º and $v_{ref}$ = 0.41 m/s when $\alpha_{ref}$ = 10º. Table 9.10 also shows the average time interval $\delta t_{ii}$ ( $i$ =1,2 and 3) and NOB that hit all four sensors.

| Test | $\varepsilon_{abs,\alpha}$ (deg) | $\varepsilon_{abs,\beta}$ (deg) | $\varepsilon_v$ (%) | $K$ |
|---|---|---|---|---|
| 1 | 6.99 | -8.89 | 0.00 | 1.00 |
| 2 | 16.48 | -80.66 | 0.00 | 1.00 |
| 3 | 4.85 | 121.80 | 8.82 | 0.92 |
| 4 | 6.10 | 110.53 | -8.82 | 1.10 |
| 5 | 3.37 | 137.20 | -2.94 | 1.03 |
| 6 | 11.74 | 33.91 | -8.82 | 1.10 |
| 7 | 13.28 | 38.04 | -5.88 | 1.06 |
| 8 | 16.91 | -1.05 | -5.88 | 1.06 |
| 9 | 13.48 | -12.78 | -2.94 | 1.03 |
| 10 | 0.43 | -52.24 | -19.51 | 1.24 |
| 11 | 6.96 | -6.35 | -14.63 | 1.17 |
| 12 | 2.34 | 86.83 | -17.07 | 1.21 |
| 13 | 2.36 | 74.00 | -17.07 | 1.21 |
| 14 | 19.43 | 32.13 | -24.39 | 1.32 |
| 15 | 22.68 | -4.99 | -31.71 | 1.46 |
| | $\bar{\varepsilon}_{abs,\alpha}$ | $\bar{\varepsilon}_{abs,\beta}$ | $\bar{\varepsilon}_v$ | Average |
| | **9.83** | **31.17** | **-10.06** | **1.13** |
| | **6.72** | **61.91** | **10.27** | |
| | $\sigma_{abs,a}$ | $\sigma_{abs,\beta}$ | $\sigma_v$ | |

**Table 9.11 Errors in the values of polar angle, azimuthal angle and velocity magnitude of the results presented in Table 9.10**

Table 9.11 shows that the mean value $\bar{\varepsilon}_{abs,\alpha}$ of the absolute error in $\varepsilon_{abs,\alpha}$ is equal to 9.83º and the standard deviation $\sigma_{abs,a}$ of $\varepsilon_{abs,\alpha}$ is equal to 6.72º. The mean value $\bar{\varepsilon}_{abs,\beta}$ of the absolute error in $\varepsilon_{abs,\beta}$ is equal to 31.17º and the standard deviation $\sigma_{abs,\beta}$ of $\varepsilon_{abs,\beta}$ is 61.91º. The mean value $\bar{\varepsilon}_v$ of the percentage error in the bubble velocity magnitude is -10.06%. The standard deviation $\sigma_v$ of $\varepsilon_v$ is 10.27%. Table 9.11 also shows that calibration factor $K$ is 1.13.

### 9.2.4 Experiment 4

The next experiment was carried out with a smaller $z_i$. The probe was made up with 0.15 mm diameter Teflon coated needles. Table 9.12 shows the probe dimensions used to collect the data where $x_1$ = -0.19 mm, $y_1$ = 0.39 mm, $z_1$= 1.05 mm, $x_2$ =

0.40 mm, $y_2$ = -0.27 mm, $z_2$ = 1.05 mm, $x_3$ = 0.06 mm, $y_3$ = -0.50 mm, $z_3$ = 1.09 mm. The data were collected at a sampling rate of 40 KHz for 80 seconds using a 10 mm bubble size, and the data were collected for the $\alpha_{ref}$ 0° and 10°, at various $\beta_{ref}$, as shown in Table 9.13.

| | 1 | 2 | 3 |
|---|---|---|---|
| $x$ | -0.19 | 0.40 | 0.06 |
| $y$ | 0.39 | -0.27 | -0.50 |
| $z$ | 1.05 | 1.05 | 1.09 |

**Table 9.12 Probe dimensions for Experiment 4**

| | $\alpha_{ref}$ | $\beta_{ref}$ | $v_{ref}$ | $\alpha_{meas}$ | $\beta_{meas}$ | $v_{meas}$ | $\delta t_{11}$ | $\delta t_{22}$ | $\delta t_{33}$ | NOB |
|---|---|---|---|---|---|---|---|---|---|---|
| Test | (deg) | (deg) | ($ms^{-1}$) | (deg) | (deg) | ($ms^{-1}$) | (s) | (s) | (s) | |
| 1 | 0 | 0 | 0.38 | **12.61** | **-** | **0.34** | 0.005858 | 0.006053 | 0.006765 | 30 |
| 2 | 0 | 0 | 0.38 | **12.85** | **-** | **0.38** | 0.004916 | 0.005978 | 0.006024 | 33 |
| 3 | 0 | 0 | 0.38 | **2.31** | **-** | **0.35** | 0.006018 | 0.006006 | 0.006299 | 24 |
| 4 | 10 | 0 | 0.41 | **14.23** | **14.04** | **0.34** | 0.006430 | 0.005750 | 0.005508 | 23 |
| 5 | 10 | 0 | 0.41 | **16.19** | **34.17** | **0.34** | 0.006229 | 0.005918 | 0.005490 | 31 |
| 6 | 10 | 90 | 0.41 | **26.90** | **99.35** | **0.31** | 0.005267 | 0.007320 | 0.006638 | 19 |
| 7 | 10 | 180 | 0.41 | **24.96** | **156.01** | **0.34** | 0.004517 | 0.006642 | 0.006993 | 15 |
| 8 | 10 | 180 | 0.41 | **24.10** | **152.12** | **0.34** | 0.004621 | 0.006734 | 0.007017 | 19 |
| 9 | 10 | 270 | 0.41 | **7.39** | **187.88** | **0.33** | 0.005954 | 0.006428 | 0.006842 | 23 |
| 10 | 10 | 270 | 0.41 | **22.23** | **228.22** | **0.31** | 0.005979 | 0.006000 | 0.007199 | 20 |

**Table 9.13 Results for reference polar angle 0° at 10° at various azimuthal angles**

Table 9.13 shows the results of measured polar angle $\alpha_{meas}$, azimuthal angle $\beta_{meas}$ and velocity magnitude $v_{meas}$ for the reference polar angle $\alpha_{ref}$ = 0º and 10 º calculated with various reference azimuthal angles $\beta_{ref}$. The reference velocity $v_{ref}$ = 0.38 m/s when $\alpha_{ref}$ = 0º and $v_{ref}$ = 0.41 m/s when $\alpha_{ref}$ = 10º. Table 9.13 also shows the average time interval $\delta t_{ii}$ ( $i$ =1, 2 and 3) and the total number of bubbles (NOB) that hit all four sensors.

| Test | $\varepsilon_{abs,\alpha}$ (deg) | $\varepsilon_{abs,\beta}$ (deg) | $\varepsilon_v$ (%) | $K$ |
|---|---|---|---|---|
| 1 | 12.61 | NA | -10.53 | 1.12 |
| 2 | 12.85 | NA | 0.00 | 1.00 |
| 3 | 2.31 | NA | -7.89 | 1.09 |
| 4 | 4.23 | 14.04 | -17.07 | 1.21 |
| 5 | 6.19 | 34.17 | -17.07 | 1.21 |
| 6 | 16.90 | 9.35 | -24.39 | 1.32 |
| 7 | 14.96 | -23.99 | -17.07 | 1.21 |
| 8 | 14.10 | -27.88 | -17.07 | 1.21 |
| 9 | -2.61 | -82.12 | -19.51 | 1.24 |
| 10 | 12.23 | -41.78 | -24.39 | 1.32 |
| | $\bar{\varepsilon}_{abs,\alpha}$ | $\bar{\varepsilon}_{abs,\beta}$ | $\bar{\varepsilon}_v$ | Average |
| | **9.38** | **-16.89** | **-15.50** | **1.19** |
| | **6.09** | **31.46** | **7.12** | |
| | $\sigma_{abs,a}$ | $\sigma_{abs,\beta}$ | $\sigma_v$ | |

**Table 9.14 Errors in the values of polar angle, azimuthal angle and velocity magnitude of the results presented in Table 9.13**

Table 9.14 shows that the mean value $\bar{\varepsilon}_{abs,\alpha}$ of the absolute error in $\varepsilon_{abs,\alpha}$ is equal to 9.38º and the standard deviation $\sigma_{abs,a}$ of $\varepsilon_{abs,\alpha}$ is equal to 6.09º. The mean value $\bar{\varepsilon}_{abs,\beta}$ of the absolute error in $\varepsilon_{abs,\beta}$ is equal to -16.89º and the standard deviation $\sigma_{abs,\beta}$ of $\varepsilon_{abs,\beta}$ is 31.46º. The mean value $\bar{\varepsilon}_v$ of the percentage error in the bubble velocity magnitude is -15.50%. The standard deviation $\sigma_v$ of $\varepsilon_v$ is 7.12%. Table 9.14 also shows that calibration factor $K$ is 1.19.

### 9.2.5 Experiment 5

The experiments were carried out with a smaller bubble size of 5 mm. The data were collected for 80 seconds at a sampling rate of 40 KHz in a stream of rising bubbles. Table 9.15 shows the probe dimensions where $x_1$ = -0.19 mm, $y_1$ = 0.39 mm, $z_1$= 1.05 mm, $x_2$ = 0.40 mm, $y_2$ = -0.27 mm, $z_2$ = 1.05 mm, $x_3$ = 0.06 mm, $y_3$ = -0.50 mm, $z_3$ = 1.09 mm. Teflon-coated needles of 0.15mm diameter were used as a sensor to collect the data.

| | 1 | 2 | 3 |
|---|---|---|---|
| $x$ | -0.19 | 0.40 | 0.06 |
| $y$ | 0.39 | -0.27 | -0.50 |
| $z$ | 1.05 | 1.05 | 1.09 |

**Table 9.15 Probe dimensions for Experiment 5**

| | $\alpha_{ref}$ | $\beta_{ref}$ | $v_{ref}$ | $\alpha_{meas}$ | $\beta_{meas}$ | $v_{meas}$ | $\delta t_{11}$ | $\delta t_{22}$ | $\delta t_{33}$ | NOB |
|---|---|---|---|---|---|---|---|---|---|---|
| Test | (deg) | (deg) | ($ms^{-1}$) | (deg) | (deg) | ($ms^{-1}$) | (s) | (s) | (s) | |
| 1 | 0 | - | 0.38 | **4.44** | **-** | **0.37** | 0.005514 | 0.005779 | 0.006081 | 34 |
| 2 | 0 | - | 0.38 | **7.5** | **-** | **0.38** | 0.00544 | 0.005347 | 0.005808 | 27 |
| 3 | 0 | - | 0.38 | **2.73** | **-** | **0.41** | 0.005051 | 0.005284 | 0.005425 | 51 |
| 4 | 10 | 0 | 0.41 | **9.01** | **337.66** | **0.39** | 0.005666 | 0.005150 | 0.005289 | 58 |
| 5 | 10 | 90 | 0.41 | **9.98** | **82.04** | **0.44** | 0.004632 | 0.005054 | 0.004914 | 65 |
| 6 | 10 | 180 | 0.41 | **6.13** | **177.65** | **0.42** | 0.004815 | 0.005194 | 0.005468 | 54 |
| 7 | 20 | 0 | 0.35 | **22.41** | **7.27** | **0.36** | 0.006263 | 0.005052 | 0.004733 | 50 |
| 8 | 20 | 0 | 0.35 | **20.49** | **16.44** | **0.36** | 0.006228 | 0.005329 | 0.004938 | 31 |
| 9 | 20 | 180 | 0.35 | **19.17** | **188.31** | **0.33** | 0.005288 | 0.006780 | 0.007402 | 14 |

**Table 9.16 Results for reference polar angle 0°, 10° and 20° at various azimuthal angles**

Table 9.16 shows results of measured polar angle $\alpha_{meas}$, azimuthal angle $\beta_{meas}$ and velocity magnitude $v_{meas}$ for the reference polar angle $\alpha_{ref}$ = 0º , 10º and 20º calculated with various reference azimuthal angles $\beta_{ref}$ . The reference velocity $v_{ref}$ = 0.38 m/s when $\alpha_{ref}$ = 0º, $v_{ref}$ = 0.41 m/s when $\alpha_{ref}$ = 10º and $v_{ref}$ = 0.35 m/s when $\alpha_{ref}$ = 20º. Table 9.16 also shows the average time interval $\delta t_{ii}$ ($i$ =1, 2 and 3) and the total number of bubbles (NOB) that hit all four sensors.

| Test | $\varepsilon_{abs,\alpha}$ (deg) | $\varepsilon_{abs,\beta}$ (deg) | $\varepsilon_v$ (%) | $K$ |
|---|---|---|---|---|
| 1 | 4.44 | - | -2.63 | 1.03 |
| 2 | 7.5 | - | 0.00 | 1.00 |
| 3 | 2.73 | - | 7.89 | 0.93 |
| 4 | -0.99 | -22.34 | -4.88 | 1.05 |
| 5 | -0.02 | -7.96 | 7.32 | 0.93 |
| 6 | -3.87 | -2.35 | 2.44 | 0.98 |
| 7 | 2.41 | 7.27 | 2.34 | 0.98 |
| 8 | 0.49 | 16.44 | 1.75 | 0.98 |
| 9 | -0.83 | 8.31 | -6.73 | 1.07 |
| | $\bar{\varepsilon}_{abs,\alpha}$ | $\bar{\varepsilon}_{abs,\beta}$ | $\bar{\varepsilon}_v$ | Average |
| | **1.32** | **-0.10** | **0.83** | **0.99** |
| | **3.17** | **10.33** | **4.72** | |
| | $\sigma_{abs,a}$ | $\sigma_{abs,\beta}$ | $\sigma_v$ | |

**Table 9.17 Errors in the values of polar angle, azimuthal angle and velocity magnitude of the results presented in Table 9.16**

In Table 9.17, the absolute errors $\varepsilon_{abs,\alpha}$ and $\varepsilon_{abs,\beta}$ in degrees, for the values of $\alpha_{meas}$ and $\beta_{meas}$ respectively, are presented. From the data, the mean value $\bar{\varepsilon}_{abs,\alpha}$ of the absolute error in $\varepsilon_{abs,\alpha}$ is equal to 1.32º and the standard deviation $\sigma_{abs,a}$ of $\varepsilon_{abs,\alpha}$ is 3.17º. The mean value $\bar{\varepsilon}_{abs,\beta}$ of the absolute error in $\varepsilon_{abs,\beta}$ is equal to -0.10º and the standard deviation $\sigma_{abs,\beta}$ of $\varepsilon_{abs,\beta}$ is 10.33º. The relatively low values of $\bar{\varepsilon}_{abs,\alpha}$ and $\bar{\varepsilon}_{abs,\beta}$ indicate that these miniature probes can be used to give a reasonably accurate estimate of the polar angle $\alpha$ and azimuthal angle $\beta$ of the bubble velocity vector. The values for the standard deviation $\sigma_{abs,a}$ and $\sigma_{abs,\beta}$ do, however, indicate that, for some of the individual tests carried out, the errors in $\alpha_{meas}$ and $\beta_{meas}$ were somewhat greater that would be suggested by inspection of $\bar{\varepsilon}_{abs,\alpha}$ and $\bar{\varepsilon}_{abs,\beta}$.

The mean value $\bar{\varepsilon}_v$ of the percentage error in the bubble velocity magnitude is 0.80%. The standard deviation $\sigma_v$ of $\varepsilon_v$ is 4.75%. The observed value of $\bar{\varepsilon}_v$ is somewhat surprising because, as stated in [1,11], a previously used conventional four-sensor

probe had a retarding effect of up to 20% and in that particular paper it was 6% on the bubble velocity magnitude. It should be noted that in Table 9.16 the values of $\alpha_{meas}$, $\beta_{meas}$ and $v_{meas}$ for a given test are averaged values obtained from (typically) 30 bubbles. It should also be noted that when $\alpha_{ref} = 0^o$ then both $\beta_{ref}$ and $\beta_{meas}$ are meaningless. Table 9.17 also shows that calibration factor $K$ is 0.99.

## 9.3 Discussion

In the above sections, the tests were conducted for two different sizes of bubble: 5mm (smaller) and 10 mm (larger), two sensor diameters (0.15mm and 0.25 mm) and the probe dimensions. The results show that bigger bubbles tend to deform more rapidly than smaller ones as they move upwards. The experiment also shows that when using a probe with 0.25mm diameter needles there is a greater possibility of affecting the shape and the trajectory of the bubble before the bubble comes into contact with the rear sensor after leaving the front sensor. A similar situation occurred during the experiment with the various lengths of the $z_i$ dimension. If the length of $z_i$ is longer (>1.5mm), it will provide enough time for the bubble to change its shape before hitting the rear sensor (note: a rising bubble continuously changes its shape and a bubble bigger than 5mm deforms/changes its shape rapidly as it flows upwards). Hence, to avoid these situations, it was suggested that the dimension of $z_i$ should be approximately 1mm and the bubble size no more than 5mm. In the meantime, as the dimension of $z_i$ becomes smaller, the data are to be collected with a higher sampling frequency (see Chapter 3 for detail). All the above mentioned experiments were carried out with a stream of bubbles. From the experiments, it was also found that, for good accuracy of results, it is important that the number of bubbles that hit all four

sensors must be approximately more than 30. Thus, to ensure the required number of bubbles hit the sensors, it is important to sample the data for more than one minute. From the above discussion, for an accurate measurement of $\alpha_{meas}$ and $\beta_{meas}$, it is recommended the following criteria should be met:

- Bubble Size: 5mm
- Sensor type: 0.15mm Teflon coated needles
- Dimension of $z_i$: 1-1.5m
- Sampling frequency: 40K Hz
- Sampling time: >1 minute
- Number of bubbles: > 30
- Stream of bubbles.

The four-sensor probe described in Chapter 3 for measuring the velocity vectors of individual gas bubbles in gas-liquid flows was used to measure the $\alpha, \beta \, and \, v$ in a stream of gas bubbles. The probe was tilted by $\alpha^*$ and rotated by $\beta^*$, as described in Chapter 7, to change velocity vector with respect to the probe. Gas bubbles were assumed to rise vertically relative to the tank. The reference velocity magnitude was calculated by using two high speed cameras arranged orthogonally to the tank. Since the gas bubbles were assumed to rise vertically relative to the tank, reference polar angle $\alpha_{ref}$ and azimuthal angle $\beta_{ref}$ were equal to $\alpha^*$ and $\beta^*$ (for further details see Chapter 7.2). The results from Experiment 5 show that there is good agreement between the reference data and the measured data. It can also be noticed that, for the smaller polar angle $\alpha$, the error is somewhat larger than that of the larger polar angle $\alpha$, which is still less then ±10%, whereas for the larger polar angles, the errors

were found to be less than ±1%. However, the results still show a few errors, which could be due to the effects described by Juila et al. [131]. These results may recommend the new technique of mounting the probes (see further works). The results also suggest improvements in calibration factor *K,* which is now around 0.99, whereas in previous experiments the value of *K* was shown to be 1.2, although that varies ± 20% [1, 11]. The improved calibration factor *K* indicates there is less retarding effect during probe-bubble interaction.

The above results also show that the greater the polar angle, the lesser the errors, which shows good agreement with the results presented by Sanaullah et al. [150], where the author states that the probe has less effect on the bubble when it is tilted by 20° (polar angle) . The author also states that the effect of the probe rises as the probe inclination becomes closer to 55° (polar angle).

The results from the high speed cameras allowed an initial simplifying assumption to be made that the velocity vector $\mathbf{V_{bt}}$ of each bubble relative to the tank was purely in the vertical direction. Given this simplifying assumption, angles $\alpha^*$ and $\beta^*$ by which the probe is rotated relative to the tank coordinate system are respectively equal to $\alpha_{ref}$ and $\beta_{ref}$. Bubble velocities relative to the water tank (as the bubble moves over a vertical probe), the COG result for $\alpha^*$ is interesting in its own right because visual observation of a rising bubble stream suggests a zigzag motion which would lead the observer to think that $\alpha^*$ was significantly greater than the actual measured value as the bubble moves over the probe. It also shows that, as bubbles move across the probe, they move in the direction of BUOYANCY force on COG (later motion appears to be suppressed). This result could not be determined without high speed cameras**.**

# CHAPTER 10

## Flow Loop Experimental Set Up

### 10.1 The multiphase flow loop for air-water experiments

Figures 10.1A and 10.1B show photographic and schematic layouts of the flow loop which was used to carry out testing of the probes in multiphase flow. The facility was capable of producing the necessary flow conditions relevant to the present investigation. Different flow conditions used in the experiment investigation described in Chapter 11 required a variety of air flow rates, water flow rates, and gas volume fractions.

It was necessary to be able to position the working section (i.e. that part of the multiphase loop where the measurements take place) perpendicular to the ground. Some of the experiments were carried out in swirling flow in which a swirler was used to generate swirl in the working section. The volumetric flow rate of the water $Q_w$ in the working section was measured using a turbine flow meter; while the gas flow rate, $Q_g$ was measured using a thermal mass flow meter, a temperature sensor and a pressure sensor. These were installed in the system as shown in Figure 10.1 B. A differential pressure (DP) cell was used for the measurement of the mean gas volume fractions $\overline{\lambda}$ in the flow loop working section. The principles of the operations of these instruments are described later in this chapter.

The flow loop that was used was capable of producing a single stream of bubbles for a single bubble flow experiment. The flow loop is also able to produce a swarm of bubbles for the experiment, with or without the presence of swirl.

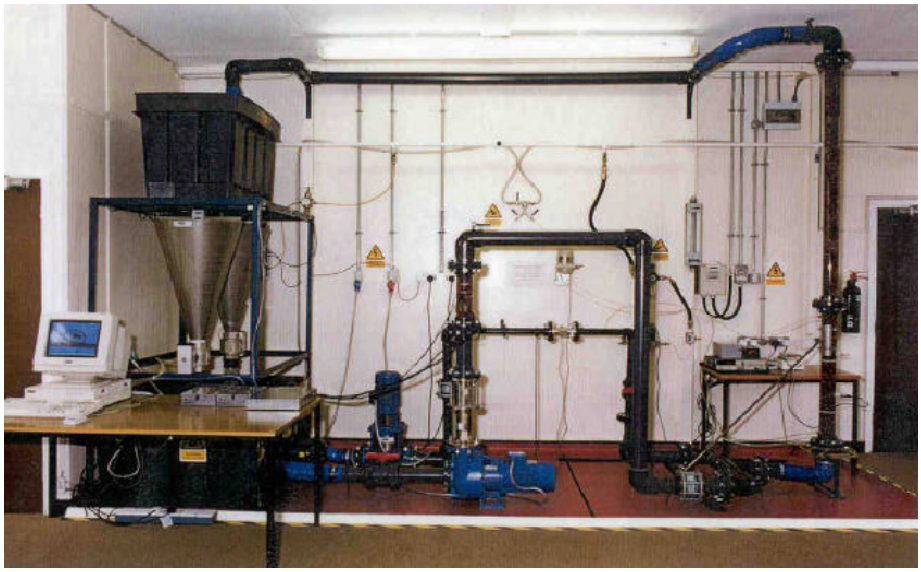

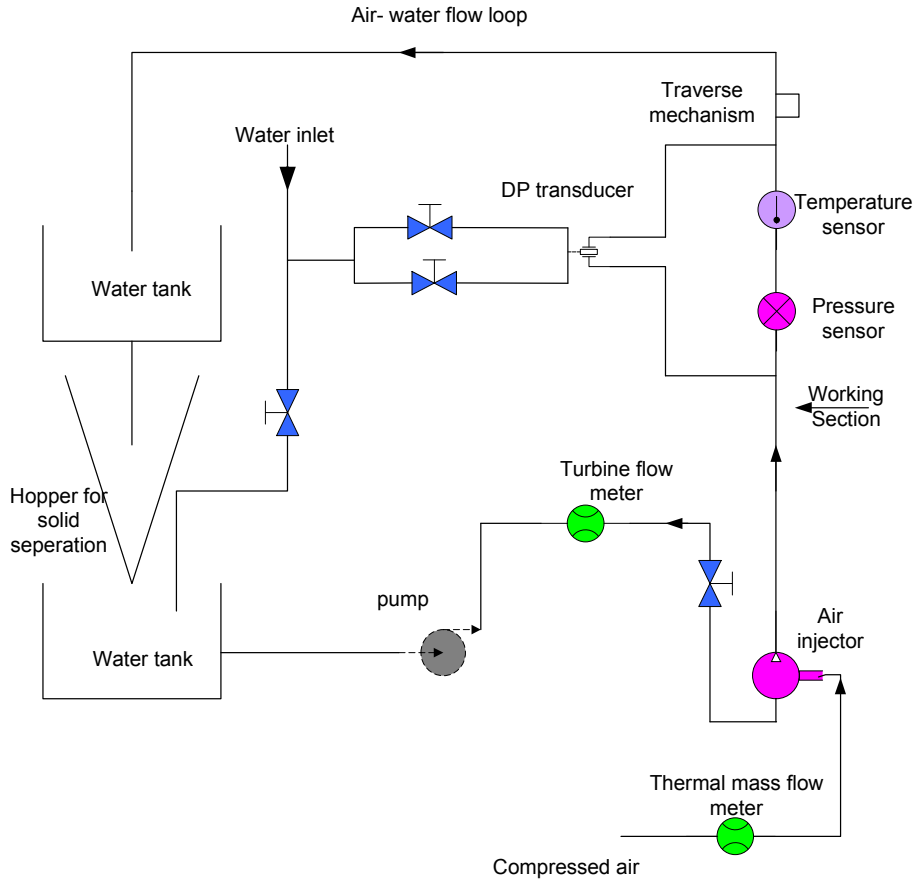


**Figure 10.1 (A) Photographic image of the flow loop which can also be used for solid-water flow and (B) Schematic diagram of air-water multiphase loop used for the current experiments.**

## 10.2 Reference measurement devices

The reference measurement devices that are described below were used in the air-water flow loop to measure volumetric flow rate of the water $Q_w$, volumetric gas flow rate $Q_g$ and mean gas volume fractions $\overline{\lambda}$.

### 10.2.1 Thermal mass flow meter

With respect to Figure 10.1, pressurised air from the laboratory compressed air supply was passed through a regulator and a thermal mass flow meter, in order to measure the gas mass flow rate $M_g$. Measurements of the absolute pressure $P_{abs}$ and absolute temperature $T_{abs}$, in the working section, enabled the mean gas volumetric flow rate $Q_g$ to be determined from the measured $M_g$ as shown in Equation 10.1.

$$Q_g = M_g \frac{T_{abs}}{P_{atm} + P_{abs}} \left(9.81\ \rho_m\right) \qquad \textbf{Equation 10.1}$$

where $P_{atm}$ denotes atmospheric pressure and $\rho_m$ mercury density. The air superficial velocity $U_{gs}$ was then calculated using the following formula:

$$U_{gs} = \frac{Q_g}{A} \qquad \textbf{Equation 10.2}$$

where $A$ represents the cross-sectional area of the working section.

### 10.2.2 Turbine meter

Turbine meters were installed in the liquid lines of the flow loop; they were used to measure the water volumetric flow rate delivered by the relevant pumps. The principle of the turbine meter operation is that the number of rotations per second of the turbine

rotor is a function of the flow rate of the liquid. Therefore, by counting the frequency of the rotations of the turbine rotor, it is possible to determine the measurement of the water flow rate. A turbine meter is designed to have a linear relationship between the flow rate and the frequency of the rotation over a range of flow rates. The relationship can be expressed by the following formula:

$$Q_w = Kf \qquad \textbf{Equation 10.3}$$

where $Q_w$ is the volumetric flow rate of water; $f$ is the frequency of the rotation and $K$ is the meter factor for the device, which can vary as the meter begins to wear. For the turbine meter, the meter factor $K$ for the liquid line of the air-water loop was given by the manufacturer as $0.0462 m^3 h^{-1} Hz^{-1}$ over a design range of $3.41 m^3 h^{-1}$ to $40.88 m^3 h^{-1}$.

### 10.2.3 Gas volume fraction measurement using a differential pressure sensor

A Honeywell ST-3000 differential pressure sensor was installed in the working section of the flow loop. This instrument was used to measure the differential pressure across a one metre length of the working section. A flushing system was installed in the DP cell in order to ensure that no air could get trapped in either the sensor or the fluid filled measurement lines which connected the sensor to the pressure tapping of the working section (see Figure 10.1A). The differential pressure sensor was used to calculate the volume fraction of the air, as demonstrated below.

The method of calculating the volume fraction of the dispersed phase is adopted as described by Panagiotopoulos et al. [12]. Assuming that the pressure tappings, which are in the working section, are separated by distance $h$ and that the pipe is inclined by

$\psi$ degrees from the vertical, which is zero in these experiments, then the mean volume fraction $\overline{\lambda}$ of the dispersed phase can be calculated as:

$$\overline{\lambda} = \frac{\Delta p + F}{(\rho_w - \rho_d)\cdot g \cdot h \cdot \cos\psi} = \frac{\Delta p + F}{(\rho_w - \rho_d)\cdot g \cdot h} \qquad \textbf{Equation 10.4}$$

where $g$ depicts the acceleration due to gravity; $\Delta p$ is measured by differential pressure; $\rho_w$ and $\rho_d$ are the densities of water and the dispersed phase (gas) respectively; $\cos\psi$ is equal to one; and $F$ is the frictional pressure loss. The frictional pressure with reference to [12] can be calculated as follows:

$$F = \frac{f \cdot h \cdot \rho_w \cdot U_h^{\,2}}{2 \cdot M} \qquad \textbf{Equation 10.5}$$

where $f$ is the single-phase friction factor given by Equation 10.6 and $M$ is the hydraulic radius of the working section flow loop and calculated as shown in Equation 10.6 :

$$f = \frac{D \Delta p}{2 \rho_w h v_w^2} \qquad \textbf{Equation 10.6}$$

where $D$ represents the diameter of the pipe; $\Delta p$ is the pressure difference; $\rho_w$ is the density of the water and $v_w$ is the velocity of the water.

$$M = R \qquad \textbf{Equation 10.7}$$

where $R$ denotes the internal radius of the working section and $U_h$ the homogeneous velocity, which is the sum of the water and gas (air) superficial velocities $U_{ws}$ and $U_{gs}$ respectively. In detail:

$$U_h = U_{ws} + U_{gs}$$ **Equation 10.8**

where

$$U_{gs} = \frac{Q_g}{\pi \cdot (R_1^2 - R_2^2)}$$ **Equation 10.9**

$$U_{ws} = \frac{Q_w}{\pi \cdot (R_1^2 - R_2^2)}$$ **Equation 10.10**

and $Q_w$ and $Q_g$ are the volumetric flow rates of water and gas respectively.

## 10.3 Experiment with a single stream of bubbles

The experiment was carried out in the stream of bubbles. The purpose of the experiment was to measure the velocity vector of a bubble using a four-sensor probe. To vary the reference velocity vector **V** of the bubble relative to the probe in the flow loop, it was not practical to use the method described in Chapter 8 to position the probe.

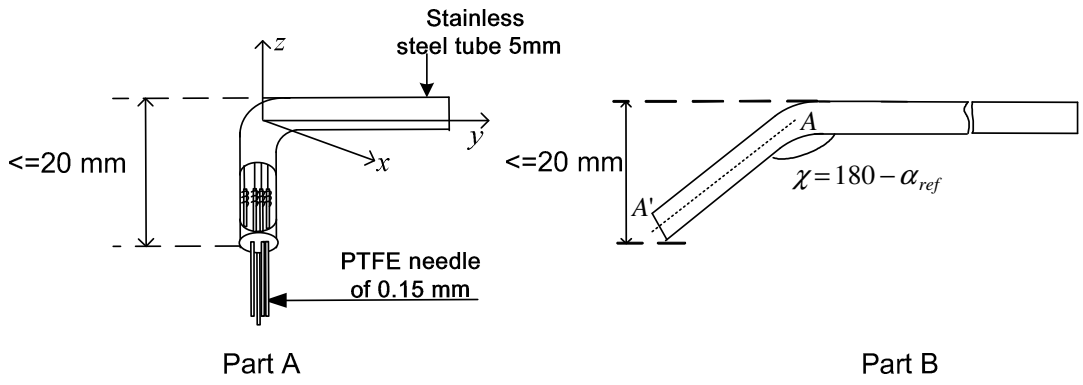


**Figure 10.2 (A) Four-sensor probe for the flow loop. (B) Probe holder with various angles**

Therefore, a new method of supporting the probe was introduced, which necessitated

making the probe in two sections. The first section (part A) of the probe contained the four sensors, as described in Chapter 3.14 (see Figure 10.2, left). The overall length of the probe was designed to be no longer than 20mm, so that the final support and mechanism would fit into the working section of the flow loop. The second section of the probe (part B in Figure 10.2), was made using a specific angle to represent the reference polar angle as shown in Figure 10.2 (B). Assuming that bubbles rise purely vertically, the velocity vector **V** of the approaching bubbles will make a reference polar angle $\alpha_{ref}$ relative to the $z$-axis of the probe.

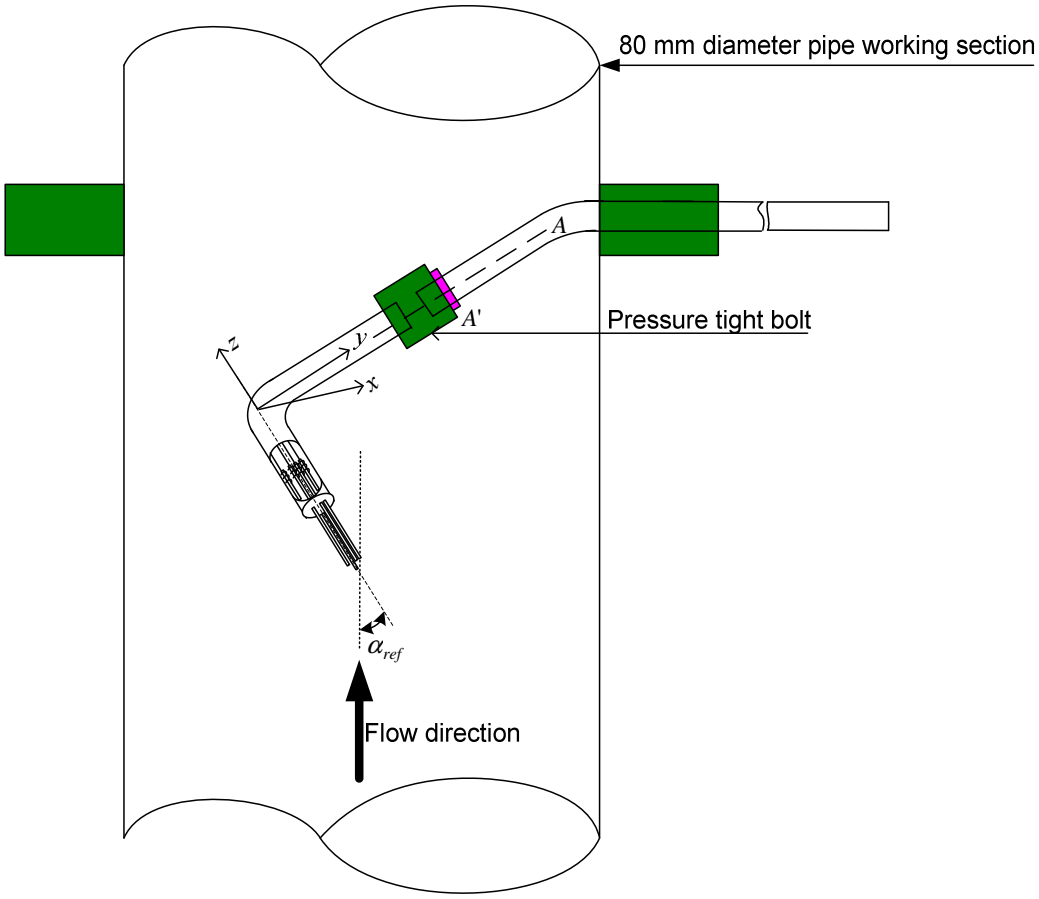


**Figure 10.3 Part A and Part B of the four-sensor probe connected with pressure tight bolts and mounted in the flow loop using a traverse mechanism.**

The probe was measured, as described in Chapter 3.3, before the probe and the holder were connected together using a pressure tight bolt (to ensure that there was no

leakage), as shown in Figures 10.3 and 10.4. When placing the probe and the probe holder together, it was ensured that the $y$ - axis of the four-sensor probe was aligned with the $AA'$ of the probe holder, as shown in Figure 10.2 B and 10.3.

Part B was connected to Part A so that both part A and part B lay within the same vertical plane when the probe was mounted in the pipe; this ensured that both $z$ and $y$ axis of the probe coordinate system also lay in the same vertical plane. This alignment ensured that the reference azimuthal angle $\beta_{ref}$ of the bubble relative to the probe coordinate system was always 0°, provided that gas bubbles rise purely vertically, which is generally the case when water is flowing[13],.

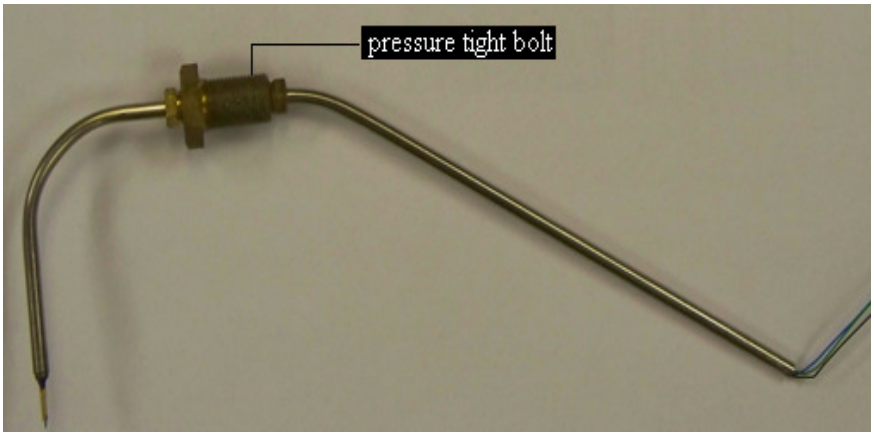


**Figure 10.4 Probe for the flow loop with 34° polar angle $\alpha$**

Probes set at various angles $\chi$ giving values of $\alpha_{ref}$ equal to 5°, 14°, 21° and 34° were manufactured, as shown in Figure 10.3.

## 10.4. Experiment with a swirler in a swarm of bubbles

The experiment was carried out in a swarm of bubbles with the presence of a swirler. The purpose of the swirler was to create a necessary azimuthal and vertical motion of the flow in which the air bubble was moving. A four-sensor probe designed with

Teflon coated needles, described in Chapter 3.2 (see Figure 3.11), was used to measure the mean gas volume fraction, azimuthal velocity, axial velocity and the radial velocity across the cross section of the pipe. A traverse mechanism was used to move the probe across the cross section of the pipe.

### 10.4.1 Swirler device

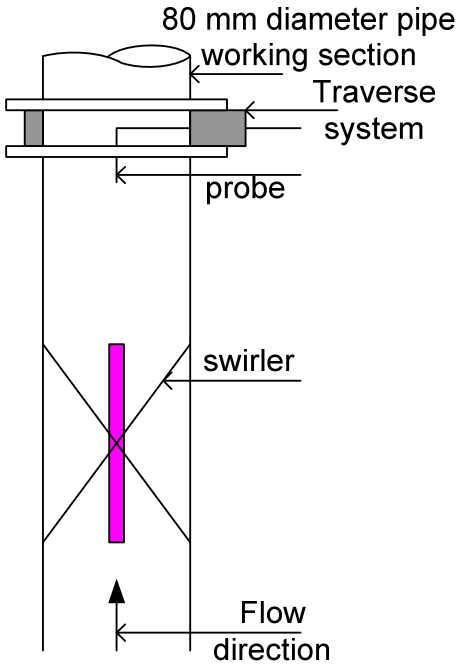


**Figure 10.5 Working section of air-water flow loop with swirler**

The swirler consisted of six brass vanes which were welded to a central brass hub measuring 10mm in diameter. For this experiment, the swirl angle was set at 20° and the design of the vanes was based on the criteria suggested by Mathur et al. [162]. In order to accommodate the swirler in the working section of the pipe, the outer diameter of the swirler measured 80mm; this, in turn, was housed in a flanged clear pipe section with an internal diameter measuring 80mm. The swirler was placed in the working section upstream of the probe, as shown in Figure 10.5. Figure 10.6 shows a picture of the swirler that was used in the experiments.

**Figure 10.6 The swirler device in the air-water flow loop.**

### 10.4.2 Traverse mechanism

A traverse mechanism was used to reposition the probe in the cross section of the pipe. In this device, two separate stepper motors were utilised to achieve the linear and the angular movements required of the probe. Both the stepper motors were powered by a programmable stepper motor driver, which supplied the chain of the pulse to each stepper motor. This, in turn, provided the necessary signal to move the probe in the correct direction.

***A) Linear Traverse Mechanism***

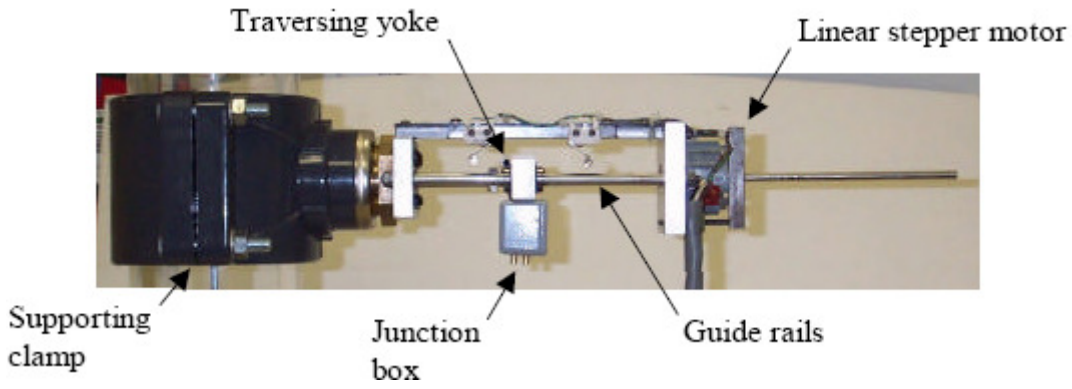


**Figure 10.7 The linear traverse mechanism**

The linear traverse mechanism, shown in Figure 10.7, consisted of a linear stepper motor, a guide rail, a traversing yoke, a supporting clamp and a junction box. The traverse mechanism was mounted on the side wall of the pipe which contained a small hole; this hole was used to insert the probe into the pipe. The supporting clamp was used to hold the linear traverse system inline with the pipe, which also provided the support for the traverse mechanism. In order to prevent leakage of water from the hole, an "O" ring was used as a seal. The body of the probe was clamped onto the traversing yoke in order to ensure rigidity. The traversing yoke itself was fixed at the guide rail, thereby enabling it to move forwards and backwards freely; it was also attached to the screwed shaft of the stepper motor. Hence, when the motor was rotated, the shaft also screwed and unscrewed, thereby additionally simultaneously moving the yoke forwards and backwards.

This resulted in the probe, attached with the traversing yoke, moving forwards and backwards, which helped to achieve the desired radial position of the probe. The linear traverse could make the probe move in increments of 0.025mm in a straight line. A junction box was used to connect the wires from the probe, which was connected to the electronic circuitry described in Chapter 5.

***A) Rotary Traverse Mechanism***

A rotary traverse mechanism was used for the angular movement of the probe within the working section of the pipe. It consisted of a stepper motor, a geared ring and a mechanical support to hold them together. The shaft of the stepper motor was connected to the geared ring, thereby allowing for the rotation of the geared ring when the stepper motor was rotated. This, in turn, rotated the pipe attached to the geared ring. When this pipe was rotated, the probe also rotated simultaneously. This rotary traverse was capable of moving the probe in angular steps of 0.015°. In order to avoid

any leakage from the traverse mechanism; it was connected to the section of the pipe with sealed stainless steel bearings mounted into flanges. Figure 10.8 shows the whole traverse mechanism used in the current experiments.

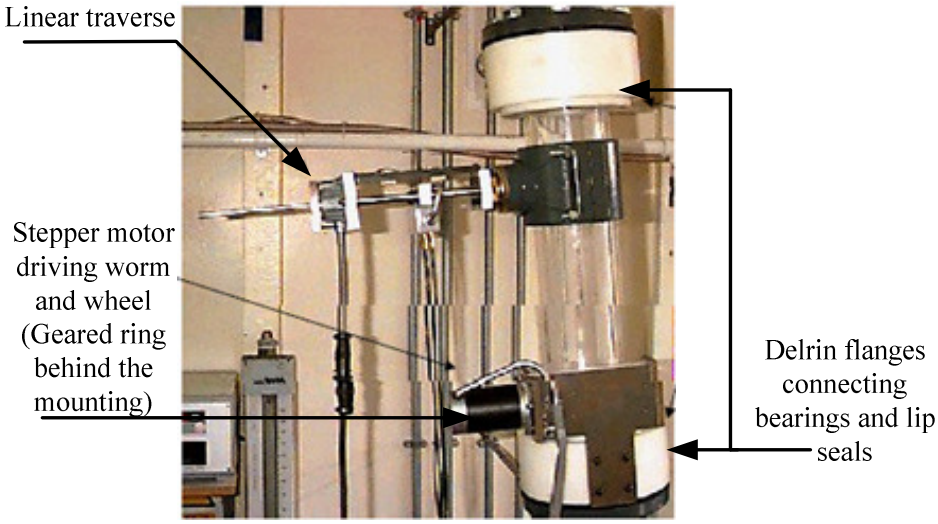


**Figure 10.8 The traverse mechanism in air-water loop [7]**

# CHAPTER 11

## Flow Loop Experimental Results

A series of experiments were carried out in a flow loop with and without the presence of swirl in a single stream of bubbles as well as a swarm of bubbles.

### 11.1 Flow loop experiments

This section presents the results from the experiment carried out in a single stream of bubbles, making the volume fraction of the dispersed phase negligible. The experiments were conducted without the presence of swirl. A turbine meter was used in order to measure the volumetric flow rate $Q_w$ of water, which in turn was used to calculate the superficial velocity of the water using Equation 11.1. At the beginning of the experiments, the velocity magnitude of the bubbles was measured using a single high speed camera at various water flow rates. The assumption was made that the measured velocity magnitude remained the same throughout the experiments at a given water flow rate, although there might have been a slight variation in the velocity magnitude of the bubble at a given flow rate due to the variation of the bubble frequency and resultant wake effects. However, an effort was made to maintain the constant bubble frequency at a given water flow rate.

Table 11.1 shows the reference velocity magnitude $v_{ref}$ of a bubble of 5 mm diameter, obtained by using the high speed camera at various water superficial velocities $U_{ws}$, given by Equation 11.1.

$$U_{ws} = \frac{Q_w}{\pi R^2}$$ **Equation 11.1**

where $Q_w$ is the volumetric flow rate of water obtained from Equation 11.2, $R$ is the internal diameter of the working section.

$$Q_w = \frac{0.0462 * f}{3600} m^3 s^{-1}$$ **Equation 11.2**

where $f$ is the frequency in Hz from the turbine flow meter installed in the flow loop.

| $U_{ws}$ (m/s) | 0.00 | 0.14 | 0.18 | 0.27 | 0.30 |
|---|---|---|---|---|---|
| $v_{ref}$ (m/s) | 0.25 | 0.34 | 0.39 | 0.49 | 0.52 |

**Table 11.1 Reference bubble velocity for given turbine meter readings**

The flow loop experiments in a single stream of bubbles were carried out for various values of water superficial velocity $U_{ws}$ with different reference polar angles $\alpha_{ref}$ at 5°, 14°, 21° and 34° at reference azimuthal angle $\beta_{ref}$ = 0°. From the results of the tank experiments, it was observed that the best probe to use was a Teflon coated probe with sensor needles with an outer diameter of 0.15mm. Hence, in these flow loop experiments, Teflon-coated probes were used, but due to the presence of flowing water velocity, 0.2mm diameter sensor needles were used instead of 0.15 mm in order to provide more rigidity. DC circuits, which were described in Chapter 5, were used to measure the conductance at the tip of each probe sensor. Data was collected for a period of 90 seconds (sampling period) for the twenty different experimental conditions described above (four values of $\alpha_{ref}$ and five values of $v_{ref}$), to ensure that as many bubbles as possible hit the probe during the sampling period. The number of bubbles (NOB) that hit the probe ranged from 21 to 74 for the different flow

conditions investigated. The signals from the probe were treated in a number of different ways, as described below, to determine the mean velocity vectors measured by the probe at each flow condition.

**A)** The collected data was analysed twice, first without signal processing (referred to as BS or "before signal processing" later in this chapter), where the data were processed without ignoring any bubbles, as described in section 6.2. The second analysis was conducted with signal processing (referred to as AS or "after signal processing" later in this chapter), where the same data was processed again, only this time the condition to ignore the bubbles was introduced, as described in section 6.2.

**B)** For each flow condition investigated, the probe that was used to collect the data was measured twice, once before collecting the data and again after collecting the data. The velocity vector of bubbles was calculated with both probe dimensions. Results calculated using the probe dimensions measured before data collection are referred to as 'PMB' (Probe Measured Before) whilst results calculated using the probe dimensions measured after data collection are referred to as 'PMA'. The purpose of this part of the investigation was to determine whether small changes in the probe dimensions, brought about by the flowing air-water mixture, would significantly affect the bubble velocity vectors measured by the probe.

**C)** The values of polar angle $\alpha_{meas,m,p}$ , azimuthal angle $\beta_{meas,m,p}$ and the velocity magnitude $v_{meas,m,p}$ measured by the probe for the $m^{th}$ flow condition and the $p^{th}$ value of $\alpha_{ref}$ were calculated in two different ways, as described below.

**I)** "Average $\delta t_{ii}$": In this method, for the $m^{th}$ flow condition and the $p^{th}$ value of $\alpha_{ref}$ the time interval $\delta t_{ii,m,p,n}$ $(i = 1,2,3)$ for each of *N* number of useful bubbles were calculated according to Equation 2.33 and then average values for $\delta t_{ii,m,p}$ $(i = 1,2,3)$ were calculated using Equation 11.3. These calculated average values for $\delta t_{ii,m,p}$ were then used in conjunction with the relevant measured probe dimensions to calculate $\alpha_{meas,m,p}$, $\beta_{meas,m,p}$ and $v_{meas,m,p}$, as described in section 2.5.1.

$$\delta t_{ii,m,p} = \frac{\sum_{n=1}^{n=N} \delta t_{ii,m,p,n}}{N} \qquad \textbf{Equation 11.3}$$

where *m* refers to $m^{th}$ flow condition and *n* refers to $n^{th}$ useful bubble $p^{th}$ value of $\alpha_{ref}$.

**II**) "Average individual bubble": In this method, for the $m^{th}$ flow condition and the $p^{th}$ value of $\alpha_{ref}$, values of $\alpha_{meas,m,p,n}$, $\beta_{meas,m,p,n}$ and $v_{meas,m,p,n}$ for each of the *N* individual useful bubbles were calculated, as described in section 2.5.1, from the measured values of $\delta t_{ii,m,p,n}$ $(i = 1, 2\ and\ 3)$ and the measured probe dimensions . From the calculated values of $\alpha_{meas,m,p,n}$, $\beta_{meas,m,p,n}$ and $v_{meas,m,p,n}$ average values $\alpha_{meas,m,p}$, $\beta_{meas,m,p}$ and $v_{meas,m,p}$ of the measured polar and azimuthal angles and the bubble velocity magnitude were obtained using Equations 11.4, 11.5 and 11.6.,

$$\alpha_{meas,m,p} = \frac{\sum_{n=1}^{n=N} \alpha_{meas,m,p,n}}{N} \qquad \textbf{Equation 11.4}$$

$$\beta_{meas,m,p} = \frac{\sum_{n=1}^{n=N} \beta_{meas,m,p,n}}{N}$$ **Equation 11.5**

$$v_{meas,m,p} = \frac{\sum_{n=1}^{n=N} v_{meas,m,p,n}}{N}$$ **Equation 11.6**

From **(A), (B)** and **(C)** above it is clear that, for the $m^{th}$ flow condition and the $p^{th}$ value of $\alpha_{ref}$, there are eight different ways of calculating $\alpha_{meas,m,p}$, $\beta_{meas,m,p}$ and $v_{meas,m,p}$. It should be noted that the range of possible values for $\beta_{meas,m,p}$ was converted to $-180^{o} \le \beta_{meas,m,p} \le 180^{o}$ using Equation 11.7 if $\beta_{meas,m,p} > 180^{o}$

$$\beta_{meas,m,p} = \beta_{meas,m,p} - 360^{o}$$ **Equation 11.7**

For the $m^{th}$ flow condition and the $p^{th}$ value of $\alpha_{ref}$, an absolute error $\varepsilon_{abs,\alpha,m,p}$, $\varepsilon_{abs,\beta,m,p}$ and $\varepsilon_{abs,v,m,p}$ in the calculated value of $\alpha_{meas,m,p}$, $\beta_{meas,m,p}$ and $v_{meas,m,p}$ was calculated. Magnitudes of the absolute error in the calculated values of $\alpha_{meas,m,p}$, $\beta_{meas,m,p}$ and $v_{meas,m,p}$ for $m^{th}$ flow condition were calculated, as shown in Equations 11.8, 11.9 and 11.10 respectively.

$$\varepsilon_{abs,\alpha,m,p} = |\alpha_{meas,m,p} - \alpha_{ref}|$$ **Equation 11.8**

$$\varepsilon_{abs,\beta,m,p} = |\beta_{meas,m,p} - \beta_{ref}|$$ **Equation 11.9**

$$\varepsilon_{abs,v,m,p} = \left( \left| \left( \frac{v_{meas,m,p} - v_{ref}}{v_{ref}} \right) 100 \right| \right)\%$$ **Equation 11.10**

From the above calculated absolute errors for the measured values of $\alpha_{meas,m,p}$, $\beta_{meas,m,p}$ and $v_{meas,m,p}$, the mean error and the standard deviation of the error for all the flow conditions investigated at the $p^{th}$ value of $\alpha_{ref}$ were also calculated, as shown in Equations 11.11 – 11.16, where $M$ is the total number of different flow conditions investigated for each value of $\alpha_{ref}$ (i.e $M$ = 5 in present study).

$$\bar{\varepsilon}_{abs,\alpha,p} = \frac{\sum_{1}^{M} \varepsilon_{abs,\alpha,m,p}}{M} \qquad \textbf{Equation 11.11}$$

$$\bar{\varepsilon}_{abs,\beta,p} = \frac{\sum_{1}^{M} \varepsilon_{abs,\beta,m,p}}{M} \qquad \textbf{Equation 11.12}$$

$$\bar{\varepsilon}_{abs,v,p} = \frac{\sum_{1}^{M} \varepsilon_{abs,v,m,p}}{M} \qquad \textbf{Equation 11.13}$$

$$\sigma_{abs,\alpha,p} = \sqrt{\frac{\sum_{1}^{M} \left(\varepsilon_{abs,\alpha,m,p} - \bar{\varepsilon}_{abs,\alpha,m,p}\right)^2}{M}} \qquad \textbf{Equation 11.14}$$

$$\sigma_{abs,\beta,p} = \sqrt{\frac{\sum_{1}^{M} \left(\varepsilon_{abs,\beta,m,p} - \bar{\varepsilon}_{abs,\beta,m,p}\right)^2}{M}} \qquad \textbf{Equation 11.15}$$

$$\sigma_{abs,v,p} = \sqrt{\frac{\sum_{1}^{M} \left(\varepsilon_{abs,v,m,p} - \bar{\varepsilon}_{abs,v,m,p}\right)^2}{M}} \qquad \textbf{Equation 11.16}$$

$\bar{\varepsilon}$ and $\sigma$ are respectively the mean error and the standard deviation of the error $\varepsilon$ in a given property for a given set of flow conditions. From the arguments above, it is clear that there are eight possible ways in which $\bar{\varepsilon}_{abs,\alpha,p}, \bar{\varepsilon}_{abs,\beta,p}, \bar{\varepsilon}_{abs,v,p}$,

$\sigma_{abs,\alpha,p}$ $\sigma_{abs,\beta,p}$ and $\sigma_{abs,v,p}$ can be calculated. These eight possible ways are summarised in Flow chart 11.1 below.

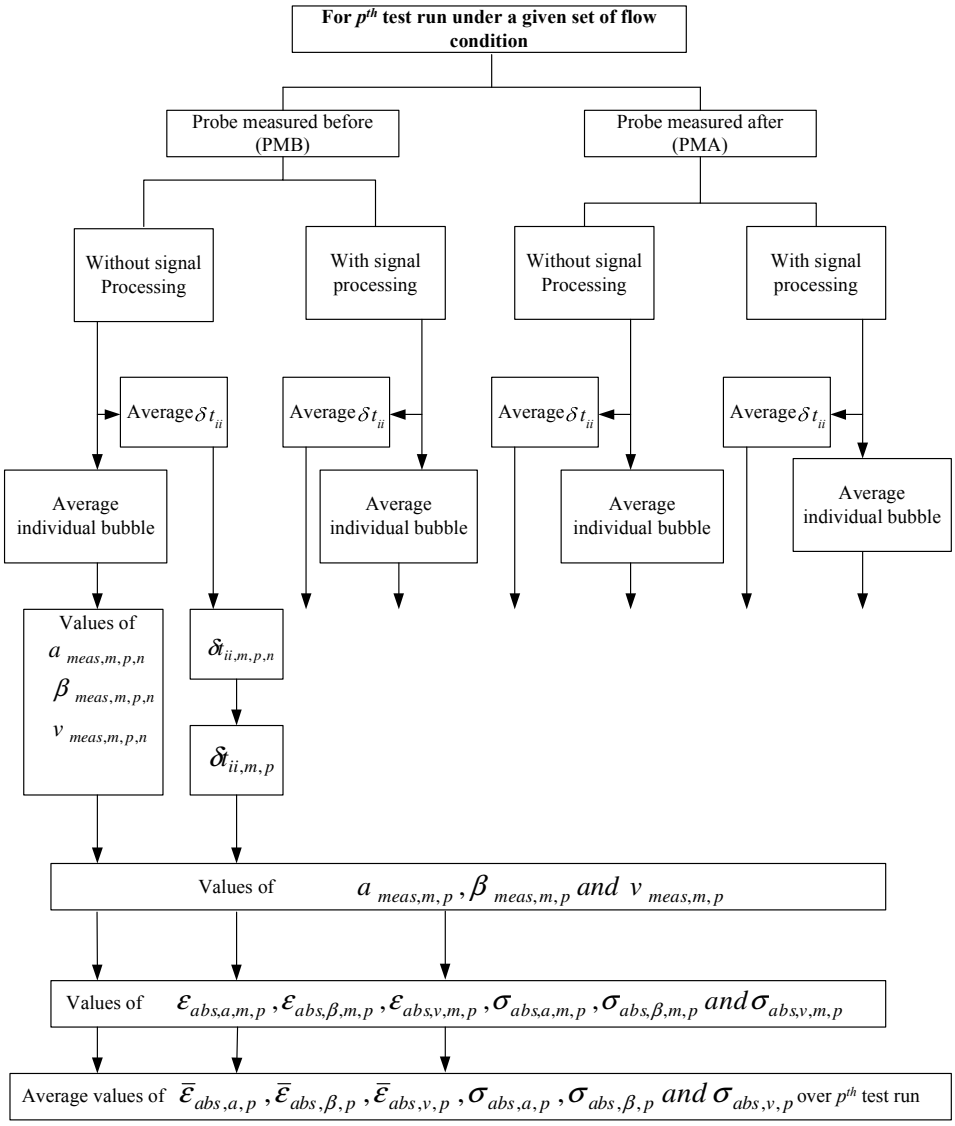


**Flow chart 11.1 Calculation of $\bar{\varepsilon}_{abs,\alpha,p}$, $\bar{\varepsilon}_{abs,\beta,p}$, $\bar{\varepsilon}_{abs,v,p}$, $\sigma_{abs,\alpha,p}$ $\sigma_{abs,\beta,p}$ and $\sigma_{abs,v,p}$ for the flow conditions investigated at the $p^{th}$ value of $\alpha_{ref}$**

### 11.1.1 Calculation of $\alpha_{meas,m}$, $\beta_{meas,m}$ and $v_{meas,m}$ for $\alpha_{ref}$ of 5°, 14°, 21° and 34° and for reference azimuthal angle $\beta_{ref}$ of 0° at various values of $v_{ref}$

This experiment was carried out in the flow loop for reference polar angles $\alpha_{ref}$ of 5°,

14°, 21° and 34° and for reference azimuthal angle $\beta_{ref}$ of 0°, with a bubble diameter of 5mm for various $U_{ws}$ and $v_{ref}$, as tabulated in Table 11.1. The four-sensor probe, designed as described earlier in Chapters 3 and 10, with the sensors made up of 0.2 mm diameter Teflon coated needles, was used for all the experiments. As mentioned earlier, the probe was measured twice; once before collecting data and once after collecting data for different values of $\alpha_{ref}$.

Figures 11.1 – 11.4 show the magnitude of the percentage difference in $x_i$ *and* $y_i$ ($i$ = 1, 2 and 3) of the probe dimensions measured before and after collecting data for $\alpha_{ref}$ 5°, 14°, 21° and 34° respectively (see Appendix C for the table of the probe dimensions measured before and after collecting data). From the measurements it was found that the change in measured probe dimensions in $z_i$ ($i$ = 1, 2 and 3) is negligible for the vertical flow, thus it is not presented in this chapter.

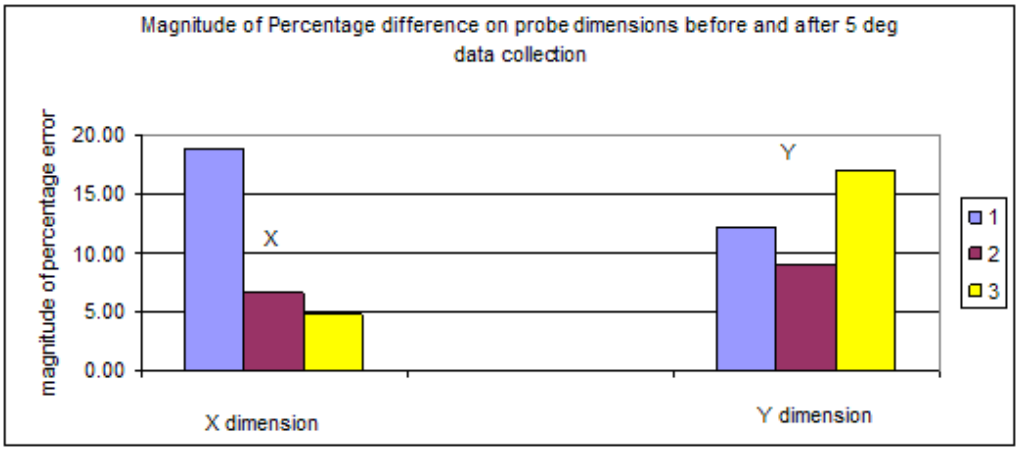


**Figure 11.1 Magnitude of percentage error in x and y probe dimensions measured before and after collecting data for $\alpha_{ref}$ 5°**

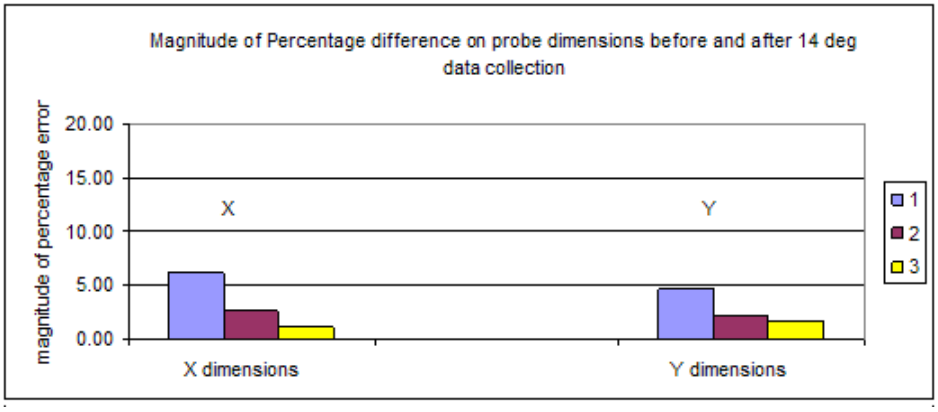


**Figure 11.2 Magnitude of percentage error in x and y probe dimensions measured before and after collecting data for $\alpha_{ref}$ 14°**

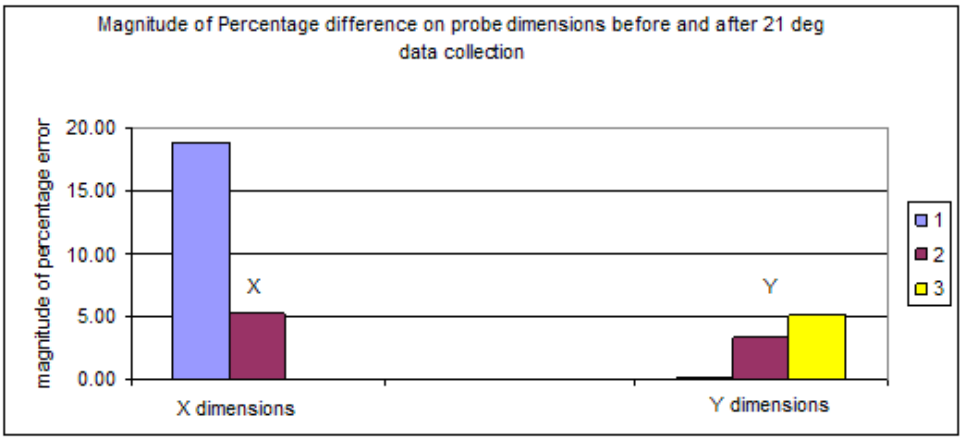


**Figure 11.3 Magnitude of percentage error in x and y probe dimensions measured before and after collecting data for $\alpha_{ref}$ 21°**

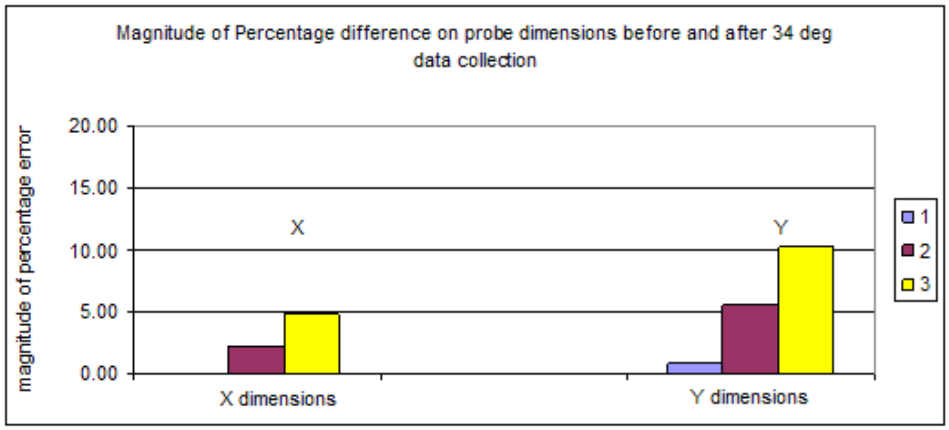


**Figure 11.4 Magnitude of percentage error in x and y probe dimensions measured before and after collecting data for $\alpha_{ref}$ 34°**

Table 11.2 shows the magnitudes of the differences between the probe dimensions $x_i$ *and* $y_i$ ($i$ = 1, 2 and 3) measured before collecting data (PMB) and the probe dimensions measured after collecting data (PMA) for the experiments undertaken at $\alpha_{ref}$ = 5°, 14°, 21° and 34°. The above results show that the dimensions of the probe change randomly during the experiments. Since $z_i$ ($i$ = 1, 2 and 3) is negligible for the vertical flow, dimensions for $z_i$ ($i$ = 1, 2 and 3) are not presented in this chapter.

| | $\alpha_{ref}$ = 5° | | $\alpha_{ref}$ =14° | | $\alpha_{ref}$ =21° | | $\alpha_{ref}$ =34° | |
|---|---|---|---|---|---|---|---|---|
| | *x* | *y* | *x* | *y* | *x* | *y* | *x* | *y* |
| 1 | 18.82% | 12.16% | 6.24% | 4.74% | 18.82% | 0.11% | 0% | 0.82% |
| 2 | 6.59% | 8.99% | 2.63% | 2.25% | 5.27% | 3.36% | 2.24% | 5.61% |
| 3 | 4.75% | 16.96% | 1.19% | 1.71% | 0% | 5.10% | 4.77% | 10.17% |

**Table 11.2 Percentage difference between the probe dimensions measured before and after collecting data**

It was evident the difference between the dimensions of the probe measured before and after collecting the data. Also the magnitude of the dimension error depends on the number of tests carried out between the measurements of the probe. Results show that when the number of the tests carried out between the measurements was fewer, the difference in the measured probe dimensions was less. It should also be noted that the possibility of making an error during the process of measuring the probe cannot be ignored, as the dimensions are measured to a resolution of millimetres and the errors within the measurements are in microns.

#### 11.1.1.1 Discussion of $\bar{\varepsilon}_{abs,\alpha,p}$

Figure 11.5 shows the comparisons between the magnitude of the results of the mean error in polar angle $\bar{\varepsilon}_{abs,\alpha,p}$ calculated using "average $\delta t_{ii}$" and "average individual

bubbles" methods for $\alpha_{ref}$ = 5°, 10°, 21°and 34° and $\beta_{ref}$ =0° and various values of $v_{ref}$ (see Table 11.1). Both the methods were calculated with and without signal processing, with the probe dimensions measured before and after collecting data.

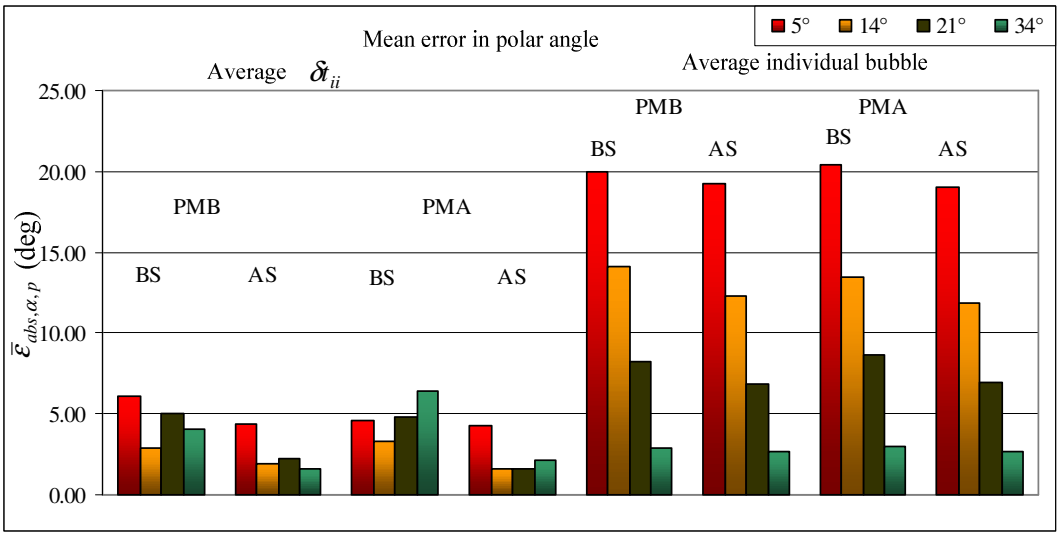


**Figure 11.5 Comparisons between the results of absolute mean error in polar angle $\bar{\varepsilon}_{abs,\alpha,p}$ with and without signal processing, calculated using "average $\delta t_{ii}$" and "average individual bubbles" methods for $\alpha_{ref}$ = 5°, 10°, 21°and 34° and $\beta_{ref}$ =0° and various values of $v_{ref}$**

From Figure 11.5 it can be seen that mean error $\bar{\varepsilon}_{abs,\alpha,p}$ in $\varepsilon_{abs,\alpha,m,p}$ calculated using the "average $\delta t_{ii}$" method is lower than when it was calculated using the "average individual bubbles" method. Figure 11.5 also indicates that, as $\alpha_{ref}$ was increased $\bar{\varepsilon}_{abs,\alpha,p}$ in $\varepsilon_{abs,\alpha,m,p}$ decreases when calculated using the "average individual bubbles" but $\bar{\varepsilon}_{abs,\alpha,p}$ in $\varepsilon_{abs,\alpha,m,p}$ only shows a slight improvement when calculated using the "average $\delta t_{ii}$" method.

Figure 11.5 also shows that $\bar{\varepsilon}_{abs,\alpha,p}$ in $\varepsilon_{abs,\alpha,m,p}$ calculated after signal processing is much closer to the $\alpha_{ref}$ as compared to $\bar{\varepsilon}_{abs,\alpha,p}$ in $\varepsilon_{abs,\alpha,m,p}$ measured before signal

processing. The probe dimensions measured before (PMB) and after (PMA) show very little effect in mean value $\bar{\varepsilon}_{abs,\alpha,p}$ of the absolute error in $\varepsilon_{abs,\alpha,m,p}$.

### 11.1.1.2 Discussion of $\sigma_{abs,\alpha,p}$

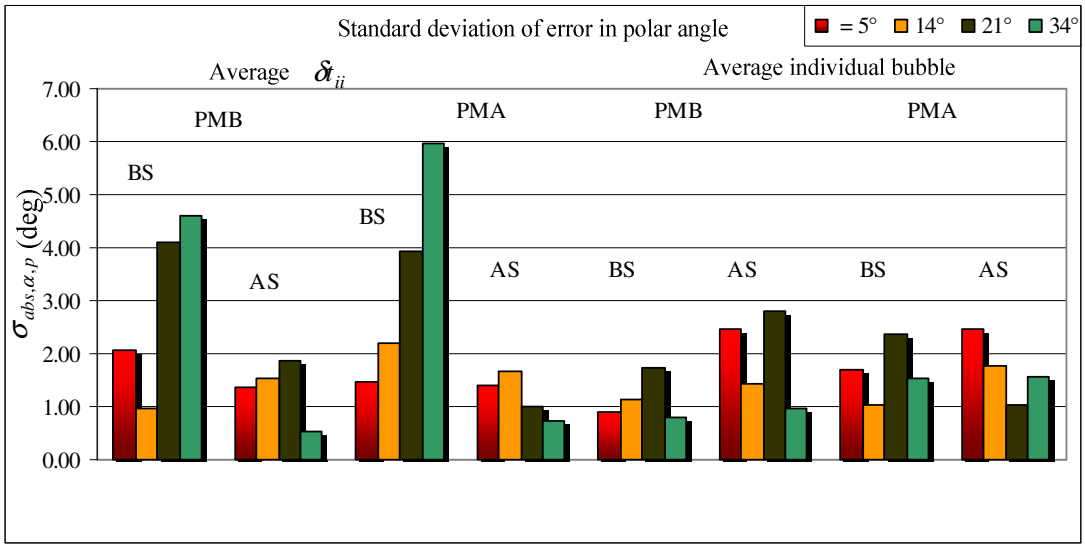


**Figure 11.6 Comparisons between the results of standard deviation $\sigma_{abs,\alpha,p}$ of error in polar angle with and without signal processing, calculated using "average $\delta t_{ii}$" and "average individual bubbles" methods for $\alpha_{ref}$ = 5°, 10°, 21°and 34° and $\beta_{ref}$ =0° and various values of $v_{ref}$**

Figure 11.6 shows the comparisons between the results of standard deviation $\sigma_{abs,\alpha,p}$ of error in the polar angle $\varepsilon_{abs,\alpha,m,p}$ with and without signal processing, calculated using the "average $\delta t_{ii}$" and "average individual bubbles" methods for $\alpha_{ref}$ = 5°, 10°, 21° and 34° and $\beta_{ref}$ =0° and various values of $v_{ref}$ (see Table 11.1). The standard deviation of the calculated individual errors is described earlier in Equations 11.14-11.16.

Figure 11.6 indicates that, for some of the individual tests carried out using the "average $\delta t_{ii}$" method, $\sigma_{abs,\alpha,p}$ of $\varepsilon_{abs,\alpha,m,p}$ were somewhat greater than with the "average individual bubble" method. However, Figure 11.6 also suggests that the error is significantly reduced when $\varepsilon_{abs,\alpha,m,p}$ was calculated after signal processing.

Figure 11.6 also shows that, with the "average $\delta t_{ii}$" method, as $\alpha_{ref}$ was increased $\sigma_{abs,\alpha,p}$ of $\varepsilon_{abs,\alpha,m,p}$ increases when $\varepsilon_{abs,\alpha,m,p}$ was calculated before signal processing, which indicates that, for some of the individual tests carried out, $\varepsilon_{abs,\alpha,m,p}$ was somewhat greater. However, after signal processing $\sigma_{abs,\alpha}$ of $\varepsilon_{abs,\alpha,m}$ tended to decrease as $\alpha_{ref}$ increased, indicating that, for some of the individual tests carried out, the errors in $\varepsilon_{abs,\alpha,m,p}$ were reduced compared with $\varepsilon_{abs,\alpha,m,p}$ when calculated before signal processing.

On the other hand when $\varepsilon_{abs,\alpha,m,p}$ was calculated using the "average individual bubble" method, $\sigma_{abs,\alpha,p}$ of $\varepsilon_{abs,\alpha,m,p}$ tended to decrease as $\alpha_{ref}$ was increased when $\varepsilon_{abs,\alpha,m,p}$ was calculated before signal processing, as well as after signal processing.

#### 11.1.1.3 Discussion of $\bar{\varepsilon}_{abs,\beta,p}$

Figure 11.7 shows the comparisons between the results of the magnitude of the mean error in the azimuthal angle $\bar{\varepsilon}_{abs,\beta,p}$ with and without signal processing, calculated using the "average $\delta t_{ii}$" and "average individual bubbles" methods for $\alpha_{ref}$ = 5°, 10°, 21° and 34° and $\beta_{ref}$ = 0° and various values of $v_{ref}$ (see Table 11.1).

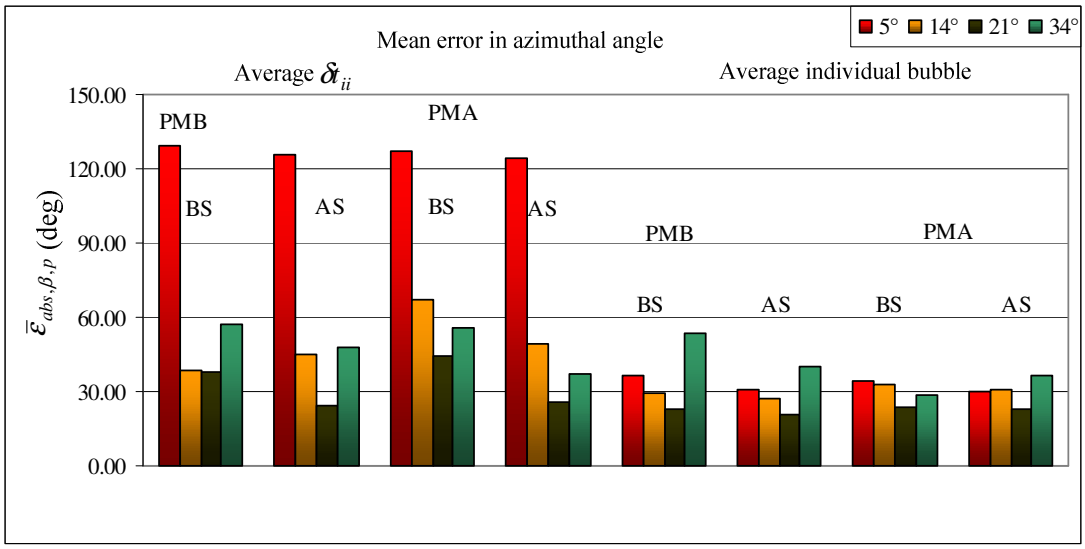


**Figure 11.7 Comparisons between the results of the absolute mean error in azimuthal angle $\bar{\varepsilon}_{abs,\beta,p}$ with and without signal processing, calculated using "average $\delta i_{ii}$" and "average individual bubbles" methods for $\alpha_{ref}$ = 5°, 10°, 21° and 34° and $\beta_{ref}$ =0° and various values of $v_{ref}$**

Figure 11.7 indicates that, when azimuthal angle $\beta_{meas,m,p}$ was calculated using the "average $\delta i_{ii}$" method, the mean azimuthal angle error $\bar{\varepsilon}_{abs,\beta,p}$ in $\varepsilon_{abs,\beta,m,p}$ shows larger errors for smaller $\alpha_{ref}$ than $\bar{\varepsilon}_{abs,\beta,p}$ in $\varepsilon_{abs,\beta,m,p}$ when calculated using the "average individual bubble" method. However the mean error $\bar{\varepsilon}_{abs,\beta,p}$ in $\varepsilon_{abs,\beta,m,p}$ tended to decrease as $\alpha_{ref}$ was increased when calculated using the "average $\delta i_{ii}$" method, but shows less effect when calculated using the "average individual bubble" method.

Figure 11.7 also indicated that $\bar{\varepsilon}_{abs,\beta,p}$ in $\varepsilon_{abs,\beta,m,p}$ tended to show a greater reduction after signal processing than before signal processing using the "average $\delta i_{ii}$" as well as the "average individual bubble" method.

Figure 11.7 also indicates that $\bar{\varepsilon}_{abs,\beta,p}$ calculated with the probe dimensions measured before and after collecting data shows very little improvement in measured $\beta_{meas,m,p}$.

#### 11.1.1.4 Discussion of $\sigma_{abs,\beta,p}$

Figure 11.8 shows the comparisons between the results for the standard deviation of the mean error in the azimuthal angle $\sigma_{abs,\beta,p}$ with and without signal processing, calculated using the "average $\delta t_{ii}$" and the "average individual bubbles" methods for $\alpha_{ref}$ = 5°, 10°, 21° and 34° and $\beta_{ref}$ =0° and various values of $v_{ref}$ (see Table 11.1). The standard deviation of the calculated individual errors is described earlier in Equations 11.14-11.16.

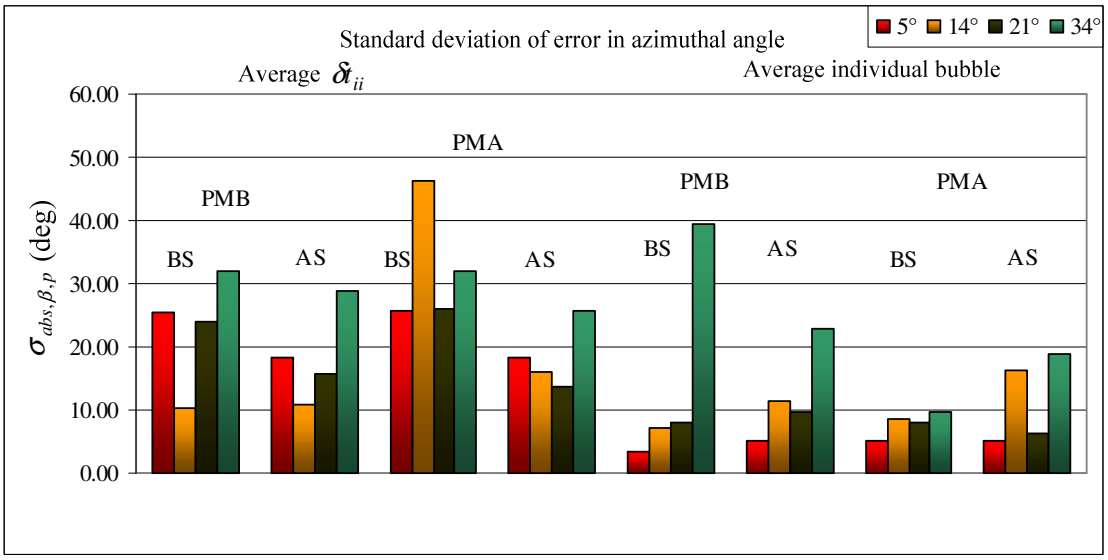


**Figure 11.8 Comparisons between the results of standard deviation of mean error in azimuthal angle $\sigma_{abs,\beta,p}$ with and without signal processing, calculated using "average $\delta t_{ii}$" and "average individual bubbles" methods for $\alpha_{ref}$ = 5°, 10°, 21° and 34° and $\beta_{ref}$ =0° and various values of $v_{ref}$**

The calculation of standard deviation $\sigma_{abs,\beta,p}$ of $\varepsilon_{abs,\beta,m,p}$ in Figure 11.8 indicates that for some of the individual bubbles the error was greater when calculated using the "average $\delta t_{ii}$" method than with the "average individual bubble" method.

It can also be seen from Figure 11.8 $\sigma_{abs,\beta,p}$ of $\varepsilon_{abs,\beta,m,p}$ decreased after signal processing compared with $\sigma_{abs,\beta,p}$ of $\varepsilon_{abs,\beta,m,p}$ calculated before signal processing, indicating the reduction of error in individual bubbles.

Figure 11.8 also indicates that $\sigma_{abs,\beta,p}$ of $\varepsilon_{abs,\beta,m,p}$ increased as $\alpha_{ref}$ increased, indicating an increase of errors in individual bubbles.

#### 11.1.1.5 Discussion of $\bar{\varepsilon}_{abs,v,p}$

Figure 11.9 shows the comparison between the magnitude of the mean errors in velocity magnitude $\bar{\varepsilon}_{abs,v,p}$ with and without signal processing, calculated using the "average $\delta t_{ii}$" and the "average individual bubbles" methods for $\alpha_{ref}$ = 5°, 10°, 21° and 34° and $\beta_{ref}$ =0° and various values of $v_{ref}$ (see Table 11.1).

Figure 11.9 indicates that the mean error $\bar{\varepsilon}_{abs,v,p}$ of the percentage error of the velocity magnitude $\varepsilon_{abs,v,m,p}$ is larger when calculated using the "average $\delta t_{ii}$" method than when calculated using the "average individual bubbles" methods. However, the improvement on $\bar{\varepsilon}_{abs,v,p}$ of the percentage error of the velocity magnitude $\varepsilon_{abs,v,m,p}$ can be noticed when calculated after signal processing using the "average $\delta t_{ii}$" method. Figure 11.9 also suggests that $\bar{\varepsilon}_{abs,v,p}$ of $\varepsilon_{abs,v,m,p}$ is almost the same when calculated before and after signal processing using the "average

individual bubbles" methods. Figure 11.9 also indicates that $\bar{\varepsilon}_{abs,v,p}$ of $\varepsilon_{abs,v,m,p}$ tended to reduce when the reference polar angle $\alpha_{ref}$ was increased.

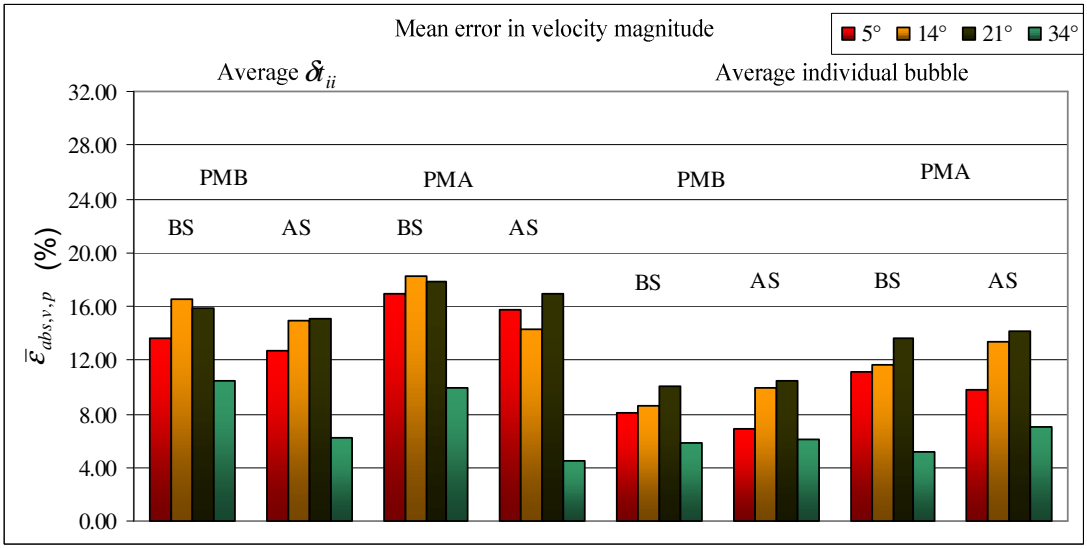


**Figure 11.9 Comparisons between the results of absolute mean error in velocity magnitude $\bar{\varepsilon}_{abs,v,p}$ with and without signal processing, calculated using "average $\delta t_{ii}$" and "average individual bubbles" methods for $\alpha_{ref}$ = 5°, 10°, 21° and 34° and $\beta_{ref}$ =0° and various values of $v_{ref}$**

### 11.1.1.6 Discussion of $\sigma_{abs,v,p}$

Figure 11.10 shows the comparisons between the results for the standard deviation $\sigma_{abs,v,p}$ of the mean error in velocity magnitude $\varepsilon_{abs,v,m,p}$ with and without signal processing, calculated using the "average $\delta t_{ii}$" and the "average individual bubbles" methods for $\alpha_{ref}$ = 5°, 10°, 21° and 34° and $\beta_{ref}$ =0° and various values of $v_{ref}$ (see Table 11.1). The standard deviation of the calculated individual errors is described earlier in Equations 11.14-11.16.

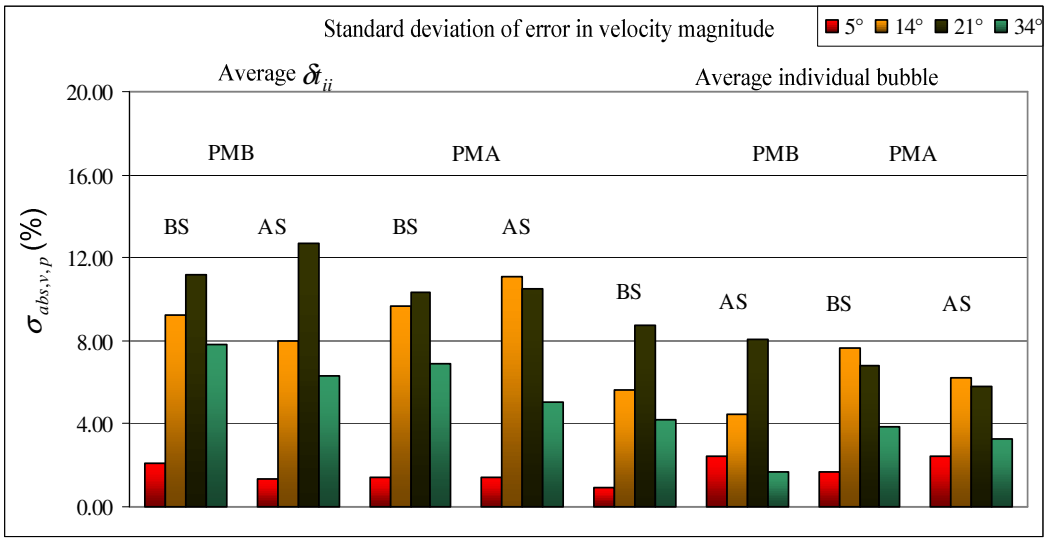


**Figure 11.10 Comparisons between the results of standard deviation $\sigma_{abs,v,p}$ of $\varepsilon_{abs,v,m,p}$ with and without signal processing, calculated using "average $\delta_{ii}$" and "average individual bubbles" methods for $\alpha_{ref}$ = 5°, 10°, 21° and 34° and $\beta_{ref}$ =0° and various values of $v_{ref}$**

As shown in Figure 11.10, the calculation of $\sigma_{abs,v,p}$ of $\varepsilon_{abs,v,m,p}$ indicates that, for some of the individual tests, the error is larger when calculated using the "average $\delta_{ii}$" method as compared to $\sigma_{abs,v,p}$ of $\varepsilon_{abs,v,m,p}$ when calculated using the "average individual bubbles" method. It can also be noticed that, for both calculation methods, $\sigma_{abs,v,p}$ of $\varepsilon_{abs,v,m,p}$ tends to increase when $\alpha_{ref}$ increases, suggesting an increase in the error in some of the individual tests.

However, Figure 11.10 indicates that, for the larger value of $\alpha_{ref}$, $\sigma_{abs,v,p}$ of $\varepsilon_{abs,v,m,p}$ tended to decrease when calculated after signal processing as compared with $\sigma_{abs,v,p}$ of $\varepsilon_{abs,v,m,p}$ calculated before signal processing, which indicates that errors in the individual bubbles reduce after signal processing

## 11.2 Swirling flow measurement

Swirling flow measurement was carried out with a swirler device (see Chapter 10.4.1) placed in the working section of the flow loop. A traverse mechanism (see Chapter 10.4.2) was used to position the probe. A turbine meter was used to measure the volumetric flow rate of the water. Similarly, a pressure-drop mechanism was used to measure the reference gas volumetric flow rate [1] and the reference mean gas volume fraction (see section 10.2).

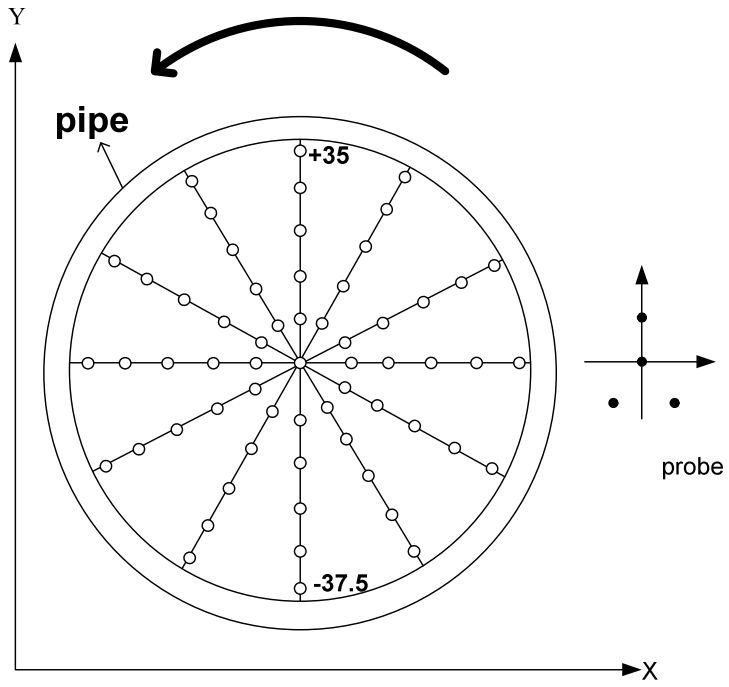


**Figure 11.11 Data collecting point using swirler**

The experiments were carried out in different flow conditions, as shown in Table 11.3, with a probe made up of 0.20 mm diameter Teflon coated needles. For each flow condition, data were collected at six radial locations on each given pipe radius. The pipe section containing the probe was rotated 30° anti-clockwise to take data along to the next radius. The same process was repeated for twelve different radii to collect the data at a total of 61 different locations, as shown in Figure 11.11. The collected data

were processed with the probe dimensions measured before collecting data and the results presented in this section are calculated after signal processing described in section 6.2.

### 11.2.1 Swirling flow experiment

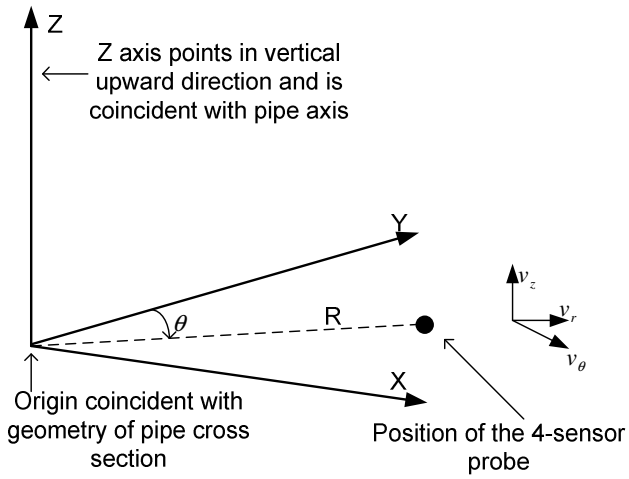


**Figure 11.12 The coordinate system of the pipe and probe, which enables the velocity vector of the bubble to be calculated**

Experiments were carried out with the superficial velocity of water $U_{ws}$ in the range 0.576 m/s to 0.763 m/s and the superficial gas velocity $U_{gs}$ in the range 0.018 m/s to 0.041m/s. The mean gas volume fraction was set to always be less than 0.1 for the experiment carried out in this section. At each flow condition, the four-sensor probe was used to measure the local axial velocity $v_z$, positive in the vertical upward direction, radial velocity $v_r$, positive in the direction pointing away from the pipe centre and azimuthal gas velocity $v_\theta$ (positive in the clockwise direction when the observer faces towards the oncoming flow; see Figure 11.12 for a definition of axial velocity $v_z$, radial velocity $v_r$ and azimuthal velocity $v_\theta$ for the given position of the probe). The mean gas volume fraction $\overline{\lambda}$ was also measured at each point, as

described in section 10.2.3. All the flows investigated were found to be axisymmetric and the results presented in this section show the variation of mean local properties across a single pipe diameter at a given set of flow conditions. For each flow condition, mean axial gas velocity $\overline{u}_{g,probe}$ was calculated, as shown in Equation 11.16.

$$\overline{u}_{g,probe} = \frac{\sum_{i=1}^{61} \lambda_{li}\, v_{z\,i}\, \Delta A_i}{\sum_{i=1}^{61} \lambda_{li}\, \Delta A_i} \qquad \textbf{Equation 11.16}$$

In Equation 11.16 $\lambda_{li}$ and $v_{z\,i}$ are the measured local gas volume fraction and the measured local axial gas velocity at the $i^{\text{th}}$ distinct probe position respectively. $\Delta A_i$ is one of 61 discrete areas into which the flow cross-section is divided.

For the given experiments, the reference gas velocity $\overline{u}_{g,ref}$ was calculated as shown in Equation 11.17.

$$\overline{u}_{g,ref} = \frac{Q_g}{A\overline{\lambda}_{ref}} = \frac{U_{gs}}{\overline{\lambda}_{ref}} \qquad \textbf{Equation 11.17}$$

where $Q_g$ is the volumetric flow rate of the dispersed phase, $U_{gs}$ is the superficial velocity of the gas (air). The reference mean air volume fraction $\overline{\lambda}_{ref}$ was measured using a DP transducer, (see section 10.2.3). The DP transducer was placed in the flow loop as shown in Figure 11.13. The high speed camera (see Figure 11.13) was also used to calculate the reference gas velocity $\overline{u}_{g,camera}$. From the calculated values of $\overline{u}_{g,ref}$ and $\overline{u}_{g,camera}$, calibration factor *K* was calculated as described below.

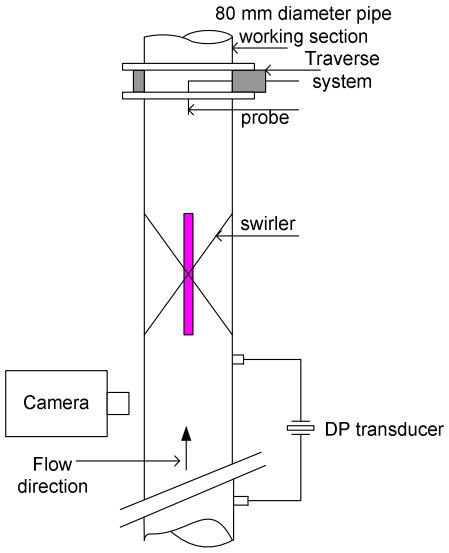


**Figure 11.13 Positioning of probe and DP transducer in the working section with swirler for the measurement of $\overline{u}_{g,probe}$ and $\overline{u}_{g,ref}$**

Lucas et al. [1] found in their results that $\overline{u}_{g,probe}$ is always less than $\overline{u}_{g,ref}$ with $\overline{u}_{g,probe}$ being typically 80% of the $\overline{u}_{g,ref}$, consequently the author made an assumption that the cause was due to the retarding effect of the probe-bubble interaction. Thus, the author introduced calibration factor *K*, which is given by:

$$K\,\overline{u}_{g,probe} = \overline{u}_{g,ref} \quad \text{or} \quad K\,\overline{u}_{g,probe} = \overline{u}_{g,camera} \qquad \textbf{Equation 11.18}$$

Table 11.3 shows the value of calibration factor *K* calculated using $\overline{u}_{g,ref}$ and $\overline{u}_{g,camera}$. Calibration factor *K* was calculated for the different flow conditions. The results of the experiments tabulated in Table 11.3 show that, as the gas superficial velocity $U_{gs}$ increased, the reference gas velocity $\overline{u}_{g,ref}$ increased compared to that of the gas velocity measured by the probe $\overline{u}_{g,probe}$. Resulting in a low value of $U_{gs}$, the calculated value of $\overline{u}_{g,ref}$ was found to be less than $\overline{u}_{g,probe}$, but as $U_{gs}$ was increased, the calculated value of $\overline{u}_{g,ref}$ was found to be higher than $\overline{u}_{g,probe}$.

However, Table 11.3 shows that the average value of $\overline{u}_{g,ref}$ was found to be 97% of $\overline{u}_{g,probe}$.

| Flow conditions | $K$ | |
|---|---|---|
| | $\overline{u}_{g,ref}$ | $\overline{u}_{g,camera}$ |
| $U_{ws}$ = 0.567m/s; $U_{gs}$ = 0.018m/s<br>$\overline{u}_{g,probe}$ = 0.847m/s; $\overline{u}_{g,camera}$ = 0.820m/s ; $\overline{u}_{g,ref}$ = 0.715m/s | 0.85 | 0.94 |
| $U_{ws}$ = 0.567m/s; $U_{gs}$ = 0.027m/s<br>$\overline{u}_{g,probe}$ = 0.851m/s; $\overline{u}_{g,camera}$ = 0.830 m/s ; $\overline{u}_{g,ref}$ = 0.825m/s | 0.97 | 0.97 |
| $U_{ws}$ = 0.567m/s; $U_{gs}$ = 0.040m/s<br>$\overline{u}_{g,probe}$ = 0.866 m/s ; $\overline{u}_{g,camera}$ = 0.830m/s; $\overline{u}_{g,ref}$ = 0.871m/s | 1.01 | 0.95 |
| $U_{ws}$ = 0.763m/s; $U_{gs}$ = 0.041m/s<br>$\overline{u}_{g,probe}$ = 1.082 m/s ; $\overline{u}_{g,camera}$ = 1.035 m/s; $\overline{u}_{g,ref}$ = 1.116m/s | 1.03 | 0.95 |
| **Average** | 0.97 | 0.95 |

**Table 11.3 Calculation of calibration factor $\overline{u}_{g,ref}$ and $\overline{u}_{g,camera}$ Vs $\overline{u}_{g,probe}$**

Lucas et al. [1] also stated that the calibration factor in their experiment was found to be 1.2 with a variation of ±20%, whereas Table 11.3 suggests that the average calibration factor is closer to 0.97 calculated with $\overline{u}_{g,ref}$ and 0.95 when calculated using $\overline{u}_{g,camera}$, suggesting that there is a much smaller retarding effect.

Although experiments were carried out for various flow conditions, the results are presented only for the flow condition tabulated in Table 11.4.

| Test condition | $\overline{\lambda}_{ref}$ | $U_{gs}$ | $U_{ws}$ |
|---|---|---|---|
| **1** | 0.025 | 0.018 | 0.567 |
| **2** | 0.038 | 0.041 | 0.763 |

**Table 11.4 Flow conditions used for experiments with and without swirler**

| r/D | $v_\theta$ | $v_r$ | $v_z$ | $\overline{\lambda}$ |
|---|---|---|---|---|
| -0.44 | -0.1189 | -0.0740 | 0.5804 | 0.0028 |
| -0.35 | -0.1289 | -0.0267 | 0.8370 | 0.0133 |
| -0.26 | -0.0982 | -0.0652 | 0.8939 | 0.0250 |
| -0.18 | -0.0767 | -0.0773 | 0.9222 | 0.0355 |
| -0.09 | -0.0711 | -0.0098 | 0.9362 | 0.0399 |
| 0.00 | -0.0577 | 0.0115 | 0.9628 | 0.0425 |
| 0.09 | -0.0711 | -0.0098 | 0.9362 | 0.0399 |
| 0.18 | -0.0767 | -0.0773 | 0.9222 | 0.0355 |
| 0.26 | -0.0982 | -0.0652 | 0.8939 | 0.0250 |
| 0.35 | -0.1289 | -0.0267 | 0.8370 | 0.0133 |
| 0.44 | -0.1189 | -0.0740 | 0.5804 | 0.0028 |

**Table 11.5 Test results for $\overline{\lambda}_{ref}$ = 0.025, $U_{gs}$ = 0.018 ms$^{-1}$ and $U_{ws}$ = 0.567ms$^{-1}$ without swirler**

| r/D | $v_\theta$ | $v_r$ | $v_z$ | $\overline{\lambda}$ |
|---|---|---|---|---|
| -0.44 | -0.2018 | 0.0051 | 0.7245 | 0.0014 |
| -0.35 | -0.1252 | -0.0015 | 0.8112 | 0.0084 |
| -0.26 | -0.1296 | -0.0524 | 0.8720 | 0.0204 |
| -0.18 | -0.0902 | -0.0413 | 0.9003 | 0.0337 |
| -0.09 | -0.0422 | -0.0229 | 0.9128 | 0.0415 |
| 0.00 | 0.0340 | -0.0190 | 0.9193 | 0.0516 |
| 0.09 | -0.0422 | -0.0229 | 0.9128 | 0.0415 |
| 0.18 | -0.0902 | -0.0413 | 0.9003 | 0.0337 |
| 0.26 | -0.1296 | -0.0524 | 0.8720 | 0.0204 |
| 0.35 | -0.1252 | -0.0015 | 0.8112 | 0.0084 |
| 0.44 | -0.2018 | 0.0051 | 0.7245 | 0.0014 |

**Table 11.6 Test results for $\overline{\lambda}_{ref}$ = 0.025, $U_{gs}$ = 0.018 ms$^{-1}$ and $U_{ws}$ = 0.567ms$^{-1}$ with swirler**

Tables 11.5 and 11.6 show the results for local axial velocity $v_z$, radial velocity $v_r$ and azimuthal gas velocity $v_\theta$ and the mean gas volume fraction $\overline{\lambda}$ without swirler

and with swirler respectively for the reference flow condition $\overline{\lambda}_{ref}$ = 0.025, $U_{gs}$ = 0.018 ms$^{-1}$ and $U_{ws}$ = 0.567ms$^{-1}$.

Tables 11.7 and 11.8 show the results for $v_z$, $v_r$, $v_\theta$ and $\overline{\lambda}$ without swirler and with swirler respectively for the reference flow condition $\overline{\lambda}_{ref}$ = 0.038, $U_{gs}$ = 0.041ms$^{-1}$ and $U_{ws}$ = 0.763ms$^{-1}$.

| r/D | $v_\theta$ | $v_r$ | $v_z$ | $\overline{\lambda}$ |
|---|---|---|---|---|
| -0.44 | -0.0837 | 0.0323 | 0.7864 | 0.0021 |
| -0.35 | -0.0742 | -0.0207 | 1.0991 | 0.0171 |
| -0.26 | -0.0301 | -0.0317 | 1.1834 | 0.0365 |
| -0.18 | -0.0407 | 0.0274 | 1.2116 | 0.0652 |
| -0.09 | 0.1022 | 0.0090 | 1.2148 | 0.0829 |
| 0.00 | 0.0157 | -0.0278 | 1.2646 | 0.0892 |
| 0.09 | 0.1022 | 0.0090 | 1.2148 | 0.0829 |
| 0.18 | -0.0407 | 0.0274 | 1.2116 | 0.0652 |
| 0.26 | -0.0301 | -0.0317 | 1.1834 | 0.0365 |
| 0.35 | -0.0742 | -0.0207 | 1.0991 | 0.0171 |
| 0.44 | -0.0837 | 0.0323 | 0.7864 | 0.0021 |

**Table 11.7 Test results for $\overline{\lambda}_{ref}$ = 0.038, $U_{gs}$ = 0.041ms$^{-1}$ and $U_{ws}$ = 0.763ms$^{-1}$ without swirler**

| r/D | $v_\theta$ | $v_r$ | $v_z$ | $\overline{\lambda}$ |
|---|---|---|---|---|
| -0.44 | -0.2190 | 0.0641 | 0.7280 | 0.0060 |
| -0.35 | -0.1845 | 0.0862 | 0.9916 | 0.0243 |
| -0.26 | -0.2676 | 0.0590 | 1.0656 | 0.0380 |
| -0.18 | -0.1721 | 0.1365 | 1.1115 | 0.0544 |
| -0.09 | -0.1183 | 0.0210 | 1.1808 | 0.0650 |
| 0 | 0.0861 | 0.0329 | 1.1906 | 0.0714 |
| 0.09 | -0.1183 | 0.0210 | 1.1808 | 0.0650 |
| 0.18 | -0.1721 | 0.1365 | 1.1115 | 0.0544 |
| 0.26 | -0.2676 | 0.0590 | 1.0656 | 0.0380 |
| 0.35 | -0.1845 | 0.0862 | 0.9916 | 0.0243 |
| 0.44 | -0.2190 | 0.0641 | 0.7280 | 0.0060 |

**Table 11.8 Test results for $\overline{\lambda}_{ref}$ = 0.038, $U_{gs}$ = 0.041ms$^{-1}$ and $U_{ws}$ = 0.763ms$^{-1}$ with swirler**

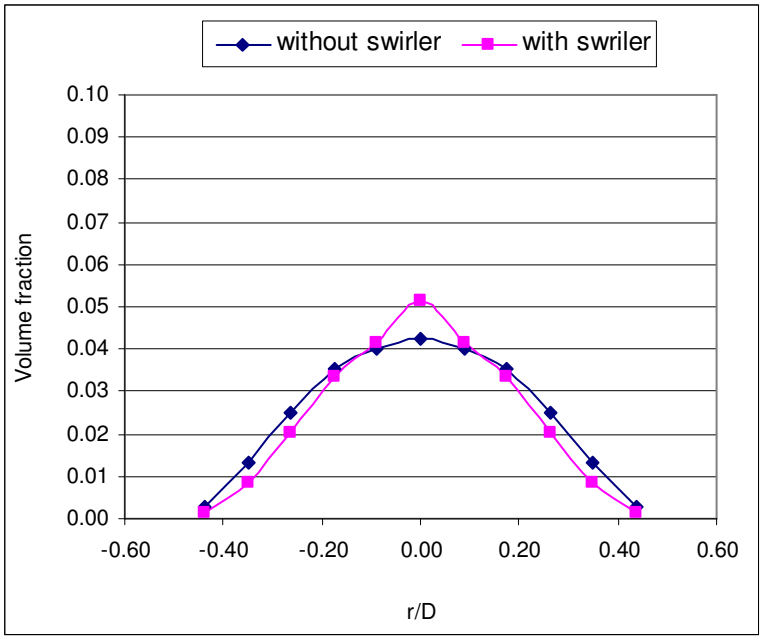


**Figure 11.14 Gas volume fraction versus non-dimensional radial position for $\overline{\lambda}_{ref}$ = 0.025, $U_{gs}$ = 0.018 ms$^{-1}$ and $U_{ws}$ = 0.567ms$^{-1}$ with and without swirler**

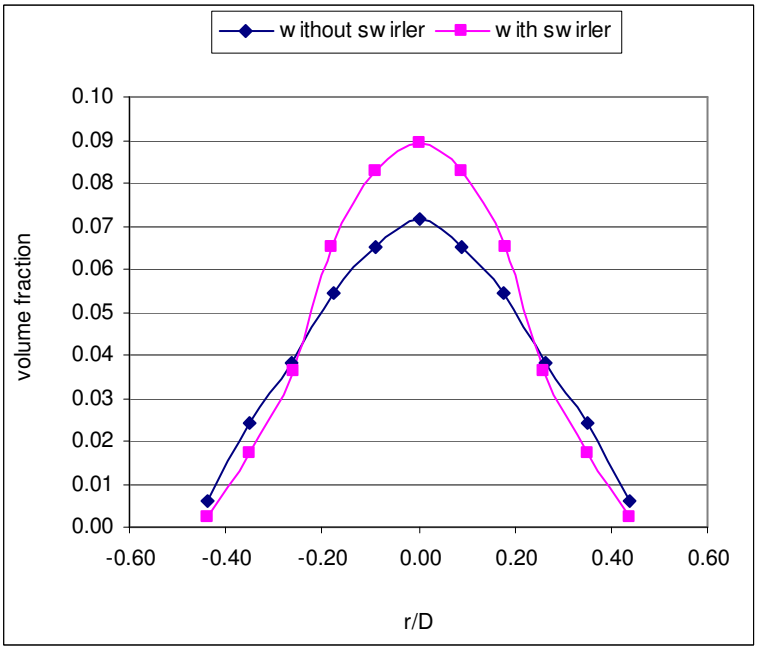


**Figure 11.15 Gas volume fraction versus non-dimensional radial position for $\overline{\lambda}_{ref}$ = 0.038, $U_{gs}$ = 0.041ms$^{-1}$ and $U_{ws}$ = 0. 76297ms$^{-1}$ with and without swirler**

Figures 11.14 and 11.15 show the variation of mean gas volume fraction $\bar{\lambda}$ with r/D, both with and without swirler, for the test conditions $\bar{\lambda}_{ref}$ = 0.025, $U_{gs}$ = 0.018 ms$^{-1}$ and $U_{ws}$ = 0.567ms$^{-1}$ and $\bar{\lambda}_{ref}$ = 0.038, $U_{gs}$ = 0.041ms$^{-1}$ and $U_{ws}$ = 0.763ms$^{-1}$ respectively. It is clear that when $U_{ws}$ is equal to 0.5670 m/s, the presence of the swirler has a very small effect on the distribution of the local gas volume fraction.

However, when $U_{ws}$ is equal to 0.763 m /s, the presence of the swirler shows a larger effect on the gas volume distribution. As Lucas et al. state in [1], at the higher value of $U_{ws}$ and with the presence of the swirler, there is a centrifugal effect which causes the low density gas to preferentially accumulate at the centre of the pipe. At the same gas and liquid flow rate without the presence of the swirler, the gas distribution is more uniform.

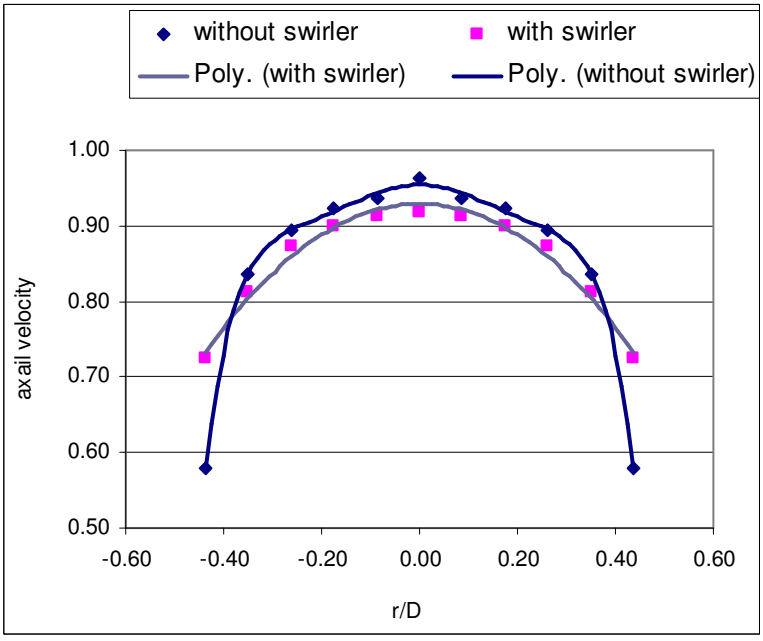


**Figure 11.16 Axial velocity (m/s) versus non-dimensional radial position for $\bar{\lambda}_{ref}$ = 0.025, $U_{gs}$ = 0.018 ms$^{-1}$ and $U_{ws}$ = 0.567ms$^{-1}$ with and without swirler.**

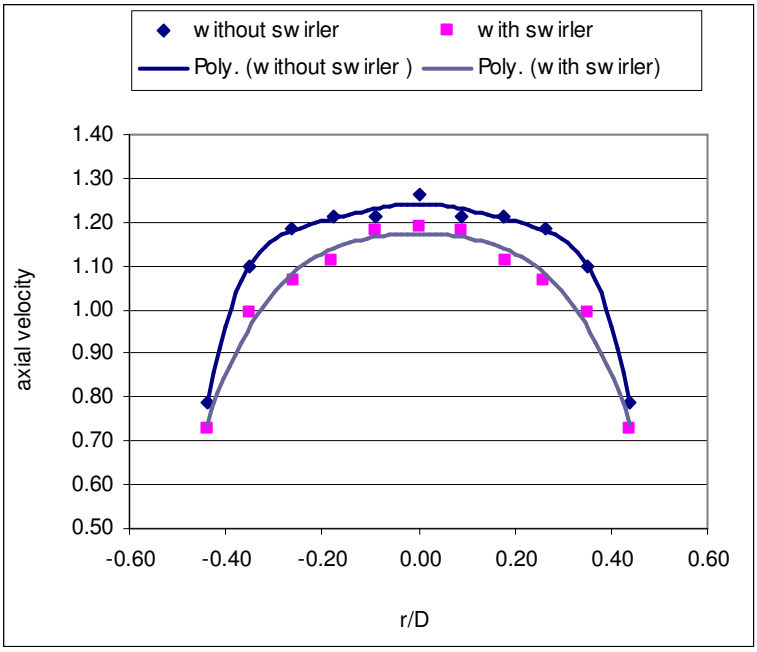


**Figure 11.17 Axial velocity (m/s) versus non-dimensional radial position for $\overline{\lambda}_{ref}$ = 0.038, $U_{gs}$ = 0.041ms$^{-1}$ and $U_{ws}$ = 0.763ms$^{-1}$ with and without swirler.**

Figures 11.16 and 11.17 show the variation of axial velocity with r/D both with and without swirler for test conditions $\overline{\lambda}_{ref}$ = 0.025, $U_{gs}$ = 0.018 ms$^{-1}$ and $U_{ws}$ = 0.567ms$^{-1}$ and $\overline{\lambda}_{ref}$ = 0.038, $U_{gs}$ = 0.041ms$^{-1}$ and $U_{ws}$ = 0.763ms$^{-1}$ respectively. It is readily evident that the presence of the swirler has very little effect (but is noticeable) on the shape of the axial velocity profile for the tested values of air and water superficial velocities. Figures 11.16 and 11.17 indicate that the axial velocity is much lower at the wall of the pipe at lower flow conditions. Figures 11.16 and 11.17 also indicate that, without the presence of the swirl, the axial velocity is much lower towards the wall of the pipe, suggesting that swirl forces the bubbles to accumulate at the centre of the pipe.

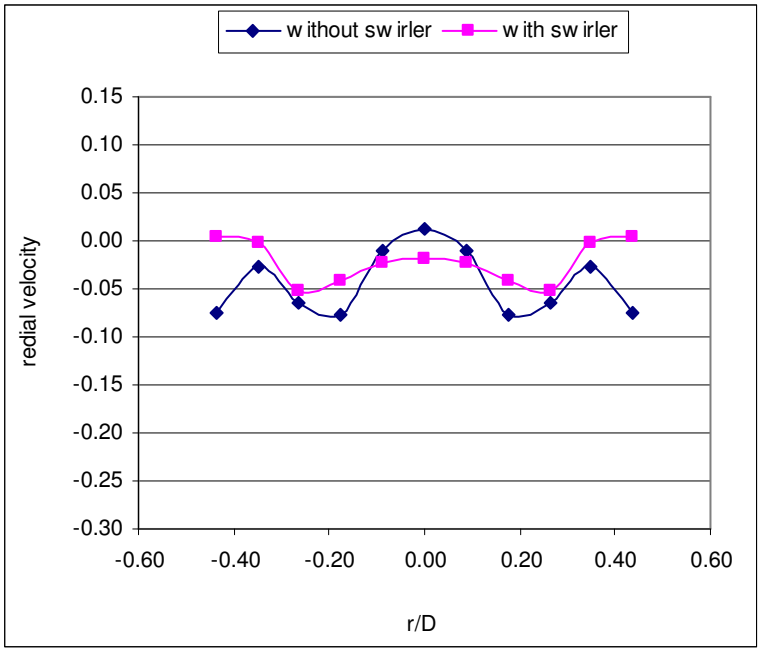


**Figure 11.18 Radial velocity (m/s) versus non-dimensional radial position for $\overline{\lambda}_{ref}$ = 0.025, $U_{gs}$ = 0.018 ms$^{-1}$ and $U_{ws}$ = 0.567ms$^{-1}$ with and without swirler.**

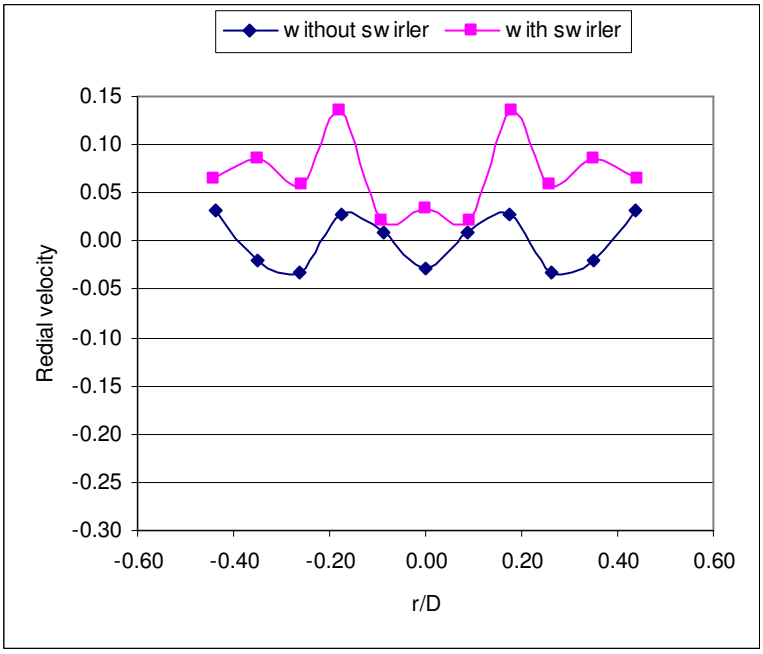


**Figure 11.19 Radial velocity (m/s) versus non-dimensional radial position for $\overline{\lambda}_{ref}$ = 0.038, $U_{gs}$ = 0.041ms$^{-1}$ and $U_{ws}$ = 0.763ms$^{-1}$ with and without swirler.**

Figure 11.18 shows the variation of radial velocity $v_r$ with non dimensional radial position r/D, both with and without swirler, for test conditions $\overline{\lambda}_{ref}$ = 0.025, $U_{gs}$ = 0.018 ms$^{-1}$ and $U_{ws}$ = 0.567ms$^{-}$. The variation of radial velocity $v_r$ with non dimensional radial position r/D for the test condition $\overline{\lambda}_{ref}$ = 0.038, $U_{gs}$= 0.041ms$^{-1}$ and $U_{ws}$ = 0.763ms$^{-1}$ with and without the swirler is shown in Figure 11.19. Both figures indicate that the radial velocity $v_r$ is always comparatively small with or without the swirler.

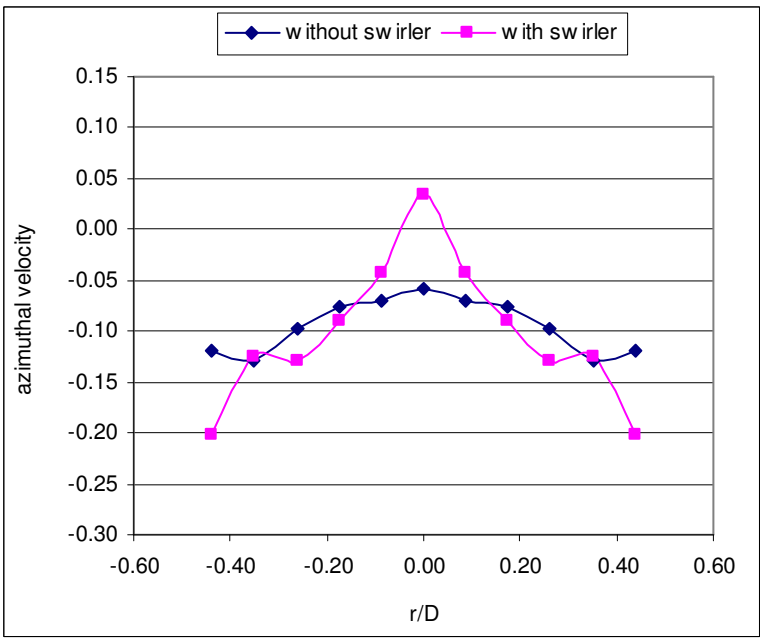


**Figure 11.20 Azimuthal velocity (m/s) versus non-dimensional radial position for $\overline{\lambda}_{ref}$ = 0.025, $U_{gs}$ = 0.018 ms$^{-1}$ and $U_{ws}$ = 0.567ms$^{-1}$ with and without swirler.**

Figures 11.20 and 11.21 show the variation of azimuthal velocity $v_\theta$ with r/D both with and without swirler for test conditions $\overline{\lambda}_{ref}$ = 0.025, $U_{gs}$ = 0.018 ms$^{-1}$ and $U_{ws}$ = 0.567ms$^{-1}$ and $\overline{\lambda}_{ref}$ = 0.038, $U_{gs}$= 0.041ms$^{-1}$ and $U_{ws}$ = 0.763ms$^{-1}$ respectively.

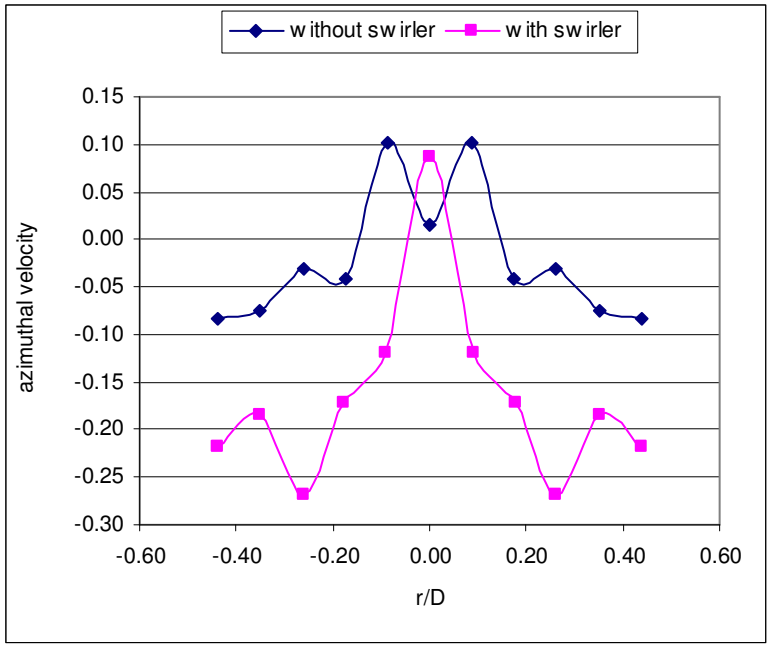


**Figure 11.21 Azimuthal velocity (m/s) versus non-dimensional radial position for $\bar{\lambda}_{ref}$ = 0.038, $U_{gs}$ = 0.041ms$^{-1}$ and $U_{ws}$ = 0.763ms$^{-1}$ with and without swirler.**

Following Lucas et al. in [1], a convention was adopted whereby the local azimuthal velocity is positive for clockwise swirl and negative for anticlockwise swirl (when the flow is moving upward along the pipe towards the observer). The swirler used in this experiment created anticlockwise swirl. It is clear from the above Figures 11.20 and 11.21 that, without the swirler, the azimuthal velocity $v_\theta$ is relatively close to zero at all positions in the flow cross section. However, in the presence of the swirler, it is also apparent from Figures 11.20 and 11.21 that there is a marked change in the distribution of $v_\theta$ across the pipe diameter. For both test conditions $\bar{\lambda}_{ref}$ = 0.025, $U_{gs}$ = 0.018 ms$^{-1}$, $U_{ws}$ = 0.567ms$^{-1}$ and $\bar{\lambda}_{ref}$ = 0.038, $U_{gs}$ = 0.041ms$^{-1}$, $U_{ws}$ = 0.763ms$^{-1}$ it was found that the presence of the swirler causes the azimuthal velocity $v_\theta$ to be strongly negative close to the pipe walls. Figure 11.21 also indicates that the magnitude of the azimuthal velocity $v_\theta$ decreases towards the pipe centre.

Table 11.9 shows the calculated swirl angle of the flow, given by Equation 11.19, where $\psi_{swirl}$ is the swirl angle of multiphase flow, for both the flow conditions.

$$\psi_{swirl} = \tan^{-1}\left(v_\theta / v_z\right) \qquad \textbf{Equation 11.19}$$

| | $\overline{\lambda}_{ref} = 0.025$, $U_{gs} = 0.018$ ms$^{-1}$ and $U_{ws} = 0.567$ms$^{-1}$ | $\overline{\lambda}_{ref} = 0.038$, $U_{gs} = 0.041$ms$^{-1}$ and $U_{ws} = 0.763$ms$^{-1}$ |
|---|---|---|
| r/D | $\tan^{-1}\left(v_\theta / v_z\right)$ | $\tan^{-1}\left(v_\theta / v_z\right)$ |
| -0.44 | 15.57° | 16.75° |
| -0.35 | 8.78° | 10.55° |
| -0.26 | 8.46° | 14.10° |
| -0.18 | 5.72° | 8.81° |
| -0.09 | 2.65° | 5.72° |
| 0 | 2.12° | 4.14 |
| 0.09 | 2.65° | 5.72° |
| 0.18 | 5.72° | 8.81° |
| 0.26 | 8.46° | 14.10° |
| 0.35 | 8.78° | 10.55° |
| 0.44 | 15.57° | 16.75° |

**Table 11.9 Calculated swirl angle for the flow**

Table 11.9 shows that for $U_{ws} = 0.567$ms$^{-1}$ the swirl angle at the wall was found to be 15.57° and for $U_{ws} = 0.763$ms$^{-1}$ the swirl angle was 16.75° in the anticlockwise direction. For both cases, the calculated angle is less than the angle of the swirler itself which is 20°. This could be due to the distance between the probe and swirler, which is 320 mm upstream; at this position, the swirl in the multiphase flow was already beginning to decay by the time the swirl reached the probe, as described by Lucas et al. [1]. However an improvement in the measured swirl angle was made with the improved miniaturized probe design, where previously the swirl angle was found to be 13° by Lucas et al. [1].

Figure 11.22 shows in 2D and 3D the variation of average velocity vector of the gas bubbles for the flow conditions $\overline{\lambda}_{ref}$ = 0.025, $U_{gs}$ = 0.018 ms$^{-1}$, $U_{ws}$ = 0.567ms$^{-1}$ (top) and $\overline{\lambda}_{ref}$ = 0.038, $U_{gs}$ = 0.041ms$^{-1}$, $U_{ws}$ = 0.763ms$^{-1}$ (bottom) with the swirler obtained from the results presented in Tables 11.6 and 11.8. It is clear that in the presence of swirl at $U_{ws}$ =0.567 m /s, the radial velocity component is negligible compared to the azimuthal velocity. At $U_{ws}$ = 0.763m/s, the radial component appears to be more significant, although these results may be due to errors in the measurement of $v_r$.

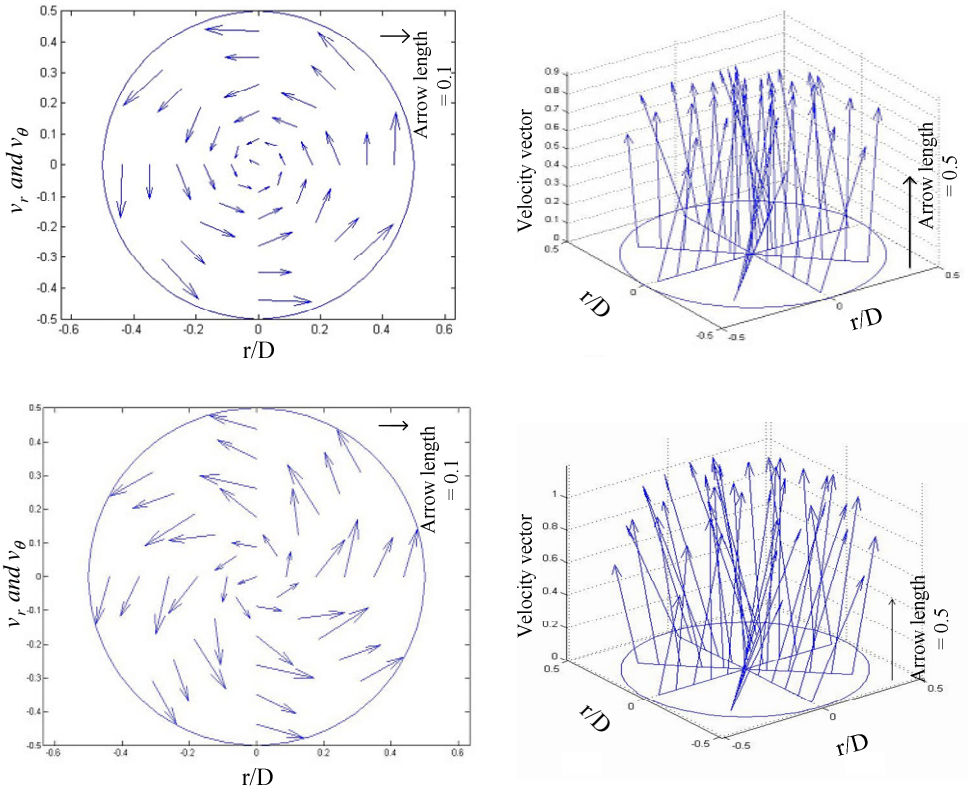


**Figure 11.22 2D and 3D variation of average velocity vector for $\overline{\lambda}_{ref}$ = 0.025, $U_{gs}$ = 0.018 ms$^{-1}$ and $U_{ws}$ = 0.567ms$^{-1}$ with swirler, top left and right respectively, and for $\overline{\lambda}_{ref}$ = 0.038, $U_{gs}$ = 0.041ms$^{-1}$ and $U_{ws}$ = 0.763ms$^{-1}$ bottom left and right respectively**

## 11.3 Conclusion

Experiment 11.1.1 was conducted in a flow loop with a stream of bubbles. A newly developed miniature four-sensor probe was used to measure velocity vector of a bubble. Teflon coated needles with a diameter of 0.2mm were used as sensors for the four-sensor probe. The tests were carried out with a bubble diameter of 5mm at various $\alpha_{ref}$ (5º, 14º, 21º and 34º) with $\beta_{ref}$ = 0 º and at various reference velocities $v_{ref}$ and water superficial velocities $U_{ws}$. $\alpha_{meas,m,p}$, $\beta_{meas,m,p}$ and $v_{meas,m,p}$ were calculated for all the above experiments with both the "average $\delta t_{ii}$" method and "average individual bubble" method, with the probe dimensions measured before and after collecting data. Each calculation was carried out with and without signal processing.

The results show that there was a remarkable improvement in the results of $\alpha_{meas,m,p}$, $\beta_{meas,m,p}$ and $v_{meas,m,p}$ due to the signal processing. As expected, the signal processing reduces the number of bubbles (NOB) that touch all four sensors by deleting the invalid signals, as described in sections 5.2.1.2 and 5.2.1.3.

With regard to the results from all the above experiments, the relatively low values of $\sigma_{abs,\alpha,p}$ $\sigma_{abs,\beta,p}$ and $\sigma_{abs,v,p}$ indicate that the miniature four-sensor probe can be used to give a reasonably accurate estimate of polar angle $\alpha_{meas,m,p}$ and azimuthal angle $\beta_{meas,m,p}$ of the bubble velocity vector in the flow loop for the various flow rates. Experiments also indicate that the measured velocity vector for the larger $\alpha_{ref}$ gives less errors when $\alpha_{meas,m,p}$, $\beta_{meas,m,p}$ and $v_{meas,m,p}$ are measured, either with "average $\delta t_{ii}$" or with an "average individual bubble" method.

As discussed earlier, the probe dimensions were measured before and after collecting the data. The measurements do show there is an effect on the probe dimensions while data is being collected, but in general the probe dimensions measured before collecting data gave fewer errors for the data collected initially, whereas the same data processed with the probe measured after collecting data gave a larger error. Similarly, the data collected just before re-measuring the probe dimensions gave fewer errors when the probe dimensions were measured after collecting the data, but gave larger errors when the probe dimensions were measured before collecting the data. This situation also depends on the number of data collected before re-measuring the probe. The flow condition presented in these experiments shows that the probe needs to be re-measured after collecting every four sets of data. Due to the fragile nature of the probe needles, it cannot handle a high flow rate of water.

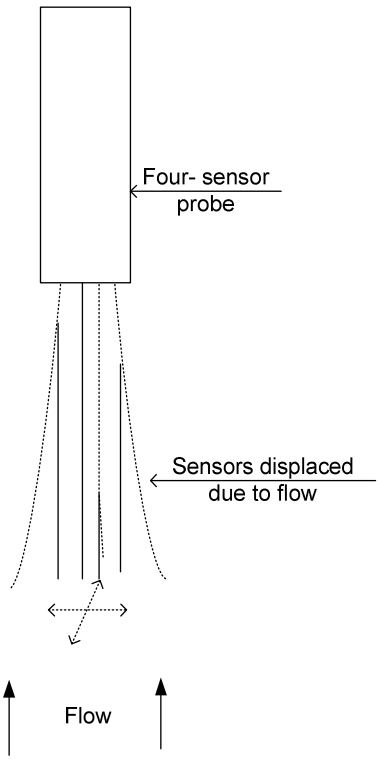


**Figure 11.23 Probe displaced due to the presence of flow**

It is also possible that, due to the flow of the water, the sensor might expand and contract in the process of collecting data, as shown in Figure 11.23; however, the hypothesis was not examined in this project.

The tables presented in Appendix C (Tables B.5- B.12) show the difference in the number of bubbles (NOB) when the data were processed with and without signal processing. The results suggest that, due to the presence of the signal processing procedure, signals with missing bubbles, small time intervals and small voltage levels were ignored, as discussed in section 5.2.1, thus resulting in fewer bubbles being recorded as only those that hit all four sensors of the probe were valid.

Experiments 11.2.1 were carried out in vertical upward bubbly air-water flow with and without the presence of a 20° swirler. The experiments were conducted using a miniature four-sensor probe to investigate the local axial velocity $v_z$, radial velocity $v_r$ and azimuthal gas velocity $v_\theta$ and the mean gas volume fraction $\bar{\lambda}$ of the dispersed phase in bubbly gas-water flow at various water and gas flow rates. Tests were carried out to investigate the distribution of mean local axial, radial and azimuthal bubble velocity. The distributions of the local gas volume fraction in such flows were also investigated.

Results from calibration factor *K* (see Table 11.2) show that the average value of *K* is equal to 0.97 when calculated with $\bar{u}_{g,ref}$ and is 0.95 when calculated with $\bar{u}_{g,camera}$. Results also indicate that when the value of *K* was calculated with $\bar{u}_{g,ref}$, the value of $K$ increased as $U_{ws}$ and $U_{gs}$ increased, which indicates that $\bar{u}_{g,probe}$ is higher than $\bar{u}_{g,ref}$ at low $U_{ws}$ and $U_{gs}$ and $\bar{u}_{g,probe}$ is lower than $\bar{u}_{g,ref}$ at high $U_{ws}$ and $U_{gs}$. This difference in $\bar{u}_{g,ref}$ and $\bar{u}_{g,probe}$ at various flow rates of gas and water led us to

assume that at $U_{gs}$ upstream and downstream the swirl varies due to the presence of the swirl itself.

Results also indicate that there is very little difference in the calculated $\overline{u}_{g,camera}$ and $\overline{u}_{g,probe}$ at various $U_{ws}$ and $U_{gs}$.

The above result indicates that the miniaturized probe investigated showed a significant improvement in calibration factor $K$, which is found to be close to 1, unlike that indicated by previous research [1]. This result further indicates that the retarding effect on the bubble due to the miniaturized probe-bubble interaction was significantly reduced.

Results (Figure 11.16 and 11.17) show that there is a relatively small effect on the local axial bubble velocity due to the presence of the swirler for the flow condition used in the above experiments. Figures 11.18 and 11.19 show that the measured radial velocity $v_r$ is always close to zero, both with and without a swirler, for the flow condition investigated.

The results presented in Figures 11.20 and 11.21 show that, without the presence of the swirler, $v_\theta$ is relatively close to zero at all positions along the pipe diameter and is slightly positive, suggesting the presence of a low level clockwise swirl. However, in the presence of the swirler, for the flow condition investigated, $v_\theta$ was found to be strongly negative towards the pipe wall and the magnitude of $v_\theta$ decreases towards the pipe centre, suggesting that part of the multiphase mixture is rotating with an approximately constant angular velocity $\omega$ (because $v_\theta = r\omega$).

Results of the gas volume fraction presented in Figures 11.14 and 11.15, with the low flow rate of $U_{gs}$ and $U_{ws}$, show that there is a small difference between the local gas volume fraction profiles with and without the swirler. Results show that the gas volume fraction profile is peakier at the pipe centre with the swirler as compared to the gas volume fraction profile without the swirler. However, with a higher flow rate of $U_{gs}$ and $U_{ws}$, the presence of the swirler shows that the more gas bubbles tend to accumulate at the centre of the pipe with the swirler, but without the swirler very few bubbles migrate to the centre of the pipe.

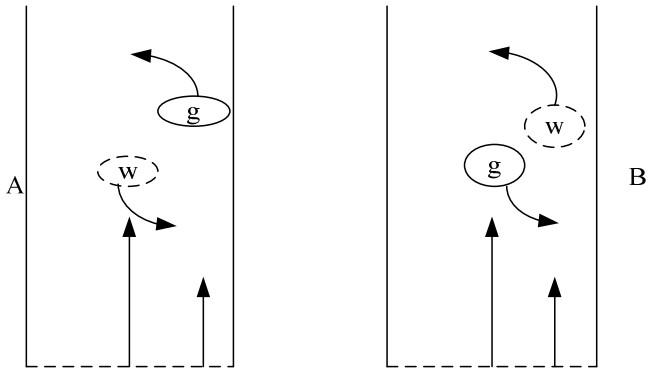


**Figure 11.24 Length of vertical arrows represents axial water velocity at different positions in the pipe. In (a), movement of gas bubble 'g', and resultant movement of water 'w', causes a reduction in the system energy. In (b) energy input would be required. Lucas et al. [14].**

This proves the theory presented by Lucas et al. [14], whereby the author explains the kinetic energy within the flow, in which the author considers a vertical upward water flow in a pipe with maximum water flow at the centre of the pipe and considerably less at the pipe walls. Let it be assumed a gas bubble is located away from the pipe centre (see Figure 11.24A). If turbulence in the flow causes the gas bubbles to move slightly toward the pipe centre, this will in turn require the equivalent volume of water to move slightly towards the pipe wall. Since water has a higher density than gas, the

overall kinetic energy of the system is now reduced and the system is in a lower energy state.

However, if a gas bubble at the pipe centre (see Figure 11.24B) was to move away from the centre of the pipe, it will then require an input of energy to the system. There is thus a natural tendency for the system to move towards a lower energy state, resulting in gas bubbles moving towards the pipe centre and once they are at the pipe centre they tend to remain at the pipe centre.

# CHAPTER 12

# Conclusions

## 12.1 Summary of main achievements of the work documented in this thesis

1. A new four-sensor probe has been designed and constructed for measuring the bubble velocity vector of air bubble in a bubbly air-water flow. The probe, denoted the PN2 probe, is constructed from Teflon coated needles and has a frontal area of 0.61mm$^2$. An ideal four-sensor probe has a calibration factor of unity. It was found that for the experiments in stationary water carried out in a tank the calibration factor *K* of the PN2 probe was 0.99. For the test in a flow loop the probe calibration factor *K* was 0.95. These values were compared with a calibration factor of 1.2 for the previous four-sensor probe described in the literature.
2. Results carried out in stationary water showed that if the PN2 probe was used in air bubbles of diameter less than or equal to 5mm, and if the axial distance between the front and the rear sensor was in the range of 1-1.5 mm the mean absolute error in the measured bubble polar angle $\bar{\varepsilon}_{abs,\alpha}$ was 1.32º, the mean absolute error in the measured azimuthal angle $\bar{\varepsilon}_{abs,\beta}$ was -0.1º and the mean percentage error in the measured bubble velocity magnitude was 0.83%.
3. Another novel feature of the work in this thesis was the use of high speed cameras to provide reference measurements of the bubble velocity vector in the tank coordinate system. A mathematical model was derived to enable the bubble

velocity vector (measured by the probe) to be transformed into the tank coordinate system (irrespective of the probe orientation in the tank). This enabled the bubble velocity vector measured by the probe to be readily compared with the reference velocity vector measured using the high speed cameras.

## 12.2 Detailed explanation of conclusions

A miniaturised four-sensor probe was designed and built with Teflon-coated needles. These sensors were capable of measuring the velocity vector of the dispersed phase (air bubble) in a bubbly two-phase flow. The probe was made up of Teflon-coated needles with an outer diameter of 0.15 and 0.2 mm, and the results were compared with previous results acquired by Mishra et al. [1] and Panagiotopoulos et al. [11]. These previous results were achieved using varnish-coated acupuncture needles with a diameter of 0.3mm to construct a four-sensor and rotating dual-sensor probe respectively.

The primary intention of this research was to miniaturize the four-sensor probe used to measure the velocity vector of the multiphase flow. The overall cross-section of the probe was reduced by introducing new Teflon coated needles of 0.15mm and 0.2mm in diameter, whereas previously 0.3mm diameter acupuncture needles was used as sensor needles. These acupuncture needles were then painted to make them electrically insulated, which in turn made these sensors thicker in diameter. A new design of ceramic guide (see Figure 3.10) was also introduced in this research, in an attempt to reduce the overall cross-section of the probe. The new ceramic guide helps to place the four sensors of the four-sensor probe in the form of an isosceles triangle (see Figure 3.12), whereas the previously used ceramic guide (See Figure 3.2) placed

the holes in a rectangular form. As a result, the difference between using the previous type of PN0 (varnish coated acupuncture needles) and the Teflon coated PN2 probes can be observed in the overall cross-sectional area of the probe, which is found to be $2.08\text{mm}^2$ and $0.61\text{mm}^2$ respectively.

This difference makes a big impact on calibration factor $K$ of the probe. The calibration factor of the conventional acupuncture probe was typically 1.2, although this value varied by about ±20% for the different flow conditions, as described in Mishra et al. [1 and 11]. On the other hand, the Teflon-coated probe shows the average value of $K$ to be between 0.95 (for the flow-loop experiments) and 0.99 (for the bench test experiments) which is much closer to unity for the four-sensor probe. This reduction in the value of $K$ indicates a significant reduction in the probe-bubble interaction effect.

As mentioned earlier in the process of designing this four-sensor probe, a new type of guide (see Figure 3.10) was introduced. This ceramic guide uses the centre hole for sensor '0' rather than using the conventional four holes aligned in a square (see Figure 3.2). The advantage of using this type of guide is that the bubble flowing from any direction always hits the front sensor before hitting the rear sensors, unlike the conventional orientation where the bubble has to flow in a particular direction (see Figure 3.14). For the mathematical model presented in section 2.5, it is important that the bubbles always hit the front sensor first. If the bubble doesn't hit the front sensor first, then time interval $\delta t_{ii}$ ($i$ =1, 2 and 3) given by Equations 2.41 – 2.43 will be negative, resulting in a larger number of bubbles to be ignored. Thus, the new orientation of the sensors helps to reduce the sampling time, as most of the bubbles hit the front sensor first, unlike the previous design. Reduced sampling time requires less

volume of data to be processed, thus increasing the speed of the signal processing procedure.

The signal processing method was made much easier and simpler when it was automated by introducing a few new parameters which detect and ignore signals from a bubble that doesn't hit the front sensor, or a bubble signal with a smaller voltage drop or with a smaller time interval caused by ambiguous bubble-probe interactions, depending on the manner in which the bubble hits the probe. This is discussed in more detail by Juila et al. [131], in which the author also introduces three main effects as:

[1] Blinding effect: since the probe detects the disturbed interface position, the local interface deformation during probe impact contributes to the error. This leads to the existence of a blind zone or, equivalently, to an effective shape detected by the probe.

[2] Crawling effect: the whole bubble is decelerated and/or deformed during the interaction.

[3] Drifting effect: the trajectory of the bubble is altered, leading to either the detection of a smaller chord or to no detection at all.

Signal processing helps to eliminate the invalid signals generated by the above situations. The signal processing scheme was also automated in order to calculate the polar angle $\alpha$ and the azimuthal angle beta $\beta$, as described in section 2.5.1.

A sensitivity analysis on the effect of errors in the measured probe dimensions was carried out, indicating that errors in the measurement of the probe have a huge influence on the calculated velocity vector of the bubble. These errors are found to be greater for the small polar angle than the larger polar angle. The error results show

when $\alpha_{ref}$ is close to 0°, a ±10% error in the value $z_i$ causes the calculated $\alpha$ to vary by 7° from the reference value. However, when $\alpha_{ref}$ reaches 30°, a ±10% error on the $z_i$ causes the calculated value of $\alpha$ to vary from a maximum of 34° to a minimum of 28°. The result would lead the observer to decide to use the tilted probe only at a certain angle, as it shows a lesser effect in terms of measurement error.

High speed cameras, which capture 250 frames per second, were used in order to measure the reference velocity of the bubble for the tank experimental results. The velocity was calculated using the centre of gravity (COG) of the bubble for each frame; the mean value is used as the reference velocity. The trajectory of single bubbles before and after hitting the probe was calculated from images captured by the camera, which shows bubble velocities relative to the water tank (as a bubble moves over a vertical probe). The trajectory of bubbles is interesting in its own right because visual observation of a rising bubble stream suggests a zigzag motion which would lead the observer to think that the polar angle was significantly greater than the actual measured value as the bubble moves over the probe.

The captured images also show that the bubble moves across the probe in the direction of the BUOYANCY force on the COG (lateral motion appears to be suppressed). This result could not be known without the use of high speed cameras.

The images were also used for the reconstruction of the bubble using an image processing scheme, which involves curve-fitting and the least square method of finding the error for particular images. From these images, the bubbles were found to have a diameter of 5-6 mm (the major axis of the bubble was taken as the bubble diameter itself) for the small bubble and 10-12 mm for the larger bubble.

To achieve a good accuracy measurement of $\alpha_{meas}$ and $\beta_{meas}$ it is recommended that the following criteria should be met:

- Bubble size: 5mm
- Sensor type: 0.15mm Teflon coated needles
- Dimension of $z_i$: 1-1.5m
- Sampling frequency: 40K Hz
- Sampling time: >1 minute
- Number of bubble: > 30
- Stream of bubbles

The experiment was also carried out in the flow loop with and without the swirler. The bubbly flow in the swirler shows that, in the presence of water velocity, a bubble tends to flow in a linear direction and experience a minimum amount of deformation compared to a bubble flowing in steady water.

As with the bench tests, various experiments were carried out in the flow loop in a stream of bubbles with different sizes of Teflon-coated needles, at various values of reference polar angles $\alpha_{ref}$. The probes were measured before and after recording each data, which showed that there was very little variation in the probe dimensions, but due to the probe's flexibility it is unknown whether or not changes in its dimensions occurred when recording the data. These data are also calculated with or without the signal processing. The velocity vector of the bubble was calculated using the "average individual bubble", as well as the "average $\delta t_{ii}$" method (see Chapter 11.1). As expected, the results after the signal processing were found to contain fewer errors than without the signal processing. It was also found that, in some cases, re-

measurement of the probe makes very little difference to the results, making the author believe that the deformation or the change in the probe dimensions is a long drawn out process which does not change after every data reading. For example, if the probe is measured before and after recording ten data readings, the probe dimensions measured prior to collecting the data result in fewer errors for the data collected at the beginning. Similarly, the dimensions measured after collecting the data give fewer errors for the data collected at the end, but as mentioned before, it is still unknown whether contraction and expansion of the probe causes any effect due to the velocity of the water.

The flow loop experimental results showed the difference in the number of bubbles (NOB) when the data were processed with and without signal processing. The results suggest that, due to the presence of the signal processing procedure, the signals which comprised missing bubbles, small time intervals and small voltage levels (as discussed in section 5.2.1) were ignored, which is about 10% of the total number of bubbles. This resulted in a fewer number of bubbles being processed in the data, as it only encompassed those that hit all four sensors of the probe.

Flow loop experiments also indicate that $\overline{\alpha}_{meas,m}$ calculated with the "average $\delta t_{ii}$" method shows fewer errors than when it is calculated with the "average individual bubbles" method. The calculated value of $\overline{\alpha}_{meas,m}$ with the signal processing (AS) gave a result much closer to $\alpha_{ref}$ as compared to $\overline{\alpha}_{meas,m}$ measured without signal processing (BS). Results also indicate that, as the value of $\alpha_{ref}$ increases, the errors reduce. Results from $\sigma_{abs,a}$ also show $\alpha_{meas,m}$ was close to $\alpha_{ref}$ when it was

calculated using the "average $\delta t_{ii}$" method with the probe dimensions measured after collecting data (PMA), with the signal processing (AS).

A flow loop experiment for the azimuthal angle shows that $\beta_{meas,m}$, calculated using the "average individual bubble" method with signal processing, gives $\bar{\varepsilon}_{abs,\beta}$ of around 30°. The values were calculated with the probe dimension measured before collecting the data (PMB). Unlike $\alpha_{meas,m}$, when $\alpha_{ref}$ is increased, the error in $\beta_{meas,m}$ is larger as it is calculated with the "average $\delta t_{ii}$" method, but the result was found to be the reverse when calculated using the "average individual bubble" method. The standard deviation of $\beta_{meas,m}$ suggests that when $\beta_{ref}$ = 34°, the calculated value of $\beta_{meas,m}$ is much more scattered than when $\beta_{ref}$ = 0°.

Flow loop results of the velocity magnitude show that when $v_{meas,m}$ is calculated using "average $\delta t_{ii}$" with signal processing, $v_{meas,m}$ gives a close comparison with a reference value of $v_{ref}$ for $v_{ref}$ = 30°. However, when $v_{ref}$ = 5°, $v_{meas,m}$ was found to be close to $v_{ref}$ when calculated using the "average individual bubble" method with signal processing.

However, the values of standard deviation $\sigma_{abs,a}$ and $\sigma_{abs,\beta}$ indicate the errors in individual measurements of $\alpha_{meas,m}$, and $\beta_{meas,m}$ were still somewhat greater than would be suggested by the values of $\bar{\varepsilon}_{abs,\alpha}$ and $\bar{\varepsilon}_{abs,\beta}$. The results also indicate that, with the presence of water, velocity bubbles flow in a straight path with reduced deformation of the bubble, unlike in steady water where the bubbles flow in a rectilinear/zigzag or rectilinear/spiral [163].

The flow loop test was also carried out in bubbly flow in the presence of the swirler, which is then compared with the results achieved without the swirler. The tests were conducted at various superficial velocities of water $U_{ws}$ and superficial gas velocities $U_{gs}$. The results show that, for the lesser $U_{ws}$, the presence of the swirler has much less effect on local gas volume fraction distribution, whereas for larger $U_{ws}$ the presence of the swirler shows a centrifugal effect, which causes the low density gas to preferentially accumulate at the centre of the pipe. At the same gas and liquid flow rate without the presence of the swirler, the gas distribution is much more uniform.

The results also show that there is very little effect on the shape of the axial velocity profile for the tested values of air and water superficial velocities, whereas the radial velocity $v_r$ is always comparatively small. It also shows that, without the presence of the swirler, azimuthal velocity $v_\theta$ is very close to or around zero at all positions, whereas in the presence of the swirler, the distribution of $v_\theta$ was found to be more negative across the pipe diameter. For both test conditions, it was found that the presence of the swirler causes the azimuthal velocity $v_\theta$ to be strongly negative close to the pipe walls. It also indicates that the magnitude of azimuthal velocity $v_\theta$ decreases at the probe's centre.

# CHAPTER 13

# Further Work

## 13.1 Local probe optimization

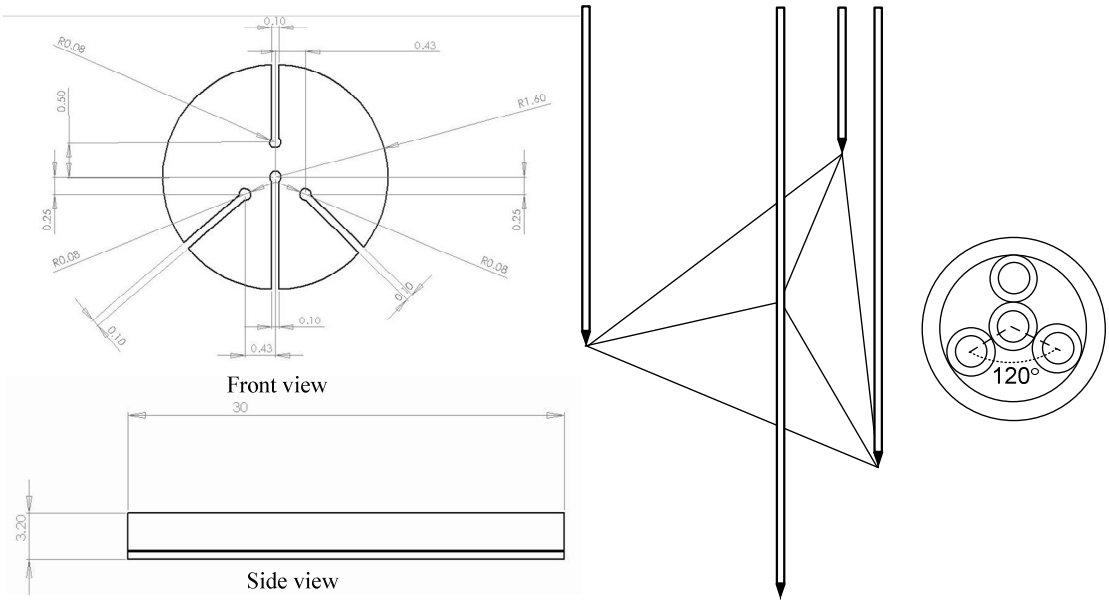


**Figure 13.1 New orientation for the miniaturized four-sensor probe**

It can be seen from the results that with the smaller cross-section of the probe there is less deformation in the bubbles during probe-bubble interaction, resulting in the measured velocity vector being close to the reference velocity vector. This can be further improved by minimizing the probe's cross-sectional area and ensuring the formation of the probe is an equilateral triangle with the sensor '0' in the centre, as shown in Figure 13.1. Currently, work is being undertaken to design a guide (as shown in Figure 13.1) where the holes are made as small as possible, so as to just fit the Teflon needle inside. The further advantage of this is that there might not be a

need to measure $x_i$ and $y_i$ of the probe dimensions. As the guides are machine-made and are very tight to the needle diameter, it is believed that $x_i$ and $y_i$ dimensions would always be constant.

The experimental results from the tank experiment and flow loop show that the improved accuracy with which the bubble velocity vector can be measured when the polar angle $\alpha$ between the bubble velocity vector and the $z$ axis of the probe coordinate system is large and when the azimuthal angle $\beta$ is close to zero arises due to the relative positions of the four sensors (i.e. the tips of the needles) 'seen' by the bubble. In most bubbly pipe flows of practical interest, including the swirling bubbly air-water pipe flows described in Chapter 11, the bubble velocity vector is predominantly in the axial direction of the pipe. In such flows it would be possible to achieve improved relative positioning of the four sensors, potentially enabling more accurate bubble velocity vector measurement, by tilting a PN2 probe relative to the pipe axis as shown in Figure 10.3 (see Chapter 10). Unfortunately, by tilting the probe in the manner shown in Figure 10.3, the large angle between the bubble velocity vector and the axis of each needle means that the resistance of the needles to the motion of the bubble is increased. The challenge is therefore to design a probe for which (i) the relative positions of the sensors as 'seen' by a bubble moving predominantly parallel to the pipe axis are the same as those 'seen' by a bubble approaching a PN2 probe with a polar angle $\alpha$ of $30^{\mathbf{o}}$ and an azimuthal angle $\beta$ of $0^{\mathbf{o}}$ relative to the probe coordinate system; but for which (ii) the axes of the needles are parallel to the pipe axis, thereby presenting minimum resistance to the motion of the bubble as shown in Figure 13.2.

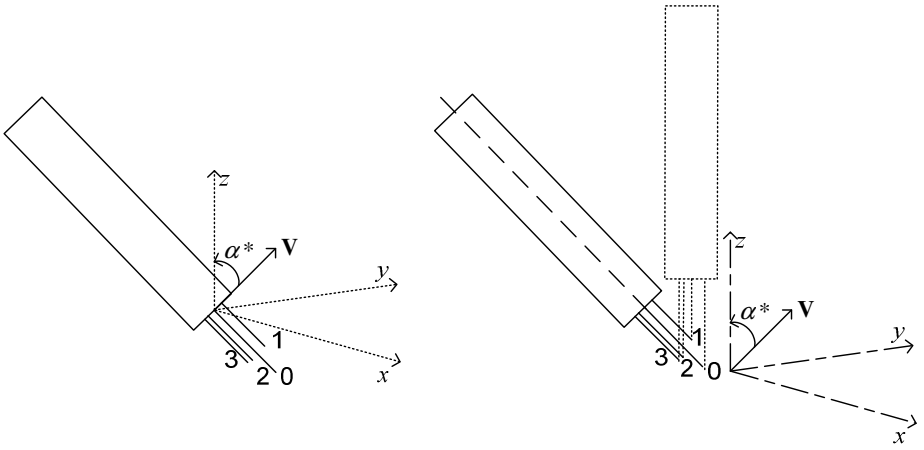


**Figure 13.2 Probe layout for $\alpha*$**

Consider a PN2 probe for which the coordinates of the $i^{th}$ rear sensor relative to the lead sensor in the $\hat{\underline{x}}_p, \hat{\underline{y}}_p, \hat{\underline{z}}_p$ probe coordinate system are $\hat{\underline{x}}_{p,i}, \hat{\underline{y}}_{p,i}, \hat{\underline{z}}_{p,i}$ $(i = 1,2,3)$. Let us now define a new coordinate system $x, y, z$ which initially coincides precisely with the $\hat{\underline{x}}_p, \hat{\underline{y}}_p, \hat{\underline{z}}_p$ probe coordinate system but which remains fixed in space whilst the $\hat{\underline{x}}_p, \hat{\underline{y}}_p, \hat{\underline{z}}_p$ coordinate system is rotated in space as shown in Figure 13.3.

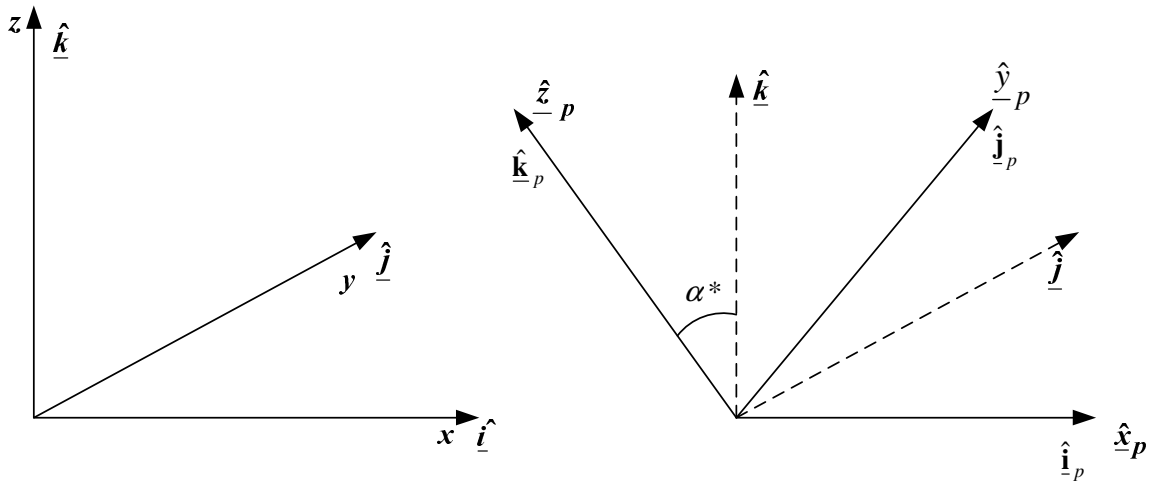


**Figure 13.3 Vector representation for new probe coordinates with respect to $\alpha*$**

Therefore, the new coordinate of $i^{th}$ rear sensor is given by:

$$x_i \hat{\underline{\mathbf{i}}}_p + y_i \hat{\underline{\mathbf{j}}}_p + z_i \hat{\underline{\mathbf{k}}}_p \qquad \textbf{Equation 13.1}$$

where $\hat{\underline{\mathbf{i}}}_p, \hat{\underline{\mathbf{j}}}_p, \hat{\underline{\mathbf{k}}}_p$ are unit vector in direction of $\hat{\underline{x}}_p, \hat{\underline{y}}_p, \hat{\underline{z}}_p$.

With reference to a Chapter 8, suppose the PN2 probe is rotated by an angle $\alpha^*$ about the $\hat{\underline{x}}_p$ axis (in the anticlockwise direction when viewed along the positive $\hat{\underline{x}}_p$ axis in the direction of the origin) and by an angle $\beta^*$ about the $\hat{\underline{z}}_p$ axis (in the anticlockwise direction when viewed along the positive $\hat{\underline{z}}_p$ axis in the direction of the origin). The new position of the $i^{th}$ rear sensor in the fixed $(x, y, z)$ coordinate system is given by:

$$x_{new,i} = \hat{\underline{x}}_{p,i} \cos\beta^* - \hat{\underline{y}}_{p,i} \sin\beta^* \qquad \textbf{Equation 13.2}$$

$$y_{new,i} = \hat{\underline{x}}_{p,i} \sin\beta^* \cos\alpha^* + \hat{\underline{y}}_{p,i} \cos\beta^* \cos\alpha^* - \hat{\underline{z}}_{p,i} \sin\alpha^* \qquad \textbf{Equation 13.3}$$

$$z_{new,i} = \hat{\underline{x}}_{p,i} \sin\beta^* \sin\alpha^* + \hat{\underline{y}}_{p,i} \cos\beta^* \sin\alpha^* + \hat{\underline{z}}_{p,i} \cos\alpha^* \qquad \textbf{Equation 13.4}$$

If we now let $\alpha^*$ equal $30^{\mathbf{o}}$ and $\beta^*$ equal $0^{\mathbf{o}}$ the new coordinates of the $i^{th}$ rear sensor in the $x, y, z$ coordinate system are

$$x_{new,i} = \hat{\underline{x}}_{p,i} \qquad \textbf{Equation 13.5}$$

$$y_{new,i} = 0.866 \hat{\underline{y}}_{p,i} - 0.5 \hat{\underline{z}}_{p,i} \qquad \textbf{Equation 13.6}$$

$$z_{new,i} = 0.5 \hat{\underline{y}}_{p,i} + 0.866 \hat{\underline{z}}_{p,i} \qquad \textbf{Equation 13.7}$$

The coordinates $x_{new,i}$, $y_{new,i}$ and $z_{new,i}$ $(i = 1,2,3)$ represent the positions of the three rear sensors relative to the lead sensor for a new probe, denoted the P30 probe. The coordinate system for this P30 probe is the $x, y, z$ coordinate system referred to above, the origin of which is at the lead sensor. The $z$ axis is parallel to the axes of the needles and also parallel to the axis of the pipe, the $y$ axis is parallel to the arm of the probe holder (refer to Figure 3.18) and the $x$ axis is at ninety degrees to the $y$ axis in the clockwise sense when the coordinate system is viewed along the increasing $z$ axis in the direction of the origin. The relative positions of the sensors in the P30 probe seen by a bubble moving parallel to the pipe axis are the same as those that would be seen by a bubble moving with a polar angle $\alpha$ of $30^{o}$ and an azimuthal angle $\beta$ of $0^{o}$ relative to the coordinate system of a PN2 probe.

## 13.2 Experimental use of the local probe system

Further experimental work can also be carried on the oil-water flow. Since the viscosity of the oil is higher than that of the water, it is believed that it would be a straightforward experiment without causing the deformation problems as experienced in air-water flow. The experiments can be carried out in both vertical and inclined oil-water flow. The necessary modification of an existing oil flow rig is already underway.

Probes could be extended to the array of probes shown in Figure 13.4 to measure the flow properties across the pipe diameter simultaneously. This array of probes could be used in unsteady air-water and oil-water flow to see how the velocity vector varies over a short period of time.

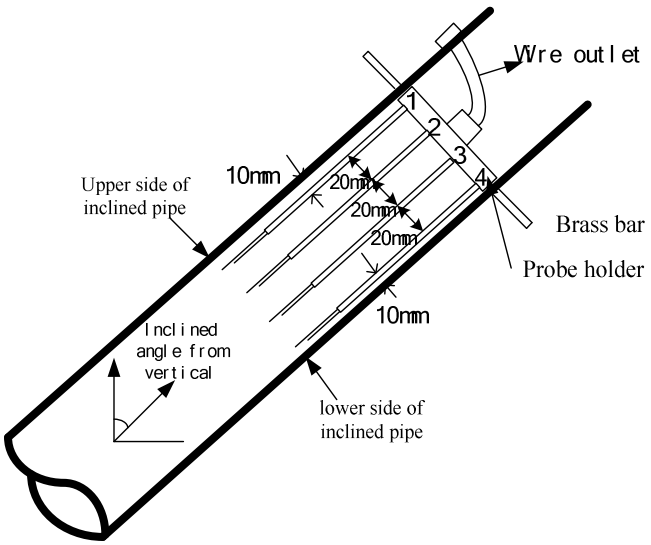


**Figure 13.4 Schematic of a dual-sensor array probe in an inclined pipe**

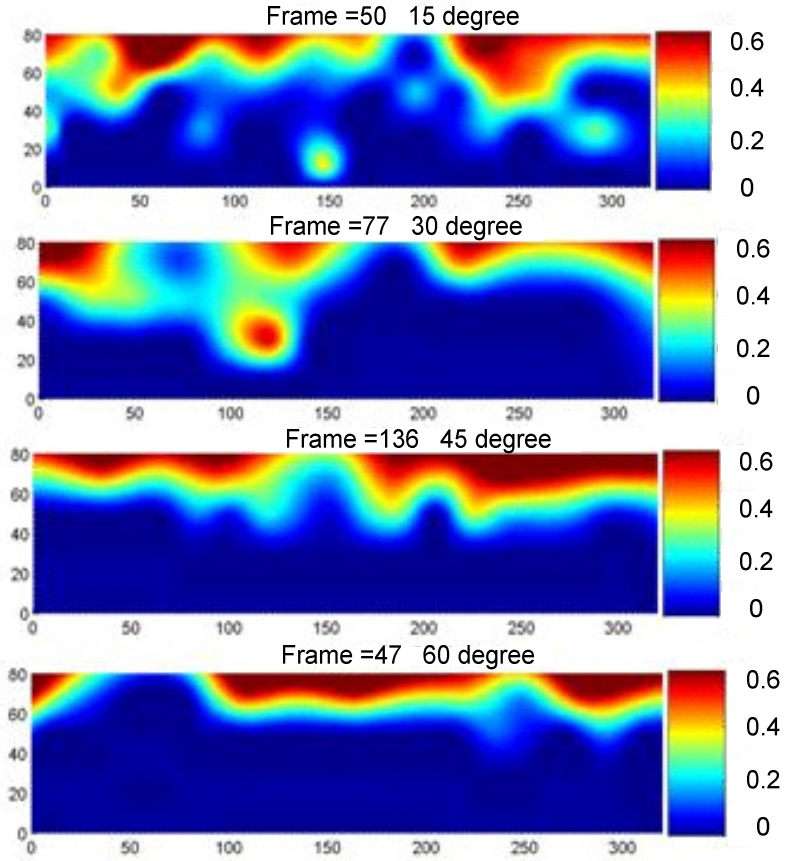


**Figure 13.5 Local oil volume fraction distributions for different inclination angles to the vertical (15°, 30°, 45° and 60°) ($Q_w$ = 3.5 m3/h; $Q_o$ = 1.0 m3/h)**

Figure 13.5 shows results from the initial experiment carried out in the inclined oil-water flow for different pipe inclinations at the same water and oil flow rates ($Q_w$ = 3.5 m3/h; $Q_o$ = 1.0 m3/h). It can be clearly seen from Figure 13.5 that the oil volume fraction is more concentrated at the upper side of the pipe for inclination angles of 45 degrees and 60 degrees than is the case for inclination angles of 15 degrees and 30 degrees. Results suggest that the array of probes can be used for further investigations.

## 13.3 Reference measurement devices

The high speed cameras used in this research can be used extensively to calculate the residence time of the probe in a bubble. Using these cameras, detailed investigation can be carried out on the effect of the probe on the bubble and the trajectory of the bubble after striking the probe. Cameras can also be used to observe effects on the probe due to the velocity of the water, which in this particular research is assumed to be zero

# References

1. Lucas G. P., Mishra R., “Measurement of bubble velocity components in a swirling gas-liquid pipe flow using a local four-sensor conductance probe.”, Meas. Sci. Technol., volume 16, pages 749-758, 2004.
2. Mishra R., Lucas G. P., Kieckhoefer H., “A model for obtaining the velocity vectors of spherical droplets in multiphase flows from measurements using an orthogonal four-sensor probe.”, Meas. Sci. Technol. volume 13, pages 1488-1498, 2002.
3. Lucas G P, Wang M, Mishra R, Dai Y and Panayotopoulos N. “Quantitative comparison of gas velocity and volume fraction profiles obtained from a dual-plane ERT system with profiles obtained from a local dual-sensor conductance probe, in a bubbly gas-liquid flow.” 3rd International Symposium on Process Tomography, Lodz, Poland, 9-10 Sept 2004, (pp.96-100).
4. X. Zhao, G. Lucas and S.Pradhan. “Signal processing method in using four-sensor probe for measuring the velocity vector of air-liquid two-phase flow.” 3rd international symposium on advanced fluid/solid science and technology in experimental mechanics,7-10 December 2008, Taiwan.
5. Pradhan S., Lucas G., Panagiotopoulos N. “Sensitivity Analysis for a 4-Sensor Probe Used for Bubble Velocity Vector Measurement” Researchers conference University of Huddersfield 2006.
6. N. Panayotopoulos, G. P. Lucas, R. Mishra, “Calculation of Volume fraction and mean bubble vector velocity using two and four sensor conductivity probes in vertical and inclined bubble air-water flows.”, School of computing & engineering Researchers’ Conference, University of Huddersfield, Nov 2005.
7. Jim Cory, “The measurement of volume fraction and velocity profiles in vertical and inclined multiphase flow”, PhD thesis, December 1999.
8. G. P. Lucas, J. C. Cory, R. C. Waterfall, Loh W. W., and Dickin F. J., “Measurement of the solids volume fraction and velocity distributions in solids-liquid flows using dual-plane electrical resistance tomography”, J. Flow Meas. Instrum., volume 10, pp. 249-258, 1999.
9. Wang M, Lucas G, Dai Y, Panayotopoulos N, Williams R “ Visualisation of bubbly velocity distribution in a swirling flow using electrical resistance tomography.” PPSC 23 (2006) pp 321-329.

10. G.P.Lucas, N Panayotopoulos “Power law approximation to gas volume fraction and velocity profile in low void fraction vertical gas-liquid flows” J. Flow Meas. Instrum., volume 15, pp. 271-283, 2004.
11. Panagiotopoulos N., Lucas G. “Simulation of a local four-sensor conductance probe using a rotating dual-sensor probe.” Meas. Sci. Technol., volume 18, pp. 2563-2569, 2007
12. Lucas G. P., Jin N. D., “Measurement of the homogeneous velocity of inclined oi-in-water flows using a resistance cross correlation flow meter.” Meas. Sci. Technol., volume 12, pp. 1529-1536, 2001.
13. S. Pradhan, G.P. Lucas, X. Zhao “Measurement of reference velocity vector for four-sensor conductance probes using orthogonal, high speed cameras” international conference of multiphase flow, Palermo 7-10 September 2008.
14. G. P. Lucas, N. Panagiotopoulos “Measurement and modelling of oil volume fraction and velocity profiles in vertical, bubbly oil-in-water flows” 11th Int. Conf. on Multiphase Flow in Industrial Plants, Palermo, Italy 2008, pp. 391-398.
15. Christophe Boyer, Anne-Marie Duquenne, Gabriel Wild, “Measuring techniques in gas-liquid-solid reactors”, Chemical Engineering Science, volume 57, pp 3185-3215, 2002.
16. Takashi Hibiki, Rong Situ, Ye Mi, Mamoru Ishii, “Local flow measurements of vertical upward bubbly flow in an annulus”, Heat and Mass Transfer, volume 46, pp 1479-1496, 2002
17. S Ghorai, V Suri, K. D. P. Nigam, “Numerical modelling of three-phase stratified flow in pipes.” Chemical Engineering Science, volume 60, pp., 6637-6648, 2005.
18. R. Constantini, R.H. Parsons “The economic and environmental impact of long distance slurry pipelines.” Hydrotransport 3, Proceedings of the 3rd International Conference on the Hydraulic Transport of Solids in Pipes, Golden, Colorado, U.S.A., 1974, pp. K1-K12.
19. P.E Goosen., R. Cooke “Design and construction of the Noordhoek kaolin slurry pipeline.” Hydrotransport 13, Proceedings of the 13th International Conference on Slurry Handling and Pipeline Transport, Johannesburg, South Africa, 1996, pp. 405-417

20. V. Seshadri, S. N. Singh, Charau Fabien, and R. Mishra, “Hold-up in multi-sized particulate solid-liquid flow through horizontal pipes.”, Indian Journal of Engineering & Materials Sciences, volume 8, pp. 84-89, April 2001.
21. J. Ling, P. V. Skudarnov, C. X. Lin, M. A. Ebadian, “Numerical Investigations of liquid-solid slurry flows in a fully developed turbulent flow region.”, International Journal of Heat and Fluid Flow, volume 24, pp. 389-398, 2003
22. Suhashini Ghorai, K. D. P. Nigam, “CFD modelling and interfacial phenomena in two-phase flow in pipes.”, Chemical engineering and Processing, volume 45, pp. 55-65, 2006.
23. Beggs, H. D., Brill, J. P., “A study of two-phase flow in inclined pipes.” J. Pet. Technol., (MAY), 607-617, 1973.
24. Dirk Lucas, Eckhard Krepper, Horst-Michael Prasser, “Prediction of radial gas profiles in vertical pipe flow on the basis of bubble size distribution.”, Int. J. Therm. Sci., volume 40, pp. 217-225, 2001
25. Tomio Okawa, Isao Kataoka, Michitsugu Mori “Numerical simulation of lateral phase distribution in turbulent upward bubbly two-phase flows” Nuclear Engineering and Design, Volume 213, Issues 2-3, April 2002, Pp. 183-197
26. Severin Waelchli, Philipp Rudolf von Rohr, “Two-phase flow characteristics in gas-liquid microreactors.”, International journal of multiphase flow, volume 32, issue 7, pp. 791-806, 2006.
27. Wei Feng, Jianping Wen, Jinghua Fan, Qing Yuan, Xiaoqiang Jia, Yan Sun, “Local hydrodynamics of gas-liquid-nanoparticles three-phase fluidization.”, Chemical engineering science, volume 60, pp. 6887-6898, 2005.
28. J. Varley, J. W. R. Boyd, S. Gallagher, A. K. Brown, P. W. Dodd, “Correlation between conductivity and liquid hold-up for a multi-segment industrial foam probe for fermentation.”, Biochemical engineering journal, volume 19, pp. 199-210, 2004.
29. Bouchaib Gourich, Christophe Vial, Abel Hafid Essadki, Fouad Allam, Mohammed Belhaj, Mahfud Ziyad, “Identification of flow regimes and transition points in a bubble column through analysis of differential pressure signal – Influence of the coalescence behaviour of the liquid phase.”, Chemical engineering and processing, volume 45, issue 3, pp. 214-223, 2006.
30. Yu Zheng, Xiaotao Wan, Zhen Qian, Fei Wei, Yong Jin, “Numerical simulation of the gas-particle turbulent flow in riser reactor based on $\kappa$-$\varepsilon$-$\kappa_p$-$\varepsilon_p$-

θ two fluid model.", Chemical engineering science, volume 56, pp. 6813-6822, 2001.

31. R. Pohorecki, W. Moniuk, P. Bielski, P. Sobieszuk, G. Dąbrowiecki, "Bubble diameter correlation via numerical experiment." Chemical engineering journal, volume 113, pp. 35-39, 2005.
32. Moshe Favelukis, Cam Hung Ly, "Unsteady mass transfer around spheroidal drops in potential flow.", chemical engineering science, volume 60, pp. 7011-7021, 2005.
33. GAO Xiqum, MA Youguang, ZHU Chunying, and YU Guocong, "Towards the mechanism of mass transfer of a single bubble.", Chinese journal of Chemical Engineering, volume 14, pp. 158-163, 2006.
34. Pyung Seob Song, Chan Gi Lee, Suk Hwan Kang, Sung Mo Son, Yong Kang, Sang Done Kim, "Drop properties and pressure fluctuations in liquid-liquid-solid fluidized-bed reactors.", Chemical engineering and processing, volume 44, pp. 1296-1305, 2005.
35. Züber N., Findlay J. A., "Average volumetric concentration in two-phase flow systems." Journal of heat transfer, volume 87, pp. 453-468, 1965.
36. Matsui G., "Identification of flow regimes in vertical gas-liquid two-phase flow using differential pressure fluctuations.", International journal of multiphase flow, volume 10, pp. 711-720, 1984.
37. Glasqow L. A., Erickson L. E., Lee C. H., & Patel S. A., "Wall pressure fluctuations and bubble size distributions at several positions in an airlift fermentor.", Chemical engineering communications, volume 29, pp. 311-336, 1984.
38. Drahos J. & Cermak J., "Diagnostics of gas-liquid flow patterns in chemical engineering systems." Chemical engineering and processing, volume 26, pp. 4069-4075, 1992.
39. Drahos J., Zadradnik J., Puncochar M., Fialova M., & Bradka F. "Effect of operating conditions of the characteristics of pressure fluctuations in a bubble column.", Chemical engineering and processing, volume 29, pp. 107-115, 1991.
40. Drahos J., Bradka F., & Puncochar M., "Fractal behaviour of pressure fluctuations in a bubble column." Chemical engineering science, volume 47, pp. 4069-4075, 1992.

41. Vial C., Camarasa E., Poncin S., Wild G., Midoux N., & Bouillard J., "Study of hydrodynamic behaviour in bubble columns and external loop airlift reactors through analysis of pressure fluctuations.", Chemical engineering science, volume 55, pp. 2957-2973, 2000.

42. Jonhsson F., Zijerveld R. C., Schouten J. C., van den Bleek C. M., and Leckner B., "Characterization of fluidization regimes by time-series analysis of pressure fluctuations.", International journal of multiphase flow, volume 26, pp. 663-715, 2000.

43. Letzel H. M., Schouten J. C., Krisma R., van den Bleek C. M., "Characterisation of regimes and regime transitions in bubble columns by chaos analysis of pressure signals.", Chemical engineering science, volume 52, pp. 4447-4459, 1997.

44. Latifi M. A., Rode S., Midoux N, Storck A., "The use of microelectrodes for the determination of flow regimes in a trickle-bed reactor.", Chemical engineering Science, volume 47, pp. 1955-1961, 1992.

45. Brians L. A., Briens C. L., Margaritis A., Hay J., "Minimum liquid fluidization velocity in gas-liquid-solid fluidized beds.", American Institute of chemical engineers journal, volume 43, pp. 1180-1189, 1997b.

46. Maucci E., Briens C. L., Martinuzzi R. J., Wild G., "Detection and characterization of piston flow regime in three-phase fluidized beds.", Powder technology, volume 103, pp. 243-259, 1999.

47. Latifi M. A., Naderifar A., Midoux N., Le Méhauté A., "Fractal behaviour of local liquid-solid mass transfer fluctuations at the wall of a trickle-bed reactor.", Chemical engineering science, volume 49, pp. 3823-3829, 1994b.

48. Luewisuthichat W., Tsutsumi A., Yoshida K., "Deterministic chaos analysis of particle dynamics in three-phase systems.", Journal of chemical engineering of japan, volume 29, pp. 675-682, 1996.

49. Lin T. –J., Juang R., -C., Chen Y. –C., Chen C. –C., "Predictions of flow transitions in a bubble column by chaotic time series analysis of pressure fluctuation signals.", Chemical engineering science, volume 56, pp. 1057-1065, 2001.

50. Bakshi B. R., Zhong H., Jiang P., Fan L-S., "Analysis of flow in gas-liquid bubble columns using multi-resolution methods.", Transactions of the

institution of chemical engineers, A: Chemical engineering research and design, volume 73, pp. 608-614, 1995.

51. Daly J. G., Patel S. A., Bukur D. B., "Measurement of gas holdups and Sauter mean bubble diameters in bubble column reactors by dynamic gas disengagement method.", Chemical engineering science, volume 47, pp. 3647-3654, 1992.
52. Camarasa E., Vial C., Poncin S., Wild G., Midoux N., Bouillard J., "Influence of coalescence behaviour of the liquid and of gas sparging on hydrodynamics and bubble characteristics in a bubble column.", Chemical engineering and processing, volume 38, pp. 329-344, 1999.
53. Lee D. j., Luo X., Fan L. –S., "Gas disengagement technique in a slurry bubble column operated in the coalesced bubble regime.", Chemical engineering science, volume 54, pp. 2227-2236.
54. Levespiel O., "Chemical reaction engineering." (3rd edition), New York: Wiley.
55. Shah Y. T., Stiegel G. J., Sharma M. M., "Backmixing in gas-liquid reactors.", American Institute of chemical engineers journal, volume 24, pp. 221-259, 1978.
56. Buffham B. A., Mason G., "Hold-up and dispersion: Tracer residence times, moments and inventory measurements.", Chemical engineering science, volume 48, pp. 3879-3887, 1993.
57. Blet V., Berne P., Chaussy C., Perrin S., Schweich D., "Characterization of a packed column using radioactive tracers.", Chemical engineering science, volume 54, pp. 91-101, 1999.
58. Pant H. J., Saroha A. K., Nigam K. D. P., "Measurement of liquid holdup and axial dispersion in trickle bed reactors using radiotracer technique.", Nukleonika, volume 45, pp. 235-241, 2000.
59. Sakai N., Onozaki M., Saegusa H., Ishibashi H., Hayashi T., Kobayashi M., Tachikawa N., Ishikawa I., Morooka S., "Fluid dynamics in coal liquefaction reactors using neutron absorption tracer technique.", American institute of chemical engineers journal, volume 46, pp. 1688-1693, 2000.
60. Larachi F., Laurent A., Wild G., Midoux N., "Some experimental liquid saturation results in fixed-bed reactors operated under elevated pressure in

cocurrent upflow and downflow of the gas and the liquid.", Industrial and engineering chemistry research, volume 30, pp. 2404-2410, 1991.

61. Garcia Ochoa J., Khalfet R., Poncin S., Wild G., "Hydrodynamics and mass transfer in a suspended solid bubble column with polydispersed high density particles.", Chemical engineering science, volume 52, pp. 3827-3834, 1997.
62. Joseph S., Shah Y. T., "Errors caused by tracer solubility in the measurement of gas phase axial dispersion." Canadian journal of chemical engineering, volume 64, pp. 380-386, 1986.
63. Lübbert A., "Characterization of bioreactors.", in H.J. Rehm, G. Reed, A. Pühler, & P. Stadler (Eds.), Biotechnology (2nd edition). Vol4. (pp. 107-148). Weinheim, New York: Verlag Chemie. 1991.
64. Begovich J. M., Watson J. S., "An electroconductivity method for the measurement of axial variation of holdups in three-phase fluidized beds.", American institute of chemical engineers journal, volume 24, pp. 351-354, 1978.
65. Uribe-Sales A., Gomez C. O., Finch J. A., "A conductivity technique for gas and solids holdup determination in three-phase reactors.", Chemical engineering science, volume 49, pp. 1-10, 1994.
66. Shen G., Finch J. A., "Bubble swarm velocity in a column." Chemical engineering science, volume 51, pp. 3665-3674, 1996.
67. Lage P. L. C., Espocito R. O., "Experimental determination of bubble size distributions in bubble columns: Prediction of mean bubble diameter and gas holdup." Powder technology, volume 101, pp. 142-150, 1999.
68. Bendjaballah N., Dhaouadi H., Poncin S., Midoux N., Hornut J. M., Wild G., "Hydrodynamics and flow regimes in external loop airlift reactors.", Chemical engineering science, volume 54, pp. 5211-5221, 1999.
69. Lin T. –J., Tsuchiya K., Fan L. –S., "Bubble flow characteristics in bubble columns at elevated pressure and temperature.", American institute of chemical engineers journal, volume 44, pp. 545-560, 1998.
70. Peterson, D. A., Tankin, R. S., & Bankoff, S. G. "Holographic measurements of bubble size and velocity in three-phase systems". In J.M. Delhaye & G. Cognet (Eds.), Measuring techniques in gas–liquid two-phase flows pp. 1–21(1984).

71. Heindel T. J., “Gas flow regime changes in a bubble column filled with a fibre suspension.”, Canadian journal of chemical engineering, volume 78, pp. 1017-1022, 2000.

72. Jamet, F. and G. Thomer, “Flash Radiography”, Elsevier Publishing Company, Inc., New York (1976).

73. Heindel, T.J. and J.L. Monefeldt, “Flash X-ray Radiography for Visualizing Gas Flows in Opaque Liquid/Fibre Suspensions,” in “6th International Symposium on Gas-Liquid Two-Phase Flows”, Vancouver, BC, June 22-26, 1997, ASME Press, New York (1997), Paper FEDSM97- 352

74. Heindel, T.J. and J.L. Monefeldt. “Observations of the Bubble Dynamics in a Pulp Suspension Using Flash X-ray Radiography.” TAPPI J. 81, No. 11, 149-158 (1998).

75. Heindel, T.J., “Bubble Size Measurements in a Fibre Suspension”, J. Pulp Pap. Sci. 25, No. 3,104-l 10 (1999).

76. Heindel, T.J. and A.E. Gamer, “The Effect of Fibre Consistency on Bubble Size”, Nord. Pulp Pap. Res. J. 14, No. 2, 171-178 (1999).

77. Hewitt, G.F., “Measurement of Two Phase Flow Parameters”, Academic Press, New York (1978).

78. Lindsay, J.D., S.M. Ghiaasiaan and SI. Abdel-Khalik. “Macroscopic Flow Structure in a Bubbling Paper Pulp-Water Slurry.” Ind. Eng. Chem. Res. 34, 3342-3354 (1995).

79. Kumar, S.B., D. Moslemian and M.P. Dudukovic, “Gas-Holdup Measurements in BubbleColumns Using Computed Tomography”, AIChE J. 43, No. 6, 1414-1425 (1997).

80. Hewitt, G.F. and D.N. Roberts, “Studies of Two-Phase Flow Patterns by Simultaneous X-ray and Flash Photography”, United Kingdom Atomic Energy Authority (UKAEA), Harwell, Berkshire (1969), Report Number: AERE-M2159.

81. Bennett, A.W., G.F. Hewitt, H.A. Kearsey, R.K.F. Keeys and P.M.C. Lacey, “Flow Visualization Studies of Boiling at High Pressure”, Proc. Inst. Mech. Eng., Part 3C 180, l-11 (1965).

82. Sato, Y. and Hishida, K., 1996. “Transport process of turbulence energy in particle-laden turbulent flow”. Int. J. Heat Fluid Flow 17, pp. 202–210.

83. Murai Y., Song X. Q., Tagari T., Ishikawa M., Yamamoto F., Ohta J., “Inverse energy cascade structure of turbulence in bubbly flow. PIV measurement and results.”, Japanese society of mechanical engineers international journal series B, Fluids and thermal engineering, volume 43, pp. 188-196, 2000.
84. A. Fujiwara, D. Minato, K. Hisida “Effect of bubble diameter on modification of turbulence in an upward pipe flow”, Int. J. Heat Fluid Flow 25 (2004) 481–488
85. Delnoij E., Kuipers J. A. M., van Swaaij W. P. M., Westerweel J., “Measurement of gas-liquid two-phase flow in bubble columns using ensemble correlation PIV.”, Chemical engineering science, volume 55, pp. 3385-3395, 2000.
86. Gladden L F 1994 “Nuclear magnetic resonance in chemical engineering: principles and applications” Chem. Eng. Sci. 49 3339–408
87. L. Gladden and P. Alexander “application of nuclear magnetic resonance imaging in process engineering” MST 7 1996 423-425
88. Sharma S., Mantle M. D., Gladden L. F., Winterbottom J. M., “Determination of bed voidage using water substitution and 3D magnetic resonance imaging, bed density and pressure drop in packed-bed reactors.”, Chemical engineering science, volume 56, pp. 587-593, 2001
89. Chaouki J., Larachi F., Dudukovic M. P., “Noninvasive tomographic and velocimetric monitoring of multiphase flows.”, Industrial and engineering chemistry research, volume 36, pp. 4476-4503, 1997.
90. G. Brenn, V. kolobaric and F. Durst “shape oscillation and path transition of bubbles rising in a model bubble column”, Chem. Eng. Sci 61 (2006) 3795-3805.
91. R.F. Mudde, J.S. Groen and H.E.A. Van den Akker, “Liquid velocity field in a bubble column: LDA experiments”, Chem. Eng. Sci. 52 (1997), pp. 4217–4229
92. R.F. Müdde, J.S. Groen and H.E.A. van den Akker , “Application of LDA to bubbly flows”. Nuclear Engineering and Design 184 (1998), pp. 329–338
93. C. Vial, R. Lainé, S. Poncin, N. Midoux and G. Wild , “Influence of gas distribution and regime transition on liquid velocity and turbulence in a 3-D bubble column”. Chemical Engineering Science 56 (2001), pp. 1085–1093.
94. Reiss L. P., Hanratty T. J., “An experimental study of the unsteady nature of the viscous sublayer.”, A.I.Ch.E. journal, volume 9, pp. 154-160, 1963.

95. M. Souhar, “Experimental study of wall turbulence in bubble flow”. International Journal of Heat Mass Transfer 30 (1987), pp. 1813–1823

96. F. Magaud, M. Souhar, G. Wild and N. Boisson , “Experimental study of bubble columns hydrodynamics”. Chemical Engineering Science 56 (2001), pp. 4597–4607.

97. Rode S., Midoux N., Latifi M. A., Storck A., “Hydrodynamics and liquid-solid mass transfer mechanisms in packed beds operating in cocurrent gas-liquid down flow: An experimental study using electrochemical shear stress sensors.” Chemical engineering science, volume 49, pp. 1383-1401, 1994.

98. Chen J., Kemoun A., Al-Dahhan M. H., Dudukovic M. P., Lee D. J., Fan L. – S., “Comparative hydrodynamics study in bubble columns using computer-automated radioactive particle tracking (CARPT)/computed tomography (CT) and particle image velocimetry (PIV).”, Chemical engineering science, volume 54, pp. 2199-2207, 1999.

99. Chaouki J., Larachi F., Dudukovic M. P., “Noninvasive tomographic and velocimetric monitoring of multiphase flows.”, Industrial and engineering chemistry research, volume 36, pp. 4476-4503, 1997

100. L.A. Shepp and B.F. Logan , “The Fourier reconstruction of a head section”. IEEE Transcations on Nuclear Science NS-21 (1974), pp. 21–43

101. Kak A. C., Slaney M., “Computerized tomographic imaging.” New York: IEEE press, 1987.

102. Kumar S. B., Moslemian D., Dudukovic M. P., “A gamma ray tomographic scanner for imaging voidage distribution in two-phase flow systems.”, Flow measurement instrumentation, volume 6, pp. 61-73, 1995.

103. Froystein T., “Flow imaging by gamma-ray Tomography: Data processing and reconstruction techniques.” Frontiers in industrial process tomography II, Delft, pp. 8-12, 1997.

104. M. Warsito, N. Ohkawa, S. Kawata and S. Uchida , “Cross-sectional distributions of gas and solid holdups in slurry bubble column investigated by ultrasonic computed tomography”. Chemical Engineering Science 54 21 (1999), pp. 4711–4728

105. Schmitz D., Mewes D. “Tomographic imaging of transient multiphase flow in bubble columns.” Chemical engineering journal, volume 77, pp. 99-104, 2000.

106. N. Reinecke, G. Petritsch, D. Schmitz and D. Mewes, “Tomographic measurement techniques—Visualisation of multiphase flow”. Chemical Engineering Technology 21 (1998), pp. 7–18

107. Wang M., “Inverse solutions for electrical impendance tomography based on conjugate gradients methods.”, Measurement science technology, volume 13, pp. 101-117, 2001

108. Mann R., Dickin F. J., Wang M., Dyakowski T., Williams R. A., Edwards R. B., Forrest A. E., Holden P. J., “Application of electrical resistance tomography to interrogate mixing processes at plant scale.”, Chemical engineering science, volume 52, pp. 2087-2097, 1997.

109. Prasse H. –M., Böttger A., Zschau J., “A new electrode-mesh tomography for gas-liquid flows.”, Flow measurement and instrumentation, volume 9, pp. 111-119, 1998.

110. Fraser D., Wang M., “Electrical resistance tomography for process applications.” Measurement science technology, volume 7, pp. 247-260, 1996.

111. Utiger M., Stüber F., Duquenne A. M., Delmas H., Guy C., “Local measurements for the study of external loop airlift hydrodynamics.”, Canadian journal of chemical engineering, colume 77, pp. 375-382, 1999.

112. Young M. A., Carbonell R. G., Ollis D. F., “Airlift bioreactors: Analysis of local two-phase hydrodynamics.” American institute of chemical engineers journal, volume 37, pp. 403-428, 1991.

113. Hosgett S., Ishii M., “Local two-phase flow measurement using sensor techniques.”, Nuclear engineering and design, volume 175, pp. 15-24, 1997.

114. Menzel T., In Der Weide T., Staudacher O., Wein O., Onken U., “Reynolds shear stress for modelling of bubble column reactors.”, Industrial and engineering chemical research, volume 29, pp. 988-994, 1990.

115. Roig V., Larrieu N., Suzanne C., “Turbulent length scales in bubbly mixing layer.”, International symposium on two-phase flow modelling and experimentation, Rome, 1995.

116. H. Toral, “A study of the hot-wire anemometer for measuring void fraction in two-phase flow”. Journal of Physics E: Science and Instruments 14 (1981), pp. 822–827

117. Bruuns H. H., “Hot wire anemometry. Principles and signal analysis.”, New York: Oxford University Press Inc., 1995.

118. Lance M., Bataille J., “Turbulence in the liquid phase of a bubbly air-water flow.”, Advances in two-phase flow and heat transfer, volume 1, pp. 403-427, NATO Specialist Meeting, Nato Advances Science Institute Series, West Germany, 1983

119. Burrn H H “Hot-film anemometry in liquid flows” Measurement Science Technology 7(1996) 1301-1312.

120. Rensen J, Luther S, Vries J and Lohse D, “Hot film anemometry in bubbly flow I: bubble-probe interaction.” International journal of multiphase flow 31 (2005) 285-301

121. Murakawa H, Kikura H, Aritomi M. “Application of ultrasonic Doppler method for bubbly flow measurement using two ultrasonic frequencies.” Experimental Thermal and Fluid Science, 29 (2005) Pp. 843-850.

122. H. Murakawa, H. Kikura and M. Aritomi, “Measurement of liquid turbulent structure in bubbly flow at low void fraction using ultrasonic Doppler method”, J. Nucl. Sci. Technol. 49 (2003), pp. 644–654.

123. Bröring F. J., Fischer J., Korte T., Sollinger S., Lübbert A., “Flow structure of the dispersed gasphase in real multiphase chemical reactors investigated by a new ultrasound-Doppler technique.”, Canadian journal of chemical engineering, volume 69, pp. 1247-1256, 1991.

124. Bouillard J., Alban B., Jacques P., Xuereb C., “Liquid flow velocity measurements in stirred tanks by ultra-sound Doppler velocimetry.”, Chemical engineering Science, volume 56, pp. 747-754, 2001

125. Stravs A. A., von Stockar U., “Measurement of interfacial areas in gas-liquid dispersions by ultrasonic pulse transmission.”, Chemical engineering science, volume 40, pp. 1169-1175, 1985.

126. Stravs A. A., Wahl J., von Stokar U., Reilly P. J., “Development of ultrasonic pulse reflection method for measuring relative size distributions of air bubbles inaqueous solutions.”, Chemical engineering science, volume 42, pp. 1677-1987, 1987

127. T. Wang, J. Wang, F. Ren and Y. Jin, “Application of Doppler ultrasound velocimetry in multiphase flow”, Chem Eng J 92 (2003), pp. 111–122.

128. F. A. Hamad, F. Imberton and H.H Bruun. “An optical probe for measurement in liquid-liquid two-phase flow.” Measurement science and technology. Vol 8 pp. 1122-1132. 1997.

129. F. A. Hamad, F. Imberton and H.H Bruun. “A dual optical probe for volume fraction, drop velocity and drop size measurement in liquid-liquid two-phase flow.” Measurement science and technology. Vol 11 pp. 1307-1318. 2000

130. S.Guet, S. Luthe, G. Ooms. “Bubble shape and orientation determination with four-point optical probe.” Experimental thermal and Fluid Science. Vol. 29 pp. 803-812. 2005.

131. J. Enrique.Julia “On the accuracy of the void fraction measurements using optical probes in bubbly flows.” Review of scientific instruments 2005

132. A. Cartellier, E. Barrau “monofiber optical probe for gas detection and gas velocity measurements: optimised sensing tips.” International journal of multiphase flow 24 (1998) pp. 1295-1315.

133. A. Cartellier, E. Barrau “Measurent of the gas phase characteristics using new monofiber optical probes and real-time signal processing.” Nuclear Engineering and Design 184 (1998) pp. 393-408.

134. E. Barrau, N. Riviere, Ch. Poupot, A. Cartellier “Single and Double optical probes in air-water two-phase flows: real time signal processing and sensor performance.” International journal of multiphase flow 1999 pp. 229-256.

135. S. Hogsett and M. Ishii , Local two-phase flow measurements using sensor techniques. Nuclear Engineering and Design 175 (1997), pp. 15–24

136. Burgess J. M., Caldebank P. H., “The measurement of bubble parameters in two-phase dispersions-I: The development of an improved probe technique.”, Chemical engineering science, volume 30, pp. 743-750, 1975.

137. Jürgen Steinmann, Rainer Buchholz, “Application of an electrical conductivity microprobe for the characterization of bubble behaviour in gas-liquid bubble flow.” Verlag Chemie GmbH, d-6940 Weinheim, pp. 102-107, 1984.

138. Saito Y., Mishima K., Tobita Y., Suzuki T., Matsubayashi M., “Measurements of liquid-metal two-phase flow by using neutron radiography and electrical conductivity probe.” Experimental thermal and fluid science, 2004.

139. Ishii M., Kim S., “Micro four-sensor probe measurement of interfacial area transport for bubbly flow in round pipes.”, Nuclear engineering and design, volume 205, pp. 123-131, 2001.

140. Kim S., Fu X. Y., Wang X., Ishii M., “Development of the miniaturised four-sensor conductivity probe and the signal processing scheme.”, International journal of heat and mass transfer, volume 43, pp. 4101-4118, 2000.

141. J.M. Delhaye, “Two phase pipe flow”. Int. Chem. Eng. 23 3 (1983), pp. 395–410.

142. Serizawa, I. Kataoka and I. Michiyoshi, “Turbulence structure of air–water bubbly flow”. 1. Measuring techniques. Int. J. Multiphase Flow 2 (1975), pp. 221–223.

143. J.H. Hills, “Radial non-uniformity of velocity and voidage in a bubble column”. Trans. Inst. Chem. Engrs 52 (1974), p. 1.

144. L.G. Neal and S.G. Bankoff, “A high resolution resistivity probe for determination of local void properties in gas–liquid flow”. AIChE J. 9 4 (1963), pp. 490–494.

145. Kocamustafaogullari and Z. Wang, “An experimental study on local interfacial parameters in a horizontal bubbly two-phase flow”. Int. J. Multiphase Flow 17 5 (1991), pp. 553–572.

146. Wu Q., Welter K., McCreary D., Reyes J. N., “Theoretical studies on the design criteria of double-sensor probe for the measurement of bubble velocity.”, J. Flow Meas. Instrum., volume 12 (issue 1), pp. 43-51, 2001

147. Q. wu, and M. Ishii, “Sensitivity study on double-sensor conductivity probe for the measurement of interfacial area concentration in bubbly flow” int. journal of multiphase flow. 25(1999) pp. 155-173

148. Hosgett S., Ishii M., “Local two-phase flow measurement using sensor techniques.”, Nuclear engineering and design, volume 175, pp. 15-24, 1997

149. Kataoka, I., Ishii, M., Serizawa, A., “Sensitivity analysis of bubble size and probe geometry on the measurements of interfacial area concentration in gas-liquid two-phase flow”. J. Nucl. Eng. & Design 146, pp. 53-70. 1994

150. K. Sanaullah, S. H. Zaidi and J. H. Hills. “A study of bubbly flow using resistivity probes in a novel configuration” J. Chem. Eng 83(2001) pp. 45-53

151. Kim S., Fu X. Y., Wang X., Ishii M., “Development of the miniaturised four-sensor conductivity probe and the signal processing scheme.”, International journal of heat and mass transfer, volume 43, pp. 4101-4118, 2000.

152. R.A. Herringe and M.R. Davis, “Structural development of gas–liquid mixture flows.” J. Fluid Mech. 73 (1976), pp. 97–123

153. W.H. Park, K.W. Kang, C.E. Capes and G.L. Osberg, “The properties of bubbles in fluidised beds of conducting particles as measured by an electro-resistivity probe.” Chem. Eng. Sci. 24 (1969), pp. 851–856

154. G.R. Rigby, G.P.V. Blockland, W.H. Park and C.E. Capes, "Properties of bubbles in three phase fluidised beds as measured by an electro-resistivity probe."Chem. Eng. Sci. 25 (1970), pp. 1729–1741.

155. D. A. Lewis, J. F. Davidson "Bubble sizes produced by shear and turbulence in a bubble column" Chemical Engineering Science, Volume 38, Issue 1, 1983, Pp. 161-167

156. A. Yasunishi, M. Fukuma and K. Muroyama, "Measurement of behaviour of gas bubbles and gas hold-up in a slurry bubble column by a dual electroresistivity probe method." J. Chem. Eng. 19 4 (1986), pp. 444–449

157. G. P. Lucas and N. D. Jin, "Investigation of a drift velocity model for predicting superficial velocities of oil and water in inclined oil-water pipe flows with a centre body", Meas. Sci. Technol., Volume 12, pp. 1546-1554, 2001.

158. S. Pradhan, G.P. Lucas, X. Zhao "Measurement of reference velocity vector for four-sensor conductance probes using orthogonal, high speed cameras" international conference of Multiphase Technology, Banff, Canada 4-6 June 2008.

159. A. Sam, C.O. Gomez, J.A. Finch "Axial velocity profiles of single bubbles in water/frother solutions." Journal of mineral processing 1996 pp. 177-196

160. G. P. Celata, M. Cumo, F. D'Annibale, A. Tomiyama "The wake effect on bubble rising velocity in one-component systems." International Journal of Multiphase Flow, Volume 30, Issues 7-8, July-August 2004, Pp. 939-961.

161. H.Tsuge and S.I.Hibino, 1972. "The motion of gas bubbles generating from a single orifice submerged in a liquid". Keio Engng. Rep. 25

162. M. L. Mathur, "A new design of vanes for swirl generation.", IE(I) Journal ME, volume 55, pp. 93-96, 1974.

163. G. Brenn, V.kolobaric, F.Drust. "Shape oscillation and path transistion of bubble rising in a model bubble coulmn" Chemical Engineering Science 61 (2006) pp. 3795-3805.

# Appendices

# Appendix A

# Non-intrusive Methods

The detailed information on global measuring techniques can be found in the references [1-66].

## 1. Local techniques

### 1.1. Visualisation techniques

Visualisation techniques yield the bubble shape and size and velocity vector. These can be further divided into photographic techniques and radiographic techniques; Particle Image Velocimetry and Nuclear Magnetic Resonance (NMR).

#### *1.1.1 Photographic techniques*

This method involves taking pictures of the flow in order to quantify several properties of the multiphase flow, as shown by Camarasa et al. [52], Lage et al. [67], Bendjaballah et al. [68], Lin et al. [69] and Peterson et al. [70].

Even though bubbles are not necessarily spherical and their shapes can vary widely, Bendjaballah et al. [68] and Camarasa et al. [52] show that quantitative image processing allows determination of the size, shape and velocity vector of the bubble.

Peterson et al. [70] used photographic techniques to determine the shape and size of the bubbles in a three-phase fluidised bed by using refractive index matching of the solid and the liquid phase.

The main drawback or limitation of this technique is that it can only capture regions in close proximity to the wall; furthermore, a transparent pipe wall, as well as a transparent continuous phase, is required. In the case of high pressure columns, a special window such the quartz windows used by Lin et al. [69] that can withstand pressures up to 20MPa is required.

*1.1.2 Radiographic techniques*

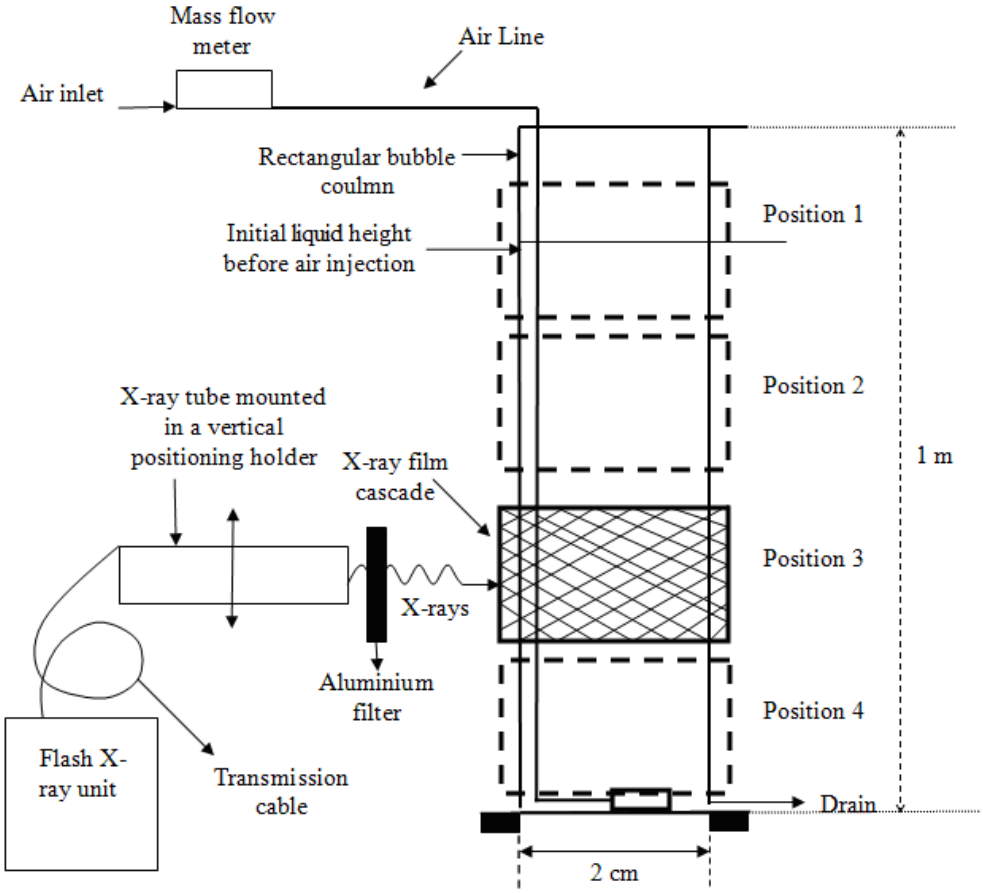


**Figure A.1 Experimental set up for a radiographic technique used by Heindel et al. [71].**

Radiation techniques such as flash x-ray radiography (FXR) can be used to visualise flow structures in opaque multiphase systems using stop-motion x-rays [74, 80, 81]. Here, an intense burst of x-ray radiation is produced for a fraction of a second to

record dynamic events on film that cannot be captured by conventional photography [72]. Figure A.1 shows a schematic diagram of the equipment used by Heindel et al. [71, 73, 74] to observe gas flow patterns and determine the evolution of bubble shape, size and position. Heindel et al. [76] also used this method to investigate cellulose fibre suspensions with fibre concentrations of up to 1.5% by mass.

Radiation techniques can also be used to measure average gas volume fraction, as shown by Hewitt [77], Lindsay et al. [78] and Kumar et al. [79] and to visualise gas flows in multiphase systems, as illustrated by Bennett et al. [80], Hewitt and Roberts [81] and Heindel et al. [74].

*1.1.3 Particle image velocimetry*

Previously the Particle Image Velocimetry (PIV) technique was only used in single phase flow in order to determine its velocity field. In this technology, a laser sheet is used in order to illuminate a well defined slice of the liquid containing seeding particles and two or more images are captured in a very short interval of time. Thus, the distance between the positions of the seeding particles yields the instantaneous velocity field of the liquid [15].

In recent years, this PIV technique has also been applied to dispersed multiphase flows. The major advantage of this technique is that it doesn't make contact with the flow; hence, it doesn't disturb the structure of the flow. The spatial interaction between the dispersed phase and the continuous phase is obtained in a short time interval. In 1996, Sato et al. [82] adopted this technique for studying dispersed solid liquid flow and in 2000 Murai et al. [83] introduced this technique for studying gas-

liquid multiphase flow in order to verify the inverse turbulence energy cascade. Figure A.2 shows the general schematic for the PIV technique [84].

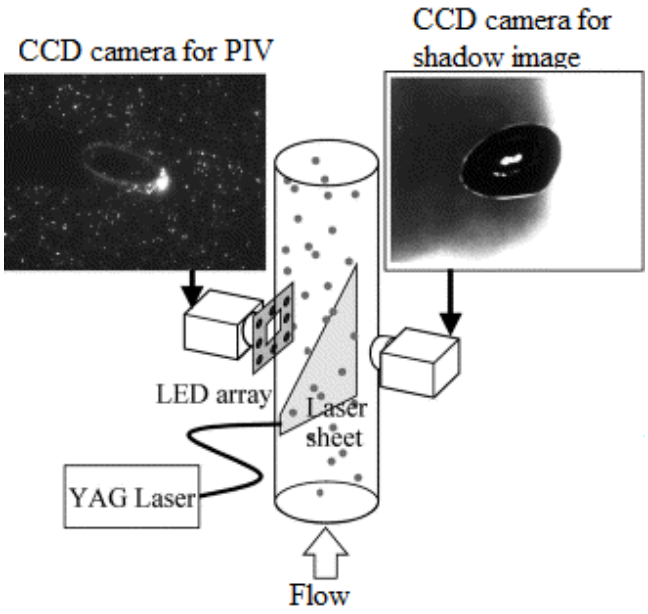


**Figure A.2 Schematic for PIV technique. Fujiwara et al. [84]**

Delonij et al. [85] also used PIV in order to measure the velocity of both the dispersed phase and the continuous phase in bubbly gas–liquid multiphase flow. In order to implement this process, Delonij et al. [85] used a single camera PIV technique in gas-water multiphase flow. The liquid was seeded with small tracer particles and a laser was used to illuminate the cross section of the flow. With the ability to distinguish between the tracer particles and the bubbles, it was possible to calculate the local velocity of both the gas and the liquid phases from the displacement of the bubbles and the tracer particles between the successive exposures.

There are certain limitations when using the PIV technique in gas-liquid multiphase flow such as: (i) it can be difficult to differentiate between the bubbles and tracer particles, (ii) problems can be caused by the scattering of light from the bubbles, (iii)

difficulties in measuring the local liquid velocity in the vicinity of the bubbles due to the presence of strong shear flow.

*1.1.4. Nuclear Magnetic Resonance (NMR)*

Nuclear Magnetic Resonance (NMR) is a spectroscopic technique based on a resonance phenomenon. The application of a large static magnetic field $B_0$ to the sample of interest removes the degeneracy of the nuclear spin states of any nucleus of non-zero nuclear spin. To induce transitions between the non-degenerate spin states, a sinusoidal radio frequency (r.f) current is applied which is of appropriate frequency to enable transitions between the spin states of the particular nucleus to be studied (Gladden [86]). The frequency of the radiation $\omega_0$ which must be applied to satisfy this resonance condition is related to the static magnetic field and the so-called gyro-magnetic ratio $\gamma$ of the nucleus of interest by the expression:

$$\omega_0 = \gamma B_0 \qquad \textbf{Equation A.1}$$

Gladden et al. [86, 87] also stated that, in order to observe the magnetic resonance phenomena of nuclei as a function of their position in real space (i.e. to perform an imaging experiment), a small magnetic field gradient is applied in addition to the uniform polarizing field $B_0$ such that the resultant field B varies according to:

$$\frac{\partial B}{\partial z} = G_z = \text{constant} \qquad \textbf{Equation A.2}$$

For the case when the field gradient is applied along the z-direction. Under such conditions, the angular frequency of spins as a function of position in the z-direction is given by:

$$\omega_z = \gamma(B_0 + G_z z) \qquad \textbf{Equation A.3}$$

From which it is clear that the resonance frequency (often called the Larmor frequency) now varies linearly with position. If the magnetic field is homogeneous, the NMR spectrum consists of one resonance line. If a magnetic field gradient is applied along the direction of the magnetic field, the NMR spectrum will consist of two lines, the separation of which is dependent on the magnitude of the gradient (Gladden et al. [87, 88]). In general, the spatial distribution of the Larmor frequency is given as:

$$\omega(r) = \gamma B_0 + \gamma G r \qquad \textbf{Equation A.4}$$

where $r$ is the position vector of the spin if the influence of relaxation is neglected, the signal $dS$ acquired from an element of volume $dV$ at position $r$ with spin density $\rho(r)$ is given by Gladden et al. [87]:

$$dS(G,t) = \rho(r) dV \exp[i(\gamma B_0 + \gamma G r)t] \qquad \textbf{Equation A.5}$$

The application of linear field gradients forms the foundation of all NMR diffusion and imaging experiments. In order to recover the spin density function, $\rho(r)$ from an imaging experiment, a data set must be acquired for a range of values of the field gradient G. Once such a dataset has been obtained, $\rho(r)$ is recovered using Equation A.5.

In order to image a 3D volume, linear gradients are applied and varied in each of the x, y and z directions. NMR is also a particularly useful tool for measuring flow phenomena; the easiest method used for flow visualisation also follows directly from

Equation A.5. The nuclei within a specific image slice are selectively excited and magnetically 'tagged' using an RF pulse sequence. At a time *t* later, the 3D distribution of these 'tagged' spins is recorded, from which the velocity distribution of those spins is obtained. Thus, 3D images of both velocity profiles and concentration distributions can be acquired and it is possible to probe flow velocities in the range $10^{-2}$ $cms^{-1}$ to $10^{2}$ $cms^{-1}$ using NMR techniques.

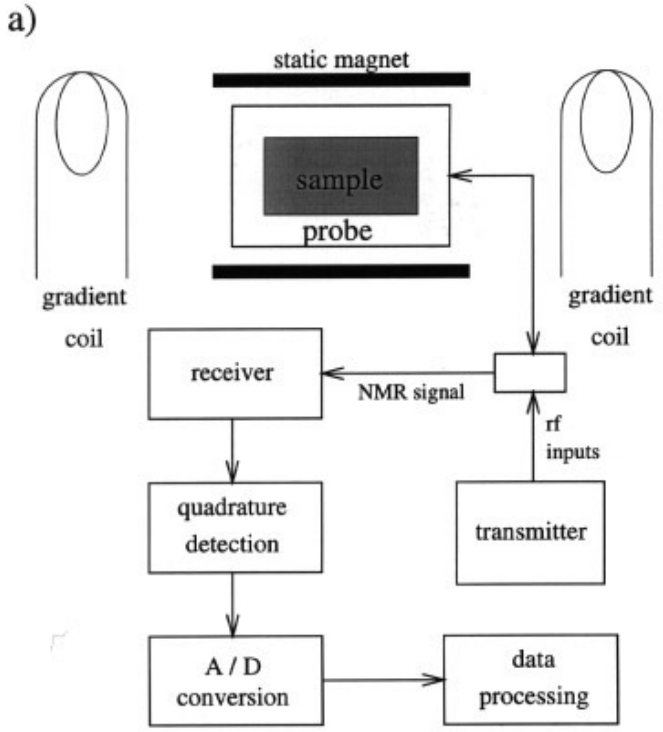


**Figure A.3 (a) A block diagram of a typical pulsed NMR experiment; the gradient coils are used for diffusion, flow and imaging experiments. Gladden et al. [87].**

A recent development in flow imaging is the dynamic NMR microscopy technique which is able to achieve a velocity resolution of a few tens of microns per second and a spatial resolution of a few tens of microns (Gladden et al. [86 – 88]).

According to Gladden et al. [88] and Chaouki et al. [89], the major limitation of NMR techniques is their inability to study ferromagnetic materials and samples containing significant amounts of paramagnetic species, making this equipment very expensive.

### 1.2 The laser Doppler anemometry technique

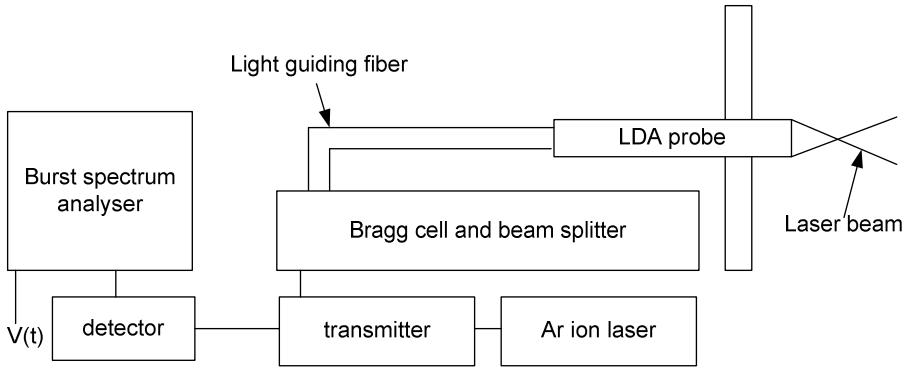


**Figure A.4 Schematic diagram of LDA technique**

In multiphase flow, the laser Doppler anemometer (LDA) is widely used to measure the velocity of the dispersed phase, as well as the continuous phase with added seeding particles. Figure A.4 shows a schematic of the LDA technique where the laser is the wave source and the seeding particles or the bubbles are the wave receivers; if there is a relative motion between the wave source and the seeding particles or the bubbles, there will be a shift in the wave frequency, caused by the Doppler effect. Hence, by measuring this shift in the frequency, it is possible to measure the velocity of the dispersed phase in a multiphase flow system (Brenn et al. [90]).

Mudde et al. [91] used alumina-coated spherical polyethylene particles of 4μm diameter (density 2.6 x $10^3$ kg/$m^3$) as seeding particles. This resulted in a maximum (average) data rate of some 1000Hz. Mudde et al. [91] also used a 2D LDA system, which makes it possible to measure the axial and azimuthal velocity components simultaneously.

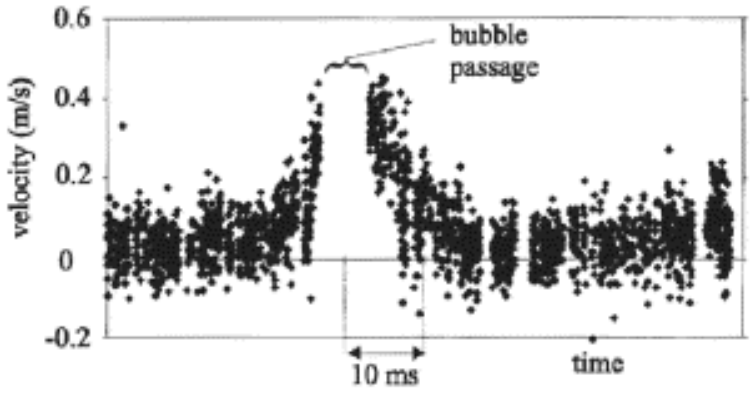


**Figure A.5 LDA velocity signal in a bubbly flow. Mudde et al. [92]**

Figure A.5 shows the velocity signal obtained by Mudde et al. [92] as a function of time in a bubble column. In this figure, one of the problems of the technique becomes apparent: during a period of the measuring time, the laser beams do not reach the place where the liquid velocity is supposed to be measured, because bubbles interrupt the beams' path. In Figure A.6, the RMS of the axial liquid velocity in a bubble column, as measured by Vial et al. [93], is presented. The results correspond to two different gas injectors.

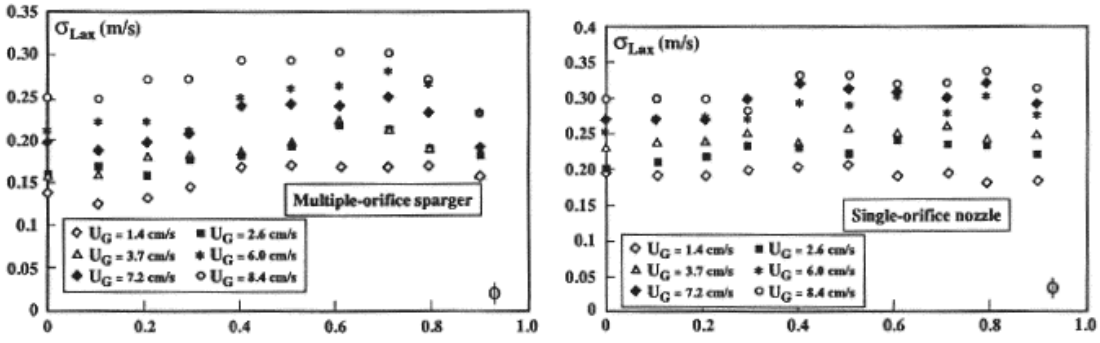


**Figure A.6 RMS of the LDA measured axial velocity in a bubble column. Vial et al. [93]**

Müdde et al [91] state that, with coalescing liquids, it is possible to make reliable measurements of gas volume fractions of up to 10% at a distance of 0.1 m from the wall. At higher gas velocities (25cm/s), it is possible that the smaller bubbles may not be distinguished from the seeding particles.

**1.3 Polarographic technique**

Polarography can be used to measure local wall shear stress. This method is based on the fast electrochemical reduction of reagent dissolved in the moving medium. Electrode potential is adjusted so that the reagent concentration on the electrodes is zero. In these conditions, the mass transfer on each probe depends only on local hydrodynamic parameters. In a simple model, Reiss et al. [94] express local wall shear stress $\tau_w$ versus delivered current $I$ as:

$$\tau_w = CI^3 \qquad \textbf{Equation A.6}$$

In bubbly flows, the polarography technique is still valid. As shown by Souhar et al. [95], a liquid film of 20 μm thickness exists near the wall, which enables mass boundary layer development. It has been used in bubble columns by Magaud et al. [96] and at the wall of trickle beds by a number of authors (Rode et al. [97]).

The advantages of this technique are: it is a non-intrusive technique yielding information on the flow behaviour in the immediate vicinity of the wall; it can be miniaturised (microelectrodes) and also give information on velocity fluctuations near the wall. The disadvantage of this method is that a conducting liquid is required and, with the presence of the support electrolyte, it can change the coalescence behaviour of the liquid (Christophe et al. [15]).

## 1.4 Radioactive tracking of particles

This method uses neutrally buoyant spheres that contain radionucleides that emit γ-rays. A number of detectors around the column receive the transmitted rays; determination of the position of the particles in the flow is then possible. The final result is that trajectories of the particles can be measured. Usually this type of method is used to validate CFD calculations, to determine axial dispersion coefficients of the solids, and to yield global circulation patterns. The only disadvantage of this technique is the long and complicated calibration procedure that is needed [98-99].

## 1.5 Tomographic techniques

### *1.5.1 Tomography by photon attenuation measurement*

This tomography method is based on the attenuation measurement of photon rays such as γ- or X-ray. This attenuation is directly proportional to the material density for a given photon energy. The resulting image gives the density at each pixel and, hence, the phase fraction map. The reconstruction algorithms are based on the inversion of the 2D Fast Fourier Transform, since all the measured attenuations are linear functions of density. The main algorithm is a filtered back-projection algorithm (Shepp et al. [100] and Kak et al. [101]). If $f(x, y)$ is the distribution function of a phase fraction inside the column, the measured attenuation corresponding to a projection of attenuation is expressed for a given angular position θ and a given distance $s$ from column axis (Figure A.7), by the following relationship:

$$p(s,\theta) = K \ln\left(\frac{I}{I_0}\right) = \int_{Ls,\theta} f(x,y)\, dl \qquad \textbf{Equation A.7}$$

where $I_0$ and $I$ are the photon fluxes, measured at cylindrical coordinates $s$ and θ, when the column is respectively filled with one phase (liquid or gas) and when it is filled with a two-phase flow. $K$ is a constant, taking into account the relationship between phase fraction and physical attenuation.

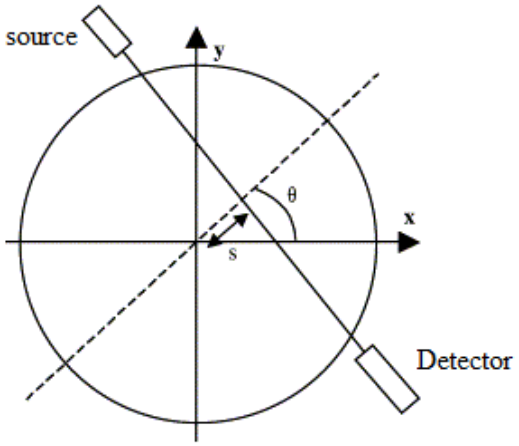


**Figure A.7 Co-ordinates describing a measured projection. Christopher et al. [15]**

X-ray tomographic systems have been applied to differently packed beds (Christophe et al. [15]). As the photon fluxes are very high with X-ray tubes, the detector sensing area is reduced and the spatial resolution can be as small as 1×1 $mm^2$. However, such photon rays generally have a rather low energy level (less than 100 keV) and their use is limited to low attenuating material or to a small column diameter. With γ-rays, the photons are more penetrating since their energy can be as high as 1 MeV. Several γ-ray tomographic systems have been devoted to the investigation of packed beds or bubble columns by Kumar et al. [102] and Froystein [103]. In these types of tomographic systems, the spatial resolution is around 1×1 $cm^2$.

*1.5.2 Ultrasonic tomography*

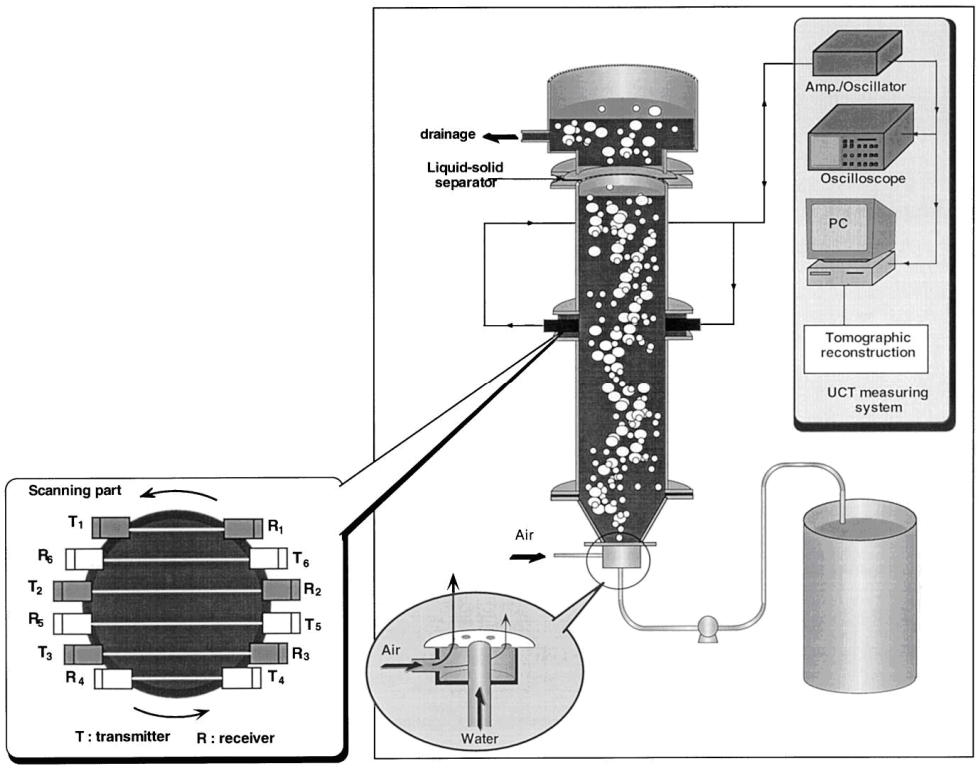


**Figure A.8 Schematic diagrams for ultrasonic tomography technology. Warsito et al. [104]**

Ultrasonic transducers can be used to obtain tomographic images through a cross-section of a pipe using ultrasonic waves. The wave propagation depends on both the phase fraction and the phase configuration (flow regime, size of dispersed particles). Research has been previously carried out to combine the measurement of ultrasonic wave attenuation and propagation velocity to detect the solid and gas-phase fractions inside a slurry bubble column (Boyer et al. [34] and Warsito et al. [104]). An array of ultrasonic emitters and receivers deployed in a parallel configuration at the column wall is rotated all around the column, as shown in Figure A.8. As shown by the above authors, at high frequencies the wave propagation velocity does not depend on gas fraction. The solid fraction is therefore determined from the ultrasonic propagation velocity and the gas fraction is obtained by interpreting the measurement of ultrasonic wave attenuation. The above authors obtained cross-sectional images of phase fractions using a reconstruction procedure performed with a filtered back projection algorithm. The results are quite interesting, but it should be noted that this application is limited to volume fractions of dispersed phases (solid and gas) below 20%, since

multiple wave reflections on gas and solid interfaces rapidly generate a strong attenuation.

*1.5.3 Electrical Resistance Tomography (ERT)*

Dual-plane Electrical Resistance Tomography (ERT) systems can be used to measure the local dispersed phase axial velocity and volume fraction distributions in two phase flows in which the continuous phase is electrically conducting and where there is a conductivity contrast between the dispersed and continuous phases (Lucas et al. [7,8 and 3]). ERT can be applied in flows in which distributions are highly non-uniform. A point-by-point correlation technique is used to measure the velocity of the dispersed phase, and is based on the assumption that the flow trajectories are parallel to each other and perpendicular to the sensor plane (Wang et al. [9]).

The dispersed phase volumetric flow rate $Q_d$ can be obtained by integrating the product of the local axial velocity $u_d$ and the local volume fraction $\lambda_l$ in the flow cross section, as shown in Equation A.8, where $A$ represents the cross sectional area of the pipe [8].

$$Q_d = \int_A \lambda_l \, u_d \, dA \qquad \textbf{Equation 2.8}$$

Investigations have been carried out in the laboratory at identical flow conditions using intrusive, miniature dual-sensor conductance probes (Lucas et al. [8 and 3]) to validate the volume fractions and velocity distributions obtained using ERT. As described in [3], Lucas et al. used both a dual-sensor conductance probe and an ERT system in bubbly-air water flow to compare the measured local gas volume fraction and axial gas velocity profiles. The experiments were carried out at various water

superficial velocities $U_{ws}$ within the range of $0.1\text{ms}^{-1}$ to $1.15\text{ms}^{-1}$. The appropriate values of the gas superficial velocity $U_{gs}$ were used in order to ensure that the flow was always in the bubbly regime.

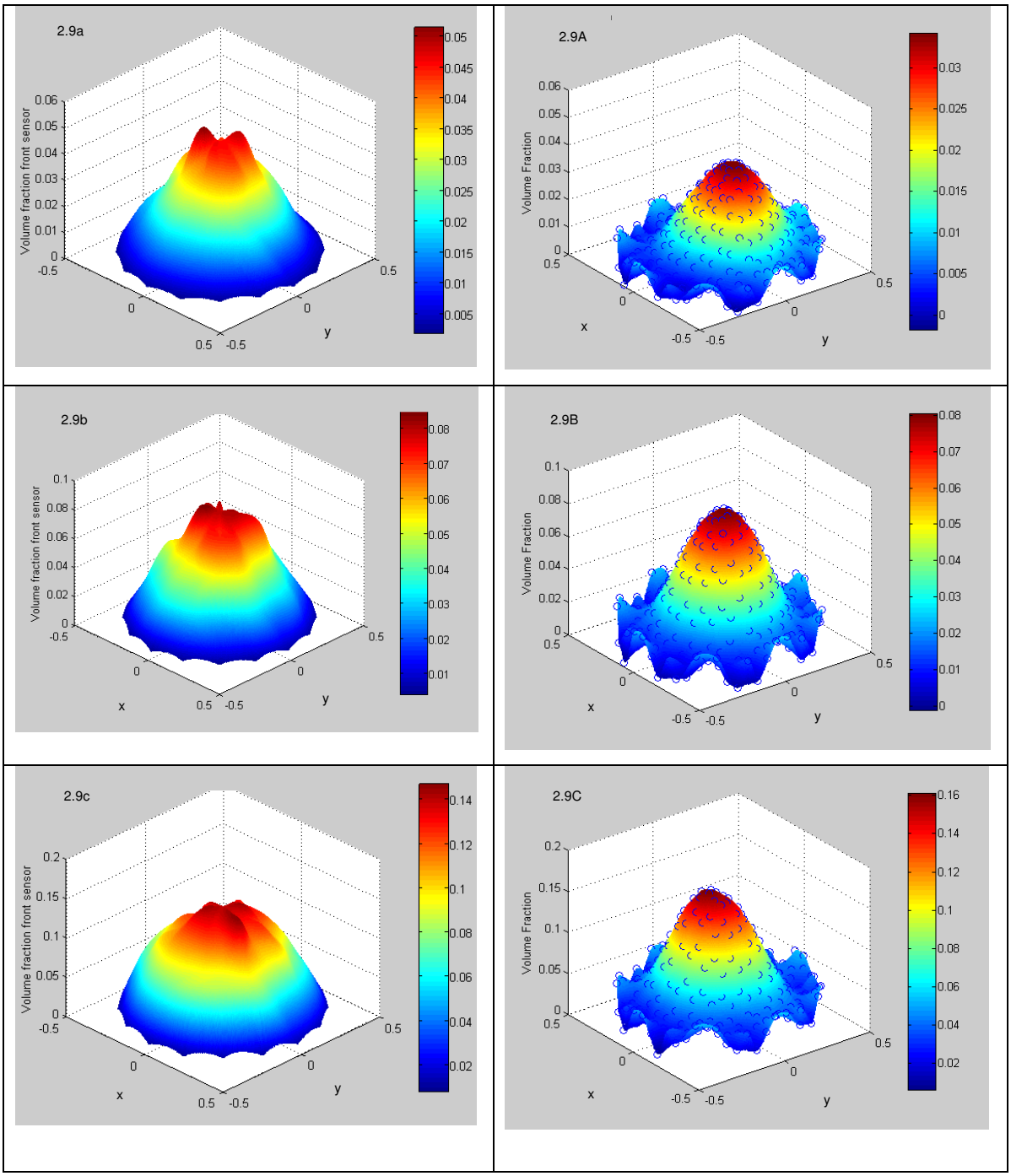


**Figure A.9 Volume fraction distribution profile obtained from dual-sensor probe (left) and ERT system (right). Lucas et al. [3]**

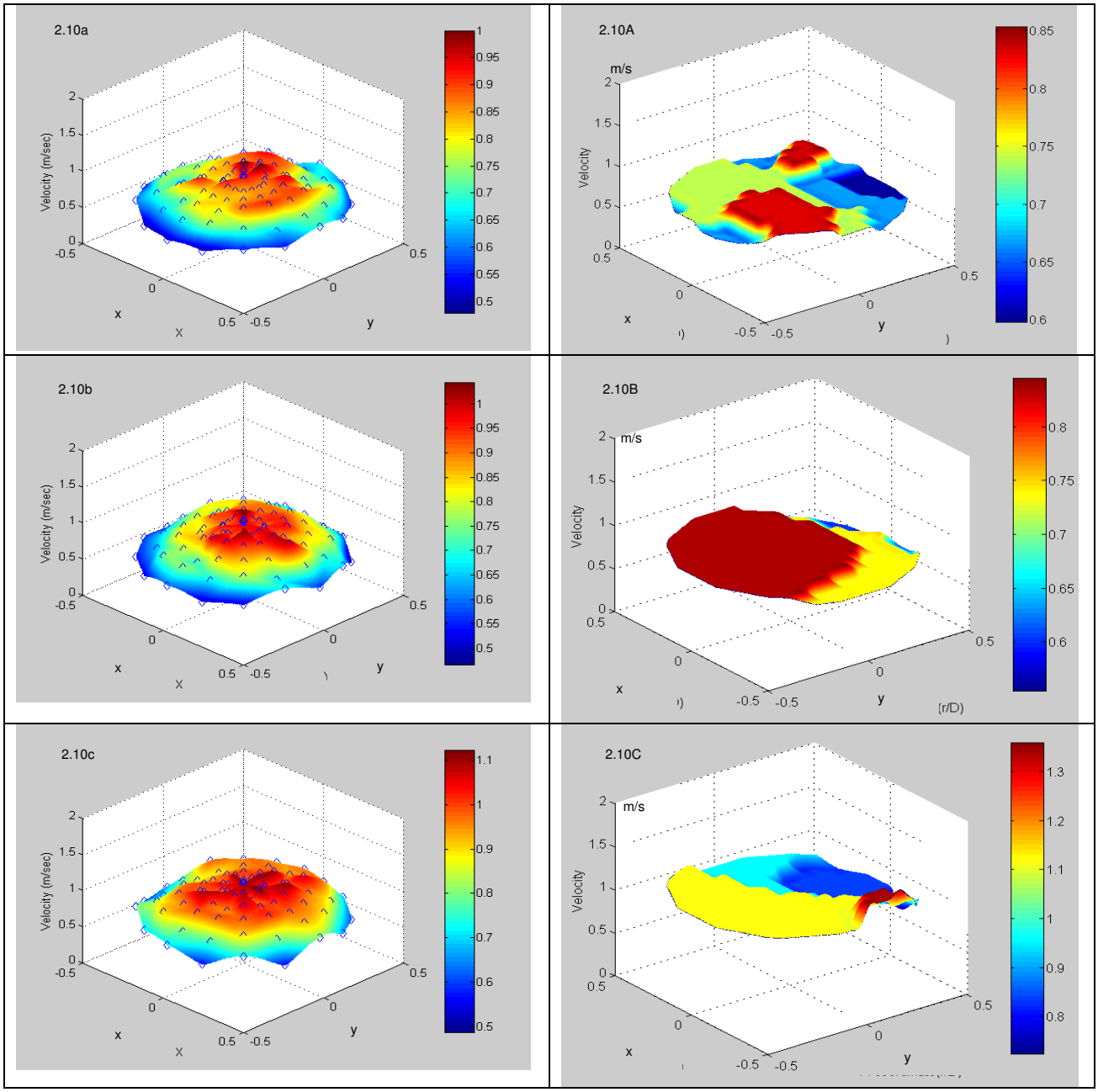


**Figure A.10 Local axial velocity distribution profile obtained from dual-sensor probe (left) and ERT system (right). Lucas et al. [3]**

Figure A.9 shows the results of the local gas volume fraction distribution $\lambda_l$ from the dual-sensor probe (left) and ERT system (right) at constant water superficial velocity $U_{ws}$ of $0.64\text{ms}^{-1}$ with the gas superficial velocity $U_{gs}$ taking values of $0.017\text{ms}^{-1}$ (a,

A), $0.035\text{ms}^{-1}$ (b, B) and $0.073\text{ms}^{-1}$ (c, C). The mean gas volume fraction $\overline{\lambda}$ from the dual-sensor probe was found to be 0.013, 0.033 and 0.062 respectively.

The dual-sensor results shows that as $\overline{\lambda}$ increases as a result of $U_{gs}$ being increased, the local gas volume fraction distribution changes from a 'peaky' profile where the gas is relatively highly concentrated at the pipe centre to a smoother profile, where the gas is more uniformly distributed in the flow cross section.

Results from the ERT system (Figure A.9 A, B, C at identical flow conditions that were used in the dual-sensor probe) show that the gas volume fraction profiles are qualitatively similar to the local probe profiles, apart from some 'noise' at the boundary. Also, the mean value of the gas volume fraction measured using the ERT system was always very close to $\overline{\lambda}_l$ for all of the flow conditions.

Lucas et al. [3] also undertook a comparison of the local bubble axial velocity distribution obtained using a local dual-sensor probe and a dual-plane ERT system at the same flow conditions. Figure A.10 shows the results obtained from local dual-sensor probe (left) and ERT system (right) with flow conditions where the water superficial velocity $U_{ws}$ was held constant at $0.38\text{ms}^{-1}$ and the gas superficial velocity $U_{gs}$ took values of $0.017\text{ms}^{-1}$ (a, A), $0.032\text{ms}^{-1}$ (b, B) and $0.072\text{ms}^{-1}$ (c, C). The measured velocity profile distribution is flatter than the local volume fraction distribution in Figure A.9.

Figure A.10 also shows that the ERT velocity profiles show large 'flat' regions, suggesting the measured velocity is essentially constant; a result which was not observed for the profiles obtained from the local dual-sensor probe. However, the

mean value of the gas velocity measured using the ERT system was generally very close to a reference measurement of the mean gas velocity, for the flow conditions that Lucas et al. [3] investigated.

Recent developments using dual-plane ERT have shown that it is possible to obtain the distribution of the vector velocity of the dispersed phase, enabling more accurate flow rate measurements and also suggesting the possibility of using ERT instruments as diagnostic tools and as a means of validating computational models of complex multiphase flows. Electrical tomographic systems have been used in bubble columns (Schmitz et al. [5]) and in three-phase monoliths and trickle beds (Reinecke et al. [6]). Advances in technologies allowed several scientists to optimise the method and the reconstruction algorithms (Wang et al. [107]). It is important to mention that ERT systems are limited to flows where the continuous phase is electrically conductive [3, 7, 105 -110].

ERT systems are now commercially available, one of which is the ITS p2000 electrical resistance tomography system. These ERT systems can be used in solid/liquid and liquid/gas mixing applications, hydrocyclones, packed columns, flotation columns, precipitation processes, liquid-liquid extraction and hydraulic conveying.

# Appendix B

# Software programmes

## 1) Continuous Data Collection

```
Dim Voltage_range As Integer, Card_number As Integer
Dim result As Integer, temp_channel As Integer, Number_of_channels As
Integer
Dim Sampling_frequency As Long, Sampling_period As Long
Dim Data_pathway As String, Total_number_samples As Long
Dim Total_number_of_bytes As Long, Scan_interval As Long
Dim Buffer1() As Integer, Buffer2() As Integer
Dim Buffer_index As Integer, Buffer_size As Long
Dim Samples_per_buffer As Long, Stop_async As Byte
Dim Access_count As Long, Channels() As Integer, temp_time As Double
Dim T1 As Double, T2 As Double, DT As Double
Dim tempstring As String, box As Integer, tempint As Integer
Dim Voltage_array() As Double, Stop_async1 As Byte
Dim Read_scans As Long, Half_ready As Byte, DT_temp As Double
Dim dig_out As Long, cw As Boolean, number_of_turns As Integer


Private Sub Acquire_Data_Command_Click()
    Exit_Command.Enabled = False
    Acquire_Data_Command.Enabled = False
    Deactivate_DAQ2006_Command.Enabled = False
    Activate_DAQ2006_Command.Enabled = False
    ROTATE_Command.Enabled = False
    RTM_Command.Enabled = False

    Info_Label.Caption = "Data are being acquired."

    Buffer_size = Number_of_channels * 16 '* Sampling_frequency
    ReDim Buffer1(Buffer_size)
    ReDim Buffer2(Buffer_size)
    result = D2K_AI_AsyncDblBufferMode(Card_number, 1)
    If (result < 0) Then
        Info_Label.Caption = "Error setting the buffer mode!"
    Else
        result = D2K_AI_ContBufferSetup(Card_number, Buffer1(0),
Buffer_size, Buffer_index)
        result = D2K_AI_ContBufferSetup(Card_number, Buffer2(0),
Buffer_size, Buffer_index)
        If (result < 0) Then
            Info_Label.Caption = "Error setting up the buffers!"
        Else
            temp_time = Sampling_period - 1
            DT_temp = 0
            Read_scans = Buffer_size / Number_of_channels
            result = D2K_AI_ContScanChannelsToFile(Card_number,
(Number_of_channels - 1), Buffer_index, Data_pathway, Read_scans,
Scan_interval, Scan_interval, ASYNCH_OP)
            While (temp_time >= 0)
```

```
                T1 = Timer
                DT = 0
                Stop_async1 = 0
                Half_ready = 0
                While (Half_ready = 0) 'And (Stop_async1 = 0)
                    result =
D2K_AI_AsyncDblBufferHalfReady(Card_number, Half_ready, Stop_async1)
                    If result < 0 Then
                        box = MsgBox("ERROR", vbYesNo)
                    End If
                Wend
                result = D2K_AI_AsyncDblBufferToFile(Card_number)
                    'While (Stop_async1 = 0)
                    '    result = D2K_AI_AsyncCheck(Card_number,
Stop_async1, Access_count)
                    'Wend
                    'result = D2K_AI_AsyncClear(Card_number, 0,
Access_count)
                    T2 = Timer
                    DT = T2 - T1
                    temp_time = temp_time - DT
                    DT_temp = DT_temp + DT
                    If DT_temp >= 1 Then
                        DT_temp = 0
                        Info_Label.Caption = "Remained time: " +
Str$(temp_time) + " sec."
                    End If
            Wend
            result = D2K_AI_ContBufferReset(Card_number)
            result = D2K_AI_AsyncClear(Card_number, 0, Access_count)
            If (result < 0) Then
                Info_Label.Caption = "Error clearing 'asyncclear' the
buffer!"
            Else
                Info_Label.Caption = "Data have been successfully
acquired."
                Exit_Command.Enabled = True
                Deactivate_DAQ2006_Command.Enabled = True
                Activate_DAQ2006_Command.Enabled = False
                Acquire_Data_Command.Enabled = True
                ROTATE_Command.Enabled = True
                RTM_Command.Enabled = True
            End If
        End If
    End If
End Sub

Private Sub Activate_DAQ2006_Command_Click()
    If (Card_number < 0) Then
        Info_Label.Caption = "Error registering the card!"
    Else
        tempstring = Voltage_Range_Combo.Text
        If (tempstring = "+-10Volts") Then
            Voltage_range = AD_B_10_V
        ElseIf (tempstring = "+-5Volts") Then
            Voltage_range = AD_B_5_V
        ElseIf (tempstring = "+-1.25Volts") Then
            Voltage_range = AD_B_1_25_V
        ElseIf (tempstring = "+5Volts") Then
            Voltage_range = AD_U_5_V
        ElseIf (tempstring = "+10Volts") Then
```

```
            Voltage_range = AD_U_10_V
        ElseIf (tempstring = "+2.5Volts") Then
            Voltage_range = AD_U_2_5_V
        ElseIf (tempstring = "+1.25Volts") Then
            Voltage_range = AD_U_1_25_V
        Else
            Voltage_range = AD_B_10_V
        End If
        Number_of_channels = Number_of_channels_Text.Text
        For tempint = 0 To (Number_of_channels - 1)
            result = D2K_AI_CH_Config(ByVal Card_number, ByVal
tempint, ByVal Voltage_range)
        Next tempint
        If (result < 0) Then
            Info_Label.Caption = "Error configuring the channels!"
        Else
            'result = D2K_AI_Config(Card_number,
DAQ2K_AI_ADCONVSRC_Int, DAK2K_AI_TRGMOD_POST Or DAQ2K_AI_TrgPositive
Or DAQ2K_AI_TRGSRC, 0, 0, 0, 1)
            result = D2K_AI_Config(Card_number, 0, 0 Or 0 Or 0, 0, 0,
0, 1)
            If (result < 0) Then
                Info_Label.Caption = "Error in AI configuration!"
            Else
                Sampling_frequency = Sampling_frequency_Text.Text *
1000
                Sampling_period = Sampling_Period_Text.Text
                Data_pathway = Data_Filename_Text.Text
                Scan_interval = 40000000 / Sampling_frequency
                Total_number_samples = Sampling_frequency *
Sampling_time * Number_of_channels
                Total_number_bytes = Total_number_of_samples * 2
                'Samples_per_buffer = Sampling_frequency *
Number_of_channels
                result = D2K_DIO_PortConfig(Card_number, Channel_P1A,
OUTPUT_PORT)
                dig_out = 32 'set angle to 0 degrees
                cw = True
                number_of_turns = 0
                result = D2K_DO_WritePort(Card_number, Channel_P1A,
dig_out)
                Info_Label.Caption = "DAQ2006 has been successfully
activated. The digital outputs of port A are all in Zero."
                Activate_DAQ2006_Command.Enabled = False
                Deactivate_DAQ2006_Command.Enabled = True
                Acquire_Data_Command.Enabled = True
            End If
        End If
    End If

End Sub

Private Sub Calculation_Command_Click()
Dim RetVal As Double

    'RetVal =
Shell("D:\Nick\PhD\SW\DAQ2006_SIMPLE_ROT\read_DAQ2006_datafile.EXE",
1)
    RetVal =
Shell("D:\Nick\PhD\SW\DAQ2006_SIMPLE_ROT\read_DAQ2006_datafile1.EXE",
1)
```

```
End Sub

Private Sub Deactivate_DAQ2006_Command_Click()
    dig_out = 16
    result = D2K_DO_WritePort(Card_number, Channel_P1A, dig_out)
    result = D2K_Release_Card(ByVal Card_number)
    If (result < 0) Then
        tempstring = Str$(result)
        Info_Label.Caption = "Error releasing DAQ2006!"
    Else
        Info_Label.Caption = "DAQ2006 has been released."
        Acquire_Data_Command.Enabled = False
        Activate_DAQ2006_Command.Enabled = True
        Exit_Command.Enabled = True
    End If
End Sub

Private Sub Exit_Command_Click()
    End
End Sub
Private Sub Form_Load()
    Card_number = D2K_Register_Card(DAQ_2006, 0)
    dig_out = 16
    result = D2K_DO_WritePort(Card_number, Channel_P1A, dig_out)
    Acquire_Data_Command.Enabled = False
    Deactivate_DAQ2006_Command.Enabled = False
End Sub

Private Sub ROTATE_Command_Click()
    Exit_Command.Enabled = False
    Acquire_Data_Command.Enabled = False
    Deactivate_DAQ2006_Command.Enabled = False
    Activate_DAQ2006_Command.Enabled = False
    ROTATE_Command.Enabled = False

If number_of_turns = 0 Then
    dig_out = 128 + 64 '0 angle cw (1 1 0)
    number_of_turns = number_of_turns + 1
ElseIf number_of_turns = 1 Then
    dig_out = 64 '90 angle cw (0 1 0)
    number_of_turns = number_of_turns + 1
ElseIf number_of_turns = 2 Then
    dig_out = 0 '180 angle cw (0 0 0)
    number_of_turns = number_of_turns + 1
Else
    dig_out = 128  '270 angle cw (1 0 0)
    number_of_turns = 0
End If
    result = D2K_DO_WritePort(Card_number, Channel_P1A, dig_out)

    'result = D2K_DIO_PortConfig(Card_number, Channel_P1A,
OUTPUT_PORT)
    'Timer1.Enabled = True
    'T1 = Timer
    'DT = 10
    'T2 = Timer
    'While (T2 <= T1 + DT)
    '    T2 = Timer
    'Wend
```

```
    'Timer1.Enabled = False
    Exit_Command.Enabled = True
    Acquire_Data_Command.Enabled = True
    Deactivate_DAQ2006_Command.Enabled = True
    Activate_DAQ2006_Command.Enabled = True
    ROTATE_Command.Enabled = True
End Sub


Private Sub RTM_Command_Click()

    Exit_Command.Enabled = False
    Acquire_Data_Command.Enabled = False
    Deactivate_DAQ2006_Command.Enabled = False
    Activate_DAQ2006_Command.Enabled = False
    ROTATE_Command.Enabled = False
    RTM_Command.Enabled = False

    Info_Label.Caption = "Data are being acquired."

    Buffer_size = Number_of_channels * 16 '* Sampling_frequency
    ReDim Buffer1(Buffer_size)
    ReDim Buffer2(Buffer_size)
    result = D2K_AI_AsyncDblBufferMode(Card_number, 1)
    If (result < 0) Then
        Info_Label.Caption = "Error setting the buffer mode!"
    Else
        result = D2K_AI_ContBufferSetup(Card_number, Buffer1(0),
Buffer_size, Buffer_index)
        result = D2K_AI_ContBufferSetup(Card_number, Buffer2(0),
Buffer_size, Buffer_index)
        If (result < 0) Then
            Info_Label.Caption = "Error setting up the buffers!"
        Else
            temp_time = Sampling_period - 1
            DT_temp = 0
            Read_scans = Buffer_size / Number_of_channels
            result = D2K_AI_ContScanChannelsToFile(Card_number,
(Number_of_channels - 1), Buffer_index, Data_pathway, Read_scans,
Scan_interval, Scan_interval, ASYNCH_OP)
            While (temp_time >= 0)
                T1 = Timer
                DT = 0
                Stop_async1 = 0
                Half_ready = 0
                While (Half_ready = 0) 'And (Stop_async1 = 0)
                    result =
D2K_AI_AsyncDblBufferHalfReady(Card_number, Half_ready, Stop_async1)
                    If result < 0 Then
                        box = MsgBox("ERROR", vbYesNo)
                    End If
                Wend
                result = D2K_AI_AsyncDblBufferToFile(Card_number)
                    'While (Stop_async1 = 0)
                    '    result = D2K_AI_AsyncCheck(Card_number,
Stop_async1, Access_count)
                    'Wend
                    'result = D2K_AI_AsyncClear(Card_number, 0,
Access_count)
                    T2 = Timer
```

```
                    DT = T2 - T1
                    temp_time = temp_time - DT
                    DT_temp = DT_temp + DT
                    If DT_temp >= 1 Then
                        DT_temp = 0
                        Info_Label.Caption = "Remained time: " +
Str$(temp_time) + " sec."
                    End If
            Wend
            result = D2K_AI_ContBufferReset(Card_number)
            result = D2K_AI_AsyncClear(Card_number, 0, Access_count)
            If (result < 0) Then
                Info_Label.Caption = "Error clearing 'asyncclear' the
buffer!"
            Else
                Info_Label.Caption = "Data have been successfully
acquired."
                Exit_Command.Enabled = True
                Deactivate_DAQ2006_Command.Enabled = True
                Activate_DAQ2006_Command.Enabled = False
                Acquire_Data_Command.Enabled = True
                ROTATE_Command.Enabled = True
                RTM_Command.Enabled = True
            End If
        End If
    End If
End Sub


Private Sub Timer1_Timer()
'If cw = True Then
If number_of_turns = 0 Then
    dig_out = 96 '0 angle cw (64+32)
    number_of_turns = number_of_turns + 1
ElseIf number_of_turns = 1 Then
    dig_out = 160 '90 angle cw (128+32)
    number_of_turns = number_of_turns + 1
ElseIf number_of_turns = 2 Then
    dig_out = 144 '180 angle cw (128+16)
    number_of_turns = number_of_turns + 1
Else
    dig_out = 80 '270 angle cw (64+16)
    number_of_turns = 0
End If
    result = D2K_DO_WritePort(Card_number, Channel_P1A, dig_out)

'End If
End Sub
```

## 2) Single Data Collection

```
#include <windows.h>
#include <stdio.h>
#include <conio.h>
#include "d2kdask.h"

#define ADCONVERTSRC  DAQ2K_AI_ADCONVSRC_Int
#define ADTRIGSRC     DAQ2K_AI_TRGSRC_ExtD
#define ADTRIGMODE    DAQ2K_AI_TRGMOD_MIDL
#define ADTRIGPOL     DAQ2K_AI_TrgPositive
#define MCENABLE      DAQ2K_AI_MCounterEn
#define BUFAUTORESET  1
#define SCAN_INTERVAL 4000//4000
#define POSTCOUNT 1000


U16 channel=3;  //4 channels
U16 range=AD_B_10_V;
char *file_name="2005d";
U32 read_count=4000;//4000;
U32 samp_intrv = 400;//40000; // makes up the sampling frequency
unsigned short ai_buf[4000];//4000];
unsigned short ai_buf2[4000];//4000];
char cardStr[2][8] = {"DAQ2005", "DAQ2006"};

main()
{
    I16 card, err, card_num, Id, card_type=DAQ_2005;
    BOOLEAN halfReady, fStop;
    U32  count=0,count1,startPos=0;//

    printf("This program inputs data from CH-0 to CH-%d of DAQ-
2005/2006 in %d Hz by\ndouble-buffer mode, and store data to file
'%s.dat'. The size of circular\nbuffer is %d. It will not stop until
you press a key.\n\nPress any key to start the operation.\n",
           channel, 1000, file_name, read_count);
    printf("Card Type: (0) DAQ_2005 or (1) DAQ2006 ? ");
    scanf(" %d", &card_type);
    printf("Please input a card number: ");
    scanf(" %d", &card_num);
    if(card_type) card_type = DAQ_2006;
    else card_type = DAQ_2005;
    if((card = D2K_Register_Card(card_type, card_num))<0) {
        printf("Register_Card error=%d\n", card);
        exit(1);
    }
    //default setting : the following two functions are removed
    /*D2K_AI_CH_Config (card, -1, range);
    err = D2K_AI_Config (card, 0,
DAQ2K_AI_ADCONVSRC_Int|DAQ2K_AI_TRGMOD_MIDL|DAQ2K_AI_TrgPositive, 18,
0, 0,1);*/
    err = D2K_AI_Config (card, ADCONVERTSRC,
ADTRIGSRC|ADTRIGMODE|MCENABLE|ADTRIGPOL, POSTCOUNT,3000, 0,
BUFAUTORESET);
    //err = D2K_AI_MiddleTrig_Config (card, ADCONVERTSRC,
ADTRIGSRC|ADTRIGPOL, POSTCOUNT,1,3000, BUFAUTORESET);
```

```
    if (err!=0) {
       printf("D2K_AI_Config error=%d", err);
       exit(1);
    }
    err = D2K_AI_AsyncDblBufferMode (card, 1);
    if (err!=0) {
       printf("DAQ2K_AI_DblBufferMode error=%d", err);
       exit(1);
    }
    err = D2K_AI_ContBufferSetup (card, ai_buf, read_count, &Id);
    if (err!=0) {
       printf("D2K_AI_ContBufferSetup error=%d for the 1st buffer",
err);
       exit(1);
    }
    D2K_AI_ContBufferSetup (card, ai_buf2, read_count, &Id);
    if (err!=0) {
       printf("D2K_AI_ContBufferSetup error=%d for the 2nd buffer",
err);
       exit(1);
    }
    err = D2K_AI_ContScanChannelsToFile (card, channel, Id,
file_name, read_count/(channel+1), samp_intrv, samp_intrv,
ASYNCH_OP);
    if (err!=0) {
       printf("D2K_AI_ContScanChannels error=%d", err);
       exit(1);
    }
    printf("\n\nPress any key to stop input operation.");
    printf("\n\nData count : \n");
    do {
        do {
             D2K_AI_AsyncDblBufferHalfReady(card, &halfReady,
&fStop);
        } while (!halfReady && !fStop);
        D2K_AI_AsyncDblBufferToFile(card);
        count += (read_count);
        printf("%d\r", count);
    }while( !fStop);
    // while (!kbhit());
    D2K_AI_AsyncClear(card, &startPos, &count1);
    count += (count1);
    D2K_Release_Card(card);
    printf("\n\n%d input data are stored in file '%s.dat'.\n", count,
file_name);
    printf("\nPress ENTER to exit the program. "); getch();
}
```

### 3) Signal Processing

```
%%'data detected' for four sensor probes
close all;
clear all;
clc;
%*************************************************************************
*
Fs = 20000;
T = 1/Fs;
%Load data file and devide the data to four data from Data_1 to
Data_4
cd('G:\PhD\matlab_sw\9th_4_08\02_teflon_probe');
Data =load('data1_20k_100s_66hz_A34_B0.txt');
%f = 10000;
%T = 1/f;
Data_1_o = Data(:,1);
Data_2_o = Data(:,2);
Data_3_o = Data(:,3);
Data_4_o = Data(:,4);
figure(1);
plot(Data_1_o,'r--');
hold on;
plot(Data_2_o,'k');
hold on;
plot(Data_3_o,'g')
hold on;
plot(Data_4_o,'b')
%*********************************************
%find the thresh voltage
MAX_DATA1= max(Data_1_o);
MAX_DATA2= max(Data_2_o);
MAX_DATA3 = max(Data_3_o);
MAX_DATA4 = max(Data_4_o);
%MAX_ARRAY = [MAX_DATA1,MAX_DATA2,MAX_DATA3,MAX_DATA4];
%MIN_DATA1_DATA4 = min(MAX_ARRAY);
THRESH1= MAX_DATA1-0.4;
THRESH2= MAX_DATA2-0.4;
THRESH3= MAX_DATA3-0.4;
THRESH4= MAX_DATA4-0.4;
%a = min(Data_2);
Data_1 = Data_1_o-THRESH1;
Data_2 = Data_2_o-THRESH2;
Data_3 = Data_3_o-THRESH3;
Data_4 = Data_4_o-THRESH4;
%[Data_2_check,num] = min(Data_2)
%*********************************************
%Find the points that touch the signals
touch_1=0;
touch_2=0;
touch_3=0;
touch_4=0;
touch_1_right = 0;
touch_2_right = 0;
touch_3_right = 0;
touch_4_right = 0;
j = 1;
for i=1:(length(Data_1)-1)
    if Data_1(i)>0&Data_1(i+1)<=0
            touch_1(j)=i;
             j= j+1;
```

```
    end
    if Data_1(i)<0&Data_1(i+1)>=0

           touch_1(j)=i+1;
           j= j+1;
    end
end
j = 1;
for i=1:(length(Data_2)-1)
    if Data_2(i)>0&Data_2(i+1)<=0
            touch_2(j)=i;
            j= j+1;
    end
    if Data_2(i)<0&Data_2(i+1)>=0

           touch_2(j)=i+1;
           j= j+1;
    end
end
j = 1;
for i=1:(length(Data_3)-1)
    if Data_3(i)>0&Data_3(i+1)<=0
            touch_3(j)=i;
            j= j+1;
    end
    if Data_3(i)<0&Data_3(i+1)>=0
           touch_3(j)=i+1;
           j= j+1;
    end
end
j = 1;
for i=1:(length(Data_4)-1)
    if Data_4(i)>0&Data_4(i+1)<=0
            touch_4(j)=i;
            j= j+1;
    end
    if Data_4(i)<0&Data_4(i+1)>=0

           touch_4(j)=i+1;
           j= j+1;
    end
end
%**********************************************************************
***88
 m =1;
min_touch =
[length(touch_1),length(touch_2),length(touch_3),length(touch_4)];
times_touch = min(min_touch);
%fs = 10000;
%T = 1/fs;
maybe_right_touch = 0;
%short_num = 20;
judge_T = 0.04/T;
 i = 1;
 j = 1;
 while j < times_touch
    if touch_1(i)< touch_2(i)
       if touch_1(i)<touch_3(i)
           if touch_1(i)<touch_4(i)
                  max_judge =
[touch_1(i+1),touch_2(i+1),touch_3(i+1),touch_4(i+1)];
```

```
                min_judge = [(touch_1(i+1)-
touch_1(i)),(touch_2(i+1)-touch_2(i)),(touch_3(i+1)-
touch_3(i)),(touch_4(i+1)-touch_4(i))];
                interval_begin_end = max(max_judge)-touch_1(i);
                short_time = min(min_judge);
                    if interval_begin_end<=judge_T&short_time>=40
                       maybe_right_touch(m) = touch_1(i);
                       maybe_right_touch(m+2) = touch_2(i);
                       maybe_right_touch(m+4) = touch_3(i);
                       maybe_right_touch(m+6) = touch_4(i);
                       maybe_right_touch(m+1) = touch_1(i+1);
                       maybe_right_touch(m+3) = touch_2(i+1);
                       maybe_right_touch(m+5) = touch_3(i+1);
                       maybe_right_touch(m+7) = touch_4(i+1);
                       m= m+8;
                       touch_1 = touch_1(i+2:length(touch_1));
                       touch_2 = touch_2(i+2:length(touch_2));
                       touch_3 = touch_3(i+2:length(touch_3));
                       touch_4 = touch_4(i+2:length(touch_4));
                       i = 1;
                       j = j+2;
                       min_touch_temp =
[length(touch_1),length(touch_2),length(touch_3),length(touch_4)];
                       if min(min_touch_temp)==0
                           j = times_touch+1;
                       end
                    else
                       touch_1 = touch_1(i+2:length(touch_1));
                       i = 1;
                       if length(touch_1)==0
                          j = times_touch+1;
                       end
                    end
            else
                touch_4 = touch_4(i+2:length(touch_4));
                i = 1;
                 if length(touch_4)==0
                    j = times_touch+1;
                 end
            end
        else
             touch_3 = touch_3(i+2:length(touch_3));
             i = 1;
              if length(touch_3)==0
                 j = times_touch+1;
              end
       end
   else
     touch_2 = touch_2(i+2:length(touch_2));
     i = 1;
     if length(touch_2)==0
        j = times_touch+1;
     end
    end
 end
maybe_right_touch;
num_bubble = length(maybe_right_touch)/8;
right_touch = rand(num_bubble,8);
for i = 1:num_bubble
    for j = 1:8
    right_touch(i,j) = maybe_right_touch(j);
```

```
    end
    k = 9;
    maybe_right_touch =
maybe_right_touch(k:length(maybe_right_touch));
end
right_touch;
num_bubble;
%******************use gary's idea that vdt method*********
t =1;
stop_num_b = num_bubble;
while t<= stop_num_b
    e1_1 = right_touch(t,1);
    e1_2 = right_touch(t,2);
    e2_1 = right_touch(t,3);
    e2_2 = right_touch(t,4);
    e3_1 = right_touch(t,5);
    e3_2 = right_touch(t,6);
    e4_1 = right_touch(t,7);
    e4_2 = right_touch(t,8);
    start_end_edge = [e1_1,e1_2,e2_1,e2_2,e3_1,e3_2,e4_1,e4_2];
    start_edge = min(start_end_edge);
    end_edge = max(start_end_edge);
    min_p1 = min(Data_1_o(e1_1:e1_2));
    min_p2 = min(Data_2_o(e2_1:e2_2));
    min_p3 = min(Data_3_o(e3_1:e3_2));
    min_p4 = min(Data_4_o(e4_1:e4_2));
    max_p1 = min(Data_1_o(e1_2:end_edge+1));
    max_p2 = min(Data_2_o(e2_2:end_edge+1));
    max_p3 = min(Data_3_o(e3_2:end_edge+1));
    max_p4 = min(Data_4_o(e4_2:end_edge+1));
    judge_vdt_1 = MAX_DATA1-min_p1;
    judge_vdt_2 = MAX_DATA2-min_p2;
    judge_vdt_3 = MAX_DATA3-min_p3;
    judge_vdt_4 = MAX_DATA4-min_p4;
    judge_vupdt_1 = max_p1-THRESH1;
    judge_vupdt_2 = max_p2-THRESH2;
    judge_vupdt_3 = max_p3-THRESH3;
    judge_vupdt_4 = max_p4-THRESH4;
    judge_vupdt_temp =
[judge_vupdt_1,judge_vupdt_2,judge_vupdt_3,judge_vupdt_4];
    min_judge_vupdt = min(judge_vupdt_temp);
    judge_vdt_temp =
[judge_vdt_1,judge_vdt_2,judge_vdt_3,judge_vdt_4];
    min_judge_vdt = min(judge_vdt_temp);
    if min_judge_vdt<=0|min_judge_vupdt<=0
        right_touch(t,:)=[];
        stop_num_b = stop_num_b-1;
    else
        right_touch(t,:) =right_touch(t,:);
        t= t+1;
    end

end
right_touch;
num_bubble = stop_num_b;
%************************************************
%9th_april_2008_020toflon_short_zx
x1 = 0.0233/1000;
x2 = .4128/1000;
x3 = -.4767/1000;
y1 = .7471/1000;
```

```
y2 = -.6322/1000;
y3 = -.6149/1000;
z1 = 0.7965/1000;
z2 = 0.9535/1000;
z3 = 0.8605/1000;
%************************************************
%calculate the seven time intervals
dt_numb = zeros(num_bubble+1,3);
%dt_0b_1a = zeros(num_bubble+1,2)
m=1;
%k=1;
while m <= num_bubble
dt0b = (right_touch(m,2)-right_touch(m,1))*T;
dt1b = (right_touch(m,4)-right_touch(m,1))*T;
dt2b = (right_touch(m,6)-right_touch(m,1))*T;
dt3b = (right_touch(m,8)-right_touch(m,1))*T;
dt1a = (right_touch(m,3)-right_touch(m,1))*T;
dt2a = (right_touch(m,5)-right_touch(m,1))*T;
dt3a = (right_touch(m,7)-right_touch(m,1))*T;
%dt_0b_1a(m,1) = dt0b;
%dt_0b_1a(m,2) = dt1a;
dt11 = dt1a+dt1b-dt0b;
dt22 = dt2a+dt2b-dt0b;
dt33 = dt3a+dt3b-dt0b;
if dt11>0&dt22>0&dt33>0
    dt_numb(m,1) = dt11;
    dt_numb(m,2) = dt22;
    dt_numb(m,3) = dt33;
    m = m+1;
    %k = k+1;
else
    right_touch(m,:) = [];
    num_bubble = num_bubble-1;
end
end
    dt_numb(num_bubble+1,1) = mean(dt_numb(1:num_bubble,1));
    dt_numb(num_bubble+1,2) = mean(dt_numb(1:num_bubble,2));
    dt_numb(num_bubble+1,3) = mean(dt_numb(1:num_bubble,3));
    %dt_0b_1a(num_bubble+1,1)= mean(dt_0b_1a(1:num_bubble,1));
    %dt_0b_1a(num_bubble+1,2)= mean(dt_0b_1a(1:num_bubble,2));
    result_bubble_v = zeros(num_bubble+3,6);
for n = 1:num_bubble+1
    dt11 =  dt_numb(n,1);
    dt22 =  dt_numb(n,2);
    dt33 =  dt_numb(n,3);
temp_beta_up = (z1/dt11-z2/dt22)*(y1/dt11-y3/dt33)-(z1/dt11-
z3/dt33)*(y1/dt11-y2/dt22);
temp_beta_down = (z1/dt11-z3/dt33)*(x1/dt11-x2/dt22)-(z1/dt11-
z2/dt22)*(x1/dt11-x3/dt33);
%*****************************************************************
*
if (temp_beta_up ==0.0) & (temp_beta_down~=0.0)
         if (temp_beta_down<0.0)
             beta=270;
         else
             beta=90;
         end
         elseif (temp_beta_up~=0.0) & (temp_beta_down==0.0)
         if (temp_beta_up<0.0)
             beta=180;
         else
```

```
            beta=0;
        end
        elseif (temp_beta_up==0.0) & (temp_beta_down==0.0)
        beta=0;
  else
            beta_temp =atand((temp_beta_up)/(temp_beta_down));
            if (beta_temp<0)&(temp_beta_up>0)
                beta1 = 180+beta_temp;
                alafa1 = atand((z2/dt22-z1/dt11)/((x1/dt11-
x2/dt22)*sind(beta1)+(y1/dt11-y2/dt22)*cosd(beta1)));
                if alafa1>0&((z2/dt22-z1/dt11)>0)
                    beta = beta1;
                    alafa = alafa1;
                elseif alafa1>0&((z2/dt22-z1/dt11)<0)
                    beta = beta1;
                    alafa = 180+alafa1;
                end
                if alafa1<0&((z2/dt22-z1/dt11)>0)
                    beta = beta1;
                    alafa = 180+alafa1;
                elseif alafa1<0&((z2/dt22-z1/dt11)<0)
                    beta = beta1;
                    alafa = 360+alafa1;
                end
            elseif (beta_temp<0)&(temp_beta_up<0)
                beta2 = 360+beta_temp;
                alafa2 = atand((z2/dt22-z1/dt11)/((x1/dt11-
x2/dt22)*sind(beta2)+(y1/dt11-y2/dt22)*cosd(beta2)));
                if alafa2>0&((z2/dt22-z1/dt11)>0)
                    beta = beta2;
                    alafa = alafa2;
                elseif alafa2>0&((z2/dt22-z1/dt11)<0)
                    beta = beta2;
                    alafa = 180+alafa2;
                end
                if alafa2<0&((z2/dt22-z1/dt11)>0)
                    beta = beta2;
                    alafa = 180+alafa2;
                elseif alafa2<0&((z2/dt22-z1/dt11)<0)
                    beta = beta2;
                    alafa = 360+alafa2;
                end
            end
            if (beta_temp>0)&(temp_beta_up>0)
                beta3 = beta_temp;
                alafa3 = atand((z2/dt22-z1/dt11)/((x1/dt11-
x2/dt22)*sind(beta3)+(y1/dt11-y2/dt22)*cosd(beta3)));
                if alafa3>0&((z2/dt22-z1/dt11)>0)
                    beta = beta3;
                    alafa = alafa3;
                elseif alafa3>0&((z2/dt22-z1/dt11)<0)
                    beta = beta3;
                    alafa = 180+alafa3;
                end
                if alafa3<0&((z2/dt22-z1/dt11)>0)
                    beta = beta3;
                    alafa = 180+alafa3;
                elseif alafa3<0&((z2/dt22-z1/dt11)<0)
                    beta = beta3;
                    alafa = 360+alafa3;
                end
```

```
            elseif (beta_temp>0)&(temp_beta_up<0)
                beta4 = 180+beta_temp;
                alafa4 = atand((z2/dt22-z1/dt11)/((x1/dt11-
x2/dt22)*sind(beta4)+(y1/dt11-y2/dt22)*cosd(beta4)));
                if alafa4>0&((z2/dt22-z1/dt11)>0)
                    beta = beta4;
                    alafa = alafa4;
                elseif alafa4>0&((z2/dt22-z1/dt11)<0)
                    beta = beta4;
                    alafa = 180+alafa4;
                end
                if alafa4<0&((z2/dt22-z1/dt11)>0)
                    beta = beta4;
                    alafa = 180+alafa4;
                elseif alafa4<0&((z2/dt22-z1/dt11)<0)
                    beta = beta4;
                    alafa = 360+alafa4;
                end
            end
end
if alafa>90&alafa<180
    alafa = alafa-90;
elseif alafa>180&alafa<270
    alafa = alafa-180;
elseif alafa>270&alafa<360
    alafa = alafa-270;
elseif alafa>0&alafa<90
    alafa = alafa;
end
mag_v =
2*(x1*sind(alafa)*sind(beta)+y1*sind(alafa)*cosd(beta)+z1*cosd(alafa)
)/dt11;
mag_v2 =
2*(x2*sind(alafa)*sind(beta)+y2*sind(alafa)*cosd(beta)+z2*cosd(alafa)
)/dt22;
mag_v3 =
2*(x3*sind(alafa)*sind(beta)+y3*sind(alafa)*cosd(beta)+z3*cosd(alafa)
)/dt33;
Vx = mag_v*sind(alafa)*sind(beta);
Vy = mag_v*sind(alafa)*cosd(beta);
Vz = mag_v*cosd(alafa);
result_bubble_v(n,1) = alafa;
result_bubble_v(n,2) = beta;
result_bubble_v(n,3) = mag_v;
result_bubble_v(n,4) = Vx;
result_bubble_v(n,5) = Vy;
result_bubble_v(n,6) = Vz;
end
    result_bubble_v(num_bubble+3,1) =
(1/(num_bubble))*sum(result_bubble_v(1:num_bubble,1));
    result_bubble_v(num_bubble+3,2) =
(1/(num_bubble))*sum(result_bubble_v(1:num_bubble,2));
    result_bubble_v(num_bubble+3,3) =
(1/(num_bubble))*sum(result_bubble_v(1:num_bubble,3));
    result_bubble_v(num_bubble+3,4) =
(1/(num_bubble))*sum(result_bubble_v(1:num_bubble,4));
    result_bubble_v(num_bubble+3,5) =
(1/(num_bubble))*sum(result_bubble_v(1:num_bubble,5));
    result_bubble_v(num_bubble+3,6) =
(1/(num_bubble))*sum(result_bubble_v(1:num_bubble,6));
    disp('    alafa      beta      mag_v      Vx       Vy       Vz')
```

```
    disp(result_bubble_v)
    result_bubble_v;
hold on
kk=result_bubble_v((1:num_bubble),2);
for i= 1:length(kk)
    if kk(i,:)>180
        kk(i,:)=360-kk(i,:);

    else
   kk(i,:)=kk(i,:);
end
kk(i,1)=kk(i,:);
end
errorindval_bubble = sum(kk)/num_bubble;
errorindval_bubble
```

### 4) Image Processing

```
Image Processing for Bubbles for the first frame
%includes the intersection poit for the first frame rather then
%just mean
clear all;
close all;
clc;
my_movie_info = aviinfo('ma_P3_50k.avi') % movie na,e
Frames=zeros(my_movie_info.Height,
my_movie_info.Width,my_movie_info.NumFrames);
for j=1:my_movie_info.NumFrames
    I(j,1) = aviread('ma_P3_50k.avi',j); %movie name
    Frames(:,:,j) = getfield(I(j,1),'cdata');
end

movie(I);
%process for frame 1
frame01= Frames(:,:,1);
imshow(frame01);
[frame_01,Map] = frame2im(I(1)); %extract frame 1
figure(1)
a2=image(frame_01);
title ('Frame1')

    saveas(gcf, 'a2', 'jpg') % save the image
    j2 = imread('a2.jpg');
    x2=imresize(j2,.5);
    imagesize2 = size(x2);
    screensize2 = get (0,'screensize');
    iptsetpref ('imshowborder','tight');

% change to gray style
    z2 = rgb2gray(x2);
    imshow(z2)
    BW_2 = edge(z2,'canny',.16);
    bw_3=(BW_2(:,:)==0);
    figure(5),imshow(bw_3)
    hold on;
    %xx=
    %yy=
    [r2 c2]= find(bw_3(300:320,340:370)==0); % first on range of y-
axis second one is range of x-axis
    bw_4= [r2 c2];
    k2=300:320; for N2=k2, I2 = find(bw_3(N2,340:370)==0);,
RR2_(:,N2) = [I2 zeros(1,50-length(I2))];, end

G2=find(max(RR2_~=0));
B2=G2';
COL2=mean(B2)
RR_2 = RR2_(:,B2)';

    %%%%%%%%%%%calculates the distance of all coordinates and gives
the
    %%%%%%%%%%%longest distance
gg=[339]+(bw_4(:,2)); % 1 less to x-axis
gg1=[299]+(bw_4(:,1));%1 less to y axis
gg=[gg gg1]
co=zeros(2,2);
d=zeros(28,28);% length of gg
for cnt=1:28
```

```
    for cntt=(cnt+1):29
    d(cnt,cntt-1)=sqrt(((gg(cnt ,1)-gg(cntt ,1)).^2) + ((gg(cnt ,2)-
gg(cntt ,2)).^2));
    end
end

f=(max(max(d)));
[a b]=find(d==f);
co(1,:)=gg(a,:);
co(2,:)=gg(b+1,:);
co

u= ((co(1,1)+co(2,1))/2.000001);
v= ((co(1,2)+co(2,2))/2.000001);
[u v] % centreeee

slope = (co(2,2)-co(1,2))/(co(2,1)-co(1,1))
m2=-(1/slope)
m5=atan(slope);
t2 =((0+pi)):(pi/60):(2*pi);
t3 =((0):(pi/60):(pi));

ad=atan(-m2)
dg=ad-(pi/2)

dots_top=find((gg(:,2)<305)&(gg(:,1)>351))
dots_top=gg(dots_top,:)

dots_bot=find((gg(:,2)>305)&(gg(:,1)>351))
dots_bot=gg(dots_bot,:)

%% slope of top dots with respect to center [u v]
for cnt=1:length(dots_top)
      slope_top(cnt,:)=((dots_top(cnt ,2)-v)/(dots_top(cnt ,1)-u));
end
slope_top;
%% slope of bottom dots with respect to center [u v]
for cnt=1:length(dots_bot)
      slope_bot(cnt,:)=((dots_bot(cnt ,2)-v)/(dots_bot(cnt ,1)-u));
end
slope_bot;

% calculation of min error on slope to make 90 deg on top half
diff_slope_top=slope_top-m2;
diff_slope_top = sqrt(diff_slope_top.^2);
min_slope_top=min(min(diff_slope_top));
[x_top y_top]=find(diff_slope_top==min_slope_top);
coord_top(1,:)=dots_top(x_top(1),:)

%%%% calculation of min error on slope to make 90 deg on bottom half
diff_slope_bot=slope_bot-m2;
diff_slope_bot = sqrt(diff_slope_bot.^2);
min_slope_bot=min(min(diff_slope_bot));
[x_bot y_bot]=find(diff_slope_bot==min_slope_bot);
coord_bot(1,:)=dots_bot(x_bot(1),:)


ad2=atan(min_slope_bot)
dg2=ad2-(pi/2)
%% calculation  minor axis of top and bottom
```

```
minor_top= (v-coord_top(1,2))
minor_bot= (coord_bot(1,2)-v)
major_ax = (co(2,1)-co(1,1))/2
slope_top =((pi/2)-slope):(pi/60):((3*pi/2)-slope);
slope_bot =((0+(3*(pi/2)))-slope):(pi/60):((2*pi)+(pi/2)-slope);
t = 0:pi/40:(2*pi);


x5 = (((coord_top(1,1)-u) * cos(dg)) + ((coord_top(1,2)-v)* -
sin(dg))+u);
y6 = (((u-coord_top(1,1))* sin(dg)) + ((v-coord_top(1,2)) *
cos(dg))+v);

%%%work for bottom minor axis
%%% substract the centre first and add them at the end after moving
axis

x9 = (((coord_bot(1,1)-u) * cos(dg2)) + ((coord_bot(1,2)-v)* -
sin(dg2))+u);
y9 = (((coord_bot(1,1)-u)* sin(dg2)) + ((coord_bot(1,2)-v) *
cos(dg2))+v);


figure(59),imshow(bw_3)
hold on;
plot([co(1,1) co(2,1)],[co(1,2) co(2,2)] ,'-')
plot([x5 u],[y6 v] ,'-')
plot([x9 u],[y9 v] ,'-')
new_re_top_m=v-y6
new_re_bot_m=v-y9
x7= (round(major_ax))*cos(t2);%************************************
y7= new_re_top_m*sin(t2);
x8 = ((x7 * cos(m5)) + (y7* -sin(m5))+u);
y8 = ((x7* sin(m5)) + (y7 * cos(m5))+v);
%plot([coord_bot(1,1) u],[coord_bot(1,2) v] ,'-')
x10= (round(major_ax))*cos(t2);%************************************
y10= new_re_bot_m*sin(t2);
x11 = ((x10 * cos(m5)) + (y10* -sin(m5))+u);
y11 = ((x10* sin(m5)) + (y10 * cos(m5))+v);
plot(x8,y8)
plot(x11,y11)
hold off


for cnt=1:length(dots_top)
    for cnt=1:length(dots_top)
          m_dots_top(cnt,:)=((dots_top(cnt ,2)-v)/(dots_top(cnt ,1)-
u));
          for cnt=1:length(m_dots_top)

dist_2_new_ell_top(cnt,:)=((((((major_ax.^2)*(new_re_top_m.^2))*((m_d
ots_top(cnt,1).^2)+1)/((new_re_top_m.^2)+(m_dots_top(cnt,1).^2)*(majo
r_ax.^2))))));
             dist_top_dots(cnt,:)=sqrt(((dots_top(cnt ,1)-u).^2) +
((dots_top(cnt ,2)-v).^2));
          end
    end
end
m_dots_top
new_top_minor=sqrt((dist_2_new_ell_top))
dist_top_dots
```

```
er_minor_top=sqrt((sum(dist_top_dots-new_top_minor)/14).^2)
new_minor_top=round(er_minor_top+new_re_top_m)

for cnt=1:length(dots_bot)
     for cnt=1:length(dots_bot)
          m_dots_bot(cnt,:)=((dots_bot(cnt ,2)-v)/(dots_bot(cnt ,1)-
u));
          for cnt=1:length(m_dots_bot)

dist_2_new_ell_bot(cnt,:)=((((((major_ax.^2)*(new_re_bot_m.^2))*((m_d
ots_bot(cnt,1).^2)+1)/((new_re_bot_m.^2)+(m_dots_bot(cnt,1).^2)*(majo
r_ax.^2))))));
             dist_bot_dots(cnt,:)=sqrt(((dots_bot(cnt ,1)-u).^2) +
((dots_bot(cnt ,2)-v).^2));
          end
     end
end
m_dots_bot
new_bot_minor=sqrt((dist_2_new_ell_bot))
dist_bot_dots
er_minor_bot=sqrt((sum(dist_bot_dots-new_bot_minor)/15).^2)
new_minor_bot=round(new_re_bot_m-er_minor_bot)

figure(60),imshow(bw_3)
hold on;
plot([co(1,1) co(2,1)],[co(1,2) co(2,2)] ,'-')
plot([x5 u],[y6 v] ,'-')
plot([x9 u],[y9 v] ,'-')

x12=
(round(major_ax))*cos(t2);%************************************
y12= new_minor_top*sin(t2);
x13 = ((x12 * cos(m5)) + (y12* -sin(m5))+u);
y13 = ((x12* sin(m5)) + (y12 * cos(m5))+v);
x14= (round(major_ax))*cos(t2);%************************************
y14= new_minor_bot*sin(t2);
x15 = ((x14 * cos(m5)) + (y14* -sin(m5))+u);
y15 = ((x14* sin(m5)) + (y14 * cos(m5))+v);
plot(x13,y13)
plot(x15,y15)
hold off
```

# Appendix C

## Measured data

| Probe measured before collecting data | | | |
|---|---|---|---|
| | ***1*** | ***2*** | ***3*** |
| *x* | -0.0930 | 0.4419 | -0.4884 |
| *y* | 0.6200 | -0.5115 | -0.3391 |
| *z* | 1.5116 | 1.4884 | 1.5291 |
| **Probe measured after collecting data** | | | |
| *x* | -0.1105 | 0.4128 | -0.5116 |
| *y* | 0.6954 | -0.4655 | -0.2816 |
| *z* | 1.5116 | 1.4884 | 1.5291 |

**Table B.1 Probe dimensions before and after collecting data for reference polar angle $\alpha_{ref}$ 5°**

| Probe measured before collecting data | | | |
|---|---|---|---|
| | ***1*** | ***2*** | ***3*** |
| *x* | -0.0930 | 0.4419 | -0.4884 |
| *y* | 0.6200 | -0.5115 | -0.3391 |
| *z* | 1.5116 | 1.4884 | 1.5291 |
| **Probe measured after collecting data** | | | |
| *x* | -0.0872 | 0.4535 | -0.4826 |
| *y* | 0.6494 | -0.5000 | -0.3333 |
| *z* | 1.5116 | 1.4884 | 1.5291 |

**Table B.2 Probe dimensions before and after collecting data for reference polar angle $\alpha_{ref}$ 14°**

| Probe measured before collecting data | | | |
|---|---|---|---|
| | ***1*** | ***2*** | ***3*** |
| *x* | -0.0930 | 0.4419 | -0.4884 |
| *y* | 0.6200 | -0.5115 | -0.3391 |
| *z* | 1.5116 | 1.4884 | 1.5291 |
| **Probe measured after collecting data** | | | |
| *x* | -0.1105 | 0.4186 | -0.4884 |
| *y* | 0.6207 | -0.4943 | -0.3218 |
| *z* | 1.5116 | 1.4884 | 1.5291 |

**Table B.3 Probe dimensions before and after collecting data for reference polar angle $\alpha_{ref}$ 21°**

| Probe Measured before collecting data | | | |
|---|---|---|---|
| | *1* | *2* | *3* |
| *x* | -0.0930 | 0.4419 | -0.4884 |
| *y* | 0.6200 | -0.5115 | -0.3391 |
| *z* | 1.5116 | 1.4884 | 1.5291 |
| **Probe Measured after collecting data** | | | |
| *x* | -0.0930 | 0.4320 | -0.4651 |
| *y* | 0.6149 | -0.4828 | -0.3046 |
| *z* | 1.5116 | 1.4884 | 1.5291 |

**Table B.4 Probe dimensions before and after collecting data for reference polar angle $\alpha_{ref}$ 34°**

| | | Average $\delta t_{ii}$ | | | Average individual bubble | | | Average | | | |
|---|---|---|---|---|---|---|---|---|---|---|---|
| Test | $v_{ref}$ | $\alpha_{meas,m,p}$ | $\beta_{meas,m,p}$ | $v_{meas,m,p}$ | $\alpha_{meas,m,p}$ | $\beta_{meas,m,p}$ | $v_{meas,m,p}$ | $\delta t_{11}$ | $\delta t_{22}$ | $\delta t_{33}$ | *NOB* |
| **Probe measured before collecting data** | | | | | | | | | | | |
| **without signal processing** | | | | | | | | | | | |
| 1 | 0.34 | 8.93 | 218.41 | 0.43 | 24.71 | 322.97 | 0.39 | 0.006636 | 0.006930 | 0.007437 | 24 |
| 2 | 0.39 | 11.64 | 274.07 | 0.43 | 25.58 | 320.54 | 0.40 | 0.007015 | 0.006333 | 0.007401 | 71 |
| 3 | 0.49 | 9.48 | 195.85 | 0.48 | 25.98 | 319.82 | 0.44 | 0.005822 | 0.005778 | 0.006422 | 59 |
| 4 | 0.52 | 10.57 | 231.40 | 0.59 | 23.37 | 328.86 | 0.54 | 0.004842 | 0.004944 | 0.005464 | 22 |
| 5 | 0.25 | 14.76 | 233.60 | 0.29 | 25.08 | 325.52 | 0.28 | 0.009565 | 0.009835 | 0.011242 | 42 |
| **Average** | | **11.08** | **230.67** | | **24.94** | **323.54** | | | | | |
| **with signal processing** | | | | | | | | | | | |
| 1 | 0.34 | 9.20 | 210.85 | 0.42 | 23.27 | 329.25 | 0.39 | 0.006736 | 0.007158 | 0.007600 | 21 |
| 2 | 0.39 | 11.64 | 262.84 | 0.44 | 23.71 | 324.65 | 0.40 | 0.006774 | 0.006283 | 0.007290 | 63 |
| 3 | 0.49 | 9.63 | 241.43 | 0.50 | 24.89 | 322.75 | 0.45 | 0.005815 | 0.005776 | 0.006426 | 51 |
| 4 | 0.52 | 8.81 | 218.88 | 0.57 | 20.92 | 336.28 | 0.54 | 0.005014 | 0.005227 | 0.005609 | 16 |
| 5 | 0.25 | 7.49 | 239.21 | 0.29 | 28.43 | 333.23 | 0.26 | 0.010122 | 0.010071 | 0.010989 | 34 |
| **Average** | | **9.35** | **234.64** | | **24.24** | **329.23** | | | | | |
| **Probe measured after collecting data** | | | | | | | | | | | |
| **without signal processing** | | | | | | | | | | | |
| 1 | 0.34 | 8.80 | 219.64 | 0.43 | 24.46 | 323.57 | 0.39 | 0.00662 | 0.006908 | 0.00741 | 24 |
| 2 | 0.34 | 11.74 | 274.44 | 0.43 | 25.52 | 320.98 | 0.40 | 0.006974 | 0.006296 | 0.007357 | 71 |
| 3 | 0.49 | 9.23 | 196.63 | 0.48 | 25.74 | 320.39 | 0.44 | 0.005780 | 0.006327 | 0.006553 | 59 |
| 4 | 0.52 | 10.48 | 232.60 | 0.59 | 23.17 | 329.24 | 0.54 | 0.004872 | 0.004974 | 0.005498 | 22 |
| 5 | 0.25 | 14.65 | 234.74 | 0.29 | 24.82 | 325.93 | 0.27 | 0.009543 | 0.009812 | 0.011215 | 42 |
| **Average** | | **9.55** | **232.72** | | **25.43** | **325.57** | | | | | |
| **with signal processing** | | | | | | | | | | | |
| 1 | 0.34 | 9.02 | 211.97 | 0.42 | 22.98 | 329.81 | 0.39 | 0.006712 | 0.007132 | 0.007572 | 21 |
| 2 | 0.34 | 11.73 | 263.47 | 0.44 | 23.66 | 325.06 | 0.40 | 0.006755 | 0.006294 | 0.007305 | 63 |
| 3 | 0.49 | 9.61 | 242.51 | 0.50 | 24.69 | 323.29 | 0.45 | 0.005813 | 0.005769 | 0.006420 | 51 |
| 4 | 0.52 | 8.67 | 219.98 | 0.57 | 20.71 | 336.73 | 0.54 | 0.004999 | 0.005211 | 0.005592 | 16 |
| 5 | 0.25 | 7.47 | 240.30 | 0.29 | 28.27 | 333.68 | 0.26 | 0.010012 | 0.010063 | 0.010980 | 34 |
| **Average** | | **9.30** | **235.65** | | **24.06** | **329.72** | | | | | |

**Table B.5 Calculation of $\alpha_{meas,p}$ , $\beta_{meas,p}$ and $v_{meas,p}$ before and after signal processing calculated using the probe dimension measured before and after collecting data with $\alpha_{ref}$ = 5° and $\beta_{ref}$ =0° and for various values of $v_{ref}$**

| ***Tests*** | **Average $\delta t_{ii}$** | | | **Average individual bubble** | | |
|---|---|---|---|---|---|---|
| | $\varepsilon_{abs,\alpha,m,p}$ (deg) | $\varepsilon_{abs,\beta,m,p}$ (deg) | $\varepsilon_{v,m,p}$ (%) | $\varepsilon_{abs,\alpha,m,p}$ (deg) | $\varepsilon_{abs,\beta,m,p}$ (deg) | $\varepsilon_{v,m,p}$ (%) |
| | **Probe measured before collecting data** | | | | | |
| | Error calculation without signal processing | | | | | |
| 1 | 3.93 | 141.59 | 26.87 | 19.71 | 37.03 | 15.13 |
| 2 | 6.64 | 85.93 | 10.90 | 20.58 | 39.46 | 1.88 |
| 3 | 4.48 | 164.15 | 1.35 | 20.98 | 40.18 | 9.64 |
| 4 | 5.57 | 128.60 | 12.77 | 18.37 | 31.14 | 3.76 |
| 5 | 9.76 | 126.40 | 16.10 | 20.08 | 34.48 | 10.02 |
| | $\bar{\varepsilon}_{abs,\alpha,p}$ | $\bar{\varepsilon}_{abs,\beta,p}$ | $\bar{\varepsilon}_{v,p}$ | $\bar{\varepsilon}_{abs,\alpha,p}$ | $\bar{\varepsilon}_{abs,\beta,p}$ | $\bar{\varepsilon}_{v,p}$ |
| | **6.08** | **129.33** | **13.60** | **19.94** | **36.46** | **8.08** |
| | $\sigma_{abs,a,p}$ | $\sigma_{abs,\beta,p}$ | $\sigma_{v,p}$ | $\sigma_{abs,a,p}$ | $\sigma_{abs,\beta,p}$ | $\sigma_{v,p}$ |
| | **2.06** | **25.52** | **8.25** | **0.90** | **3.33** | **4.75** |
| | Error calculation with signal processing | | | | | |
| 1 | 4.20 | 149.15 | 23.55 | 18.27 | 30.75 | 14.42 |
| 2 | 6.64 | 97.16 | 11.58 | 18.71 | 35.35 | 3.28 |
| 3 | 4.63 | 118.57 | 1.25 | 19.89 | 37.25 | 7.73 |
| 4 | 3.81 | 141.12 | 9.60 | 15.92 | 23.72 | 3.39 |
| 5 | 2.49 | 120.79 | 17.28 | 23.43 | 26.77 | 5.46 |
| | $\bar{\varepsilon}_{abs,\alpha,p}$ | $\bar{\varepsilon}_{abs,\beta,p}$ | $\bar{\varepsilon}_{v,p}$ | $\bar{\varepsilon}_{abs,\alpha,p}$ | $\bar{\varepsilon}_{abs,\beta,p}$ | $\bar{\varepsilon}_{v,p}$ |
| | **4.35** | **125.36** | **12.65** | **19.24** | **30.77** | **6.86** |
| | $\sigma_{abs,a,p}$ | $\sigma_{abs,\beta,p}$ | $\sigma_{v,p}$ | $\sigma_{abs,a,p}$ | $\sigma_{abs,\beta,p}$ | $\sigma_{v,p}$ |
| | **1.35** | **18.31** | **7.49** | **2.46** | **5.07** | **4.12** |
| | **Probe measured after collecting data** | | | | | |
| | Error calculation without signal processing | | | | | |
| 1 | 3.80 | 140.36 | 26.49 | 19.46 | 36.43 | 15.09 |
| 2 | 6.74 | 85.56 | 27.65 | 20.52 | 39.02 | 17.11 |
| 3 | 4.23 | 163.37 | 1.83 | 20.74 | 39.61 | 9.54 |
| 4 | 5.48 | 127.40 | 12.53 | 18.17 | 30.76 | 3.79 |
| 5 | 2.47 | 119.70 | 15.82 | 23.27 | 26.32 | 9.90 |
| | $\bar{\varepsilon}_{abs,\alpha,p}$ | $\bar{\varepsilon}_{abs,\beta,p}$ | $\bar{\varepsilon}_{v,p}$ | $\bar{\varepsilon}_{abs,\alpha,p}$ | $\bar{\varepsilon}_{abs,\beta,p}$ | $\bar{\varepsilon}_{v,p}$ |
| | **4.55** | **127.28** | **16.86** | **20.43** | **34.43** | **11.08** |
| | $\sigma_{abs,a,p}$ | $\sigma_{abs,\beta,p}$ | $\sigma_{v,p}$ | $\sigma_{abs,a,p}$ | $\sigma_{abs,\beta,p}$ | $\sigma_{v,p}$ |
| | **1.46** | **25.58** | **9.54** | **1.69** | **5.12** | **4.68** |
| | Error calculation with signal processing | | | | | |
| 1 | 4.02 | 148.03 | 23.09 | 17.98 | 30.19 | 14.23 |
| 2 | 6.73 | 96.53 | 28.23 | 18.66 | 34.94 | 18.75 |
| 3 | 4.61 | 117.49 | 1.17 | 19.69 | 36.71 | 7.61 |
| 4 | 3.67 | 140.02 | 9.28 | 15.71 | 23.27 | 3.20 |
| 5 | 2.47 | 119.70 | 17.18 | 23.27 | 26.32 | 5.41 |
| | $\bar{\varepsilon}_{abs,\alpha,p}$ | $\bar{\varepsilon}_{abs,\beta,p}$ | $\bar{\varepsilon}_{v,p}$ | $\bar{\varepsilon}_{abs,\alpha,p}$ | $\bar{\varepsilon}_{abs,\beta,p}$ | $\bar{\varepsilon}_{v,p}$ |
| | **4.30** | **124.35** | **15.79** | **19.06** | **30.28** | **9.84** |
| | $\sigma_{abs,a,p}$ | $\sigma_{abs,\beta,p}$ | $\sigma_{v,p}$ | $\sigma_{abs,a,p}$ | $\sigma_{abs,\beta,p}$ | $\sigma_{v,p}$ |
| | **1.40** | **18.16** | **9.66** | **2.48** | **5.06** | **5.79** |

**Table B.6 Errors in the values of polar angle, azimuthal angle and velocity magnitude measured by the probe with $\alpha_{ref}$ = 5° and $\beta_{ref}$ =0° and for various values of $v_{ref}$**

| | | Average $\delta t_{ii}$ | | | Average individual bubble | | | | | | |
|---|---|---|---|---|---|---|---|---|---|---|---|
| Test | $v_{ref}$ | $\alpha_{meas,m,p}$ | $\beta_{meas,m,p}$ | $v_{meas,m,p}$ | $\alpha_{meas,m,p}$ | $\beta_{meas,m,p}$ | $v_{meas,m,p}$ | $\delta t_{11}$ | $\delta t_{22}$ | $\delta t_{33}$ | *NOB* |
| **Probe measured before collecting data** | | | | | | | | | | | |
| **Before signal processing** | | | | | | | | | | | |
| 1 | 0.34 | 11.06 | 316.68 | 0.44 | 26.01 | 326.46 | 0.40 | 0.007192 | 0.006051 | 0.006898 | 45 |
| 2 | 0.39 | 17.26 | 305.40 | 0.44 | 27.98 | 339.62 | 0.41 | 0.007148 | 0.005575 | 0.006910 | 98 |
| 3 | 0.49 | 15.97 | 337.03 | 0.45 | 28.84 | 319.06 | 0.43 | 0.007201 | 0.005573 | 0.006385 | 36 |
| 4 | 0.52 | 15.87 | 323.95 | 0.48 | 28.68 | 335.93 | 0.52 | 0.006698 | 0.005198 | 0.006144 | 55 |
| 5 | 0.25 | 9.52 | 325.23 | 0.31 | 29.21 | 331.62 | 0.27 | 0.010218 | 0.008753 | 0.009729 | 33 |
| **Average** | | **13.94** | **308.06** | | **28.14** | **330.54** | | | | | |
| **After signal processing** | | | | | | | | | | | |
| 1 | 0.34 | 13.58 | 305.43 | 0.43 | 24.91 | 325.96 | 0.40 | 0.007309 | 0.006012 | 0.007133 | 35 |
| 2 | 0.39 | 15.13 | 330.13 | 0.45 | 26.62 | 343.93 | 0.41 | 0.007163 | 0.005616 | 0.006502 | 74 |
| 3 | 0.49 | 18.83 | 315.70 | 0.48 | 28.40 | 330.54 | 0.44 | 0.006645 | 0.004962 | 0.006163 | 30 |
| 4 | 0.52 | 15.93 | 322.44 | 0.59 | 26.95 | 346.79 | 0.54 | 0.005437 | 0.004224 | 0.005011 | 39 |
| 5 | 0.25 | 15.36 | 300.12 | 0.30 | 24.40 | 315.73 | 0.28 | 0.010409 | 0.008440 | 0.010275 | 21 |
| **Average** | | **15.76** | **314.76** | | **26.26** | **332.59** | | | | | |
| **Probe measured after collecting data** | | | | | | | | | | | |
| **Before signal processing** | | | | | | | | | | | |
| 1 | 0.34 | 11.82 | 294.71 | 0.43 | 26.25 | 324.06 | 0.40 | 0.007216 | 0.006184 | 0.007246 | 42 |
| 2 | 0.34 | 17.15 | 304.72 | 0.44 | 27.75 | 339.21 | 0.42 | 0.007157 | 0.005583 | 0.006919 | 98 |
| 3 | 0.49 | 15.78 | 336.20 | 0.45 | 28.64 | 318.66 | 0.43 | 0.007226 | 0.005592 | 0.006407 | 36 |
| 4 | 0.52 | 15.72 | 323.11 | 0.48 | 28.46 | 335.51 | 0.52 | 0.006708 | 0.005211 | 0.006159 | 55 |
| 5 | 0.25 | 6.40 | 204.98 | 0.30 | 26.27 | 319.36 | 0.27 | 0.009605 | 0.010055 | 0.010506 | 33 |
| **Average** | | **13.38** | **292.74** | | **27.48** | **327.36** | | | | | |
| **After signal processing** | | | | | | | | | | | |
| 1 | 0.34 | 14.07 | 303.9 | 0.41 | 25.21 | 325 | 0.4 | 0.007668 | 0.006266 | 0.007490 | 33.5 |
| 2 | 0.34 | 14.97 | 329.25 | 0.45 | 26.40 | 343.52 | 0.42 | 0.007182 | 0.005631 | 0.006520 | 74 |
| 3 | 0.49 | 18.69 | 314.93 | 0.48 | 28.22 | 330.13 | 0.44 | 0.006661 | 0.004975 | 0.006172 | 29 |
| 4 | 0.52 | 15.78 | 321.63 | 0.59 | 26.74 | 346.35 | 0.54 | 0.005450 | 0.004234 | 0.005023 | 39 |
| 5 | 0.25 | 14.42 | 283.08 | 0.26 | 22.92 | 300.95 | 0.28 | 0.011706 | 0.010026 | 0.012148 | 23 |
| **Average** | | **15.59** | **310.56** | | **25.90** | **329.19** | | | | | |

**Table B.7 Calculation of $\alpha_{meas,p}$ , $\beta_{meas,p}$ and $v_{meas,p}$ before and after signal processing**

**calculated using the probe dimension measured before and after (table 11.5) collecting data with**

**$\alpha_{ref}$ = 14° and $\beta_{ref}$ =0° at different $v_{ref}$**

| ***Tests*** | **average $\delta t_{ii}$** | | | **average individual bubble** | | |
|---|---|---|---|---|---|---|
| | $\varepsilon_{abs,\alpha,m,p}$ (deg) | $\varepsilon_{abs,\beta,m,p}$ (deg) | $\varepsilon_{v,m,p}$ (%) | $\varepsilon_{abs,\alpha,m,p}$ (deg) | $\varepsilon_{abs,\beta,m,p}$ (deg) | $\varepsilon_{v,m,p}$ (%) |
| | **Probe measured before collecting data** | | | | | |
| | Error calculation before signal processing | | | | | |
| 1 | 2.94 | 43.32 | 30.69 | 12.01 | 33.54 | 17.38 |
| 2 | 3.26 | 54.60 | 13.45 | 13.98 | 20.38 | 6.32 |
| 3 | 1.97 | 22.97 | 7.68 | 14.84 | 40.94 | 11.82 |
| 4 | 1.87 | 36.05 | 7.21 | 14.68 | 24.07 | 0.79 |
| 5 | 4.48 | 34.77 | 23.70 | 15.21 | 28.38 | 6.95 |
| | $\bar{\varepsilon}_{abs,\alpha,p}$ | $\bar{\varepsilon}_{abs,\beta,p}$ | $\bar{\varepsilon}_{v,p}$ | $\bar{\varepsilon}_{abs,\alpha,p}$ | $\bar{\varepsilon}_{abs,\beta,p}$ | $\bar{\varepsilon}_{v,p}$ |
| | **2.90** | **38.34** | **16.55** | **14.14** | **29.46** | **8.65** |
| | $\sigma_{abs,a,p}$ | $\sigma_{abs,\beta,p}$ | $\sigma_{v,p}$ | $\sigma_{abs,a,p}$ | $\sigma_{abs,\beta,p}$ | $\sigma_{v,p}$ |
| | **0.95** | **10.43** | **9.23** | **1.14** | **7.23** | **5.59** |
| | Error calculation after signal processing | | | | | |
| 1 | 0.42 | 54.57 | 26.72 | 10.91 | 34.04 | 17.14 |
| 2 | 1.13 | 29.87 | 14.77 | 12.62 | 16.07 | 6.38 |
| 3 | 4.83 | 44.30 | 1.89 | 14.40 | 29.46 | 10.78 |
| 4 | 1.93 | 37.56 | 13.20 | 12.95 | 13.21 | 4.14 |
| 5 | 1.36 | 59.88 | 18.04 | 10.40 | 44.27 | 11.26 |
| | $\bar{\varepsilon}_{abs,\alpha,p}$ | $\bar{\varepsilon}_{abs,\beta,p}$ | $\bar{\varepsilon}_{v,p}$ | $\bar{\varepsilon}_{abs,\alpha,p}$ | $\bar{\varepsilon}_{abs,\beta,p}$ | $\bar{\varepsilon}_{v,p}$ |
| | **1.93** | **45.24** | **14.92** | **12.26** | **27.41** | **9.94** |
| | $\sigma_{abs,a,p}$ | $\sigma_{abs,\beta,p}$ | $\sigma_{v,p}$ | $\sigma_{abs,a,p}$ | $\sigma_{abs,\beta,p}$ | $\sigma_{v,p}$ |
| | **1.53** | **10.93** | **8.02** | **1.45** | **11.51** | **4.48** |
| | **Probe measured after collecting data** | | | | | |
| | Error calculation before signal processing | | | | | |
| 1 | 2.18 | 65.30 | 27.05 | 12.25 | 35.94 | 16.67 |
| 2 | 3.15 | 55.28 | 30.31 | 13.75 | 20.79 | 22.50 |
| 3 | 1.78 | 23.80 | 7.37 | 14.64 | 41.34 | 11.53 |
| 4 | 1.72 | 36.89 | 6.98 | 14.46 | 24.49 | 0.43 |
| 5 | 7.60 | 155.02 | 19.56 | 12.27 | 40.64 | 6.89 |
| | $\bar{\varepsilon}_{abs,\alpha,p}$ | $\bar{\varepsilon}_{abs,\beta,p}$ | $\bar{\varepsilon}_{v,p}$ | $\bar{\varepsilon}_{abs,\alpha,p}$ | $\bar{\varepsilon}_{abs,\beta,p}$ | $\bar{\varepsilon}_{v,p}$ |
| | **3.28** | **67.26** | **18.25** | **13.48** | **32.64** | **11.61** |
| | $\sigma_{abs,a,p}$ | $\sigma_{abs,\beta,p}$ | $\sigma_{v,p}$ | $\sigma_{abs,a,p}$ | $\sigma_{abs,\beta,p}$ | $\sigma_{v,p}$ |
| | **2.22** | **46.17** | **9.69** | **1.04** | **8.46** | **7.64** |
| | Error calculation after signal processing | | | | | |
| 1 | 0.07 | 56.10 | 20.59 | 11.21 | 35.00 | 17.60 |
| 2 | 0.97 | 30.75 | 32.01 | 12.40 | 16.48 | 22.60 |
| 3 | 4.69 | 45.07 | 1.66 | 14.22 | 29.87 | 10.40 |
| 4 | 1.78 | 38.37 | 13.47 | 12.74 | 13.65 | 4.55 |
| 5 | 0.42 | 76.92 | 4.00 | 8.92 | 59.05 | 11.87 |
| | $\bar{\varepsilon}_{abs,\alpha,p}$ | $\bar{\varepsilon}_{abs,\beta,p}$ | $\bar{\varepsilon}_{v,p}$ | $\bar{\varepsilon}_{abs,\alpha,p}$ | $\bar{\varepsilon}_{abs,\beta,p}$ | $\bar{\varepsilon}_{v,p}$ |
| | **1.59** | **49.44** | **14.34** | **11.90** | **30.81** | **13.40** |
| | $\sigma_{abs,a,p}$ | $\sigma_{abs,\beta,p}$ | $\sigma_{v,p}$ | $\sigma_{abs,a,p}$ | $\sigma_{abs,\beta,p}$ | $\sigma_{v,p}$ |
| | **1.66** | **16.07** | **11.13** | **1.77** | **16.22** | **6.20** |

**Table B.8 Errors in the values of polar angle, azimuthal angle and velocity magnitude measured by the probe for table 11.6 for $\alpha_{ref}$ = 14° and $\beta_{ref}$ =0° at different $v_{ref}$**

| | | Average $\delta_{ii}$ | | | Average individual bubble | | | | | | |
|---|---|---|---|---|---|---|---|---|---|---|---|
| Test | $v_{ref}$ | $\alpha_{meas,m,p}$ | $\beta_{meas,m,p}$ | $v_{meas,m,p}$ | $\alpha_{meas,m,p}$ | $\beta_{meas,m,p}$ | $v_{meas,m,p}$ | $dt_{11}$ | $dt_{22}$ | $dt_{33}$ | $NOB$ |
| **Probe measured before collecting data** | | | | | | | | | | | |
| **Before signal processing** | | | | | | | | | | | |
| 1 | 0.34 | 22.15 | 333.92 | 0.43 | 27.02 | 340.25 | 0.40 | 0.00756 | 0.00527 | 0.00643 | 45 |
| 2 | 0.39 | 19.13 | 310.20 | 0.39 | 27.51 | 332.18 | 0.39 | 0.00812 | 0.00609 | 0.00767 | 58 |
| 3 | 0.49 | 31.58 | 282.23 | 0.44 | 31.74 | 323.84 | 0.45 | 0.00634 | 0.00448 | 0.00689 | 58 |
| 4 | 0.52 | 30.33 | 25.41 | 0.45 | 29.86 | 342.49 | 0.52 | 0.00697 | 0.00510 | 0.00471 | 53 |
| 5 | 0.25 | 19.03 | 351.28 | 0.33 | 29.97 | 345.55 | 0.30 | 0.00990 | 0.00740 | 0.00824 | 30 |
| **Average** | | **24.44** | **321.17** | | **29.22** | **336.86** | | | | | |
| **After Signal Process** | | | | | | | | | | | |
| 1 | 0.34 | 21.72 | 332.80 | 0.42 | 26.41 | 339.43 | 0.40 | 0.007734 | 0.005427 | 0.006626 | 40 |
| 2 | 0.39 | 21.60 | 322.24 | 0.43 | 26.99 | 338.86 | 0.41 | 0.007474 | 0.005281 | 0.006666 | 45 |
| 3 | 0.49 | 19.86 | 320.86 | 0.49 | 28.32 | 327.95 | 0.45 | 0.006551 | 0.004777 | 0.005933 | 39 |
| 4 | 0.52 | 26.30 | 346.73 | 0.56 | 30.11 | 343.14 | 0.53 | 0.005828 | 0.003817 | 0.004551 | 40 |
| 5 | 0.25 | 17.73 | 357.70 | 0.34 | 27.51 | 347.72 | 0.30 | 0.009586 | 0.007392 | 0.007996 | 24 |
| **Average** | | **21.44** | **336.07** | | **27.87** | **339.42** | | | | | |
| **Probe measured after collecting data** | | | | | | | | | | | |
| **Before signal processing** | | | | | | | | | | | |
| 1 | 0.34 | 13.79 | 296.22 | 0.41 | 31.62 | 337.42 | 0.39 | 0.007595 | 0.006361 | 0.007588 | 58 |
| 2 | 0.39 | 19.52 | 309.69 | 0.39 | 28.03 | 332.00 | 0.39 | 0.008131 | 0.006101 | 0.007683 | 58 |
| 3 | 0.49 | 18.90 | 339.06 | 0.38 | 25.98 | 344.14 | 0.40 | 0.008583 | 0.006369 | 0.007399 | 52 |
| 4 | 0.52 | 32.39 | 281.70 | 0.44 | 32.33 | 323.63 | 0.45 | 0.006372 | 0.004471 | 0.006875 | 58 |
| 5 | 0.25 | 19.34 | 351.34 | 0.33 | 30.47 | 345.45 | 0.30 | 0.009909 | 0.007404 | 0.008245 | 30 |
| **Average** | | **20.79** | **320.85** | | **29.68** | **336.53** | | | | | |
| **After Signal Process** | | | | | | | | | | | |
| 1 | 0.34 | 23.73 | 332.58 | 0.42 | 29.14 | 337.18 | 0.40 | 0.007743 | 0.005278 | 0.006549 | 50 |
| 2 | 0.39 | 22.00 | 321.87 | 0.43 | 27.51 | 338.66 | 0.40 | 0.007488 | 0.005291 | 0.006679 | 45 |
| 3 | 0.49 | 20.26 | 339.48 | 0.43 | 26.28 | 336.10 | 0.41 | 0.007594 | 0.005513 | 0.006462 | 42 |
| 4 | 0.52 | 20.23 | 320.48 | 0.49 | 28.88 | 327.75 | 0.45 | 0.006564 | 0.004783 | 0.005945 | 39 |
| 5 | 0.25 | 18.03 | 357.82 | 0.34 | 27.99 | 347.61 | 0.30 | 0.009592 | 0.007397 | 0.008001 | 24 |
| **Average** | | **20.85** | **334.45** | | **27.96** | **337.46** | | | | | |

**Table B.9 Calculation of $\alpha_{meas,p}$ , $\beta_{meas,p}$ and $v_{meas,p}$ before and after signal processing calculated using the probe dimension measured before and after (table 11.8) collecting data with $\alpha_{ref}$ = 21° and $\beta_{ref}$ =0° at different $v_{ref}$**

| ***tests*** | **Average $\delta_{ii}$** | | | **Average individual bubble** | | |
|---|---|---|---|---|---|---|
| | $\varepsilon_{abs,\alpha,m,p}$ (deg) | $\varepsilon_{abs,\beta,m,p}$ (deg) | $\varepsilon_{v,m,p}$ (%) | $\varepsilon_{abs,\alpha,m,p}$ (deg) | $\varepsilon_{abs,\beta,m,p}$ (deg) | $\varepsilon_{v,m,p}$ (%) |
| | **Probe measured before collecting data** | | | | | |
| | Error calculation before signal processing | | | | | |
| 1 | 1.15 | 26.08 | 25.65 | 6.02 | 19.75 | 18.76 |
| 2 | 1.88 | 49.80 | 0.29 | 6.51 | 27.82 | 1.23 |
| 3 | 10.58 | 77.77 | 9.56 | 10.74 | 36.16 | 8.39 |
| 4 | 9.33 | 25.41 | 12.61 | 8.86 | 17.51 | 0.26 |
| 5 | 1.97 | 8.72 | 31.28 | 8.97 | 14.45 | 21.51 |
| | $\bar{\varepsilon}_{abs,\alpha,p}$ | $\bar{\varepsilon}_{abs,\beta,p}$ | $\bar{\varepsilon}_{v,p}$ | $\bar{\varepsilon}_{abs,\alpha,p}$ | $\bar{\varepsilon}_{abs,\beta,p}$ | $\bar{\varepsilon}_{v,p}$ |
| | **4.98** | **37.56** | **15.88** | **8.22** | **23.14** | **10.03** |
| | $\sigma_{abs,a,p}$ | $\sigma_{abs,\beta,p}$ | $\sigma_{v,p}$ | $\sigma_{abs,a,p}$ | $\sigma_{abs,\beta,p}$ | $\sigma_{v,p}$ |
| | **4.09** | **23.99** | **11.19** | **1.74** | **7.88** | **8.76** |
| | Error calculation after signal processing | | | | | |
| 1 | 0.72 | 27.20 | 24.07 | 5.41 | 20.57 | 17.25 |
| 2 | 0.60 | 37.76 | 9.47 | 5.99 | 21.14 | 3.87 |
| 3 | 1.14 | 39.14 | 0.07 | 7.32 | 32.05 | 7.74 |
| 4 | 5.30 | 13.27 | 7.50 | 9.11 | 16.86 | 1.82 |
| 5 | 3.27 | 2.30 | 34.44 | 6.51 | 12.28 | 21.76 |
| | $\bar{\varepsilon}_{abs,\alpha,p}$ | $\bar{\varepsilon}_{abs,\beta,p}$ | $\bar{\varepsilon}_{v,p}$ | $\bar{\varepsilon}_{abs,\alpha,p}$ | $\bar{\varepsilon}_{abs,\beta,p}$ | $\bar{\varepsilon}_{v,p}$ |
| | **2.21** | **23.93** | **15.11** | **6.87** | **20.58** | **10.49** |
| | $\sigma_{abs,a,p}$ | $\sigma_{abs,\beta,p}$ | $\sigma_{v,p}$ | $\sigma_{abs,a,p}$ | $\sigma_{abs,\beta,p}$ | $\sigma_{v,p}$ |
| | **1.86** | **15.77** | **12.65** | **2.82** | **9.72** | **8.07** |
| | **Probe measured after collecting data** | | | | | |
| | Error calculation before signal processing | | | | | |
| 1 | 7.21 | 63.78 | 21.21 | 10.62 | 22.58 | 14.40 |
| 2 | 1.48 | 50.31 | 0.11 | 7.03 | 28.00 | 1.09 |
| 3 | 2.10 | 20.94 | 21.71 | 4.98 | 15.86 | 17.75 |
| 4 | 11.39 | 78.30 | 14.92 | 11.33 | 36.37 | 13.94 |
| 5 | 1.66 | 8.66 | 31.42 | 9.47 | 14.55 | 20.97 |
| | $\bar{\varepsilon}_{abs,\alpha,p}$ | $\bar{\varepsilon}_{abs,\beta,p}$ | $\bar{\varepsilon}_{v,p}$ | $\bar{\varepsilon}_{abs,\alpha,p}$ | $\bar{\varepsilon}_{abs,\beta,p}$ | $\bar{\varepsilon}_{v,p}$ |
| | **4.77** | **44.40** | **17.87** | **8.68** | **23.47** | **13.63** |
| | $\sigma_{abs,a,p}$ | $\sigma_{abs,\beta,p}$ | $\sigma_{v,p}$ | $\sigma_{abs,a,p}$ | $\sigma_{abs,\beta,p}$ | $\sigma_{v,p}$ |
| | **3.94** | **26.03** | **10.33** | **2.36** | **8.07** | **6.77** |
| | Error calculation after signal processing | | | | | |
| 1 | 2.73 | 27.42 | 23.07 | 8.14 | 22.82 | 16.43 |
| 2 | 1.00 | 38.13 | 9.69 | 6.51 | 21.34 | 3.75 |
| 3 | 0.74 | 20.52 | 12.07 | 5.28 | 23.90 | 15.89 |
| 4 | 0.77 | 39.52 | 5.52 | 7.88 | 32.25 | 13.28 |
| 5 | 2.97 | 2.18 | 34.53 | 6.99 | 12.39 | 21.31 |
| | $\bar{\varepsilon}_{abs,\alpha,p}$ | $\bar{\varepsilon}_{abs,\beta,p}$ | $\bar{\varepsilon}_{v,p}$ | $\bar{\varepsilon}_{abs,\alpha,p}$ | $\bar{\varepsilon}_{abs,\beta,p}$ | $\bar{\varepsilon}_{v,p}$ |
| | **1.64** | **25.55** | **16.97** | **6.96** | **22.54** | **14.13** |
| | $\sigma_{abs,a,p}$ | $\sigma_{abs,\beta,p}$ | $\sigma_{v,p}$ | $\sigma_{abs,a,p}$ | $\sigma_{abs,\beta,p}$ | $\sigma_{v,p}$ |
| | **0.99** | **13.63** | **10.52** | **1.03** | **6.34** | **5.80** |

**Table B.10 Errors in the values of polar angle, azimuthal angle and velocity magnitude measured by the probe for $\alpha_{ref}$ = 21° and $\beta_{ref}$ =0° at different $v_{ref}$**

| | | Average $\delta t_{ii}$ | | | Average individual bubble | | | Average (Avg) | | | |
|---|---|---|---|---|---|---|---|---|---|---|---|
| Test | $v_{ref}$ | $\alpha_{meas,m,p}$ | $\beta_{meas,m,p}$ | $v_{meas,m,p}$ | $\alpha_{meas,m,p}$ | $\beta_{meas,m,p}$ | $v_{meas,m,p}$ | $\delta t_{11}$ | $\delta t_{22}$ | $\delta t_{33}$ | *NOB* |
| **Probe measured before collecting data Before Signal processing** | | | | | | | | | | | |
| 1 | 0.34 | 16.89 | 275.33 | 0.39 | 36.92 | 327.10 | 0.37 | 0.007350 | 0.006828 | 0.008324 | 35 |
| 2 | 0.39 | 28.79 | 337.14 | 0.41 | 34.22 | 328.60 | 0.39 | 0.007889 | 0.004853 | 0.006249 | 15 |
| 3 | 0.49 | 32.59 | 327.65 | 0.50 | 37.61 | 325.00 | 0.46 | 0.006330 | 0.003576 | 0.005099 | 46 |
| 4 | 0.52 | 23.45 | 257.98 | 0.47 | 37.31 | 251.35 | 0.52 | 0.005837 | 0.005259 | 0.006898 | 48 |
| 5 | 0.25 | 34.28 | 323.71 | 0.30 | 32.22 | 342.61 | 0.28 | 0.010410 | 0.005669 | 0.008482 | 16 |
| **Avg** | **0.40** | **27.20** | **304.36** | **0.41** | **35.65** | **314.93** | **0.40** | 0.007350 | 0.006828 | 0.008324 | 32 |
| **After Signal processing** | | | | | | | | | | | |
| 1 | 0.34 | 31.32 | 334.36 | 0.41 | 35.33 | 336.65 | 0.39 | 0.007819 | 0.004548 | 0.006133 | 30 |
| 2 | 0.39 | 30.15 | 340.11 | 0.39 | 33.13 | 333.77 | 0.38 | 0.008286 | 0.004974 | 0.006387 | 13 |
| 3 | 0.49 | 34.82 | 323.64 | 0.48 | 37.52 | 324.44 | 0.45 | 0.006490 | 0.003488 | 0.005270 | 34 |
| 4 | 0.52 | 31.94 | 340.53 | 0.60 | 35.31 | 345.37 | 0.56 | 0.005361 | 0.003100 | 0.004049 | 35 |
| 5 | 0.25 | 35.87 | 272.91 | 0.25 | 37.21 | 289.65 | 0.24 | 0.010382 | 0.007459 | 0.012119 | 5 |
| **Avg** | **0.40** | **32.82** | **322.31** | **0.42** | **35.70** | **325.98** | **0.40** | 0.007819 | 0.004548 | 0.006133 | 23 |
| **Probe measured after collecting data Before Signal processing** | | | | | | | | | | | |
| 1 | 0.34 | 17.51 | 274.84 | 0.39 | 37.88 | 43.05 | 0.37 | 0.007616 | 0.006552 | 0.008154 | 35 |
| 2 | 0.39 | 29.64 | 337.65 | 0.40 | 35.26 | 328.98 | 0.39 | 0.008063 | 0.004958 | 0.006386 | 15 |
| 3 | 0.49 | 33.47 | 327.96 | 0.49 | 38.61 | 325.93 | 0.45 | 0.006431 | 0.003631 | 0.005181 | 46 |
| 4 | 0.52 | 24.36 | 257.59 | 0.47 | 38.24 | 341.75 | 0.51 | 0.005787 | 0.005211 | 0.006840 | 48 |
| 5 | 0.25 | 35.17 | 323.93 | 0.30 | 32.92 | 342.67 | 0.27 | 0.010357 | 0.005636 | 0.008439 | 16 |
| **Avg** | **0.40** | **28.03** | **304.39** | **0.41** | **36.58** | **276.48** | **0.40** | 0.007616 | 0.006552 | 0.008154 | 32 |
| **After Signal processing** | | | | | | | | | | | |
| 1 | 0.34 | 32.21 | 334.81 | 0.35 | 36.33 | 36.03 | 0.38 | 0.009124 | 0.005306 | 0.007156 | 29 |
| 2 | 0.39 | 31.05 | 340.65 | 0.38 | 34.13 | 334.15 | 0.38 | 0.008475 | 0.005086 | 0.006533 | 13 |
| 3 | 0.49 | 35.71 | 323.87 | 0.47 | 38.50 | 324.64 | 0.45 | 0.006593 | 0.003542 | 0.005354 | 34 |
| 4 | 0.52 | 32.89 | 341.05 | 0.60 | 36.27 | 345.78 | 0.55 | 0.005338 | 0.003086 | 0.004032 | 35 |
| 5 | 0.25 | 36.93 | 272.42 | 0.25 | 38.16 | 289.45 | 0.24 | 0.010238 | 0.007346 | 0.011950 | 5 |
| **Avg** | **0.40** | **33.76** | **322.56** | **0.41** | **36.68** | **266.01** | **0.40** | 0.009124 | 0.005306 | 0.007156 | 23 |

**Table B.11 Calculation of $\alpha_{meas,p}$ , $\beta_{meas,p}$ and $v_{meas,p}$ before and after signal processing calculated using the probe dimension measured before and after (table 11.11) collecting data with $\alpha_{ref}$ = 34° and $\beta_{ref}$ =0° at different $v_{ref}$**

| | Average $\delta t_{ii}$ | | | Average individual bubble | | |
|---|---|---|---|---|---|---|
| ***tests*** | $\varepsilon_{abs,\alpha,m,p}$ (deg) | $\varepsilon_{abs,\beta,m,p}$ (deg) | $\varepsilon_{v,m,p}$ (%) | $\varepsilon_{abs,\alpha,m,p}$ (deg) | $\varepsilon_{abs,\beta,m,p}$ (deg) | $\varepsilon_{v,m,p}$ (%) |
| **Probe measured before data collection** | | | | | | |
| Error calculation before signal processing | | | | | | |
| 1 | 17.11 | 84.67 | 14.19 | 2.92 | 32.90 | 8.27 |
| 2 | 5.22 | 22.86 | 3.98 | 0.22 | 31.40 | 0.90 |
| 3 | 1.41 | 32.35 | 1.28 | 3.61 | 35.00 | 6.54 |
| 4 | 10.55 | 102.02 | 9.49 | 3.31 | 108.65 | 0.38 |
| 5 | 0.28 | 36.29 | 20.46 | 1.78 | 17.39 | 10.71 |
| | $\bar{\varepsilon}_{abs,\alpha,p}$ | $\bar{\varepsilon}_{abs,\beta,p}$ | $\bar{\varepsilon}_{v,p}$ | $\bar{\varepsilon}_{abs,\alpha,p}$ | $\bar{\varepsilon}_{abs,\beta,p}$ | $\bar{\varepsilon}_{v,p}$ |
| | **4.08** | **56.89** | **10.41** | **2.90** | **53.68** | **5.88** |
| | $\sigma_{abs,a,p}$ | $\sigma_{abs,\beta,p}$ | $\sigma_{v,p}$ | $\sigma_{abs,a,p}$ | $\sigma_{abs,\beta,p}$ | $\sigma_{v,p}$ |
| | **4.60** | **31.95** | **7.86** | **0.80** | **39.53** | **4.24** |
| Error calculation after signal processing | | | | | | |
| 1 | 2.68 | 25.64 | 20.13 | 1.33 | 23.35 | 13.24 |
| 2 | 3.85 | 19.89 | 0.97 | 0.87 | 26.23 | 2.03 |
| 3 | 0.81 | 36.36 | 2.85 | 3.52 | 35.56 | 7.66 |
| 4 | 2.06 | 19.47 | 14.95 | 1.31 | 14.63 | 6.93 |
| 5 | 1.87 | 87.09 | 0.65 | 3.21 | 70.35 | 3.72 |
| | $\bar{\varepsilon}_{abs,\alpha,p}$ | $\bar{\varepsilon}_{abs,\beta,p}$ | $\bar{\varepsilon}_{v,p}$ | $\bar{\varepsilon}_{abs,\alpha,p}$ | $\bar{\varepsilon}_{abs,\beta,p}$ | $\bar{\varepsilon}_{v,p}$ |
| | **1.58** | **47.64** | **6.15** | **2.68** | **40.18** | **6.10** |
| | $\sigma_{abs,a,p}$ | $\sigma_{abs,\beta,p}$ | $\sigma_{v,p}$ | $\sigma_{abs,a,p}$ | $\sigma_{abs,\beta,p}$ | $\sigma_{v,p}$ |
| | **0.55** | **28.73** | **6.29** | **0.98** | **22.98** | **1.71** |
| **Probe measured after data collection** | | | | | | |
| Error calculation before signal processing | | | | | | |
| 1 | 16.50 | 85.16 | 13.81 | 3.88 | 43.05 | 7.36 |
| 2 | 4.36 | 22.35 | 3.67 | 1.26 | 31.02 | 0.02 |
| 3 | 0.53 | 32.04 | 0.83 | 4.61 | 34.07 | 7.45 |
| 4 | 9.64 | 102.41 | 10.26 | 4.24 | 18.25 | 1.27 |
| 5 | 1.17 | 36.07 | 19.84 | 1.08 | 17.33 | 9.90 |
| | $\bar{\varepsilon}_{abs,\alpha,p}$ | $\bar{\varepsilon}_{abs,\beta,p}$ | $\bar{\varepsilon}_{v,p}$ | $\bar{\varepsilon}_{abs,\alpha,p}$ | $\bar{\varepsilon}_{abs,\beta,p}$ | $\bar{\varepsilon}_{v,p}$ |
| | **6.44** | **55.61** | **9.68** | **3.01** | **28.74** | **5.20** |
| | $\sigma_{abs,a,p}$ | $\sigma_{abs,\beta,p}$ | $\sigma_{v,p}$ | $\sigma_{abs,a,p}$ | $\sigma_{abs,\beta,p}$ | $\sigma_{v,p}$ |
| | **5.97** | **31.96** | **6.86** | **1.53** | **9.78** | **3.85** |
| Error calculation after signal processing | | | | | | |
| 1 | 1.79 | 25.19 | 2.94 | 2.33 | 36.03 | 12.31 |
| 2 | 2.95 | 19.35 | 1.31 | 0.13 | 25.85 | 2.74 |
| 3 | 1.71 | 36.13 | 3.37 | 4.50 | 35.36 | 8.48 |
| 4 | 1.11 | 18.95 | 14.47 | 2.27 | 14.22 | 6.00 |
| 5 | 2.93 | 87.58 | 0.74 | 4.16 | 70.55 | 5.28 |
| | $\bar{\varepsilon}_{abs,\alpha,p}$ | $\bar{\varepsilon}_{abs,\beta,p}$ | $\bar{\varepsilon}_{v,p}$ | $\bar{\varepsilon}_{abs,\alpha,p}$ | $\bar{\varepsilon}_{abs,\beta,p}$ | $\bar{\varepsilon}_{v,p}$ |
| | **2.10** | **37.44** | **4.57** | **2.68** | **36.40** | **6.96** |
| | $\sigma_{abs,a,p}$ | $\sigma_{abs,\beta,p}$ | $\sigma_{v,p}$ | $\sigma_{abs,a,p}$ | $\sigma_{abs,\beta,p}$ | $\sigma_{v,p}$ |
| | **0.73** | **25.83** | **5.05** | **1.57** | **18.82** | **3.24** |

**Table B.12 Errors in the values of polar angle, azimuthal angle and velocity magnitude measured by the probe for table 11.1 for $\alpha_{ref}$ = 34° and $\beta_{ref}$ =0° at different $v_{ref}$**